

Dissertation
submitted to the
**Combined Faculty of Mathematics, Engineering and Natural
Sciences of Heidelberg University, Germany**
for the degree of
Doctor of Natural Sciences

Put forward by
Maria Selina Nitschai
born in Mülheim an der Ruhr, Germany
Oral examination: 2nd of July 2024

Dynamics of the Milky Way Disk and Spectroscopic Analysis of ω Centauri

Referees: Dr. Nadine Neumayer
Prof. Dr. Michela Mapelli

Abstract

The Milky Way is the perfect laboratory to study galaxy evolution and formation due to our unique position inside its disk. Recent surveys and instruments can provide an extensive amount of data for our Galaxy that are the key to revealing its assembly history. In this thesis, I first combine *Gaia* EDR3 and APOGEE data throughout Galactocentric radii between $5.0 \leq R \leq 19.5$ kpc and construct a dynamical model. Using the spherically-aligned Jeans Anisotropic Method I model the stellar velocities and the velocity dispersions of the Galactic disk. This model can capture the main kinematic features and give an accurate mass density of the Galaxy, making it a fundamental test for both galaxy dynamics in general and the mass distribution of the Milky Way. Further, I focus on Omega Centauri (ω Cen), the most massive globular cluster in the Milky Way, which has long been suspected to be the stripped nucleus of a dwarf galaxy that fell into the Galaxy a long time ago. This merger event was the last significant merger the Galaxy has experienced and is therefore an important event in its evolution. Firstly, I present a MUSE spectroscopic dataset with more than 300,000 extracted stellar spectra, reaching more than two magnitudes below the main sequence turn-off. This massive spectroscopic dataset will enable future studies that will transform our understanding of ω Cen. Secondly, I investigate the underlying metallicity distributions as well as the spatial variations of the populations within the cluster for the red giant branch stars. For that, I combine the new MUSE spectroscopy with new *HST* photometry and show that there appears to be no gradient in metallicity, indicating that the cluster is well mixed and any merger happened many years ago. Finally, I conclude with future studies that will investigate the stellar populations, ages, abundances, kinematics, and dynamics of ω Cen in great detail.

Zusammenfassung

Die Milchstraße ist das perfekte Testobjekt, um die Entwicklung und Entstehung von Galaxien zu untersuchen, da wir uns innerhalb ihrer Scheibe befinden. Neue Messungen und Instrumente liefern eine große Menge an Daten für unsere Galaxie, die der Schlüssel zur Untersuchung ihrer Entstehungsgeschichte sind. In meiner Arbeit kombiniere ich zunächst *Gaia* EDR3- und APOGEE-Daten über galaktozentrische Radien zwischen $5.0 \leq R \leq 19.5$ kpc und konstruiere ein dynamisches Modell. Unter Verwendung der sphärisch ausgerichteten Jeans-Anisotropie-Methode modellierte ich die stellaren Geschwindigkeiten und die Geschwindigkeitsdispersionen der Galaktischen Scheibe. Dieses Modell kann die wichtigsten kinematischen Merkmale erfassen und die Massendichte der Galaxie genau zu bestimmen, was es zu einem grundlegenden Test sowohl für Galaxiendynamik als auch für die Massenverteilung der Milchstraße macht. Außerdem konzentriere ich mich auf Omega Centauri (ω Cen), den massereichsten Kugelsternhaufen in der Milchstraße, von dem seit langem vermutet wird, dass er der Kernsternhaufen einer Zwerggalaxie ist, die vor langer Zeit in die Galaxie gefallen ist. Dieser Merger war die letzte große Interaktion der Milchstraße mit einer anderen Galaxie und somit ein wichtiges Ereignis in ihrer Entwicklung. Zunächst präsentierte ich einen MUSE-spektroskopischen Datensatz mit mehr als 300.000 extrahierten Sternspektren, die mehr als zwei Größenordnungen unterhalb des Abknickpunkts der Hauptreihe liegen. Dieser umfangreiche spektroskopische Datensatz wird zukünftige Studien ermöglichen, die unser Verständnis von ω Cen verändern werden. Danach untersuche ich die zugrundeliegenden Metallizitätsverteilungen sowie die räumlichen Variationen der Populationen innerhalb des Haufens für die Sterne des Roten Riesenastes. Dazu kombiniere ich die neue MUSE-Spektroskopie mit neuer *HST*-Photometrie und zeige, dass es keinen Gradienten in der Metallizität zu geben scheint, was darauf hindeutet, dass der Haufen gut durchmischt ist und ein Merger vor vielen Jahren stattgefunden hat. Schlussendlich schließe ich mit zukünftigen Studien, die die stellaren Populationen, das Alter und die Elementhäufigkeit der Sterne, die Kinematik und die Dynamik von ω Cen im Detail untersuchen werden.

Contents

List of Abbreviations	XIV
List of Figures	XVI
List of Tables	XVII
1 FOREWORD	19
1.1 Motivation	19
1.2 Outline	19
2 INTRODUCTION	21
2.1 Milky Way	21
2.1.1 Morphology	22
2.1.2 Accretion History	25
2.2 Stripped Nuclei	27
2.2.1 Globular Clusters	27
2.2.2 Nuclear Star Clusters	28
2.2.3 Formation of Stripped Nuclei	29
2.2.4 Black Holes and NSCs	30
2.3 Omega Centauri	31
Take away points	34
3 DYNAMICAL MODEL OF THE MILKY WAY	35
3.1 Introduction	36
3.2 Data	38
3.2.1 Data Set	38
3.2.2 Kinematic Maps	39
3.3 Methods	41
3.3.1 Mass Distribution of the Milky Way Model	41
3.3.1.1 Distribution with an Exponential Disk Model	41
3.3.1.2 Distribution with a Flared Disk Model	42
3.3.2 MGE with Negative Gaussians but Nonnegative Density Everywhere	44
3.3.3 Modeling	45
3.4 Results	46
3.4.1 Exponential Disk Model	46
3.4.2 Assessing Systematic Errors Due to Nonaxisymmetries	49

3.4.3	Flared Disk Model	51
3.5	Conclusion	52
Appendices	53
3.A	Posterior Distribution	53
3.B	The Dark Matter Axial Ratio (q_{DM}) as a Free Parameter	55
3.C	Investigating the Offset of V_{circ} between Our Result and Previous Work	55
	Take away points	56
4	MUSE SPECTROSCOPY OF ω CENTAURI	57
4.1	Introduction	58
4.2	Data	60
4.2.1	Observations and Data Sets	60
4.2.2	Data Reduction	61
4.3	Analysis Methods	62
4.3.1	Spectral Extraction	62
4.3.2	Completeness	63
4.3.3	Spectral Fitting	64
4.4	Analysis	66
4.4.1	Reliability Parameter	66
4.4.2	Error Analysis	67
4.4.3	Combining Multiple Measurements	70
4.4.4	Membership	71
4.4.5	Atomic Diffusion Correction	72
4.4.6	Perspective rotation	74
4.4.7	Catalog	75
4.4.8	Literature Comparison	76
4.5	Conclusion	77
Appendices	78
4.A	Data Conditions	78
4.B	PAMELMUSE Tests	80
4.C	Surface Gravity $\log(g)$	80
4.C.1	Free $\log(g)$	82
4.C.2	Metal Rich Stars	82
4.C.3	Literature $\log(g)$	82
4.D	SNR Test	83
4.E	Catalog Columns	84
	Take away points	84
5	SPATIALLY WELL-MIXED POPULATIONS OF ω CENTAURI	87
5.1	Introduction	88
5.2	Data	89
5.2.1	Spectroscopic Data	89
5.2.2	Photometric Data	90
5.2.3	Quality Cuts	91
5.3	Results	92
5.3.1	Metallicity Distribution	92
5.3.2	Chromosome Map	95
5.3.2.1	Metallicity Dependency	96
5.3.2.2	The Metal-Poor Component and Its Multiple Populations	97

5.3.3	Spatial 2D Metallicity Distribution	98
5.3.4	Metallicity Gradients	100
5.3.4.1	Overall Cluster Gradient	100
5.3.4.2	Spatial Differences between Subpopulations	101
5.3.4.3	Differences in the Two Streams of [M/H] vs $\Delta_{F275W,F814W}$	102
5.4	Conclusion	103
Appendices	104
5.A	Completeness	104
5.B	[M/H] Bias	104
5.C	Details for the Chromosome Map	105
Take away points	109
6	OUTLOOK	111
6.1	Line-of-Sight Kinematics	111
6.1.1	Velocity Maps	113
6.1.2	Kinematic Analysis	113
6.2	Follow up Projects	114
6.2.1	Intermediate Mass Black Hole in ω Cen	114
6.2.2	Ages and Subpopulation Identification	116
6.2.3	Abundance Differences between the Subpopulations	117
6.2.4	Elemental Abundance Catalog for ω Cen	118
6.3	Future Projects	119
6.4	Conclusion	119
Take away points	120
7	CONCLUSION	121
Software and Data		125
Acknowledgement		127
List of Publications		129
Bibliography		131

List of Abbreviations

ω Cen	Omega Centauri
<i>HST</i>	<i>Hubble Space Telescope</i>
1G	first-generation
2G	second-generation
2MASS	Two Micron All Sky Survey
ACS	Advanced Camera for Surveys
AD	atomic diffusion
ADC	atomic diffusion correction
AGB	asymptotic giant branch
AO	adaptive optics
BIC	Bayes Information Criterion
BSS	blue stragglers sequence
CDF	cumulative distribution function
CMD	colour-magnitude diagram
DD-Payne	Data-Driven Payne
Dec	declination
DR2	data release 2
EDR3	early data release 3
ESA	European Space Agency
ESO	European Southern Observatory
FWHM	full width at half maximum
GC	globular cluster
gNFW	generalized Navarro, Frenk and White profile
GO	General Observer
GTO	guaranteed time observation
HB	horizontal branch
IFU	integral field unit
IMBH	intermediate-mass black hole
JAM	Jeans Anisotropic modeling
JAM _{cyl}	cylindrically-aligned Jeans Anisotropic modeling
JAM _{sph}	spherically-aligned Jeans Anisotropic modeling
KDE	kernel density estimator
LOESS	locally weighted regression
LOS	line-of-sight

MCMC	Markov chain Monte Carlo
MGE	multi-Gaussian expansion
MS	main sequence
MSTO	main sequence turn-off
MUSE	Multi-Unit Spectroscopic Explorer
NFM	narrow field adaptive optics mode
NFW	Navarro, Frenk and White profile
NSC	nuclear star cluster
OB	observing block
PA	position angle
PI	principal investigator
PSF	point spread function
RA	right ascension
RGB	red giant branch
SDSS	Sloan Digital Sky Survey
SGB	subgiant branch
SMBH	supermassive black hole
SNR	signal-to-noise ratio
UCD	ultra-compact dwarf galaxy
VLT	Very Large Telescope
WFC	Wide Field Channel
WFC3	Wide Field Camera 3
WFM	wide field mode
WISE	Wide-field Infrared Survey Explorer

List of Figures

2.1	Milky Way Image from the <i>Gaia</i> Early Data Release 3	22
2.2	Warp and Flare of the Galactic Disk	23
2.3	Galactic Bulge and Bar	24
2.4	Galactic Center	25
2.5	<i>Gaia</i> -Enceladus Members	26
2.6	Globular Cluster NGC 6388	27
2.7	Nuclear Star Clusters	28
2.8	Sagittarius Dwarf Merger with the Milky Way	29
2.9	Mass-Size Plane	30
2.10	ESO Image of ω Cen	31
2.11	CMD of ω Cen Showing 15 Subpopulations	32
2.12	Fimbulthul Stream	32
2.13	M_{NSC} vs M_{\star} Host Galaxy Mass	33
3.1	Velocity Maps for the Combined Data from Gaia EDR3 with That from Hogg et al. (2019)	39
3.2	Uncertainty Maps for the Combined Data	40
3.3	Luminosity Density Profile of the Milky Way without and with Flaring	43
3.4	New MGE Basis Function	44
3.5	Best Fit for the JAM _{sph}	46
3.6	Circular Velocity for the JAM _{sph} Model without Flaring	48
3.7	Surface Density for the JAM _{sph} Model without Flaring	50
3.8	The Difference between the JAM _{sph} without and with a Flared Disk	51
3.9	Posterior Distribution for the Best-Fitting JAM _{sph} with an Exponential Disk Model	53
3.10	Posterior Distribution for the Best-Fitting JAM _{sph} with a Flared Disk Model	54
3.11	Circular Velocity Curve Same Assumptions as in Eilers et al. (2019)	55
4.1	MUSE Image of ω Cen	59
4.2	Image of ω Cen and Footprint of the MUSE Pointings	61
4.3	All Extracted GO Stars	62
4.4	GO Completeness Plots	63
4.5	CMD of GO stars	64
4.6	Example Spectra	65
4.7	Error Analysis Correction	69
4.8	Error Analysis CDF	69

4.9	Membership Probabilities Using Radius and Velocity for a SNR>10	71
4.10	Atomic Diffusion Correction	73
4.11	M/H of RGB vs. MSTO Post AD Correction	74
4.12	Perspective Rotation	74
4.13	SNR in the Catalog	75
4.14	Comparison to Literature Values	77
4.15	Discrepancy between Spectral Parameters with Free and Fixed log(g)	81
4.16	Metal Rich	82
4.17	Literature Comparison log(g)	83
4.18	SNR Test	84
5.1	Footprint of Data Sets	88
5.2	Color-Magnitude Diagrams	90
5.3	Metallicity Distribution	93
5.4	Chromosome Map of ω Cen	96
5.5	Δ Values as a Function of M/H	97
5.6	Multiple Populations in the Metal-Poor Stars	98
5.7	Metallicity Maps	99
5.8	Overall Metallicity Gradient	100
5.9	Chromosome Map Showing the Four Different Subgroups	101
5.10	Spatial Distribution of the Subgroups	101
5.11	The Two Streams in M/H vs $\Delta_{F275W,F814W}$	102
5.12	Spatial Distribution of the Two Streams in M/H vs $\Delta_{F275W,F814W}$	103
5.13	Completeness and Magnitude	104
5.14	Metallicity Bias	105
5.15	Metallicity Distribution GO and GTO	106
5.16	The Three Subsamples Used to Calculate the Chromosome Map	107
5.17	Final Fiducial Lines	108
5.18	Chromosome Map Color-Coded with the Subgroups Identified in the Metallicity Distribution	109
6.1	Line-of-Sight Velocity Maps	112
6.2	Kinematic Profiles	114
6.3	KINEMETRY Results	115
6.4	Fast Moving Stars in ω Cen	116
6.5	Age Spread in ω Cen	117
6.6	Subpopulations in ω Cen	117
6.7	Stacked Spectra for Each Subpopulation	118
6.8	Anticorrelation between Na vs O	119

List of Tables

3.1	Best-fitting Parameters	47
3.2	Best-fitting Parameters for the Four Sectors	50
3.3	Best-fitting Parameters for the Model with q_{DM} Free	54
4.1	Error Analysis	68
4.2	Observing Conditions	78
4.3	Catalog Columns	85
5.1	Data Samples	92
5.2	Multi-Gaussian Components of the Metallicity Distribution	94
5.3	Final Chromosome Map Values	108

Chapter 1

FOREWORD

1.1 Motivation

Thanks to a vast amount of data and new instruments we are constantly breaking observational records and pushing the limits of our observations to unprecedented distances into the Universe.

Especially thanks to the *Hubble* and the *James Webb Space Telescope* we are finding progressively more distant objects, with the current record for a galaxy being observed ~ 400 million years (Robertson et al., 2023) and for a single star ~ 900 million years after Bing Bang (Welch et al., 2022). The search for distant star clusters is also ongoing, and thanks to gravitational lensing we find more and more distant globular clusters (e.g., Welch et al., 2022; Mowla et al., 2022; Lee et al., 2022; Mowla et al., 2024; Adamo et al., 2024). These distant globular clusters allow us to better understand the early stages of globular clusters and investigate the connection between their formation and galaxy assembly.

However, our home galaxy, the Milky Way, remains a unique laboratory for understanding galaxy evolution and assembly. It remains the only galaxy that we can observe in great detail and resolution. We can resolve individual stars, inside the Galaxy and in its stellar clusters, and obtain spectroscopic information and three-dimensional positions and velocities making it the best case study for the fundamental properties of galaxies.

One specific star cluster that seems to have played a key part in the build-up of the Milky Way is ω Centauri. It is suspected to be a remnant of the last significant merger event our galaxy experienced and the stripped nucleus of a dwarf galaxy. In general, ω Centauri can provide crucial information for our understanding of nuclear star clusters, globular clusters, dwarf galaxies, multiple stellar populations, and even intermediate-mass black holes.

In this thesis, I test our understanding of galaxy dynamics on the Milky Way and constrain its mass distribution. At the same time, I investigate ω Centauri and its multiple populations, which can provide insights into its interactions with the Galaxy and its formation history.

1.2 Outline

I start the thesis with a summary of the main background knowledge in Chapter 2, which includes our current understanding of the Milky Way, globular clusters, nuclear clusters,

and ω Centauri. I then continue in Chapter 3 presenting a dynamical model of the Milky Way disk using data from *Gaia* and APOGEE. I describe in Chapter 4 the compilation of a spectroscopic catalog for ω Centauri using MUSE data for over 300,000 stars within the half-light radius that will enable future investigations into the stellar populations, ages, and kinematics in great detail. In Chapter 5 I combine the spectroscopic catalog presented in Chapter 4 with multi-band photometry and I investigate the underlying metallicity distributions as well as the spatial variations of the populations within the cluster. Further, I include an outlook on future ω Centauri studies. Specifically, I present first insights into the kinematics of the cluster and a summary of follow-up studies that are in preparation in Chapter 6. Finally, I summarize the results from the thesis and conclude in Chapter 7.

To help readers quickly navigate through the content of the thesis, especially if they are familiar with the topics, I include two types of boxes: The Summary box at the beginning of each chapter

Summary/Abstract

A summary of the chapter that follows.

and a box with the key points at the end.

Take away points

The main results and the take away points from the above chapter.

Chapter 2

INTRODUCTION

Summary

Understanding the Milky Way is crucial for our general understanding of galaxy evolution, formation, and the Universe itself. It is the closest galaxy observable to us, making it the best case study we can get. Many new surveys provide us with huge amounts of data that allow us to study its current state but also infer information about its formation and interactions with other smaller galaxies. Globular clusters can provide crucial information about interactions because they are the oldest components of a galaxy and they can survey mergers. Further, some of them might even hide their true nature, since they can be stripped nuclei of smaller galaxies that have been completely disrupted. One of the long-suspected candidates to be a stripped nucleus, due to its complex stellar populations, is ω Centauri. A detailed study of its stars will give us unique insights into nuclear star clusters, galaxy formation, and the merger history of the Milky Way.

Chapter Contents:

2.1	Milky Way	21
2.1.1	Morphology	22
2.1.2	Accretion History	25
2.2	Stripped Nuclei	27
2.2.1	Globular Clusters	27
2.2.2	Nuclear Star Clusters	28
2.2.3	Formation of Stripped Nuclei	29
2.2.4	Black Holes and NSCs	30
2.3	Omega Centauri	31
	Take away points	34

2.1 Milky Way

“No matter which part of it one targets with the telescope, one finds a huge number of stars, several of which are quite large and very striking; yet, the number of small stars is, however, absolutely unfathomable.”

- Galileo Galilei, 1610

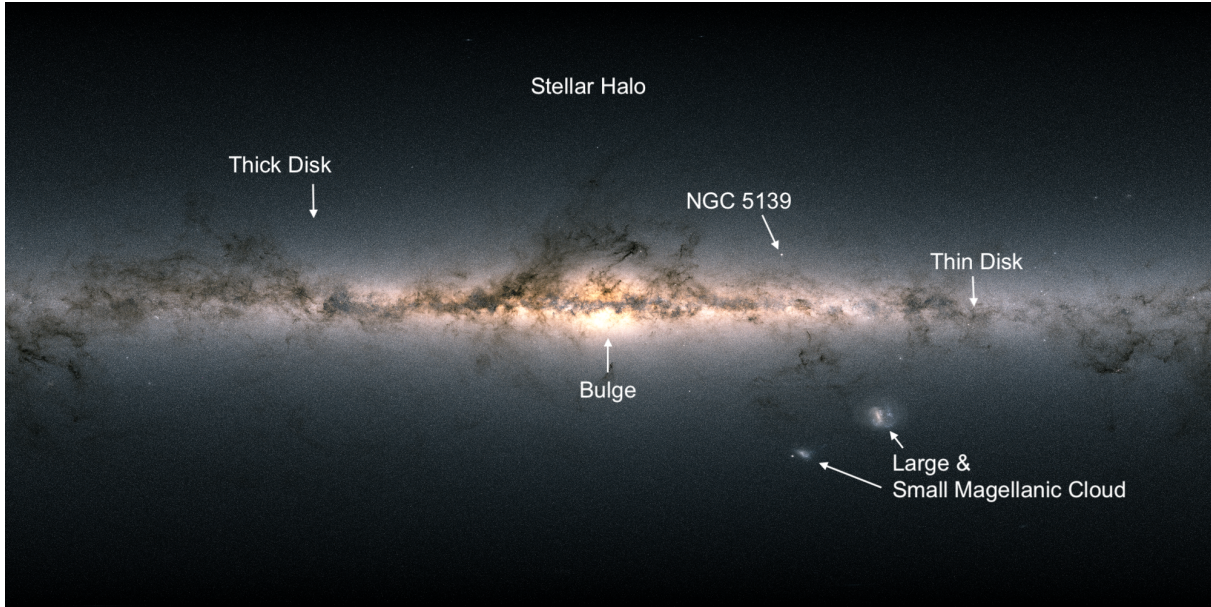


Figure 2.1: Milky Way Image from the Gaia Early Data Release 3. The figure shows the total brightness and color of more than 1.8 billion stars observed with Gaia. The bright horizontal band is the edge-on view of the disk, in the middle of the image inside the bulge lies the Galactic Center, the Large and Small Magellanic Clouds can be seen in the lower right, and many other galaxies and globular clusters are visible as dots above and below the disk. The dark patches are caused due to interstellar dust and gas that absorb the light of the stars lying behind them.

Image Credit: ESA/Gaia/DPAC and Acknowledgement: A. Moitinho.

One of the most beautiful sights in the night sky is a continuous band of light that appears to circle the Earth, the Milky Way. Galileo was the first to realize that this band consists of a vast collection of individual stars and later Kant and Wright proposed that it is a stellar disk and our Solar System is one component of it (Carroll and Ostlie, 2017). Today, we know that indeed the Milky Way is our home galaxy and that it is a barred spiral galaxy. Overall, if we compare the Milky Way with all the galaxies we know today in the Universe, it is in many ways a very typical disk galaxy (see e.g., Bland-Hawthorn and Gerhard, 2016, for a review), however, it remains a very special case to us because it is our home galaxy.

Our position inside the Galaxy allows us to observe it in much greater detail and resolution than we could do for any other galaxy. This makes it the only galaxy where we can obtain detailed information about individual stars, like the 3-dimensional position and velocity, elemental abundances, and ages (Rix and Bovy, 2013) and hence an ideal test object for our understanding of the fundamental properties and behavior of galaxies.

2.1.1 Morphology

Our Galaxy has several visible components: a thin disk and a thick disk, a bulge and bar, and a stellar halo (see Figure 2.1). Each of these components is physically distinct since they differ in their spatial distributions, kinematics, ages, and chemical distributions, but the exact boundaries between them can be difficult to find since the transitions are not sharp. Thanks to several extensive surveys in the last years, like *Gaia* (Gaia Collaboration et al., 2016), APOGEE (Allende Prieto et al., 2008) and Sloan Digital Sky Survey (SDSS, York et al., 2000), significant progress in characterizing these structures has been made. Studying them allows us to learn about the buildup of the Galaxy throughout its life and

how its future evolution will proceed.

Disk

The Disk is the dominant stellar component with three-quarters of the stars and it can be further divided into two components, the thin disk and the thick disk.

The thin disk is the bright band of light we see in the night sky. It is a highly flattened structure with an exponential radial scale length of ~ 2.6 kpc and scale height of ~ 0.3 kpc (e.g., López-Corredoira et al., 2002; Jurić et al., 2008; McMillan, 2011; Bland-Hawthorn and Gerhard, 2016). It contains younger and more metal-rich stars since it is the sight of ongoing star formation and they are on fairly circular orbits and with lower velocity dispersions (Rix and Bovy, 2013). The thick disk contains older and metal-poor stars, with the suggested age difference between the thin and thick disk being at least ~ 1.6 Gyr (Kilic et al., 2017). The older stars make the structure thicker, more diffuse, and hotter (Rix and Bovy, 2013). In the past, the disks were distinguished only spatially, however, we now know that using stellar chemistry is more appropriate. Specifically the $[\alpha/\text{Fe}]$ vs. $[\text{Fe}/\text{H}]$ abundances reveal a bimodality with the “low- α ” and the “high- α ” components separating the thin and thick disk respectively (e.g., Haywood et al., 2013; Bensby et al., 2014).

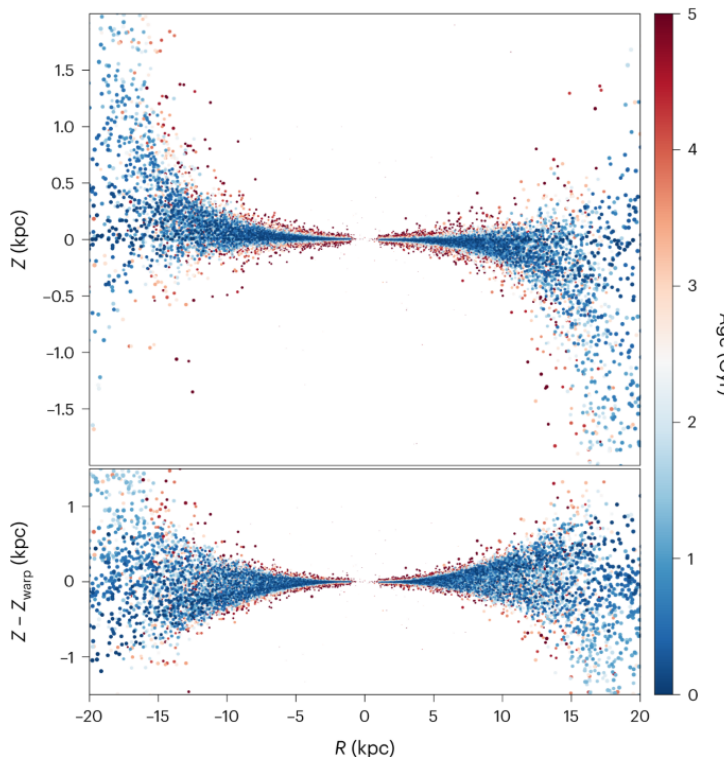


Figure 2.2: Warp and Flare of the Galactic Disk. The figure shows the present-day distribution of simulated stars in Galactocentric cylindrical coordinates. The top panel shows the warp and the bottom panel the vertical deviation from the warp, demonstrating the flare of the disk. The stars are color-coded with age and stars with negative R have azimuthal angles within 90° of the northern warp while stars with positive R are within 90° of the southern warp.

Figure Credit: Taken from Han et al. (2023)

Thanks to a large amount of data the *Gaia* satellite mission provided we can study the disk in great detail, confirming what was already seen before (e.g., Churchwell et al., 2009), that there is a lot of substructure due to a complex assembly history (Gaia Collaboration et al., 2018b; Antoja et al., 2018; Bland-Hawthorn et al., 2019, e.g.). Further, even though the exact number and location of the spiral arms are still uncertain, a lot of work has gone into investigating them (Antoja et al., 2016; Rezaei Kh. et al., 2018; Gaia Collaboration et al., 2023a). For the outer parts of the disk, the exact structure is complicated and debated. We know though that the outer part slowly warps away from the Galactic plane

and that the disk flares (e.g., May et al., 1993; Carney and Seitzer, 1993; Derriere and Robin, 2001; Carraro et al., 2015; Skowron et al., 2019; Han et al., 2023), see Figure 2.2 for a simulation of the warp and flaring.

Bulge and Bar

The classical bulge is expected to result from the hierarchical formation early in the evolution of the Galaxy (Kormendy and Kennicutt, 2004), but its mass contribution has been constrained to be small ($\leq 8\%$ of the mass of the disk Shen et al., 2010). Additionally, it is now established that the bulge stars are in a boxy bulge (or “peanut-shaped” or b/p-bulge, e.g., McWilliam and Zoccali, 2010; Nataf et al., 2010; Ness et al., 2012) representing the inner, three-dimensional part of a bar structure. It shows cylindrical rotation and consists of mostly old and metal-enriched stars (Ortolani et al., 1995).

A stable structure of a bar is a common feature of spiral galaxies and it can also be found in the Milky Way (e.g., Binney et al., 1991; Weiland et al., 1994). Many other studies have investigated the Galactic bar and we now know that it has a radius of about ~ 5 kpc (e.g., Wegg et al., 2015b; Bovy et al., 2019), an angle of about $28^\circ - 33^\circ$ (Wegg et al., 2015b) and a pattern speed of $\Omega_b = 41 \pm 3 \text{ km s}^{-1} \text{kpc}^{-1}$ (Bovy et al., 2019). The projections of the Galactic bar and bulge can be seen in Figure 2.3.

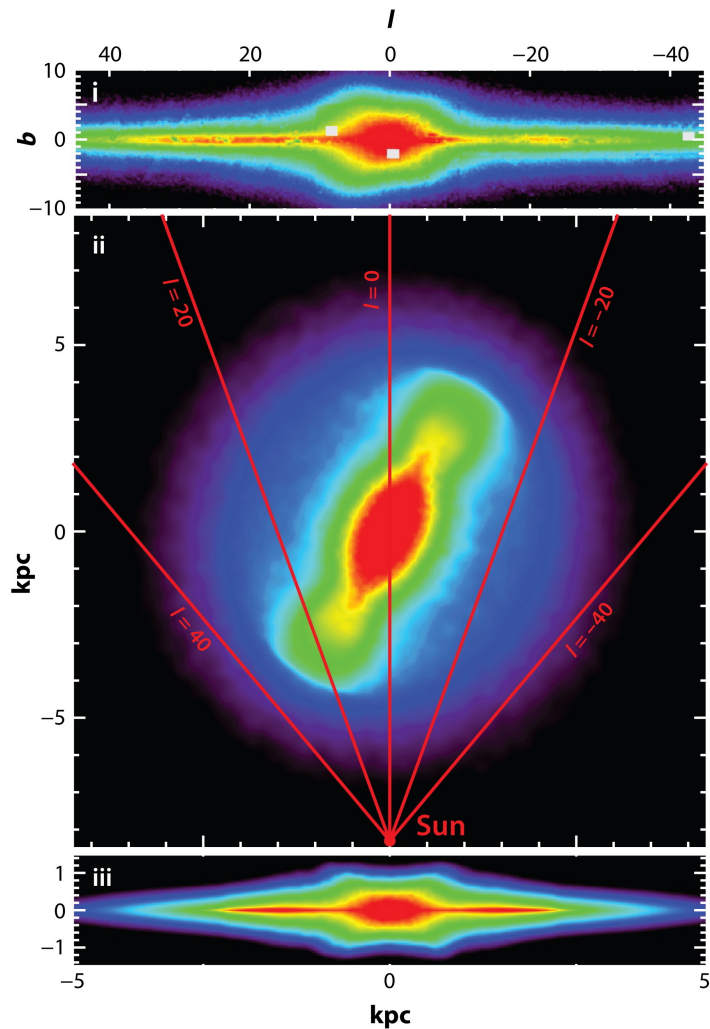


Figure 2.3: Galactic Bulge and Bar. The figure shows the projections of the Galactic bulge and bar using near-infrared star counts. The top panel shows the inner Galaxy as seen from the Sun, and the middle is the projection of a best-fitting model as seen from the North Galactic Pole, with viewing directions from the Sun indicated for longitudes $|l| = 0^\circ; 20^\circ; 40^\circ$. The bottom panel is the side-on view showing the transition from the bulge to the long bar and disk.

Figure Credit: Taken from Bland-Hawthorn and Gerhard (2016)

Galactic Center

In the very central part of the bulge, a nuclear star cluster (NSC) has been found (Becklin and Neugebauer, 1968; Eckart et al., 1995), see Figure 2.4, and at the very center of that cluster lies a supermassive black hole (SMBH), Sgr A*. It has a mass of $M_{\text{SMBH}} = (4.28 \pm 0.10_{\text{stat}} \pm 0.14_{\text{syst}}) M_{\odot}$ (Gillessen et al., 2017) and is at a distance of $R_{\odot} = (8,178 \pm 13_{\text{stat.}} \pm 22_{\text{syst.}})$ pc (Gravity Collaboration et al., 2019) from the Sun.



Figure 2.4: Galactic Center. The image is taken with the Spitzer Space Telescope’s infrared cameras and the bright central spot inside the white circle is the Nuclear Star Cluster.
Image Credit: NASA, Caltech, Susan Stolovy (SSC, Caltech)

Stellar Halo

The last luminous component of the Galaxy is the stellar halo and it makes up only 1 % of its total stellar mass (Bland-Hawthorn and Gerhard, 2016). The halo stars show large random motions, little if any rotation, have a spheroidal to spherical spatial distribution, and can belong to the oldest and the most metal-poor stars in the Galaxy. As a result of large stellar surveys, we know that the stellar halo has a complex structure, with multiple components, and unrelaxed substructures, and that it accretes smaller galaxies (e.g., Ibata et al., 1997). Because of the long dynamical timescales in the halo, tidal tails, shells, and other overdensities due to accretion events remain observable over Gyrs (see Section 2.1.2). From cosmological simulations, we expect the Galaxy to have accreted ~ 100 satellite galaxies, but most of the halo was built ~ 10 Gyr ago from the disruption of one or just a few massive satellites (Bland-Hawthorn and Gerhard, 2016).

Dark Matter Halo

The total mass of the luminous matter is around $5 \times 10^{10} M_{\odot}$ (Bland-Hawthorn and Gerhard, 2016) but this mass is too small to explain the orbits of stars at distances greater than R_{\odot} , hence another mass component is needed. Indeed the Galaxy is embedded in a dark matter halo, where most of the mass of the system is located. Estimates for the virial mass are $\sim 1.3 \times 10^{12} M_{\odot}$ (Posti and Helmi, 2019; Watkins et al., 2019) which is two orders of magnitude higher than the stellar mass alone.

2.1.2 Accretion History

Galaxies tend to live in groups and clusters together, but when they come too close to each other they start to interact and/or merge. These interactions drastically affect their

morphology and their evolution, e.g., they can disrupt their disk, change star formation rates, or even trigger nuclear activity. Major mergers are interactions between two galaxies of a similar mass (mass ratio $\geq 1/3$) and minor mergers are between two galaxies of different masses (mass ratio $\leq 1/4$). Major mergers are violent events that strongly shape the evolution of galaxies, but they are rare events, while minor mergers occur more often (Fakhouri and Ma, 2008), and are presumed to play an important role in the growth and evolution of galaxies. Galaxies can be satellites of larger galaxies and under the constant influence of their tidal fields, eventually sinking toward the center of the potential of the dominant galaxy while getting tidally disrupted and losing its stellar component as streams (e.g., Helmi and White, 2001; Mayer et al., 2002). In the end, the body of the satellite is disrupted and accreted by the dominant galaxy.

Within the cold dark matter cosmological model, the Galaxy is built up over billions of years through hierarchical accretion (see Helmi 2020 for a review). However, we know that it has not experienced any major merger for the past 10 Gyr (Stewart et al., 2008). In recent years many surveys like *Gaia* (Gaia Collaboration et al., 2016), APOGEE (Al-lende Prieto et al., 2008), SDSS (York et al., 2000), and others have provided us with a tremendous data set for our Galaxy. Especially thanks to *Gaia* billions of stars have been measured and millions of stars have now 3D phase-space coordinates, which allows us to identify and study the remnants of the accretion events in the formation history of the Milky Way.

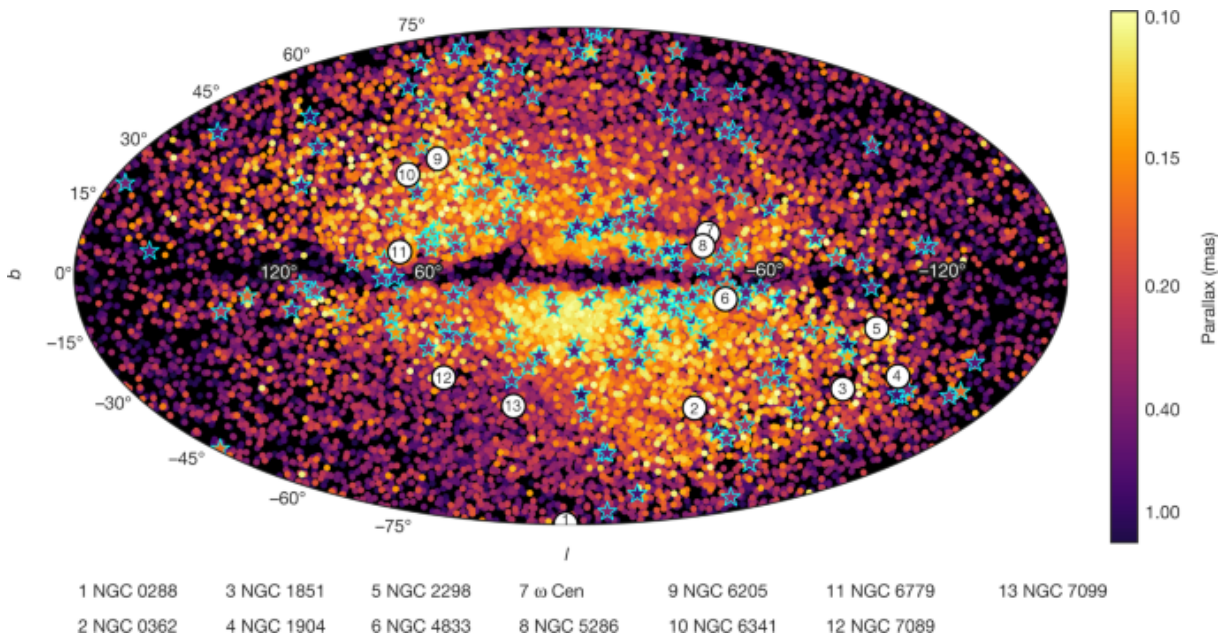


Figure 2.5: Gaia-Enceladus Members. The Figure shows the sky distribution of members from a *Gaia* subsample, color-coded by their distance from the Sun (dark red is near and light yellow is far). The green stars are *Gaia* RR Lyrae stars and the numbers show globular clusters potentially associated with Gaia-Enceladus.

Figure Credit: Taken from Helmi et al. (2018)

The most prominent merger event found today is the *Gaia*-Enceladus or *Gaia*-Sausage (Helmi et al., 2018), see Figure 2.5. It was first seen in Belokurov et al. (2018) but it could not be definitively assigned to a merger event, only with *Gaia* DR2 there was no doubt that these stars were accreted. Its stellar mass has been estimated to be slightly more massive than the Small Magellanic Cloud, making it a 4:1 mass-ratio merger (Helmi et al., 2018). Further, it has a retrograde mean motion and a distinct chemical sequence.

This merger would have caused dynamical heating of the progenitor of the Galactic thick disk perturbing it, approximately 10 Gyr ago and causing significant star formation in the thick disk.

Another significant merger event has been with a dwarf galaxy called Sequoia (Myeong et al., 2019). The stars associated with it have a more retrograde motion and a lower metallicity than *Gaia*-Enceladus. On the other hand, an ongoing example of accretion is the Sagittarius dwarf galaxy, which is wrapped in a stream around the Milky Way created through tidal stripping over the last several Gyr (Ibata et al., 1997; Laporte et al., 2018). In addition, several smaller substructures have been identified in the nearby halo probably associated with past accretion events. The Helmi streams ($\sim 10^8 M_\odot$, Koppelman et al., 2019c), Sequoia ($\sim 10^7 M_\odot$, Koppelman et al., 2019a), Thamnos ($\sim 5 \times 10^6 M_\odot$, Koppelman et al., 2019a), Gaia-Enceladus ($\sim 10^9 M_\odot$, Fattah et al., 2019; Mackereth et al., 2019), and Sagittarius ($\sim 5 \times 10^8 M_\odot$, Dierickx and Loeb, 2017; Fardal et al., 2019), are the largest building blocks of the halo, but it is still not yet clear how and if they are related to each other (Helmi, 2020). Several large substructures have also been known for a while thanks to wide-field photometric surveys, but the relation between these and the so-far identified building blocks, if there are any, has not been understood.

2.2 Stripped Nuclei

In this section, I will focus on a specific product of mergers and interactions between galaxies, the stripped nuclei. For that, we first need to understand what globular clusters and nuclear star clusters are, before looking at the formation of stripped nuclei.

2.2.1 Globular Clusters



Figure 2.6: Globular Cluster NGC 6388.
This figure shows the globular cluster NGC 6388 of the Milky Way observed by the European Southern Observatory (ESO).
Image Credit: ESO, F. Ferraro (University of Bologna)

Globular clusters (GCs) are bound star clusters with up to 10^4 to 10^6 stars. They have on average masses between $10^4 M_\odot$ to $10^6 M_\odot$ and half-light radii of 1 pc to 10 pc. In the Milky Way we have detected around 160 GCs (e.g., Harris, 1996, 2010) with ages

$\gtrsim 6$ Gyr (Kharchenko et al., 2013), see Figure 2.6 for one example of a Milky Way GC. Two origin scenarios for GCs have been suggested, depending on the metallicity of the cluster. The first one is in-situ formation in massive haloes for the more red (metal-rich) GCs, and the second one is accretion from the disruption of a smaller galaxy for the blue (metal-poor) GCs (e.g., Brodie and Strader, 2006; Marín-Franch et al., 2009; Forbes and Bridges, 2010; Leaman et al., 2013).

For many years, GCs were thought to be perfect examples for simple stellar populations, where all stars have the same age and same abundances. However, now we know that almost all GCs host significant abundance spreads within them, but we do not have a conclusive explanation for them (see Bastian and Lardo, 2018, for a review). In GCs we call first-generation (1G) of stars, stars that have primordial composition, and second-generation (2G) stars, stars that are enriched in light elements.

Since GCs are among the oldest objects in the Universe, they are the remaining evidence of the formation and evolution history of their host galaxy.

2.2.2 Nuclear Star Clusters

Nuclear star clusters (NSCs) are massive ($10^6 M_\odot$ to $10^8 M_\odot$) and small (half-light radii of 1 pc to 10 pc, Georgiev and Böker, 2014; Sánchez-Janssen et al., 2019; Neumayer et al., 2020), compact stellar systems at the dynamical center of most galaxies (see Figure 2.7). Due to their size and mass, they are the densest stellar systems in the Universe, $\geq 10^6 M_\odot \text{ pc}^{-3}$ (Neumayer et al., 2020) and they can be found in a wide range of galaxies, with an occupation fraction peaking at galaxy masses in the range of $10^8 M_\odot$ to $10^{10} M_\odot$ (e.g., Sánchez-Janssen et al., 2019; Hoyer et al., 2021). Further, they seem to host multiple stellar populations with differences in metallicity and age of a few Gyr (e.g., Carson et al., 2015; Kacharov et al., 2018).

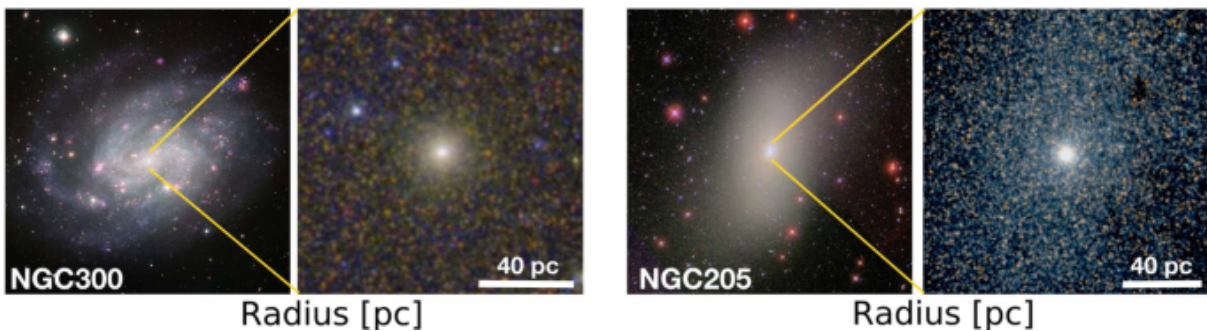


Figure 2.7: Nuclear Star Clusters. The figure shows the galaxy-wide images with zoom-ins into the central regions for the late-type spiral NGC 300 (left) and the early-type galaxy NGC 205 (M110, right). Image Credit: Taken from Neumayer et al. (2020)

There are two proposed mechanisms to explain NSC formation (see Neumayer et al., 2020, for a review), accretion of GCs and in-situ formation (e.g., Milosavljević, 2004). These two formation paths might not be exclusive, and both can contribute to the NSC formation and growth. The accretion scenario can explain the old, metal-poor population in NSCs, and the in-situ scenario would explain the metal-rich population and extended star formation histories, including young stars. Recent studies indicate that more massive NSCs formed predominantly via in situ while lower-mass NSCs have predominantly formed by mergers with GCs (Fahrion et al., 2021, 2022).

Even though GCs and NSCs have similar sizes, they have important differences. NSCs are the most central and nearly always also the brightest cluster in the galaxy. Compared to GCs they are denser, have longer relaxation times, have deeper potential wells, and have well-documented multiage populations (e.g., Kacharov et al., 2018).

2.2.3 Formation of Stripped Nuclei

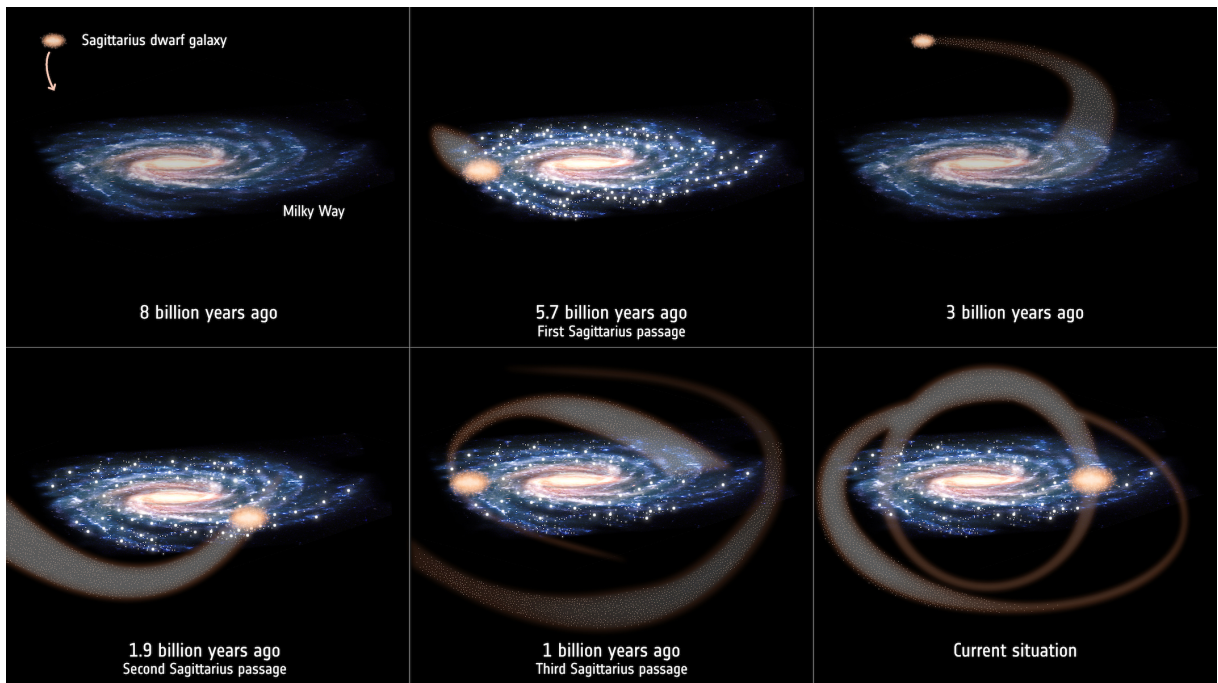


Figure 2.8: Sagittarius Dwarf Merger with the Milky Way. Illustration of how the Sagittarius dwarf galaxy fell into the Milky Way over 8 billion years ago and is still getting disrupted until today, losing its stellar content as streams around the Galaxy. The nuclear star cluster however remains intact and is known as the globular cluster M54.

Image Credit: European Space Agency (ESA)

In Section 2.1.2 I already mentioned the hierarchical growth of galaxies and that the Milky Way shows a lot of substructures because of its merger history. We know that GCs can survive the strong tidal effects, thus we expect that NSCs, the densest star clusters we know, also survive. During the accretion of a smaller galaxy, the main stellar body of the satellite gets disrupted, but its NSC will survive and end as a stripped nucleus (e.g., Pfeffer and Baumgardt, 2013), orbiting in the halo of the larger galaxy (see Figure 2.8 for an illustration of this process). NSCs, if they are stripped, will look like massive GCs, and hence be able to hide amongst the hundreds of globular clusters in the galaxy. Recent semi-analytic models predict 2-6 stripped nuclei in our halo (Pfeffer et al., 2014; Kruijssen et al., 2019).

For the Sagittarius dwarf galaxy, its nucleus, the globular cluster M54, was discovered long before the remainder of the galaxy was found. Detailed studies of M54 have revealed that, unlike a typical GCs (but typical of NSCs), it has stellar populations with a wide range of metallicities and ages (e.g., Siegel et al., 2007; Alfaro-Cuello et al., 2019). Based on their chemodynamical properties several other GCs have been suggested to originate as NSCs (e.g., Pfeffer et al., 2021).

Because the masses and star formation histories of NSCs track the galaxies they live

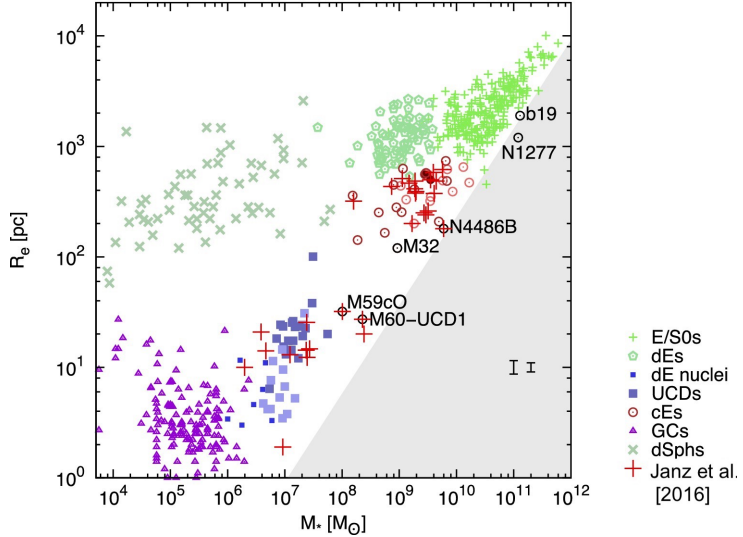


Figure 2.9: Mass-Size Plane. The plot shows size versus stellar mass for GCs, dwarf galaxies, NSCs, and UCDs. Uncertainties for the sizes are shown in the lower-right corner and the grey shaded area indicates the zone of avoidance (Misgeld and Hilker, 2011).
Figure Credit: Taken from Janz et al. (2016)

in (e.g., Kacharov et al., 2018; Sánchez-Janssen et al., 2019), stripped nuclei can tell us about the mass of their original host and the time of merging, and are much longer lived than stellar streams, making them a record of a galaxy’s accretion history.

Ultra-Compact Dwarf Galaxies

Further, ultra-compact dwarf galaxies (UCDs) might be stripped NSCs. They have masses of $10^6 < M < 10^8 M_\odot$, effective radii between 7 and 100 pc, and old ages > 10 Gyr (e.g., Drinkwater et al., 2003; Evstigneева et al., 2007; Mieske et al., 2013). UCDs are comparable to GCs and NSCs, but can be more extended, and in the mass-size plane, they occupy the region between star clusters and compact elliptical galaxies (e.g., Misgeld and Hilker, 2011; Janz et al., 2016), see Figure 2.9.

There is evidence that UCDs are a mix of stellar systems from different formation pathways (Brodie et al., 2011; Janz et al., 2016). Nonetheless, there are several UCDs where the stripped NSC scenario is further supported due to the presence of an SMBH (e.g., Seth et al., 2014; Afanasiev et al., 2018). High-mass UCDs typically were once the nuclei of stripped massive galaxies with initial masses $> 10^9 M_\odot$ (e.g., Norris and Kannappan, 2011; Seth et al., 2014; Afanasiev et al., 2018), but also the remnant nuclei of stripped dwarf galaxies should be found among the low-mass UCDs ($< 10^7 M_\odot$) (Pfeffer and Baumgardt, 2013).

2.2.4 Black Holes and NSCs

In galaxies with stellar masses above $\sim 10^{10} M_\odot$ one always finds SMBHs at their centers (see reviews Kormendy and Ho, 2013; Neumayer et al., 2020). However, there are several cases where nuclear star clusters and massive black holes are found to co-exist, like in the Milky Way (e.g., Seth et al., 2008; Neumayer and Walcher, 2012; Nguyen et al., 2019). This indicates that NSCs do not replace black holes as the central compact object. However, it seems that the growing black hole contributes to the disappearance of the NSC (Antonini et al., 2019). One explanation is that the change over from NSC to SMBH dominance at the center, happens when the dynamical time is about equal to the Salpeter time (Nayakshin et al., 2009), meaning that the central massive black hole in low-dispersion galaxies with dynamical times shorter than the Salpeter cannot grow quickly enough to

affect the gas infall, which can accumulate at the center and form an NSC.

The formation of SMBHs remains still a mystery, but several seeding channels have been suggested. Massive seed black holes ($\sim 10^4 - 10^6 M_\odot$) could have formed through the direct collapse of gas clouds (e.g., Loeb and Rasio, 1994; Bromm and Loeb, 2003; Begelman et al., 2006; Lodato and Natarajan, 2006), while less massive seed black holes ($\sim 100 M_\odot$) could form with the death of massive Pop-III stars (e.g., Fryer et al., 2001) or intermediate-mass black holes (IMBHs) (black hole masses $\sim 10^3 - 10^4 M_\odot$) could form by runaway collisions in the centers of star clusters (see review by Inayoshi et al., 2020).

The idea of an IMBHs within a dense stellar cluster has long existed (e.g., Begelman and Rees, 1978; Portegies Zwart and McMillan, 2002; Freitag et al., 2006b,a). These IMBHs within GCs can survive and migrate to a galaxy center, where through gas accretion they can become a nuclear star cluster with a black hole, or the black hole may form early and then grow along with the present-day NSC (see Greene et al., 2020). In addition, UCDs are interesting to study for the growth of black holes, especially in understanding the role of later-time accretion versus initial formation, since UCDs were stripped and thus less late-time growth is expected.

In general, the black hole population in stripped nuclei can give us insight into black hole growth and constrain the formation scenarios.

2.3 Omega Centauri



Figure 2.10: *ESO Image of ω Cen.*
This image is taken with the WFI camera from ESO's La Silla Observatory.
Image Credit: ESO

Omega Centauri (ω Cen, NGC 5139, see Figure 2.10) is the brightest, most massive globular cluster in the Milky Way ($\sim 3.55 \times 10^6 M_\odot$ Baumgardt and Hilker, 2018) and it is at a distance of 5.43 kpc (Baumgardt and Vasiliev, 2021). It was first identified as a nonstellar object by E. Haley in 1677 (Halley, 1715) and recognized as a globular cluster by J. Dunlop in 1826 (Dunlop, 1828).

Due to the complexity of its stellar populations and its retrograde orbit, it has long been suspected to be the stripped former nucleus of a galaxy that merged with the Milky Way a long time ago (e.g., Bekki and Freeman, 2003). Evidence for the multiple populations of stars in the cluster comes from the multiple sequences in its color-magnitude

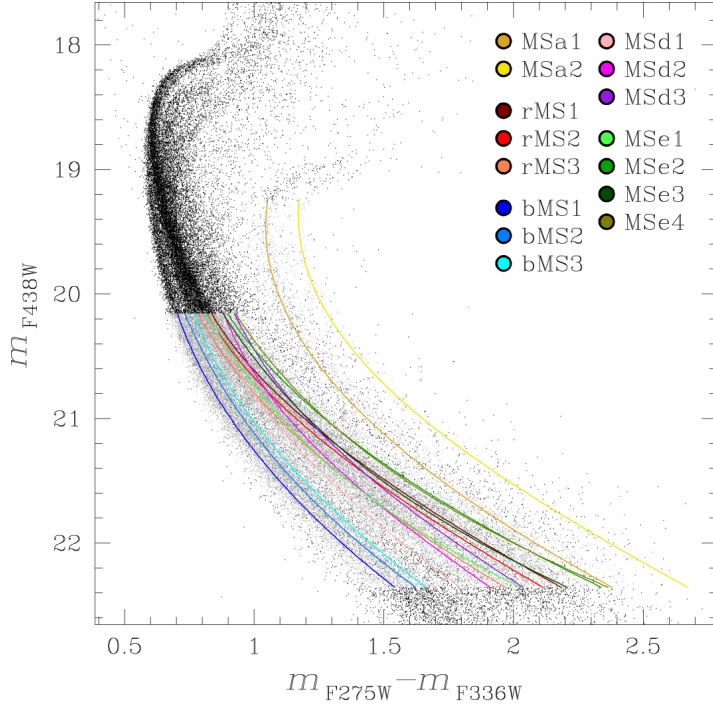


Figure 2.11: CMD of ω Cen Showing 15 Subpopulations. The CMD centered at the main sequence and subgiant branch of the cluster with fiducial lines for 15 subpopulations.

Figure Credit: Taken from Bellini et al. (2017b)

diagram (CMD, e.g., Anderson, 1997; Bedin et al., 2004; Bellini et al., 2010; Milone et al., 2017a, see Figure 2.11), a large spread in metallicity (e.g., Freeman and Rodgers, 1975; Johnson and Pilachowski, 2010), and possibly also in age (Hilker et al., 2004; Villanova et al., 2014). How prolonged the star formation in ω Cen was is still controversial, i.e. investigations vary from 4 Gyr to 5 Gyr (Villanova et al., 2007) to 1 Gyr to 2 Gyr (Joo and Lee, 2013). In addition, in the kinematic information of the cluster one finds the presence of a central stellar disk and a bias toward tangential orbits in the outer parts (van de Ven

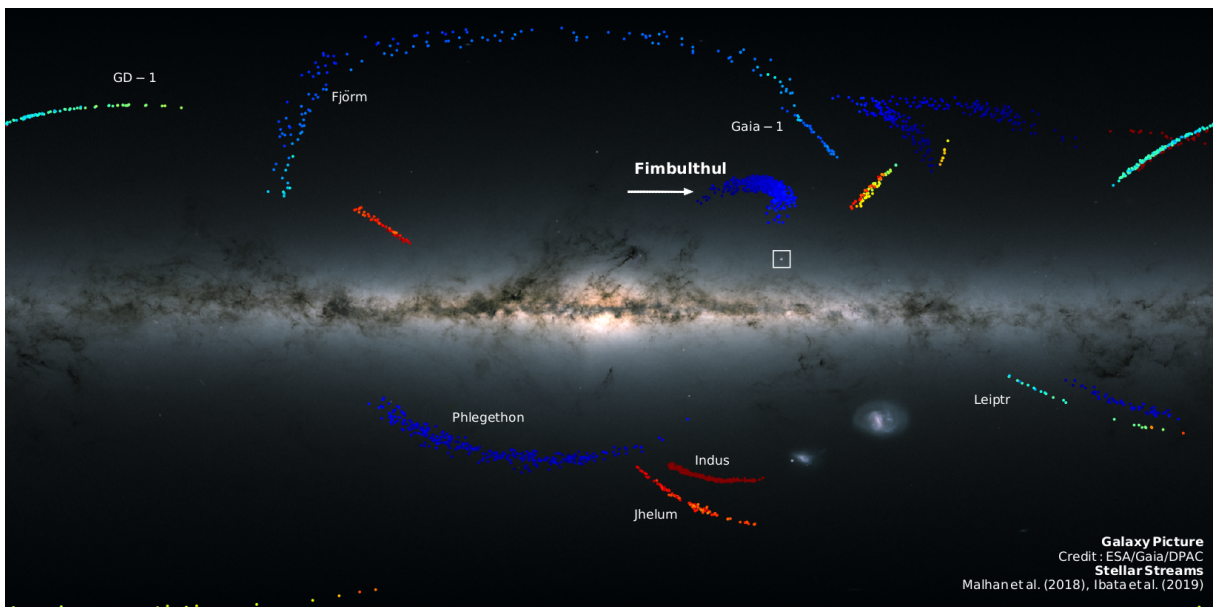


Figure 2.12: Fimbulthul Stream. The Image gives an overview of some of the tidal stellar streams found in ESA/Gaia DR2 using the STREAMFINDER algorithm. Fimbulthul stream associated with ω Cen (inside the white box) is indicated with an arrow.

Image Credit: ESA/Gaia/DPAC, stellar stream (Malhan et al., 2018; Ibata et al., 2019).

et al., 2006a), a counter rotation in the very central region (Pechetti et al., 2024) and fast-moving stars in the inner 3 arcsec (Häberle et al., 2024b) indicating the presence of a black hole.

The recent revolution of Galactic archaeology using *Gaia* data has further strengthened ω Cen’s status as a stripped nuclear star cluster through the identification of stars that may be associated with its progenitor galaxy (see Figure 2.12), as well as the fact that ω Cen has the highest binding energy among the star clusters associated to the *Gaia*-Enceladus structure (e.g., Majewski et al., 2012; Ibata et al., 2019; Massari et al., 2019; Limberg et al., 2022). Additionally, the predicted mass for the nucleus of *Gaia*-Enceladus matches perfectly to ω Cen, see Figure 2.13. However, its host galaxy has been largely diffused since the time of infall and its initial orbit cannot be well constrained.

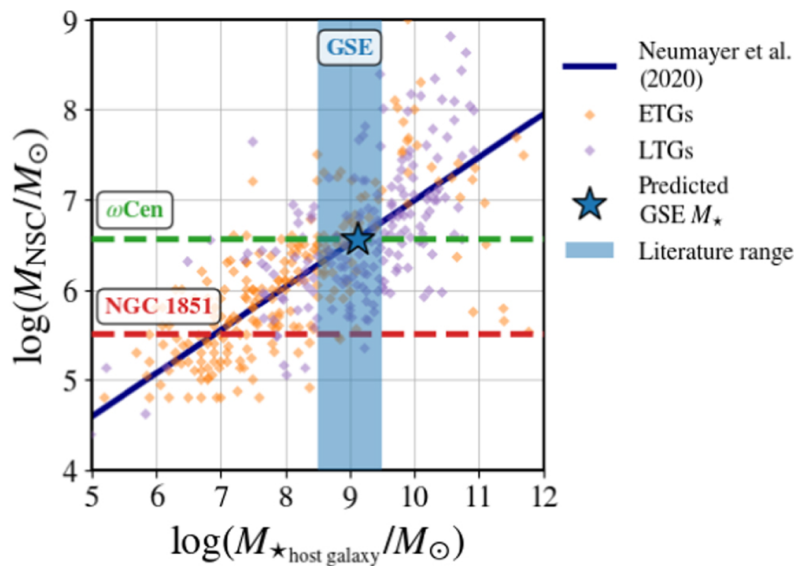


Figure 2.13: M_{NSC} vs M_{\star} Host Galaxy Mass. Orange and purple diamonds are early- and late-type galaxies (ETGs and LTGs), the dark blue line is the fit to these data from Neumayer et al. (2020), the lighter blue area covers the Gaia-Enceladus (GSE) mass range with the blue star being the predicted mass and the dashed lines indicate the masses (Baumgardt and Hilker, 2018) of both ω Cen (green) and NGC 1851 (red).

Figure Credit: Taken from Limberg et al. (2022)

ω Cen is, therefore, our closest NSC, even closer than our Galactic center, and not heavily obscured by dust (Schlafly and Finkbeiner, 2011, $E(B - V) = 0.12$). Due to its proximity, it can be observed and studied in great detail, making it the perfect laboratory for studying NSCs, stripped nuclei, and multiple populations. It can also inform us about the assembly history of our galaxy since its progenitor was most likely part of one of the last most massive mergers of the Milky Way.

Take away points

- The Milky Way as our home galaxy is an ideal test laboratory for studying the evolution and formation of galaxies.
- A new plethora of data, specifically from the *Gaia* mission, allows us to study the Galaxy in detail, disentangling its merger and assembly history.
- Stripped nuclei are remnants of mergers and can tell us a lot about their original host galaxy and their interactions.
- ω Cen is the closest nucleus to us and probably the stripped nucleus of the *Gaia*-Enceladus merger.

Chapter 3

DYNAMICAL MODEL OF THE MILKY WAY

This chapter has been published in Nitschai et al. (2021), formatting and small text edits have been made to match this thesis. The discussion and comparison with literature works have been performed only with works available before the publication in 2021. I conducted the scientific work and wrote all of the text with the support of the co-authors, except for Section 3.3.2, which was written and implemented by co-author Prof. Dr. Michele Cappellari. Suggestions and corrections from my co-authors and the referee of the paper are included in the text.

Abstract

We construct a dynamical model of the Milky Way disk from a data set, which combines *Gaia* EDR3 and APOGEE data throughout Galactocentric radii between $5.0 \leq R \leq 19.5$ kpc. We make use of the spherically-aligned Jeans Anisotropic Method to model the stellar velocities and their velocity dispersions. Building upon our previous work, our model now is fitted to kinematic maps that have been extended to larger Galactocentric radii due to the expansion of our data set, probing the outer regions of the Galactic disk. Our best-fitting dynamical model suggests a logarithmic density slope of $\alpha_{\text{DM}} = -1.602 \pm 0.079_{\text{syst}}$ for the dark matter halo and a dark matter density of $\rho_{\text{DM}}(R_{\odot}) = (8.92 \pm 0.56_{\text{syst}}) \times 10^{-3} \text{ M}_{\odot} \text{ pc}^{-3}$ ($0.339 \pm 0.022_{\text{syst}}$ GeV cm $^{-3}$). We estimate a circular velocity at the solar radius of $v_{\text{circ}} = (234.7 \pm 1.7_{\text{syst}})$ km s $^{-1}$ with a decline towards larger radii. The total mass density is $\rho_{\text{tot}}(R_{\odot}) = (0.0672 \pm 0.0015_{\text{syst}}) \text{ M}_{\odot} \text{ pc}^{-3}$ with a slope of $\alpha_{\text{tot}} = -2.367 \pm 0.047_{\text{syst}}$ for $5 \leq R \leq 19.5$ kpc and the total surface density is $\Sigma(R_{\odot}, |z| \leq 1.1 \text{ kpc}) = (55.5 \pm 1.7_{\text{syst}}) \text{ M}_{\odot} \text{ pc}^{-2}$. While the statistical errors are small, the error budget of the derived quantities is dominated by the 3 to 7 times larger systematic uncertainties. These values are consistent with our previous determination, but systematic uncertainties are reduced due to the extended data set covering a larger spatial extent of the Milky Way disk. Furthermore, we test the influence of nonaxisymmetric features on our resulting model and analyze how a flaring disk model would change our findings.

Chapter Contents:

3.1 Introduction	36
----------------------------	----

3.2	Data	38
3.2.1	Data Set	38
3.2.2	Kinematic Maps	39
3.3	Methods	41
3.3.1	Mass Distribution of the Milky Way Model	41
3.3.1.1	Distribution with an Exponential Disk Model	41
3.3.1.2	Distribution with a Flared Disk Model	42
3.3.2	MGE with Negative Gaussians but Nonnegative Density Everywhere	44
3.3.3	Modeling	45
3.4	Results	46
3.4.1	Exponential Disk Model	46
3.4.2	Assessing Systematic Errors Due to Nonaxisymmetries	49
3.4.3	Flared Disk Model	51
3.5	Conclusion	52
	Appendices	53
3.A	Posterior Distribution	53
3.B	The Dark Matter Axial Ratio (q_{DM}) as a Free Parameter	55
3.C	Investigating the Offset of V_{circ} between Our Result and Previous Work	55
	Take away points	56

3.1 Introduction

Dynamical models are important for our understanding of galaxies. They describe the distribution of stars over orbits in a gravitational potential (Binney and Tremaine, 2008). Hence, we can describe a galaxy as stars orbiting in a smooth gravitational potential by interpreting the combined stellar position and velocity information (e.g., Rix et al., 1997; Syer and Tremaine, 1996; Binney and McMillan, 2011; Cappellari, 2008). This allows us to infer the gravitational potential, the circular velocity curve, mass distribution, and dark matter density of a galaxy (e.g., Rix and Bovy, 2013).

For most external galaxies dynamical models usually suffer from degeneracies due to limited data. Since only line-of-sight observations are available, the data cannot provide the three-dimensional information that is needed to fully constrain dynamical models. There are only very few cases where the full velocity information is available and usually, they have a limited quality of data (e.g., van de Ven et al., 2006b; Watkins et al., 2015a). However, our own Galaxy can be observed in great detail with high-precision measurements from various stellar surveys as already mentioned in Chapter 2. In the past years, there has been a plethora of surveys for the Milky Way, such as APOGEE (Allende Prieto et al., 2008; Majewski et al., 2017) and *Gaia* (Gaia Collaboration et al., 2016), providing astrometric and spectroscopic information for a large sample of stars.

Many different dynamical models can be found in the literature (see Rix and Bovy, 2013), such as Jeans modeling (e.g., Cappellari, 2008; Bovy and Tremaine, 2012; Zhang et al., 2013), action based models (e.g., Binney and McMillan, 2011; Binney, 2012; Bovy and Rix, 2013), Schwarzschild models (e.g., Rix et al., 1997; van der Marel et al., 1998; Gebhardt et al., 2000; Cappellari et al., 2006; van den Bosch et al., 2008) and made-to-measure models (e.g., Syer and Tremaine, 1996; de Lorenzi et al., 2009; Dehnen, 2009; Portail et al., 2017; Wegg et al., 2015a). In this work, we will use the Jeans modeling approach. Jeans models are based on the Jeans equations (Jeans, 1915, 1922), which are derived from the steady-state Boltzmann equation under the assumption of axisymmetry.

The steady-state collisionless Boltzmann equation needs to be satisfied by the distribution function of the system, which describes the position and velocity of the stars in equilibrium and steady state under the gravitational influence of a smooth potential (Binney and Tremaine, 2008). The solutions of the Jeans equations describe the moments of the velocity distribution and the density of a collection of stars in a gravitational potential. However, to obtain a unique solution one has to assume the shape and orientation of the velocity ellipsoid. Cappellari (2008) reviews the possible natural choices for this alignment, which are prolate spheroidal coordinates, spherical coordinates, and cylindrical ones.

The known deviations from equilibrium and axisymmetry for the Milky Way (Widrow et al., 2012; Antoja et al., 2018; Gaia Collaboration et al., 2018b) which conflict with our model assumptions, are not uncommon for other galaxies too, but models are still able to recover the average kinematic properties (Cappellari et al., 2013b), even from less precise data. In the case of the Jeans Anisotropic modeling (JAM) method, it has been used to model integral-field stellar kinematics of large numbers of external galaxies (Cappellari, 2016). It has been tested against N-body simulations (Lablanche et al., 2012; Li et al., 2016) and in real galaxies against CO circular velocities (Leung et al., 2018), including barred and non-perfectly-axisymmetric galaxies similar to the Milky Way. In both cases, it recovers unbiased density profiles, even more accurately than the Schwarzschild (Schwarzschild, 1979) approach (Leung et al., 2018), which was also confirmed (Jin et al., 2019) by using Illustris cosmological N-body simulation (Vogelsberger et al., 2014). Hence, we expect that JAM will be able to capture the main kinematic features of the Milky Way and give accurate results for the total density and circular velocity.

In this work, we build upon Nitschai et al. (2020a) (my Master thesis topic), where we used the *Gaia* data release 2 (DR2) kinematics to construct an axisymmetric dynamical model of the Milky Way disk with full 6D phase-space coordinates. Making the Milky Way the first galaxy for which all intrinsic phase space coordinates are available, and with kinematics that are superior to the best integral-field kinematics of other galaxies where JAM has been extensively used. This removes the long-standing dynamical degeneracies and it is highly overconstrained by kinematics, making our ability to fit the data a fundamental test for both galaxy dynamics and the mass distribution in the Milky Way.

In Nitschai et al. (2020a) we used the spherically-aligned Jeans Anisotropic modeling (JAM_{sph} , Cappellari, 2020) method since the *Gaia* data (Hagen et al., 2019; Everall et al., 2019) showed that the velocity ellipsoid is closer to being spherically aligned than cylindrically (JAM_{cyl} , Cappellari, 2008). But we also compared the results against JAM_{cyl} and found negligible differences.

The new work (Nitschai et al., 2021) presented in this thesis extends the maximal Galactocentric radius of the data from ~ 12 kpc to ~ 20 kpc. This allows us to extend our model to the outer parts of the Galactic disk and to better constrain the model parameters. Furthermore, we improve our model by including the uncertainties of the kinematic maps at each position. The extended data set also allows us to test our model when using a flared outer disk, as suggested by e.g., Gyuk et al. (1999); Momany et al. (2006); López-Corredoira and Molgó (2014) and Li et al. (2019).

The outline of this chapter is as follows: We describe the data set and the derived kinematic maps with their uncertainties in Section 3.2. In Section 3.3 we describe the components of our mass model for the Galaxy and our modeling method. In the end, we show our results for this extended data set and the investigation of the effect of the nonaxisymmetries in Section 3.4, and we also show the results for a model with a flared

disk. Finally, in Section 3.5 we summarize our results and we include some further tests in the Appendix.

3.2 Data

In this work we combine two data sets, one are giant stars from *Gaia* early data release 3 (EDR3) with radial velocities (Gaia Collaboration et al., 2021), and one are the red giant branch (RGB) stars from Hogg et al. (2019). This combined data set will allow us to reach out to large Galactocentric radii.

3.2.1 Data Set

Gaia provides precise parallax information locally but further away from the Sun the distance uncertainties dominate. In addition, it is known that there is a parallax offset in the *Gaia* DR2 (Lindegren et al., 2018; Zinn et al., 2019; Schönrich et al., 2019) and also in *Gaia* EDR3 a parallax bias has been discovered (Lindegren et al., 2021b). There has been an attempt to map the dependencies of the parallax bias, but since the dependencies are non-trivial it is not possible to have a definitive correction (Lindegren et al., 2021a).

In this work, we update the data from Nitschai et al. (2020a) using *Gaia* EDR3 (Gaia Collaboration et al., 2021). The important update for our study is the higher precision in the astrometry in EDR3, however, the radial velocities have not been updated and have been adopted from DR2. In addition, EDR3 does not have extinction or reddening values, hence we cross-matched EDR3 with DR2 using the given crossmatch catalog by Torra et al. (2021) to get these values. For distances, we use the photogeometric distance estimates by Bailer-Jones et al. (2021) for the *Gaia* EDR3 in order to avoid the parallax bias and high uncertainties further away from the Sun.

The selection criteria we apply are the same as we already had in Nitschai et al. (2020a). Since giant stars are the main contribution in *Gaia* at distances larger than 1 kpc from the Sun and can be measured out to large distances due to their brightness, we select only them in this subsample. They are selected based on their absolute magnitude, $M_G = m_G - 5 \cdot \log d + 5 - A < 3.9$, given the extinction by *Gaia* DR2 and d being the distance from Bailer-Jones et al. (2021), their intrinsic colour $(G_{BP} - G_{RP})_0 > 0.95$, with the reddening taken from *Gaia* DR2 and parallaxes with relative uncertainty $\varpi/\epsilon_\varpi > 5$.

These data are precise only around the Sun but not far beyond. In order to probe larger Galactocentric distances Hogg et al. (2019) obtained precise spectrophotometric distance estimates for 44,784 red giant stars with a data-driven model. They combined spectroscopic data from APOGEE (Majewski et al., 2017) DR14 (Abolfathi et al., 2018) with photometric information from *Gaia* (Gaia Collaboration et al., 2016) DR2 (Gaia Collaboration et al., 2018a), the Two Micron All Sky Survey (2MASS, Skrutskie et al., 2006) and the Wide-field Infrared Survey Explorer (WISE, Wright et al., 2010). These data allow us to probe larger distances, out to Galactic radii of ~ 20 kpc, than with *Gaia* data alone. These RGB stars were selected with a cut at $\log g < 2.2$, in order to have stars more luminous than the red clump. For more details on quality cuts for these stars see Hogg et al. (2019).

To extend our data set to larger Galactocentric radii, we combine the data set based on *Gaia* EDR3 with that from Hogg et al. (2019). For the combined data set we require that the proper motion and line-of-sight velocities of all stars are finite and that they are

in the area of $-30^\circ < \phi < 30^\circ$. For sources that are in both data sets, we prefer the values from Hogg et al. (2019) for our further calculations.

The remaining stars after our selections from the Hogg et al. (2019) data are 34,180 and 2,823,509 stars that are only in *Gaia*. In total, we have 2,857,689 stars that will be used in the following analysis.

3.2.2 Kinematic Maps

In order to calculate the kinematic maps of the Milky Way, we transform the positions and velocities of the stars in our combined data set, into a Galactocentric reference frame.

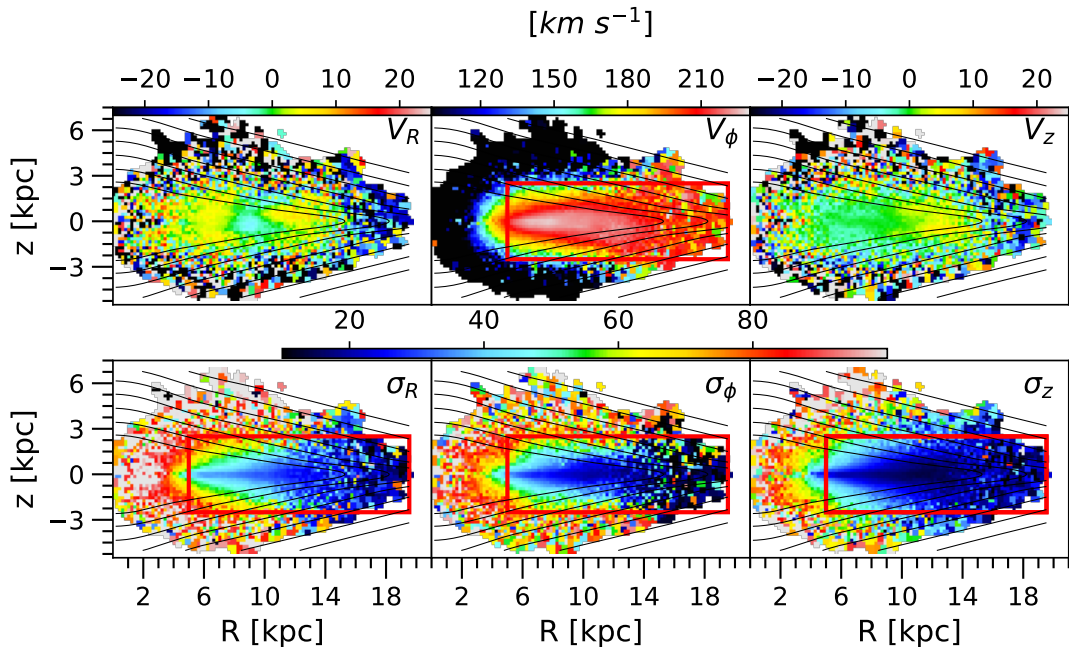


Figure 3.1: Velocity Maps for the Combined Data from Gaia EDR3 with That from Hogg et al. (2019). The color represents the mean velocity or dispersion of the Voronoi bins, as described in Section 3.2.2. In the top panels are the velocities and in the bottom panels the velocity dispersions. From left to right are the velocities and velocity dispersions in R , ϕ and z . All color maps are in km s^{-1} . Inside the red boxes are the data that we will use for the JAM model and the black lines are the stellar density (as described in Section 3.3.1.1) contours.

We assume as distance to the Galactic centre $R_\odot = 8.178$ kpc (Gravity Collaboration et al., 2019), a vertical displacement of the Sun from the midplane of $z_\odot = 0.02$ kpc (Joshi, 2007) and as solar velocities in cylindrical Galactic coordinates $(U_\odot, V_\odot, W_\odot) = (-11.1, 247.4, 7.2)$ km s^{-1} (from Schönrich et al., 2010; Gravity Collaboration et al., 2019; Reid et al., 2009, respectively). We require the data to have $|z| \leq 7$ kpc because we have more stars towards positive z values, which do not cover the whole area and create gaps in our data. Hence, to not have a data set that is highly asymmetric and not continuous, we exclude from the beginning stars with too high z values. These stars that are excluded would anyways not be considered in our further analysis, since they are halo stars and lie outside of the disk region we want to model. We then divide our data in 200 pc \times 200 pc cells and do Voronoi binning, using the vorbin package¹ (Cappellari and Copin, 2003) on this cells, requiring a minimum of five stars for each Voronoi bin. We use the

¹We use the Python version 3.1.4 of the vorbin package available from <https://pypi.org/project/vorbin/>

Voronoi binning on our already divided into $200 \text{ pc} \times 200 \text{ pc}$ data, to fully make use of the data, especially towards larger radii and z where the stars are not as dense and we would not get more than five stars in a cell. With this method, we can combine the data from cells without enough stars in them but still keep as the smallest bin the $200 \text{ pc} \times 200 \text{ pc}$ cell in the central region of our kinematic maps around the solar position, where we have numerous stars. For each bin, we calculate the mean and standard deviation of the velocities. The final number of bins is 2899 and covers a volume with extreme cylindrical coordinates $0.18 \text{ kpc} \leq R \leq 19.5 \text{ kpc}$ and $-5.02 \text{ kpc} \leq z \leq 6.8 \text{ kpc}$.

The created velocity maps of the combined data set in cylindrical coordinates are shown in Figure 3.1. As expected the stars around the solar position extend to larger Galactocentric heights z than at larger or smaller radii. However, thanks to the Voronoi binning we get a continuous covered area up to a radius of 19.5 kpc without any gaps in the kinematics.

The selection function of *Gaia* DR2 (Boubert et al., 2020; Boubert and Eoverall, 2020) and specifically of the radial velocity sample (Rybicki et al., 2021), since we only select stars in EDR3 that have radial velocities in DR2 and for APOGEE (Bovy et al., 2014; Mackereth and Bovy, 2020) will not affect our model significantly, since we study the kinematics of the observed stars, at a given position. The stellar tracer density is assumed, not fitted and the selection function at a given position does not depend strongly on the velocities of the objects.

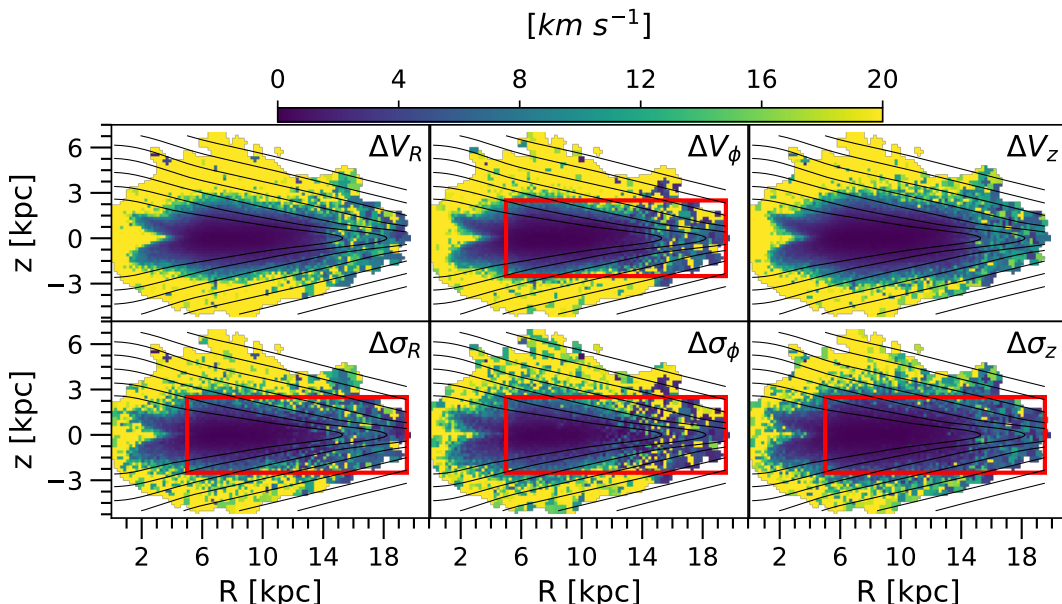


Figure 3.2: Uncertainty Maps for the Combined Data. Similar to Figure 3.1, the colors represent the uncertainty value for each Voronoi bin. In the top panels are again the velocities and in the bottom panels the velocity dispersions. From left to right are the velocities and velocity dispersions in R , ϕ and z . Inside the red boxes are the errors that we will use in calculating the χ^2 of our JAM model and the black lines are the stellar density (Section 3.3.1.1) contours.

To find the uncertainties for our kinematic maps, we choose to use the bootstrapping method (e.g., Efron and Tibshirani, 1993). We selected this method and not error propagation because it provides a more robust estimate of the uncertainties. The propagated uncertainties from radial velocities and proper motion measurements tend to underestimate the true uncertainties. In detail, we draw 100 random samples of stars with their

velocities and redo the Voronoi binning, again calculating the mean velocity and velocity dispersion for each bin for each of the samples. Afterward, we find the uncertainties of the bin by calculating the standard deviation of the 100 mean velocities and velocity dispersions.

The uncertainty maps are shown in Figure 3.2. Errors around the Sun and the mid-plane are much smaller ($\leq 4 \text{ km s}^{-1}$) than at larger heliocentric distances, because there are more stars detected and their measurements are more precise since they are closer to us.

The uncertainties are also higher towards the Galactic Center. In this area, starting at 5 kpc, the bar dominates the kinematics (Wegg et al., 2015a; Bovy et al., 2019) and hence would break the axisymmetry assumptions of our model. To avoid that, we exclude data with $R < 5 \text{ kpc}$. Additionally, we also exclude stars with $|z| \geq 2.5 \text{ kpc}$, which is the same range we had in Nitschai et al. (2020a), to exclude halo stars. Similar to Nitschai et al. (2020a), we ignore the halo distribution since it is not well known, and in this regime, we expect to mainly have disk stars. The red boxes in Figure 3.1 and 3.2 show the area we will investigate and they have 1,404 bins, the data outside the boxes are excluded from further analysis.

3.3 Methods

3.3.1 Mass Distribution of the Milky Way Model

To construct a dynamical model we need an estimate of the tracer distribution and the mass density of the Galaxy. We will assume the same model for the Milky Way as in Nitschai et al. (2020a), a detailed description and explanation can be found there and we give a brief summary in this section. In addition to this model, we also investigate a model with a flaring disk in Section 3.3.1.2.

3.3.1.1 Distribution with an Exponential Disk Model

Our main stellar model makes use of the Jurić et al. (2008) disk stellar distribution, normalized to the local luminosity density from Flynn et al. (2006). However, we ignore the stellar halo component because in the area we are probing with our data set, the stellar mass distribution is dominated by the disk component.

The disk is decomposed into a sum of two exponential components, the thin and the thick disk, with different scale lengths ($L_{\text{thin}}, L_{\text{thick}} = (2.6, 3.6) \text{ kpc}$ and heights ($H_{\text{thin}}, H_{\text{thick}} = (0.3, 0.9) \text{ kpc}$ (Jurić et al., 2008)):

$$\rho_D(R, z, L, H) = \rho(R_\odot, 0) \exp\left(-\frac{R - R_\odot}{L} - \frac{|z|}{H}\right) \quad (3.1)$$

$$\begin{aligned} \rho_D(R, z) = & \rho_D(R, z, L_{\text{thin}}, H_{\text{thin}}) \\ & + f \cdot \rho_D(R, z, L_{\text{thick}}, H_{\text{thick}}) \end{aligned} \quad (3.2)$$

where $f = 0.12$ is the thick disk normalization relative to the thin disk (Jurić et al., 2008). In addition, we combined that with an axisymmetric bulge (McMillan, 2017; Bissantz and Gerhard, 2002). The luminosity density profile of this model is shown in the top panel of Figure 3.3.

We approximate this stellar model with a multi-Gaussian expansion (MGE, Emsellem et al., 1994; Cappellari, 2002), using the MGE fitting method (Cappellari, 2002) and MG-EFIT software package², which is necessary in order to apply the JAM model (Cappellari, 2008, 2020).

For the mass density of the Galaxy, we need to include also the gas and dark matter contribution. For the gas component, we add the H₂ and H_{II} distribution from McMillan (2017). For simplicity, we ignore the hole in the center of the density profile, since the hole is outside of the range we are probing. In Nitschai et al. (2020a) we have shown that this does not change the dynamical model significantly. As for the stellar model, we use the MG-EFIT package (Cappellari, 2002) to fit the created image of the gas density. This MGE will be added to the potential density and be kept fixed during the model fit to the quoted mass by (McMillan, 2017).

As a dark matter halo, we assume a generalized Navarro-Frenk-White profile (gNFW, Wyithe et al., 2001):

$$\rho_{\text{DM}} = \rho_s \left(\frac{m}{r_s} \right)^{\alpha_{\text{DM}}} \left(\frac{1}{2} + \frac{1}{2} \frac{m}{r_s} \right)^{-3-\alpha_{\text{DM}}} \quad (3.3)$$

where:

$$m^2 = R^2 + (z/q_{\text{DM}})^2, \quad (3.4)$$

r_s the scale radius, α_{DM} the dark matter slope and q_{DM} the axial ratio. If $\alpha_{\text{DM}} = -1$, the profile represents the classical Navaro-Frenk-White (NFW) dark matter profile (Navarro et al., 1996).

The dark matter profile is a one-dimensional profile and we fit this with Gaussians using the MGE_FIT_1D routine from the MG-EFIT package. It can be made oblate or prolate, for use with the model depending on the value of q_{DM} .

The model assumptions cause systematic uncertainties that strongly depend on the values we choose for the different parameters but also on the model itself. We have tested the effects of the disk parameters in Nitschai et al. (2020a) for the circular velocity and total density, in order to get an understanding of these uncertainties.

3.3.1.2 Distribution with a Flared Disk Model

We know that the outer part of our Galaxy, beyond 15 kpc, is warped and flared, but the details of its shape are still uncertain (Bland-Hawthorn and Gerhard, 2016). These structures were first detected in the gas component of the disk (Kerr, 1957; Oort et al., 1958; Grabelsky et al., 1987; May et al., 1997), but can also be detected in the three-dimensional distribution of stars (e.g., Liu et al., 2017; Anders et al., 2019; Skowron et al., 2019).

A flared disk means that the vertical scale height grows with increasing radius. The stellar flare in the outer Galactic disk has been observed and the scale height modeled as a function of the radius by many studies for the outer disk (e.g., Gyuk et al., 1999; Alard, 2000; López-Corredoira et al., 2002; Yusifov, 2004; Momany et al., 2006; Reylé et al., 2009; López-Corredoira and Molgó, 2014; Li et al., 2019).

Since we are probing a large range of Galactic radii up to ~ 20 kpc, our data extends to the regime where the flare is visible. Hence, in addition to our main exponential model

²We use the Python version 5.0.12 of the MG-EFIT package available from <https://pypi.org/project/mgefit/>

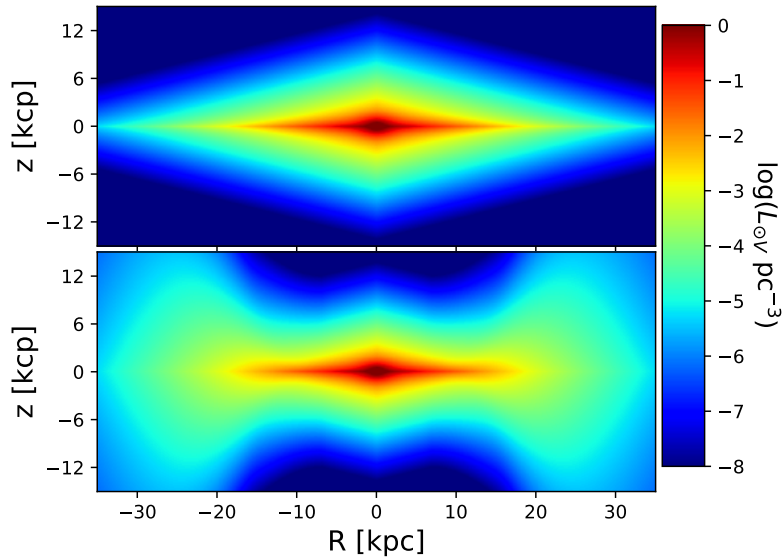


Figure 3.3: Luminosity Density Profile of the Milky Way without and with Flaring. The top panel shows the stellar luminosity density for our main model described in Section 3.3.1.1. The bottom panel shows the flared Milky Way model (see Section 3.3.1.2). The x -axis is the radial direction, R , reaching up to ± 35 kpc away from the Galactic Center at $(0, 0)$ kpc, and the y -axis is the displacement from the midplane, z , ranging up to ± 15 kpc. The color map is the logarithmic luminosity density.

described in the previous subsection, we investigate how a flared disk would change our results.

Even though, there are many studies of the flare there is no single parametrization for it. We decided to base the flare we use on the work of López-Corredoira and Molgó (2014) because they give a parametrization for the scale height for the thin and thick disk. In detail, we keep the density profile the same as for our main model and only modify the scale heights, H_{thin} , H_{thick} , for larger radii:

$$H_{\text{thin}} = H_{\text{thin}}(R_{\odot}) \left[1 + \sum_{i=1}^2 k_{i,\text{thin}} (R - R_{\odot})^i \right], R > R_{\odot} \quad (3.5)$$

$$H_{\text{thick}} = H_{\text{thick}}(R_{\text{ft}}) \left[1 + \sum_{i=1}^2 k_{i,\text{thick}} (R - R_{\text{ft}})^i \right], R > R_{\text{ft}} \quad (3.6)$$

with $k_{i,\text{thin}} = (-0.037 \text{ kpc}^{-1}, 0.052 \text{ kpc}^{-2})$, $k_{i,\text{thick}} = (0.021 \text{ kpc}^{-1}, 0.006 \text{ kpc}^{-2})$ and $R_{\text{ft}} = 6.9$ kpc (López-Corredoira and Molgó, 2014).

Since the flare starts only at larger radii, we assume the scale height for the thin disk to also be constant up to the solar position. For $R < R_{\odot}$, $H_{\text{thin}} = H_{\text{thin}}(R_{\odot})$ and for $R < R_{\text{ft}}$, $H_{\text{thick}} = H_{\text{thick}}(R_{\text{ft}})$. As values for the scale heights at the solar position, we use the values from Jurić et al. (2008), $H_{\text{thin}}(R_{\odot}) = 300$ pc and $H_{\text{thick}}(R_{\odot}) = 900$ pc. See Figure 3.3 bottom panel for the density profile with flare.

3.3.2 MGE with Negative Gaussians but Nonnegative Density Everywhere

An MGE with only positive Gaussians cannot describe a density distribution like the one in Figure 3.3. A good fit can be obtained, for a restricted spatial extent, allowing for negative Gaussians (keyword `negative=True` in `MGE_FIT_SECTORS` of the `MGEFIT` package of [Cappellari 2002](#)). However, we verified that in this case the resulting MGE has a strongly negative density at larger radii and produces clearly nonphysical results when used with JAM. The inability to constrain the density to be positive, and the need to test for the positivity of the total density, is a general problem when allowing for negative Gaussian in MGE fits.

To obtain an acceptable MGE fit to the flared disk, while guaranteeing a positive total density, we needed to make some modifications to the `MGE_FIT_SECTORS` procedure. For this, in addition to the usual positive Gaussians basis functions in the MGE, we introduced a set of new basis functions, which we produced by coadding four positive and negative Gaussians with the same absolute peak value, in such a way that their sum is everywhere positive, as follows:

$$G(R, z) = e^{-\frac{1}{2\sigma^2} \left(\frac{R^2}{f^2} + \frac{z^2}{f^2 q^2} \right)} + e^{-\frac{1}{2\sigma^2} \left(R^2 + \frac{z^2}{q^2} \right)} - e^{-\frac{1}{2\sigma^2} \left(\frac{R^2}{f^2} + \frac{z^2}{q^2} \right)} - e^{-\frac{1}{2\sigma^2} \left(R^2 + \frac{z^2}{f^2 q^2} \right)}. \quad (3.7)$$

Here, σ and q are two parameters that change for different MGE components (like the corresponding parameters for the MGE Gaussians), while $f = 0.9$ is a constant $f \lesssim 1$, which is the same for all basis functions. With this definition, the new MGE basis function is $G(R, z) = 0$ along the R - or z -axis, and presents four bisymmetric maxima, as illustrated in Figure 3.4.

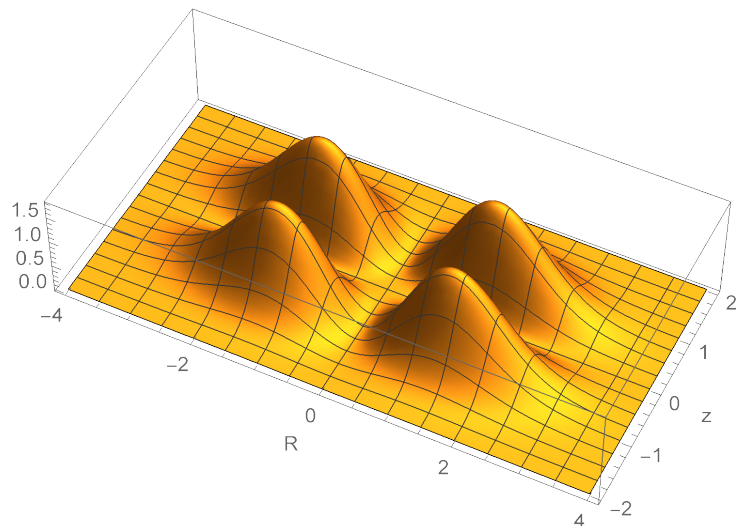


Figure 3.4: New MGE Basis Function. This basis function consists of four positive/negative Gaussians centered on the origin. When combined with the usual positive Gaussians, it allows for extra flexibility in the MGE fitting while still guaranteeing a non-negative density everywhere.

The new basis function $G(R, z)$ has an asymptotic behavior at large radii $G \sim \exp(-r^2)$ for $r \rightarrow \infty$, as the standard MGE, while along the axes, $G \sim R^2$ for $R \rightarrow 0$ and $G \sim z^2$ for $z \rightarrow 0$. This implies that, while it can describe decreasing profiles towards the center, it cannot approximate drops of the central density profile steeper than $\rho \propto r^2$. For this reason, it can only approximate the flared density of Figure 3.3 down to a certain isophote.

Apart from the introduction of the new basis function, the fit is obtained using the same algorithm described in Cappellari (2002), while still enforcing positivity constraints for all basis functions. Once the fit converges, all four Gaussian basis functions are split into their four individual Gaussian components in output, producing an MGE that is composed of both positive and negative Gaussians. In this way, no further changes are required to use the produced MGE model with other software like JAM.

The new MGE has 49 Gaussians, but these come from 28 basis functions, some of which are constructed from groups of four Gaussians, which are fitted as single basis functions. This new implementation of the MGE fit is/will included in the new release of the MGE package (footnote 2).

3.3.3 Modeling

As a dynamical model we use the JAM_{sph} approach³ (Cappellari, 2020), which is based on the solution of the axisymmetric Jeans equations and assumes a spherically aligned velocity ellipsoid (Bacon et al., 1983; Bacon, 1985). The spherical alignment has proven to describe the *Gaia* data in the outer halo (Wegg et al., 2019) and in the disk region (Hagen et al., 2019; Everall et al., 2019). This was also confirmed by the results in Nitschai et al. (2020a).

In Figure 3.1 we have drawn a red square around the data we will use for our model: we only fit the axisymmetric in-plane kinematics ($v_\phi, \sigma_r, \sigma_\phi, \sigma_z$). Neither vertical motion, nor tracer distribution are fit. Due to the steady state assumption of our model, v_R and v_z are assumed to be zero and therefore they do not need to be fitted. The deviations from zero in the data due to nonaxisymmetric signatures (Antoja et al., 2018; Gaia Collaboration et al., 2018b) are small enough for the purpose of our model.

The features we do not include in our stellar distribution of the Galaxy are the bar in the inner region and warp in the outer disk since both signatures are nonaxisymmetric and we cannot model them with JAM. In particular, the bar dominates within 5 kpc from the Galactic Centre (Wegg et al., 2015a; Bovy et al., 2019), but as previously mentioned (see Section 3.2.2, cut at 5 kpc), we remove all the stars in the central area for our model. For the outer disk, one would need to add a measurement of the warp, $z_w(R, \phi)$ (e.g., Li et al., 2019), to the stellar distribution. However, since our model is axisymmetric, we cannot add this to our model. In future works, one could investigate if a shift in the z direction would be a possible parametrization of the warp for an axisymmetric model like ours.

For our modeling, we keep the scale radius of the dark matter halo, r_s , constant at 14.8 kpc (Eilers et al., 2019), since we know that it is not constrained well with our JAM model (Nitschai et al., 2020a). In addition, 14.8 kpc agrees with literature values ranging from (~ 10 to 20 kpc). Further, because our data are limited to the disk region, they do not strongly constrain the dark matter axial ratio. Hence, we keep q_{DM} fixed to 1.3 (Posti and Helmi, 2019), which they derive using globular clusters. See Appendix 3.B for a model with free q_{DM} .

The standard model has 7 free parameters: (i) the inner logarithmic slope of the dark matter halo (α_{DM}); (ii) the dark matter fraction within a sphere with radius R_\odot (f_{DM}); (iii-vi) the velocity dispersion ratios or anisotropies (σ_θ/σ_r and σ_ϕ/σ_r) for both the flattest

³We use the Python version 6.1.2 of the JAMPY package available from <https://pypi.org/project/jampy/>

$(q_{\text{MGE}} < 0.2)$ Gaussian components (subscript 1) of the MGE and the rest (subscript 2); and (vii) the mass-to-light ratio of the stellar component in the V -band [$(M_*/L)_V$].

The fit to the data is performed using the EMCEE python package of Foreman-Mackey et al. (2013), which implements the affine invariant ensemble sampler for Markov chain Monte Carlo (MCMC) proposed by Goodman and Weare (2010).

3.4 Results

3.4.1 Exponential Disk Model

Using the data and uncertainties described in Section 3.2 we perform MCMC fits, for the Milky Way distribution without flaring as described in Section 3.3.1.1.

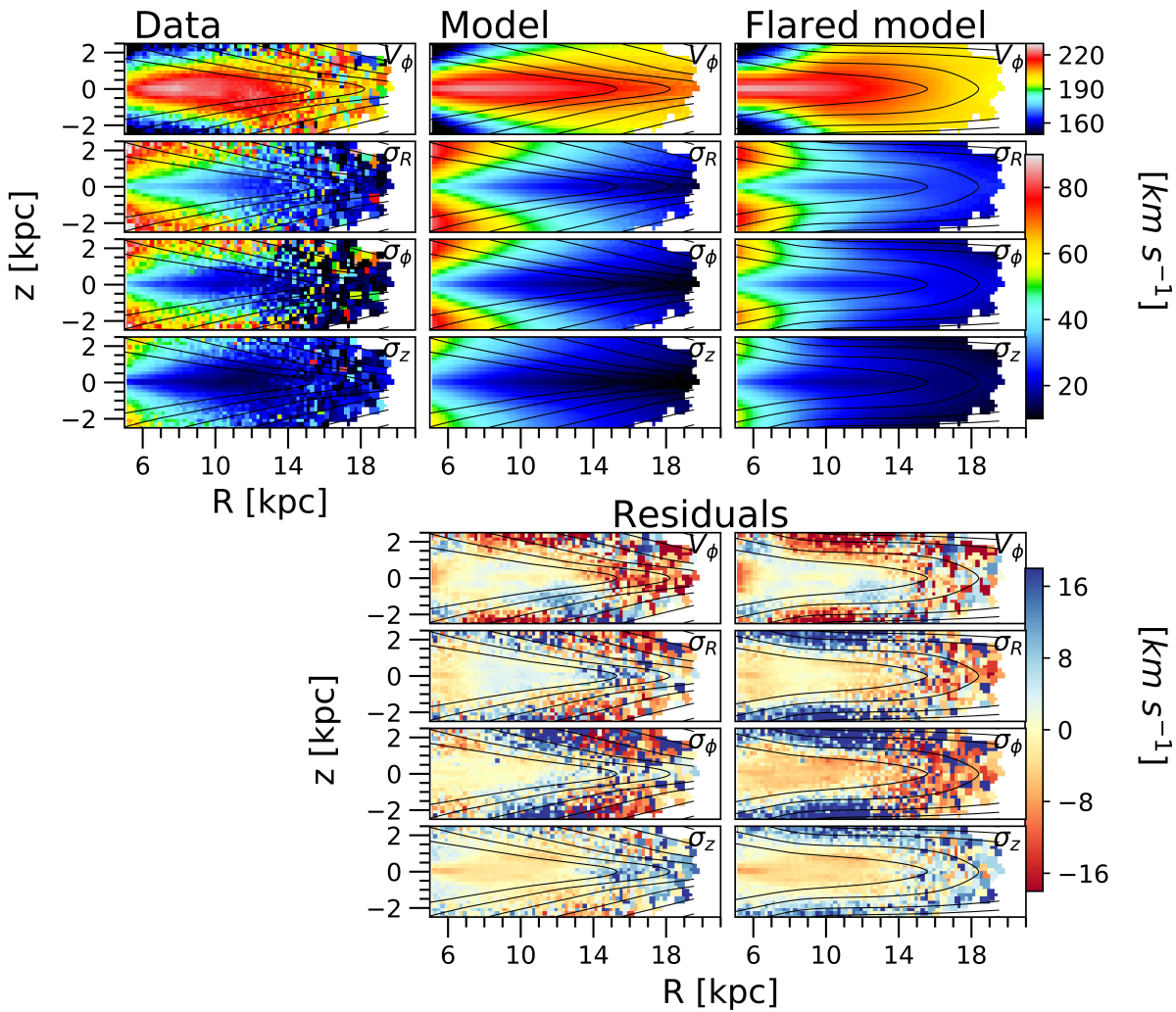


Figure 3.5: Best Fit for the JAM_{sph} . From left to right the columns show the data, the JAM model with the Jurić et al. (2008) stellar density distribution and the JAM model with flaring. At the bottom are the residuals (data-model) for the two JAM models. From top to bottom the rows show V_ϕ , σ_R , σ_ϕ , σ_z . The black lines are the stellar density (as described in Section 3.3.1.1) contours, except for the flared model which has the contours of the flared disk model described in Section 3.3.1.2.

The best fitting model gives a $\chi^2 \sim 9.2$ which is much larger than 1 that we want. This is mainly because there are systematic uncertainties due to nonaxisymmetric fea-

Table 3.1: Best-fitting Parameters

Parameters	Model			Free Anisotropies			Flared Model	
α_{DM}	-1.602	\pm	0.015 _{stat}	\pm	0.079 _{syst}	-1.592	\pm	0.029 _{stat}
f_{DM}	0.811	\pm	0.006 _{stat}	\pm	0.014 _{syst}	0.819	\pm	0.013 _{stat}
$(\sigma_\theta/\sigma_r)_1$	0.663	\pm	0.006 _{stat}	\pm	0.021 _{syst}	-		0.610
$(\sigma_\theta/\sigma_r)_2$	0.577	\pm	0.011 _{stat}	\pm	0.038 _{syst}	-		0.632
$(\sigma_\phi/\sigma_r)_1$	0.711	\pm	0.016 _{stat}	\pm	0.028 _{syst}	-		0.848
$(\sigma_\phi/\sigma_r)_2$	1.001	\pm	0.019 _{stat}	\pm	0.054 _{syst}	-		0.853
$(M_*/L)_V$	0.413	\pm	0.012 _{stat}	\pm	0.031 _{syst}	0.396	\pm	0.028 _{stat}
χ^2_{DOF}			0.91			0.81		1.3
$v_{\text{circ}}(R_\odot)$ [km s ⁻¹]	234.7	\pm	0.3 _{stat}	\pm	1.7 _{syst}	234.6	\pm	0.4 _{stat}
a_{circ} [km s ⁻¹ kpc ⁻¹]	-1.78	\pm	0.05 _{stat}	\pm	0.34 _{syst}	-1.69	\pm	0.08 _{stat}
						0.34 _{syst}		-2.39
							\pm	0.05 _{stat}

The uncertainties are given in this table as statistical errors are derived from the posterior distributions and are the formal errors. For the estimate of the systematic uncertainties we also used the values from Table 3.2 in Section 3.4.2 and we estimate them to be half of the difference between minimum and maximum of all our models with an exponential disk without flaring.

tures, spiral structure, the equilibrium assumption of JAM, and the choice of the tracer distribution, which our model cannot take into account. This also explains why we get very small statistical errors for our free parameters. The systematic errors would dominate here and we can use this result to get an estimate of the systematic uncertainties, which are otherwise impossible to determine.

To get more reasonable errors, we check the precision to which our model explains the data. To do this we add quadratically a value in km s⁻¹ to our bootstrapped errors:

$$\text{errors}_i^2 = \text{errors}_{\text{bootstr.,}i}^2 + \text{errors}_{\text{s.,}i}^2. \quad (3.8)$$

Where $\text{errors}_{\text{s.,}i}$ such that we get a $\chi^2 = 1$ for each component $i = (v_\phi, \sigma_R, \sigma_\phi, \sigma_z)$. The added values for this model are (6.03, 5.01, 6.55, 3.32) km s⁻¹, respectively. With these higher errors for the data we do a new MCMC fit and the best-fitting values are listed in the second column ('Model') of Table 3.1.

However, the statistical uncertainties from the posterior of our best-fitting parameters are only formal errors, which are quite small also because of the large number of stars that we use, and systematic uncertainties dominate. To estimate our systematics we investigate the axisymmetry assumption of our model in Section 3.4.2 and we give the systematic errors as half of the difference between the minimum and maximum of all our models with an exponential disk without flaring.

The posterior distribution is shown in the Appendix 3.A Figure 3.9 and the JAM model is shown in the second column of Figure 3.5.

The circular velocity is plotted in Figure 3.6 and has a value of $(234.7 \pm 0.3_{\text{stat}} \pm 1.7_{\text{syst}})$ km s⁻¹ at the solar radius. The slope of the circular velocity curve between 6.2 kpc and 20.2 kpc, which is the region where it can be approximated by a straight line, is declining at $(-1.78 \pm 0.05_{\text{stat}} \pm 0.34_{\text{syst}})$ km s⁻¹ kpc⁻¹. This is consistent with the results of Eilers et al. (2019). A test to investigate the small offset between our and Eilers et al. (2019) measurements of the circular velocity can be found in the Appendix 3.C. In Figure 3.6, we also show the contribution of the different components to the total circular velocity according to our best fit. However, one has to note that because of the covariance of the mass-to-light ratio, the dark matter fraction, and the dark matter slope (see Figure 3.9), which is expected, it is not the only possible decomposition. One could decrease the dark matter contribution while increasing the stellar component and still get the same total result, which is what we constrain. The smaller than NFW ($\alpha_{\text{DM}} = -1$) dark matter slope also increases the dark matter contribution towards smaller radii inside R_\odot . This makes

the dark matter contribution more dominant for our circular velocity at small radii in comparison to other works (e.g., Eilers et al., 2019, and what we see in Appendix 3.C Figure 3.11) where usually an NFW profile is assumed. Hence, we only tightly constrain the total circular velocity and not the different components of it, which depends on the assumed stellar and dark matter density profiles.

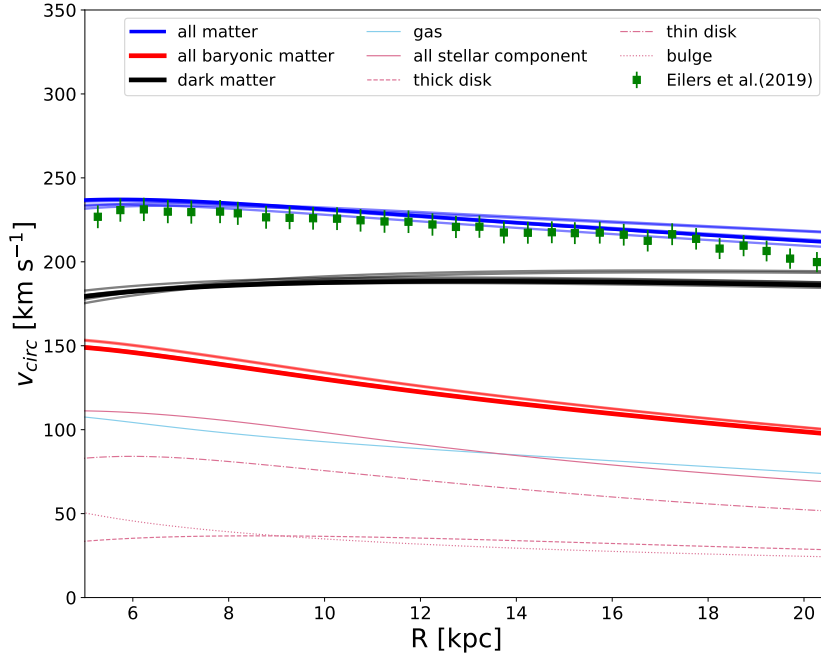


Figure 3.6: Circular Velocity for the JAM_{sph} Model without Flaring. The blue solid line is our total circular velocity from our best fit, the green squares are the measurements by Eilers et al. (2019) with systematic uncertainties of 3 percent, the dark matter contribution is shown as a black solid line, and the baryonic contribution as a red solid line. For each of these three lines, there are five fainter lines (close around them), which are the best-fitting results from the four different sectors of the data (Section 3.4.2), and the model with free anisotropies and they give as an estimate of the systematic uncertainty. Only for the best-fitting solution of our main model without flaring we also have plotted the gas contribution as a light blue line and the total stellar contribution as a light violet solid line, while this can be separated further into the bulge (light violet dotted line), the thin (light violet dashed-dotted line) and thick disk (light violet dashed line). The contribution of the different components plotted here depends on the assumed stellar and dark matter density profiles, and with our model, we only constrain tightly the total circular velocity.

One should also note that even though we use giant stars, we do not take the asymmetric drift into account, since we use the full Jeans equations with JAM. The circular velocity is a result of the gravitational potential that we get from our best fit to the individual velocities.

Additionally, for the best fitting model the dark matter density at the solar radius is $\rho_{\text{DM}}(R_\odot) = (0.00892 \pm 0.00007_{\text{stat}} \pm 0.00056_{\text{syst}}) \text{ M}_\odot \text{ pc}^{-3}$ and the total density $\rho_{\text{tot}}(R_\odot) = (0.0672 \pm 0.0006_{\text{stat}} \pm 0.0015_{\text{syst}}) \text{ M}_\odot \text{ pc}^{-3}$. The total density logarithmic slope in the range of $5 \leq R \leq 19.5$ kpc is $\alpha_{\text{tot}} = -2.367 \pm 0.007_{\text{stat}} \pm 0.047_{\text{syst}}$. All statistical errors are formal errors from the posterior distribution and do not include the systematic uncertainties that would increase the errors.

Comparing these results to our previous work (Nitschai et al., 2020a), the JAM model agrees with our previous results and all parameters agree within the respective errors. Specifically, the total density, and in particular the total slope and dark matter fraction, have smaller uncertainties and are more reliable because we have a longer radial baseline

and more data. The discrepancy between the total logarithmic density slope of our best fitting model and that from Nitschai et al. (2020a) can be explained due to the different radial range probed ($3.5 \leq R \leq 12.5$ kpc) and the different r_s (20 kpc) assumed for the dark matter halo. If we constrain our slope to a similar range as in Nitschai et al. (2020a), our value would decrease to roughly $-2.278 \pm 0.007_{\text{stat}} \pm 0.047_{\text{syst}}$ and would get even smaller for a scale radius of 20 kpc. So, in a similar range, our finding for the total density slope is also consistent with that of Nitschai et al. (2020a).

In addition, we also have calculated the total surface density as a function of radius by analytically integrating the MGE Gaussians. The integral of one Gaussian, between the cylindrical radii R_1 and R_2 and within the height range $|z| < z_{\max}$ is given by the following expression

$$M = (2\pi)^{3/2} \rho_0 q \sigma^3 \left(e^{-\frac{R_1^2}{2\sigma^2}} - e^{-\frac{R_2^2}{2\sigma^2}} \right) \operatorname{erf} \left(\frac{z_{\max}}{q\sigma\sqrt{2}} \right). \quad (3.9)$$

This integral was performed for all the MGE Gaussians for the stellar, gas, and dark matter components for $-1.1 \text{ kpc} \leq z \leq 1.1 \text{ kpc}$ for direct comparison with Bovy and Rix (2013). The resulting surface density is shown in Figure 3.7. Our surface density is a little bit lower for radii smaller than R_\odot but agrees within the uncertainties at the solar radius, $\Sigma(R_\odot, |z| \leq 1.1 \text{ kpc}) = (55.5 \pm 0.5_{\text{stat}} \pm 1.7_{\text{syst}}) \text{ M}_\odot \text{ pc}^{-2}$. Moreover, Piffl et al. (2014) give for the solar radius $\Sigma(|z| \leq 0.9 \text{ kpc}) = (69 \pm 15) \text{ M}_\odot \text{ pc}^{-2}$ and our value of $\Sigma(R_\odot, |z| \leq 0.9 \text{ kpc}) = (51.1 \pm 0.4_{\text{stat}} \pm 1.7_{\text{syst}}) \text{ M}_\odot \text{ pc}^{-2}$ lies within their 3σ range. Since also our total surface density agrees within the uncertainties with previous findings, it gives us another confirmation that our model constrains well the total density, circular velocity, and potential, and only the exact decomposition into the different components (dark matter, stellar, and gas), which is not the scope of this work, is not tightly constrained.

Further, we also performed a fit allowing the 18 Gaussians in the MGE model of the stellar component, to have a different anisotropy value, (σ_θ/σ_r) and (σ_ϕ/σ_r) . This model has a total of 39 free parameters and the ones that are not the anisotropies are listed in column ‘Free anisotropies’ in Table 3.1. This model gives a better fit to the data, since it has more parameters but all ‘interesting’ parameters agree within the 3σ error range with our main model.

3.4.2 Assessing Systematic Errors Due to Nonaxisymmetries

Our Galaxy contains nonaxisymmetric features due to the Galactic bar (e.g., Monari et al., 2016; Khoperskov et al., 2019), spiral arms (e.g., Reid et al., 2019; Eilers et al., 2020), the warp of the disk (e.g., Vázquez et al., 2008; Li et al., 2020), or interactions and mergers with satellite galaxies (e.g., Helmi et al., 2018; Koppelman et al., 2019b). We now investigate how the model assumption of axisymmetry affects our results by dividing the data set into four sectors, depending on positive or negative z and ϕ : $[z \geq 0 \text{ kpc}, \phi \geq 0^\circ]$, $[z \geq 0 \text{ kpc}, \phi < 0^\circ]$, $[z < 0 \text{ kpc}, \phi \geq 0^\circ]$ and $[z < 0 \text{ kpc}, \phi < 0^\circ]$. If the Milky Way was perfectly axisymmetric, our axisymmetric model should give the same results within the errors for each of the four sectors. Hence, we now fit each sector separately and compare the different results, in order to estimate how much the nonaxisymmetric features of our Galaxy influence our model and estimate the systematic uncertainties of the free parameters.

For these fits we use the same errors as for the fit to all data points. The resulting circular velocities are plotted in Figure 3.6 as fainter and thinner blue lines and all the

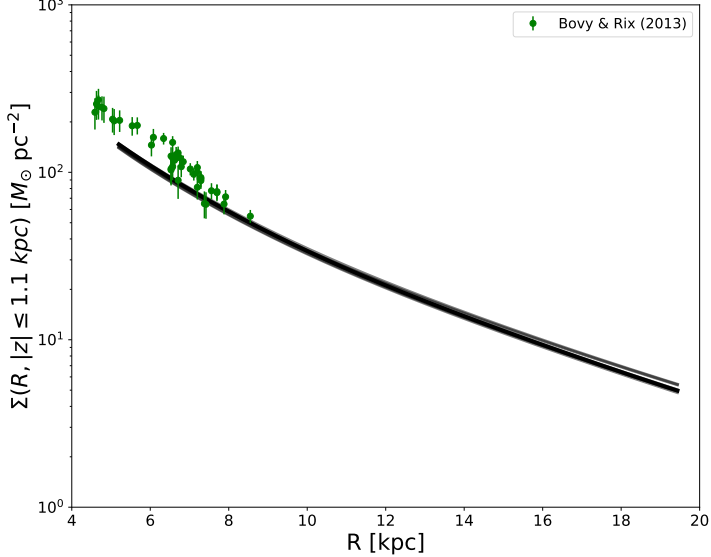


Figure 3.7: Surface Density for the JAM_{sph} Model without Flaring.

The total surface density is calculated between $-1.1 \text{ kpc} \leq z \leq 1.1 \text{ kpc}$ for our best-fitting model. The green dots are the values from Bovy and Rix (2013) and the five fainter black lines (close around it) are calculated with the best-fitting results from the four different sectors of the data (Section 3.4.2) and the model with free anisotropies. The radial range (5 kpc to 19.1 kpc) of the surface density in this plot, is between the minimum and maximum radius of the data which we used for our best-fitting model (see Figure 3.5).

fit parameters are listed in Table 3.2. The results show us that there are some differences depending on which part of the Galaxy we model, however, most of the free parameters are within the 3σ range of each other and with the total model. Higher discrepancies exist between α_{DM} , which are outside the 3σ range of the statistical errors.

Table 3.2: Best-fitting Parameters for the Four Sectors

Parameters	$z \geq 0 \text{ kpc}, \phi \geq 0^\circ$	$z \geq 0 \text{ kpc}, \phi < 0^\circ$	$z < 0 \text{ kpc}, \phi \geq 0^\circ$	$z < 0 \text{ kpc}, \phi < 0^\circ$	Mean	Syst. error
α_{DM}	$-1.623 \pm 0.017_{\text{stat}}$	$-1.627 \pm 0.018_{\text{stat}}$	$-1.469 \pm 0.019_{\text{stat}}$	$-1.487 \pm 0.019_{\text{stat}}$	-1.552 ± 0.079	± 0.079
f_{DM}	$0.837 \pm 0.007_{\text{stat}}$	$0.830 \pm 0.008_{\text{stat}}$	$0.816 \pm 0.007_{\text{stat}}$	$0.838 \pm 0.007_{\text{stat}}$	0.830 ± 0.011	± 0.014
$(\sigma_a/\sigma_r)_1$	$0.653 \pm 0.006_{\text{stat}}$	$0.655 \pm 0.008_{\text{stat}}$	$0.666 \pm 0.008_{\text{stat}}$	$0.709 \pm 0.010_{\text{stat}}$	0.671 ± 0.021	± 0.021
$(\sigma_a/\sigma_r)_2$	$0.569 \pm 0.011_{\text{stat}}$	$0.610 \pm 0.014_{\text{stat}}$	$0.601 \pm 0.013_{\text{stat}}$	$0.568 \pm 0.014_{\text{stat}}$	0.587 ± 0.038	± 0.038
$(\sigma_\phi/\sigma_r)_1$	$0.695 \pm 0.017_{\text{stat}}$	$0.702 \pm 0.017_{\text{stat}}$	$0.702 \pm 0.018_{\text{stat}}$	$0.771 \pm 0.019_{\text{stat}}$	0.718 ± 0.028	± 0.028
$(\sigma_\phi/\sigma_r)_2$	$0.911 \pm 0.021_{\text{stat}}$	$0.983 \pm 0.024_{\text{stat}}$	$0.940 \pm 0.023_{\text{stat}}$	$0.894 \pm 0.024_{\text{stat}}$	0.932 ± 0.045	± 0.054
$(M_*/L)_V$	$0.355 \pm 0.015_{\text{stat}}$	$0.361 \pm 0.016_{\text{stat}}$	$0.401 \pm 0.015_{\text{stat}}$	$0.352 \pm 0.015_{\text{stat}}$	0.367 ± 0.025	± 0.031
χ^2_{DOF}	0.98	0.97	1.03	1.05	-	-
$v_{\text{circ}}(R_\odot) [\text{km s}^{-1}]$	$233.7 \pm 0.3_{\text{stat}}$	$231.4 \pm 0.3_{\text{stat}}$	$234.3 \pm 0.3_{\text{stat}}$	$232.9 \pm 0.3_{\text{stat}}$	233.1 ± 1.5	± 1.7
$a_{v\text{circ}} [\text{km s}^{-1} \text{ kpc}^{-1}]$	$-1.71 \pm 0.06_{\text{stat}}$	$-1.76 \pm 0.07_{\text{stat}}$	$-1.18 \pm 0.07_{\text{stat}}$	$-1.11 \pm 0.06_{\text{stat}}$	-1.44 ± 0.33	± 0.34

The uncertainties given in this table as statistical errors are derived from the posterior distributions and are the formal errors. For the estimate of the systematic uncertainties we used these values and the values from Table 3.1, in addition, we give the mean value of the four sectors and its error, which is half of the difference of the minimum and maximum of the individual sectors (error = (max - min) / 2).

We can use the discrepancies between the parameters for the different sectors to get an estimate for the systematic uncertainty of our model because of nonaxisymmetric features in the data. The mean values in Table 3.2 are the mean of the individual sectors and the errors are half of the differences between the maximum and the minimum of the individual sectors. The last column of the table is the total systematic errors = (max-min)/2, including the best fitting values from Table 3.1 without flaring and the model with free anisotropies. These systematic errors from the sectors and from all our models without flaring might be the same if the minimum and maximum values are from the four sectors.

Additionally, for the four sectors, the mean dark matter density at the solar radius is, $\rho_{\text{DM}}(R_\odot) = (0.00935 \pm 0.00056_{\text{syst}}) M_\odot \text{ pc}^{-3}$ and the mean total density, $\rho_{\text{tot}}(R_\odot) = (0.0654 \pm 0.0015_{\text{syst}}) M_\odot \text{ pc}^{-3}$. The mean total density logarithmic slope, $\alpha_{\text{tot}} = -2.322 \pm 0.047_{\text{syst}}$ for $5 \leq R \leq 19.5 \text{ kpc}$ and the mean local surface density $\Sigma(R_\odot, |z| \leq 1.1 \text{ kpc}) = (54.6 \pm 1.7_{\text{syst}}) M_\odot \text{ pc}^{-2}$. All the errors given here are the same systematic errors as in Section 3.4.1 using the four sectors, the best-fitting model, and

the model with free anisotropies.

3.4.3 Flared Disk Model

In Section 3.3.1.2 we also explained how we can change our stellar distribution to account for the flaring of the disk. Using this distribution, we test how that affects our model.

We use the same errors as before and the fit results are listed in Table 3.1 with their formal errors. The model result is shown in the third column of Figure 3.5 and the posterior distribution is shown in the Appendix 3.A Figure 3.10. From the posterior distribution and the table, one can notice that the statistical uncertainty of $(\sigma_\theta/\sigma_r)_1$ is an order of magnitude smaller than for the rest of the velocity dispersion ratios, even though the fit has converged properly. This confirms that the formal errors are not reliable since they are too small and the systematic uncertainties of the model would dominate.

Further, the dark matter density at the solar radius $\rho_{\text{DM}}(R_\odot) = (0.00715 \pm 0.00007_{\text{stat}}) M_\odot \text{ pc}^{-3}$ and the total density $\rho_{\text{tot}}(R_\odot) = (0.08561 \pm 0.00073_{\text{stat}}) M_\odot \text{ pc}^{-3}$. The total density logarithmic slope $\alpha_{\text{tot}} = -2.451 \pm 0.010_{\text{stat}}$ for $5 \leq R \leq 19.5$ kpc and the local surface density $\Sigma(R_\odot, |z| \leq 1.1 \text{ kpc}) = (64.1 \pm 0.6_{\text{stat}}) M_\odot \text{ pc}^{-2}$.

From the χ^2 value, one can see that the fit with flaring is not as good as without it, which could be due to our choice of flare parameters. Also, if we compare the residuals of the two models, one can notice that the residuals get higher away from the midplane for the model with flaring. On the other hand, around the midplane, it seems to be similarly good or only slightly higher than the model without the flaring. The differences between the models with and without flaring can also be seen in Figure 3.8.

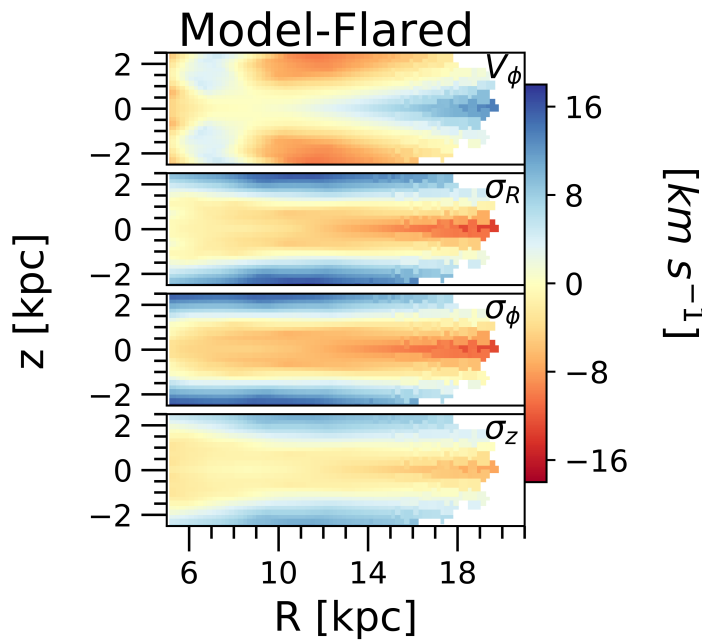


Figure 3.8: The Difference between the JAM_{sph} without and with a Flared Disk. From top to bottom the rows show $V_\phi, \sigma_R, \sigma_\phi, \sigma_z$.

We do not have systematic uncertainties because the investigation in the previous section was with a different Milky Way model without flaring and the flared model does not fit the data as well, thus, we cannot assume that they have the same systematics, and further study would be needed. As mentioned above, the flared model might give a slightly worse fit to our data only because of the flare parameters we selected, since we just added a parametrization of the scale height, $h(z)$, to our normal model without

flaring. Additionally, to fully test if the flared model provides a better fit to the data, one would need to do a detailed study of the flare and test which parametrization for the scale heights is the best for the Milky Way disk. This is beyond the scope of this work, and we just want to get a first idea of how our model changes if we include a flare.

3.5 Conclusion

In this work, we construct a dynamical Jeans model of the Milky Way disk using the JAM_{sph} code (Cappellari, 2020). The data we use are based on *Gaia* EDR3, combined with the Hogg et al. (2019) data set, which are combined APOGEE, *Gaia* DR2, 2MASS, and WISE data with precise spectrophotometric distance estimates. The combined data set enlarges the range of Galactocentric distances that we cover. We probe an area in the range of $5.0 \leq R \leq 19.5$ kpc and $-2.5 \leq z \leq 2.5$ kpc.

Our main results are consistent with Nitschai et al. (2020a) within the uncertainties, but more are reliable because of the more extended radial range of our data. The best fit value for the dark matter slope is $\alpha_{\text{DM}} = -1.602 \pm 0.015_{\text{stat}} \pm 0.079_{\text{syst}}$ which is smaller than -1 (NFW) and the dark matter density at solar radius is $(0.00892 \pm 0.00007_{\text{stat}} \pm 0.00056_{\text{syst}}) M_{\odot} \text{ pc}^{-3}$. These values agree with our previous work (Nitschai et al., 2020a) and are consistent with other works for the dark matter slope which indicate that a steeper slope than NFW is needed for the disk region (Portail et al., 2017; Cole and Binney, 2017). The dark matter density at solar position is slightly smaller than previous works (McKee et al., 2015; McMillan, 2017; Nitschai et al., 2020a), which might be because we constrain the total density and the decomposition is more uncertain, similar for what we explained for the circular velocity. However, the values still agree in the 3σ range of the uncertainties. The circular velocity at the solar position is $(234.7 \pm 0.3_{\text{stat}} \pm 1.7_{\text{syst}}) \text{ km s}^{-1}$ with a mild decline towards larger radii of $a_{\text{circ}} = (-1.78 \pm 0.05_{\text{stat}} \pm 0.34_{\text{syst}}) \text{ km s}^{-1} \text{ kpc}^{-1}$, which is consistent with the results from Eilers et al. (2019). The total density at the solar radius is $\rho_{\text{tot}}(R_{\odot}) = (0.0672 \pm 0.0006_{\text{stat}} \pm 0.0015_{\text{syst}}) M_{\odot} \text{ pc}^{-3}$ and total density logarithmic slope is $\alpha_{\text{tot}} = -2.367 \pm 0.007_{\text{stat}} \pm 0.047_{\text{syst}}$ for $5 \leq R \leq 19.5$ kpc and $-2.278 \pm 0.007_{\text{stat}} \pm 0.047_{\text{syst}}$ for $3.5 \leq R \leq 12.5$ kpc. All these values are consistent with our previous work (Nitschai et al., 2020a) within the errors. The total density slope is also consistent with the slope inferred from early-type disk galaxies (Cappellari et al., 2015) and the total solar density is again smaller compared to other works but agrees within the 3σ uncertainties of the work by McKee et al. (2015). Further, the local surface density is $\Sigma(R_{\odot}, |z| \leq 1.1 \text{ kpc}) = (55.5 \pm 0.5_{\text{stat}} \pm 1.7_{\text{syst}}) M_{\odot} \text{ pc}^{-2}$ which is slightly lower than other findings (e.g., Bovy and Rix, 2013; Piffl et al., 2014) but still within the uncertainties.

Additionally, we also test how nonaxisymmetries of the gravitational potential change our result. We further investigate how a flared disk would change our results. It provides a similarly good fit, but in the future, one could perform a more thorough analysis of the parameter space to better constrain the flaring of the disk given its dynamical properties.

The regions that are not included in our model are the bar in the inner part and the warp in the outer disk. These features are nonaxisymmetric and we cannot reproduce them with our model. We avoid the bar influence by excluding the region inside 5 kpc, but the warp is still affecting our model. Hence, one should note that the regions of our data strongly influenced by this feature (the outer disk) are not well reproduced with our model due to the axisymmetry assumption.

The kinematics used in this paper and the MGE components can be found in the file in the online version of the Paper ([Nitschai et al., 2021](#)).

Appendices

3.A Posterior Distribution

The posterior distribution of the best-fitting model without flaring (see Section 3.4.1) is shown in Figure 3.9. Additionally, Figure 3.10 shows the posterior distribution for the best-fitting model with a flared disk (see Section 3.4.3). We have also tested how the result changes with JAM_{cyl} ([Cappellari, 2008](#)) for the flared model and we see that the results are almost the same. The only difference is that the small formal errors of $(\sigma_\theta/\sigma_r)_1$ are getting off the same order as the other ratios and that χ^2_{DOF} is slightly smaller ($\chi^2_{\text{DOF}} = 1.07$), which can be a coincidence since the flared model we use might be wrong, and the cylindrical alignment may happen to compensate for that.

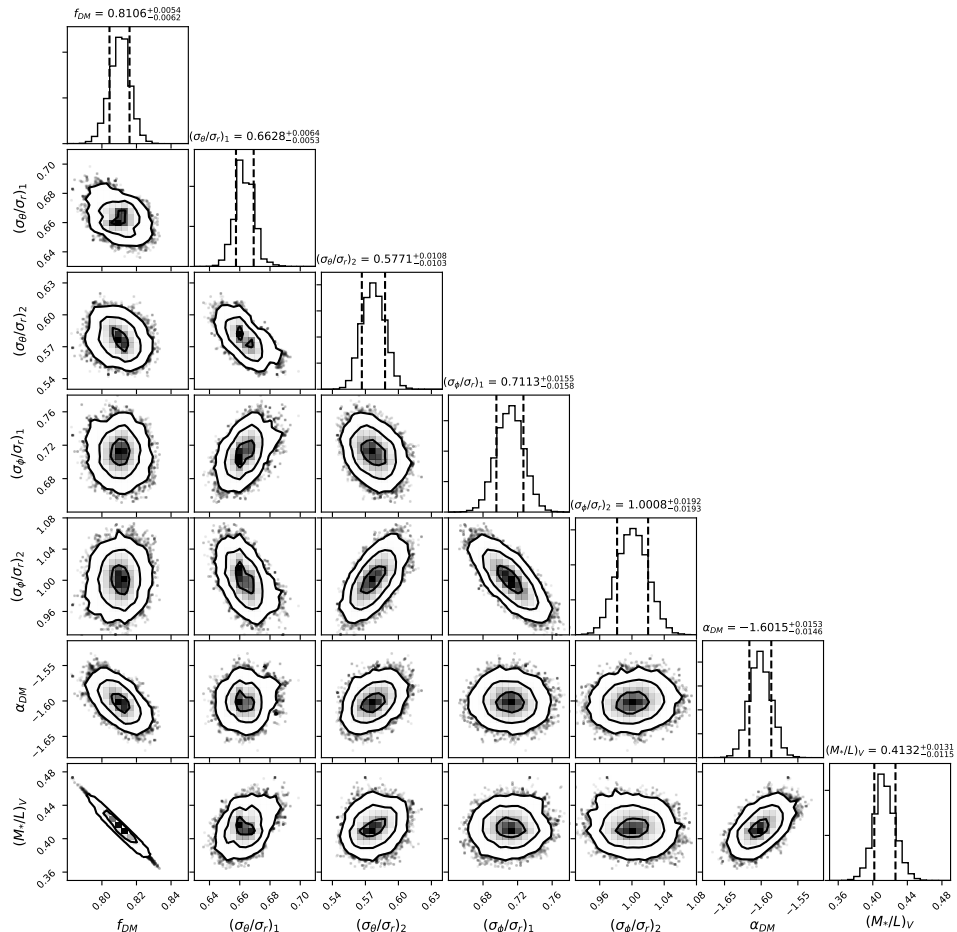


Figure 3.9: Posterior Distribution for the Best-Fitting JAM_{sph} with an Exponential Disk Model. This is the corner plot for the fit without a flared disk (see Section 3.4.1). The panels show posterior probability distributions marginalized over two dimensions (contours) and one dimension (histograms). The thick contours represent the 1σ , 2σ , and 3σ confidence levels for one degree of freedom. The numbers with errors on top of each plot are the median and 16th and 84th percentiles of the posterior for each parameter (black dashed lines).

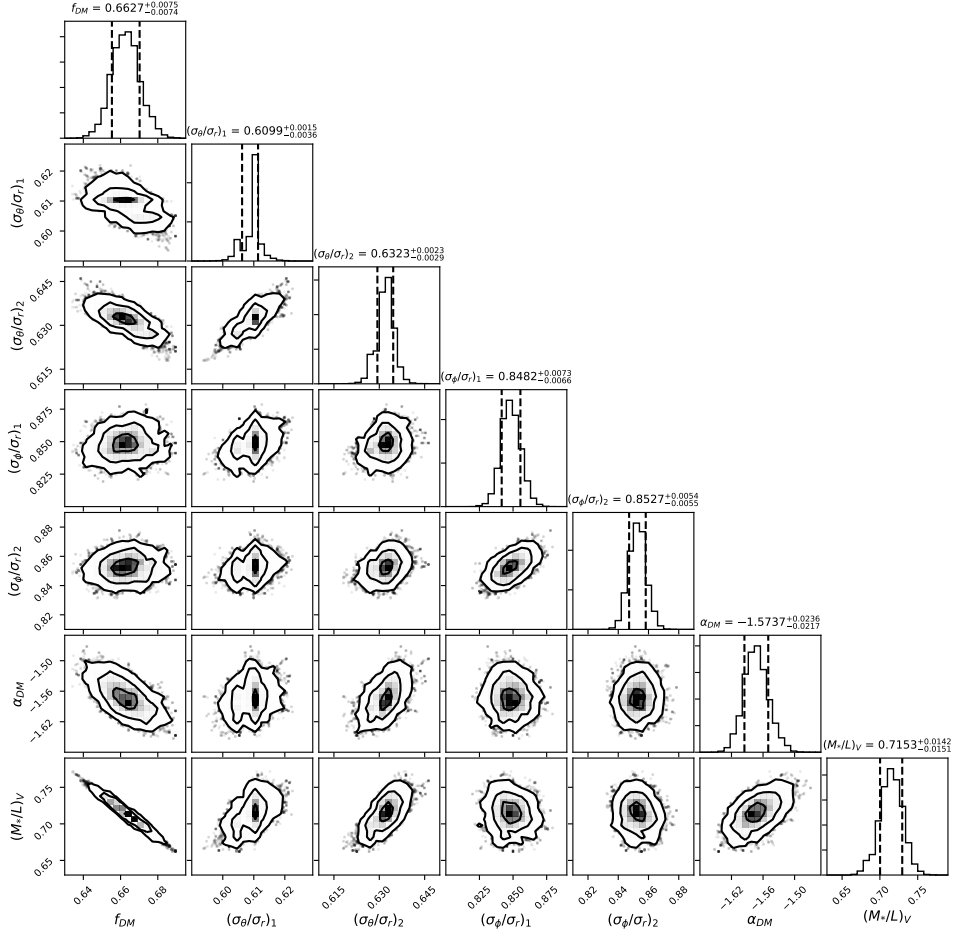


Figure 3.10: Posterior Distribution for the Best-Fitting JAM_{sph} with a Flared Disk Model. This is the corner plot for the fit with a flared disk (see Section 3.4.3). The panels show posterior probability distributions marginalized over two dimensions (contours) and one dimension (histograms). The thick contours represent the 1σ , 2σ , and 3σ confidence levels for one degree of freedom. The numbers with errors on top of each plot are the median and 16th and 84th percentiles of the posterior for each parameter (black dashed lines).

Table 3.3: Best-fitting Parameters for the Model with q_{DM} Free

Parameters	q_{DM} free
α_{DM}	$-1.576 \pm 0.026_{\text{stat}}$
f_{DM}	$0.788 \pm 0.009_{\text{stat}}$
$(\sigma_\theta/\sigma_r)_1$	0.664 ± 0.007
$(\sigma_\theta/\sigma_r)_2$	$0.572 \pm 0.010_{\text{stat}}$
$(\sigma_\phi/\sigma_r)_1$	$0.707 \pm 0.016_{\text{stat}}$
$(\sigma_\phi/\sigma_r)_2$	$1.004 \pm 0.021_{\text{stat}}$
$(M_*/L)_V$	$0.480 \pm 0.026_{\text{stat}}$
χ^2_{DOF}	0.906
q_{DM}	$1.473 \pm 0.068_{\text{stat}}$
$v_{\text{circ}}(R_\odot) [\text{ km s}^{-1}]$	$235.21 \pm 0.27_{\text{stat}}$
$a_{vcirc} [\text{ km s}^{-1} \text{ kpc}^{-1}]$	$-1.83 \pm 0.05_{\text{stat}}$

All uncertainties given in this table are statistical errors derived from the posterior distributions.

3.B The Dark Matter Axial Ratio (q_{DM}) as a Free Parameter

For our main model, we have fixed $q_{\text{DM}}=1.3$ (Posti and Helmi, 2019), here we show a model if we allow q_{DM} to be free. The resulting free parameters with a free q_{DM} for a model without flaring are listed in Table 3.3.

What we see also from the posterior distribution, is that q_{DM} tends to get high values and has a correlation with the mass-to-light ratio $[(M_*/L)_V]$. Since a too high q_{DM} value is nonphysical we keep it fixed for our models in the main text.

3.C Investigating the Offset of V_{circ} between Our Result and Previous Work

Additionally, we have investigated the offset that we found between the circular velocity from Eilers et al. (2019) and ours. We had already seen an offset in the previous calculation with the best-fitting JAM model in Nitschai et al. (2020a).

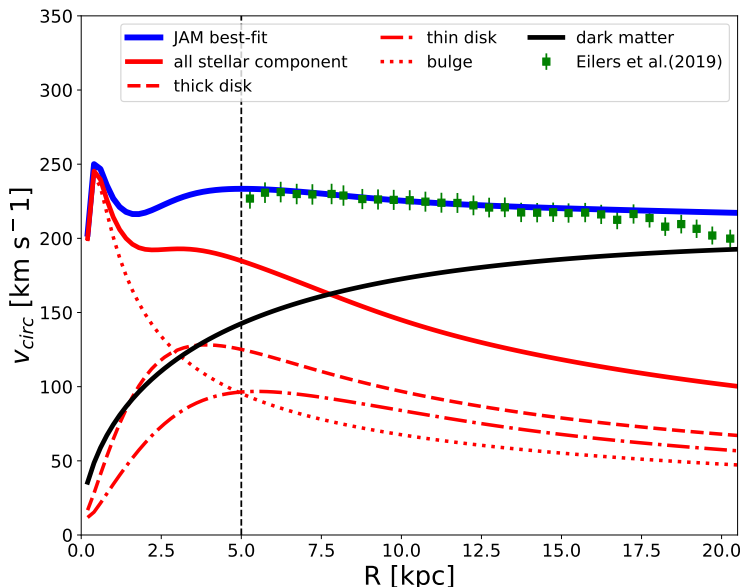


Figure 3.11: Circular Velocity Curve Same Assumptions as in Eilers et al. (2019). The green dots are the measurements from Eilers et al. (2019) with 3 % systematic errors. Our circular velocity curve using the potential we get using JAM is shown in blue, the stellar component is shown as a red solid line while the thin disk is a red dashed/dotted line, the thick disk is a dashed line, and the bulge is dotted. The dark matter halo is shown as the black solid line. The inner part of the galaxy, i.e. $R < 5 \text{ kpc}$ (indicated by the black dashed line), was excluded from the analysis by Eilers et al. (2019) due to the nonaxisymmetric influence of the Galactic bar.

To do that, we assume the same Milky Way model as in Eilers et al. (2019). We adopt a spherical NFW profile (Navarro et al., 1996), for the thin and thick disk we assume Miyamoto–Nagai profiles (Miyamoto and Nagai, 1975), and for the bulge, we assume a spherical Plummer potential (Plummer, 1911), while adapting the parameter values of Pouliasis et al. (2017, model I). Furthermore, we use only the Hogg et al. (2019) data

that satisfy $|z| < 0.5$ kpc or $\tan(z/R) < 6^\circ$ and have more than 3 stars in each $200 \text{ pc} \times 200 \text{ pc}$ bin. Finally, we assume $R_\odot = 8.122$ kpc (Gravity Collaboration et al., 2018), $z_\odot = 0.025$ kpc (Jurić et al., 2008) and as solar velocities in cylindrical Galactic coordinates $(U_\odot, V_\odot, W_\odot) = (-11.1, 245.8, 7.8)$ km s $^{-1}$ (Reid and Brunthaler, 2004).

Using the JAM_{cyl} (Cappellari, 2008) and the above assumptions we can reproduce almost perfectly the velocity curve by Eilers et al. (2019), see Figure 3.11 which is plotted as Fig. 3 in Eilers et al. (2019) for comparison.

This proves that the offset we have in our main model is not caused by the modeling method but by the data set and the Galaxy model we assume. Small discrepancies are towards the Center where we do not have data and towards higher radii. The last one confirms our suspicion that the Pouliasis et al. (2017) model overestimates the mass in the inner parts and therefore underestimates the stellar mass towards larger radii to compensate for it, which causes a high dark matter mass at larger radii.

Take away points

- We construct a dynamical Jeans model of the Milky Way disk using the JAM_{sph} code (Cappellari, 2020).
- Data: *Gaia* EDR3 and Hogg et al. (2019) data set, covering an area in the range of $5.0 \leq R \leq 19.5$ kpc and $-2.5 \leq z \leq 2.5$ kpc.
- We test the effect of nonaxisymmetries of the gravitational potential and a flared disk on our model.
- Our work demonstrates that we have an accurate knowledge of the mass distribution in our Milky Way.
- We can describe the main average characteristics of the observed stellar kinematics, regardless of the known deviations from equilibrium and axisymmetry.

Chapter 4

MUSE SPECTROSCOPY OF ω CENTAURI

This chapter has been published in Nitschai et al. (2023). Formatting and editing have been adjusted to match this thesis. I conducted the scientific work with the help of the co-authors and wrote all of the text, except for Section 4.4.5, which was written and implemented by co-author Callie Clontz. Suggestions and corrections from my co-authors and the referee of the paper are included in the text.

Abstract

Omega Centauri (ω Cen) is the most massive globular cluster of the Milky Way and has been the focus of many studies that reveal the complexity of its stellar populations and kinematics. However, most previous studies have used photometric and spectroscopic datasets with limited spatial or magnitude coverage, while we aim to investigate it having full spatial coverage out to its half-light radius and stars ranging from the main sequence to the tip of the red giant branch. This chapter has been published as the first paper in a new survey of ω Cen that combines uniform imaging and spectroscopic data out to its half-light radius to study its stellar populations, kinematics, and formation history. In this chapter, we present an unprecedented MUSE spectroscopic dataset combining 87 new MUSE pointings with previous observations collected from guaranteed time observations. We extract spectra of more than 300,000 stars reaching more than two magnitudes below the main sequence turn-off. We use these spectra to derive metallicity and line-of-sight velocity measurements and determine robust uncertainties on these quantities using repeat measurements. Applying quality cuts, for the main sequence stars (red giant branch stars) of magnitude $18 \text{ mag} < \text{mag}_{\text{F625W}} < 22 \text{ mag}$ ($10 \text{ mag} < \text{mag}_{\text{F625W}} < 16 \text{ mag}$) we achieve signal-to-noise ratios of 16.47 (73.51) and mean metallicity errors of 0.174 (0.031) dex. We correct the metallicities for atomic diffusion and identify foreground stars. This massive spectroscopic dataset will enable future studies that will transform our understanding of ω Cen, allowing us to investigate the stellar populations, ages, and kinematics in great detail.

Chapter Contents:

4.1	Introduction	58
4.2	Data	60

4.2.1	Observations and Data Sets	60
4.2.2	Data Reduction	61
4.3	Analysis Methods	62
4.3.1	Spectral Extraction	62
4.3.2	Completeness	63
4.3.3	Spectral Fitting	64
4.4	Analysis	66
4.4.1	Reliability Parameter	66
4.4.2	Error Analysis	67
4.4.3	Combining Multiple Measurements	70
4.4.4	Membership	71
4.4.5	Atomic Diffusion Correction	72
4.4.6	Perspective rotation	74
4.4.7	Catalog	75
4.4.8	Literature Comparison	76
4.5	Conclusion	77
Appendices	78
4.A	Data Conditions	78
4.B	PAMELMUSE Tests	80
4.C	Surface Gravity log(g)	80
4.C.1	Free log(g)	82
4.C.2	Metal Rich Stars	82
4.C.3	Literature log(g)	82
4.D	SNR Test	83
4.E	Catalog Columns	84
	Take away points	84

4.1 Introduction

Ω Cen is an ideal case to study a stripped nucleus, multiple populations, and the merger history of the Milky Way (see Section 2.3). With the oMEGACat project, we aim to assemble unprecedented spectroscopic, photometric, and astrometric data sets out to the cluster’s half-light radius to decode its formation history and interactions with the Galaxy. Combining these data sets will give us the full 3D velocity vector and metallicity information for hundreds of thousands of stars, which allows us to identify subpopulations and make detailed chemo-dynamical modeling. Further, we can study the age-metallicity relation, abundances, multiple subpopulations, fast-moving stars indicating the presence of an intermediate-mass black hole (Häberle et al., 2024b) at the center of the cluster, and many more interesting science questions (see Chapter 6 for more details).

The astro-photometric catalog is based on archival and new *Hubble Space Telescope* (*HST*) observations and contains proper-motion measurements and 6-band photometry for 1,399,455 stars (Häberle et al., 2024a). In this chapter, I present the first publication of the oMEGACat project, providing spectroscopy for 300,000 stars within the half-light radius of the cluster.

To study the cluster in detail and specifically the multiple populations, spectroscopic data are important for metallicity and abundance measurements. Due to the high crowding in the cluster many spectroscopic surveys, like *Gaia* (Gaia Collaboration et al., 2016, 2023b, , even in the Focused Product Release) and APOGEE (Mészáros et al., 2021),

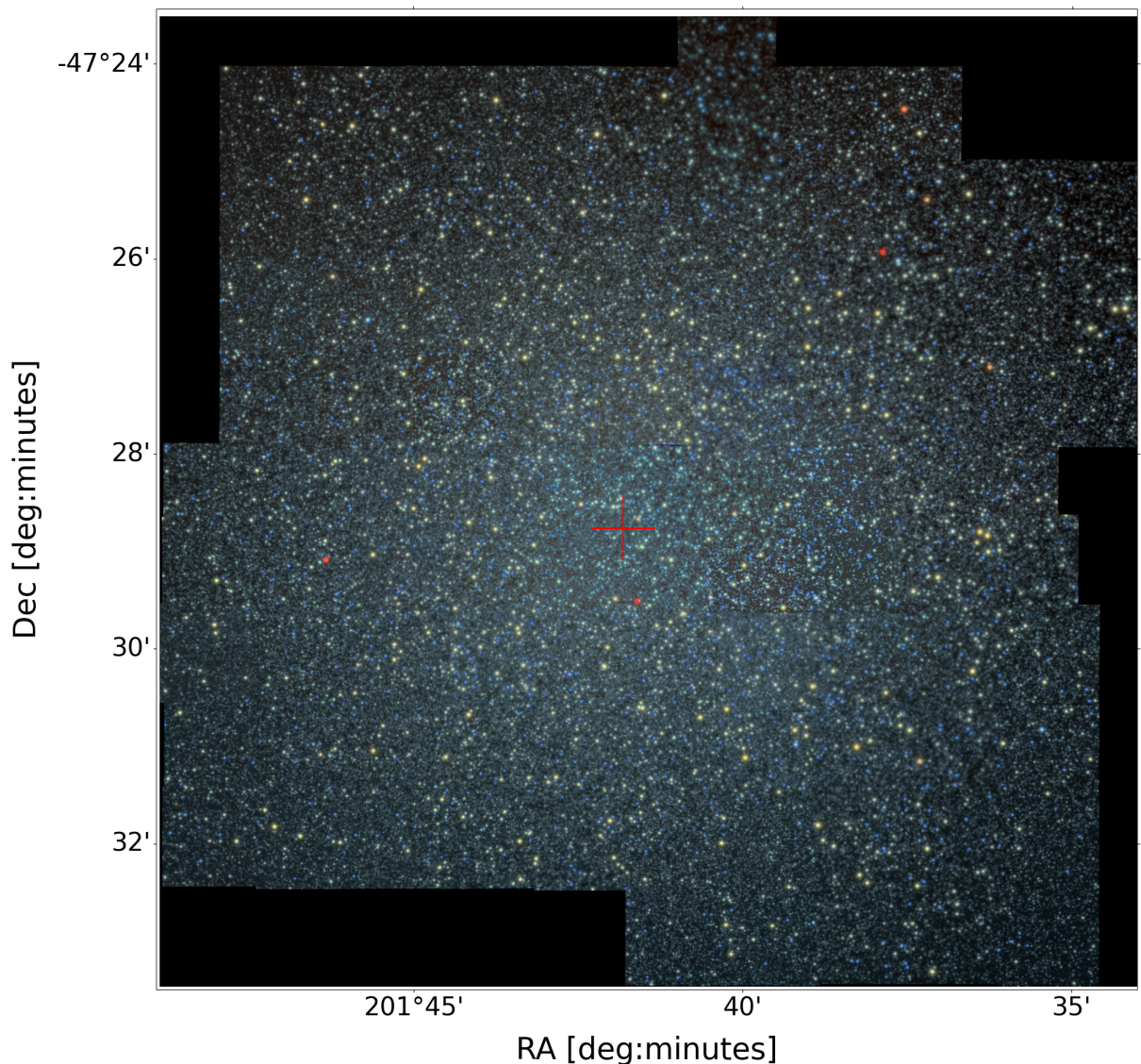


Figure 4.1: MUSE Image of ω Cen. A three-color RGB image of ω Cen created from MUSE WFM data using synthetic SDSS *i*, *r*, and *g* filters. The image displays the coverage of all WFM data (both GTO and GO). The red cross indicates the center of the cluster.

are limited to a few bright stars often only at the outskirts of dense clusters like ω Cen. Other studies like [Johnson and Pilachowski \(2010\)](#); [Johnson et al. \(2020\)](#) have spectroscopic data covering the central region but only for the brightest stars. The largest spectroscopic survey for multiple Galactic globular clusters, including ω Cen, has been presented in [Kamann et al. \(2018\)](#). This survey covers the very center of the cluster having thousands of spectra from the main sequence (MS) up to the red giant branch (RGB). We aim to further extend that sample out to the half-light radius.

The Multi-Unit Spectroscopic Explorer (MUSE) is the perfect instrument to investigate individual stars in clusters, as has been shown in other studies, e.g., [Husser et al. \(2016\)](#); [Kamann et al. \(2018\)](#); [Alfaro-Cuello et al. \(2019, 2020\)](#) and [Kacharov et al. \(2022\)](#). In this work, we present a large MUSE dataset, covering ω Cen out to its half-light radius, and the spectroscopic analysis of hundreds of thousands of individual stars, by far the

largest spectroscopic dataset ever assembled for ω Cen, or in any cluster.

The chapter is divided into the following sections: In Section 4.2 we present the observations and in Section 4.3 we describe the methods used to get the physical parameters for our catalog. In addition, in Section 4.4 we explain the analysis performed on that catalog to clean and test it. Further tests are also shown in the Appendix. Finally, in Section 4.5 we summarize and give an outlook on further works in progress using this catalog.

4.2 Data

4.2.1 Observations and Data Sets

The data presented in this work were acquired with MUSE (Bacon et al., 2010, 2014), a second-generation Very Large Telescope (VLT) instrument located at the UT4 at the Paranal Observatory in Chile. Two sets of data are combined in this work; the first are existing data, part of the MUSE guaranteed time observations (hereafter “GTO data”), with program IDs: 094.D-0142, 095.D-0629, 096.D-0175, 097.D-0295, 098.D-0148, 099.D-0019, 0100.D-0161, 0101.D-0268, 0102.D-0270, 0103.D-0204, 0104.D-0257, 105.20CR, and 109.23DV. These GTO data consist of 10 pointings with multi-epoch data that have been analyzed already in several papers (Kamann et al., 2018; Husser et al., 2020; Latour et al., 2021) as well as six central pointings using the MUSE narrow field adaptive optics mode (NFM), presented in Pechetti et al. (2024). The second dataset is from the General Observer (GO) program 105.20CG.001 (PI: N. Neumayer); this includes 87 new MUSE pointings taken between February 2021 and September 2022 – we refer to this dataset as the “GO data” and describe this dataset in more detail below.

MUSE is an integral-field spectrograph, based on image-slicing with 24 identical integral field units (IFUs). The field of view in the wide field mode (WFM), which was used for the GO data, is $59''.9 \times 60''.0$ for each pointing with a spatial pixel scale of $0''.2 \text{ pix}^{-1}$. The instrument observes in the optical domain (480 nm– 930 nm) with a resolving power increasing with wavelength from 1770 to 3590 and a spectral sampling of $0.125 \text{ nm pix}^{-1}$. For the GTO NFM data, the field of view of each pointing is $7''.5 \times 7''.5$, they have a sampling of $0''.025 \text{ pix}^{-1}$ and the resolving power is increasing with wavelength from 1740 to 3450. In both the GO and GTO data, some central pointings are also taken using the VLT Adaptive Optics Facility (AOF) (Arsenault et al., 2010; Ströbele et al., 2012). In adaptive optics (AO) mode the NaD lines are blocked using a filter, causing a gap in the spectra between 580 nm and 597 nm (Weilbacher et al., 2016).

In the GO data, each field has three exposures with a rotation of 90° between them (no dithering), and the exposure time was 200 s. The observations were requested in service mode at an airmass less than 1.4 and a seeing better than $0''.8$. These conditions were almost always fulfilled, see Table 4.2 in the Appendix for more details on the observing conditions. We note that one observing block (OB 1.3) was initially observed using AO with the wrong offset, causing a small gap in our dataset. Therefore, it was repeated without AO in September 2022 once more, to fill in the gap.

We show the spatial coverage of our combined dataset in Figure 4.1 and Figure 4.2. The combined dataset includes a total of 97 WFM pointings as well as six central NFM pointings, providing complete coverage out to the half-light radius of ω Cen ($4'.65$ or 7.04 pc , Baumgardt and Hilker, 2018).

The reduction and analysis of the GTO data were already done, details on the GTO

WFM data are presented in Kamann et al. (2018), while the NFM data are presented in Pechetti et al. (2024). For the GO data, we duplicated the GTO WFM reduction procedure as closely as possible.

For the rest of the work, most of the data reduction and analysis steps refer to just the GO data, except where clearly specified to also include the GTO data.

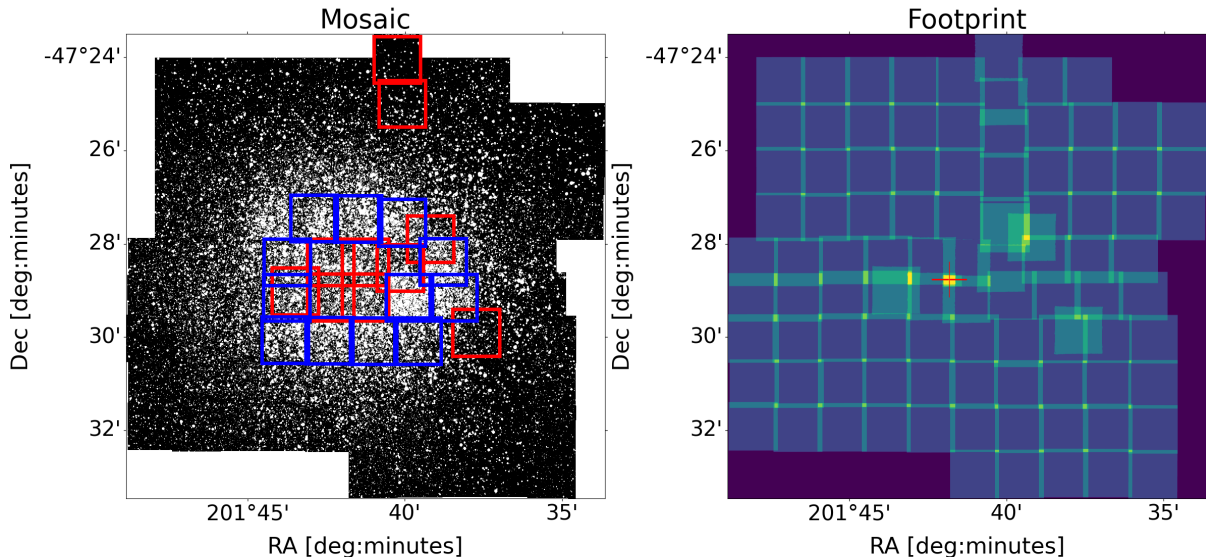


Figure 4.2: Image of ω Cen and Footprint of the MUSE Pointings. On the left is a grayscale image created from the combined GO and GTO MUSE WFM data. Overlaid blue colored squares indicate the GO AO pointings, red squares the WFM GTO data, while the region without squares is where the non-AO GO WFM pointings lie. On the right is the footprint of the individual pointings showing the overlap of the data. At the center of the right-hand figure, the NFM data are within the yellow region at the center of the image, indicated with a red cross. The x-axis is right ascension (RA) and the y-axis is the declination (Dec).

4.2.2 Data Reduction

We use the MUSE pipeline, version 2.8.3 (Weilbacher et al., 2016, 2020), to reduce the GO data. This pipeline uses CPL (Streicher, 2016) and the ESOREX (ESO CPL Development Team, 2015) packages and contains all necessary procedures for the data reduction process, including bias subtraction, flat fielding, illumination correction, and wavelength calibration. Further, the pipeline flux calibrates the exposures using a standard star, corrects for the barycentric motion of the Earth, and combines the three single exposures into one for each field. We use the default settings for most parts of the pipeline, except for sky subtraction, where we use a sky continuum file containing zeroes as the model, so that only the emission lines are subtracted, but not the sky continuum. Removing the sky continuum also removes starlight in a crowded region like ours since even the darkest spaxels still contain starlight. This leaves sky continuum in our final data cubes, but since we do a point spread function (PSF)-based extraction (see Section 4.3.1) these emissions will not be in the spectra we extract but in the background components determined during the extraction.

In addition, we are not doing any Raman correction since the field of view is too crowded or the Telluric correction, since our spectral fitting routine can remove them

better. Hence, the Telluric lines are included in our spectral fit and are removed then from the spectra, see Section 4.3.3.

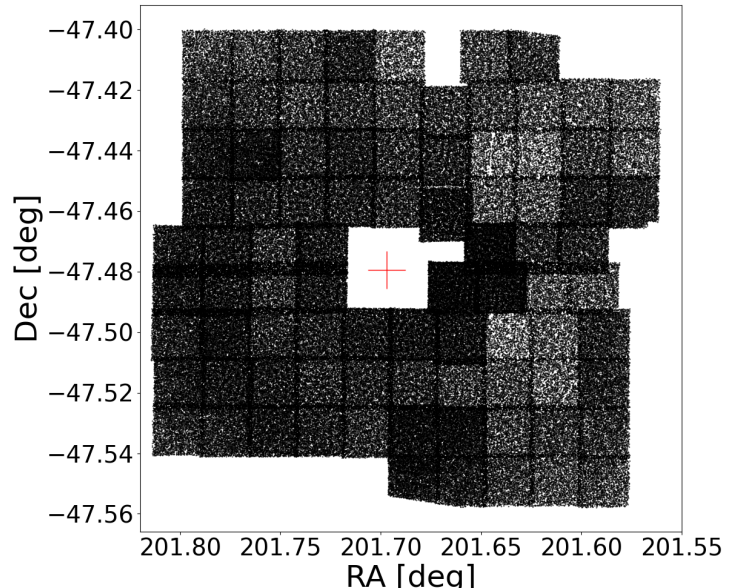
The total MUSE data coverage is shown in Figure 4.2, where the red squares indicate where the WFM GTO pointings lie and the blue squares where the 12 new WFM-AO pointings are, while all other pointings are WFM without AO, 75 in total. The GTO NFM data are within the yellow region at the center of the right panel of Figure 4.2 (the small yellow square where the red cross lies). The gaps in our GO pointings, visible in Figure 4.3, in the center and upper part of the image are filled in with the GTO pointings so that we have full coverage of the cluster without gaps when combining the two datasets.

4.3 Analysis Methods

After the reduction of the MUSE mosaic, the next step is to get spectroscopic information for individual stars. Therefore, we need to extract the spectra of individual stars and measure physical parameters from these spectra.

4.3.1 Spectral Extraction

Figure 4.3: All Extracted GO Stars. The figure shows the positions of all extracted GO stars using the [Anderson and van der Marel \(2010\)](#) photometric catalog. The red cross indicates the center, while the holes at the top and the center are later filled with the GTO stars. Some edges are cut off because the *HST* footprint does not perfectly cover the MUSE footprint. The overlap regions are denser since more stars are observed because there are two or more exposures. The variation in the number of stars seen in different fields is due to varying observing conditions that impact our completeness.



To extract individual spectra for the stars in the MUSE fields we use PAMPELMUSE¹ ([Kamann et al., 2013](#)) and the *HST* catalog from [Anderson and van der Marel \(2010\)](#). PAMPELMUSE takes the photometry and position of the stars in the *HST* catalog as a reference for the stars in the field of view of the MUSE data. It fits the PSF as a function of wavelength. Forced PSF photometry performed at each wavelength for all the stars in the catalog allows PAMPELMUSE to separate sources efficiently even in crowded regions. The [Anderson and van der Marel \(2010\)](#) catalog includes F625W and F435W magnitudes for 1.2×10^6 stars and covers a field of $10' \times 10'$ with a pixel scale of 50 mas pix^{-1} . We use a Moffat profile ([Moffat, 1969](#)) for the PSF as defined in Section 4.2 of [Kamann et al. \(2013\)](#) and allow it to vary its ellipticity, positional angle, β -parameter, and full width at half maximum (FWHM), while the initial value for the FWHM is set to be the mean

¹<https://PampelMuse.readthedocs.io/en/latest/about.html>

value of the seeing at the time of the observation. The extracted spectra also get a quality flag assigned from PAMPELMUSE where 0 is the best flag a spectrum can get. While there are 4 other criteria for the flags there can also be a combination of them, 1: more than one source contributing, 2: signal-to-noise ratio (SNR) < 10 , 4: the flux is negative, and 8: the centroid of the source is outside the field of view of the data cube.

We have performed an additional analysis on some OBs using a different extraction setup and find that the final results for spectra with an SNR > 10 do not change significantly, see Appendix 4.B.

In total we extract with PAMPELMUSE 355,682 stars from the GO MUSE dataset, see Figure 4.3, where we show their positions.

4.3.2 Completeness

We investigate how complete our GO data are after the spectral extraction compared to the *HST* catalog (Anderson and van der Marel, 2010).

For each MUSE pointing we mask the edges of the pointings by $5''$, to not get edge effects, and we divide our sample in 0.5-mag-wide bins and define the completeness in each bin as the ratio between the number of stars in the *HST* catalog and the number of stars for which we actually extract a spectrum from the MUSE data. We computed the completeness excluding spectra with an SNR lower than specific thresholds, i.e., 1, 5, 10, 15, 20, 25, and 30.

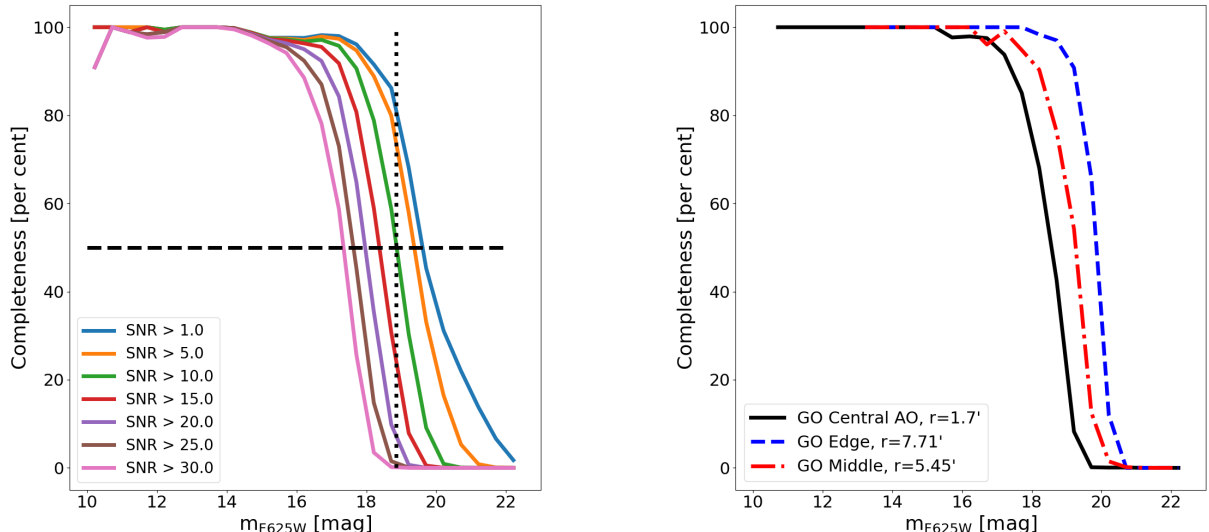


Figure 4.4: GO Completeness Plots. On the left is the overall GO completeness (the combined completeness for all 87 GO pointings) for different SNR cuts, from left to right the SNR is decreasing. The dashed line indicates 50 % completeness and the dotted line is 18.86 mag in F625W. The right panel shows for an SNR > 10 the individual completeness for 3 pointings at different radii from the center (r).

We show the overall completeness curves as a function of magnitude for different SNR cuts in the left panel of Figure 4.4. The completeness is almost 100 % for the brightest stars and falls off towards fainter stars. In addition, it shows that the overall completeness is above 50 % for stars brighter than ~ 18.86 mag (F625W Filter) for an SNR threshold of 10, while for higher SNR this is shifted to lower magnitudes. The right panel shows that in the central regions, the completeness is lower for the fainter stars due to crowding.

4.3.3 Spectral Fitting

After extracting the spectra, we use SPEXXY² (Husser et al., 2016) version 2.5 to measure the physical parameters of the stars. The observed spectra are compared to synthetic spectra from the Phoenix library (Husser et al., 2013) to derive each star’s effective temperature T_{eff} , and metallicity [M/H] using a χ^2 minimization. The range of the spectral parameters are: $-4 \text{ dex} \leq [M/H] \leq 1 \text{ dex}$, $2300 \text{ K} \leq T \leq 15,000 \text{ K}$ and $0 \leq \log(g) \leq 6$. We also include a SPEXXY fit to the telluric absorption lines (which were not corrected previously, see Section 4.2.2) for H₂O and O₂. We use all spectra we could extract in this analysis part regardless of their quality at this point.

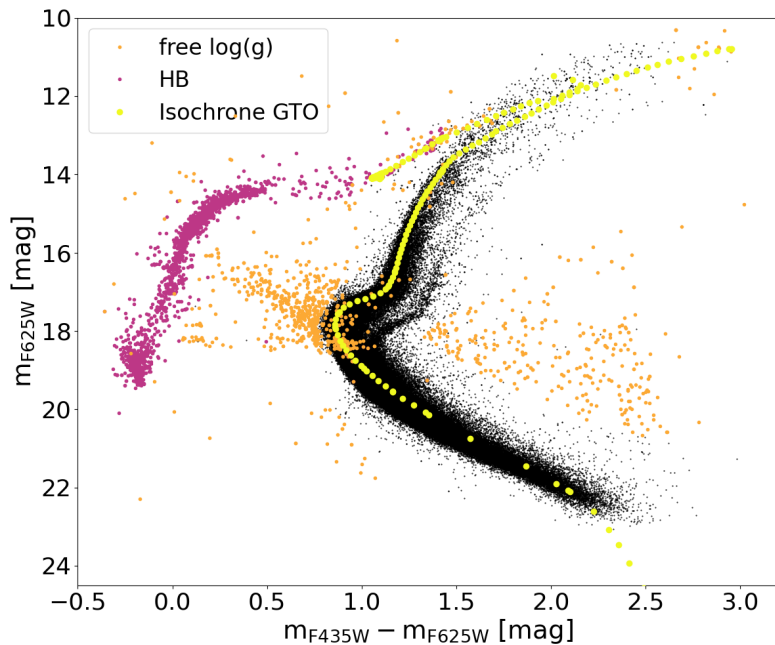


Figure 4.5: CMD of GO stars. CMD of the stars in the GO dataset. The black dots show the stars with fixed $\log(g)$ in our SPEXXY fit while the orange points have free $\log(g)$ and the purple are the HB stars which are disregarded in the current analysis. The yellow points indicate the position of the isochrone used to infer the $\log(g)$.

The initial values for $\log(g)$ and T_{eff} were determined as outlined in Husser et al. (2016) and Kamann et al. (2018). In summary, the photometry from Anderson and van der Marel (2010) was fitted with an isochrone from the PARSEC database (Marigo et al., 2017), and each observed star was assigned the stellar parameter from the nearest isochrone point, in the magnitude-color plane. For that, a two-dimensional polynomial is fitted to the temperature and $\log(g)$ from the isochrone as a function of color and magnitude. This isochrone has an age of 13.7 Gyr, a metallicity of -0.94 dex, extinction (A_v) of 0.23 mag, a distance of 5320 pc, and is shown as yellow dots in Figure 4.5. Since it is known that ω Cen has multiple populations, one isochrone is not ideal to describe all populations but here we only want to get initial values and a reliable $\log(g)$ for our spectral fit. A detailed population analysis will follow in upcoming work. The same is true for binary stars or multiple stellar systems, which are also offset in the colour-magnitude diagram (CMD). However, the binary fraction of ω Cen is small, less than 5 % (Elson et al., 1995; Mayor et al., 1996) and in recent work even lower at $2.70 \% \pm 0.08 \%$ (Bellini et al., 2017b) and because of multiple populations, the binary sequence is also intertwined with the main sequence track. Since $\log(g)$ does not strongly affect the [M/H] determination (Husser et al., 2016; Kamann et al., 2016, see also Appendix 4.C.1) and we only require reliable $\log(g)$ parameters, one isochrone is sufficient even if the cluster is much more complex. We show the CMD in Figure 4.5. During the fit with SPEXXY, $\log(g)$ is fixed

²<https://github.com/thusser/speaxy>

to the value provided by the isochrone ranging from 0 to 6, the α -enhancement is kept constant at $[\alpha/\text{Fe}] = 0.3$ dex (similar to Latour et al., 2021), while T_{eff} and $[\text{M}/\text{H}]$ are determined. SPEXXY also measures the line-of-sight (LOS) velocity, v_{los} , for the observed spectra. For that, we need initial values, which we get from a first cross-correlation with templates before starting the run with SPEXXY. If the result of the cross-correlation is not good enough, and we obtain $r_{cc} \leq 4$ from the r-statistics (Tonry and Davis, 1979), we set the initial value to 234 km s^{-1} , which is the mean LOS velocity of the whole cluster (Baumgardt et al., 2019b).

For the spectral fit, we use the whole wavelength range of the MUSE spectra, excluding only the NaD line or AO region (578 nm – 599 nm) and any other bad pixels identified. Four example spectra are shown in Figure 4.6 together with their best-fitting template spectrum in red. The light red shaded areas are the masked regions excluded from the fit. In addition, the SNR is also determined by SPEXXY from the fit residuals providing a good indicator of the quality of the data.

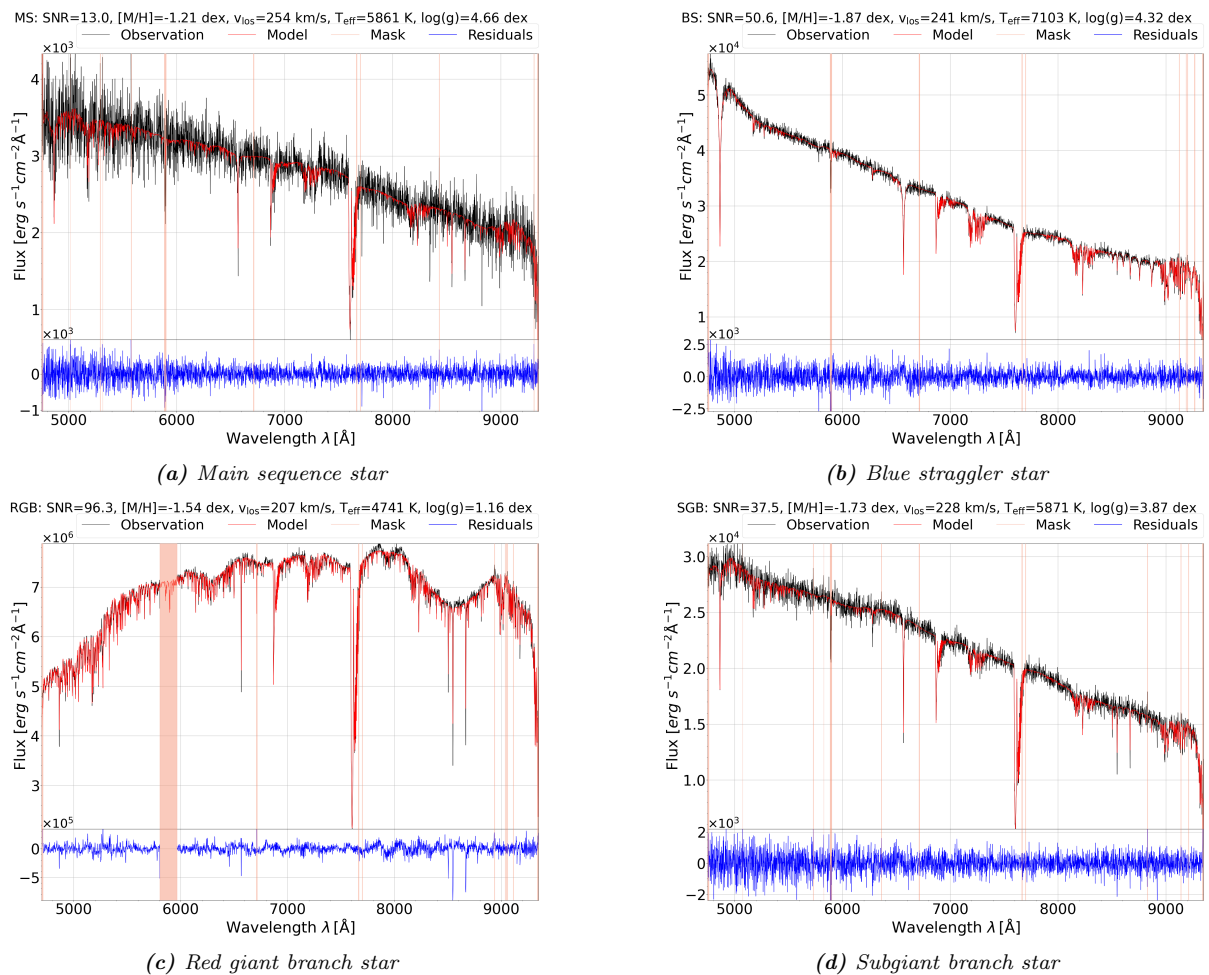


Figure 4.6: Example Spectra. (a)-(d); Spectra of stars at different stages of evolution plotted in black, with best-fitting SPEXXY models in red. The light red shaded areas are the excluded/masked regions during the fit; note that the RGB star (d.) is observed with AO and the NaD line is blocked. The bottom panels show the data-model residuals in blue. We note that the deep broad absorption features at 6800 and 7600 \AA are telluric features that are fit by SPEXXY along with the stellar properties. The best-fitting parameters for SNR, $[\text{M}/\text{H}]$, v_{los} , T_{eff} , and the $\log(g)$ value are given on top of each spectrum.

In summary, with SPEXXY we derive values for $[\text{M}/\text{H}]$, v_{los} , T_{eff} , SNR, telluric parameters and their statistical errors. However, the results for stars lying further away from

the isochrone (e.g., blue stragglers sequence (BSS) or asymptotic giant branch (AGB)) that is used to provide the $\log(g)$ values have to be considered biased. Hence, for stars not lying on the main isochrone, i.e. stars indicated with orange dots in Figure 4.5, we rerun SPEXXY allowing the $\log(g)$ parameter to vary freely during the fit. These stars are either not following the main CMD track (this might be nonmember stars or have unreliable photometry measurements from *HST*) or belong to the BSS or AGB. For stars that could be BSS/AGB or be part of the main CMD track, we keep both sets of values with free and fixed $\log(g)$. These are the orange dots that lie on top of the black dots in Figure 4.5. This increases the number to 356,065 measurements due to the duplicates added from the overlap regions.

For further analysis, we do not include the horizontal branch (HB) stars, indicated as purple dots in Figure 4.5. Stars hotter than $\sim 11,000$ K have chemically peculiar atmospheres due to diffusion and require dedicated model atmospheres for proper analysis (see [Latour et al., 2023](#)). The analysis of the HB stars included in our GO data will be presented elsewhere.

4.4 Analysis

In Section 4.3 we explained how we get a spectroscopic catalog from our MUSE data. This catalog needs to be further analyzed to remove contamination from foreground/background stars and to obtain robust measurements. Our overall goal is to keep as many stars as possible in the catalog and provide all parameters needed to perform the relevant quality cuts depending on the science case.

For our final catalog, we combine both the GO and GTO datasets. The GTO catalog contains 795,944 measurements belonging to 75,416 unique stars (see Section 4.4.3). As described in the previous section, the GO analysis followed that of the GTO data with three main differences: (1) the GTO data have multiple epochs of observations as opposed to a single epoch for the GO data, (2) the GTO use two *HST* catalogs for source positions, the catalog created by [Anderson et al. \(2008\)](#) for the Advanced Camera for Surveys (ACS) survey of Galactic GCs ([Sarajedini et al., 2007](#)) and the [Anderson and van der Marel \(2010\)](#) catalog, and (3) during SPEXXY fits the $\log(g)$ for the BSS in the GTO data set was kept fixed to 4.2 dex, while we fit for $\log(g)$ for these stars.

4.4.1 Reliability Parameter

To have one overall parameter evaluating the quality of the derived LOS velocities, we calculate a reliability parameter R , as explained in Section 3.2 of [Giesers et al. \(2019\)](#):

$$R = (2R_{SNR} + 10R_{cc} + R_{\epsilon_{vcc}} + 3R_v + 2R_{\epsilon_v} + 5R_{v=vcc})/23. \quad (4.1)$$

The different components can be either false (0) or true (1), allowing the range of R to be from 0 to 1 with higher values being more reliable than lower ones. The first component, R_{SNR} , is an SNR cut, while the other parameters are different checks of the credibility of the LOS velocity calculations. In detail, they check the quality of the cross-correlation (R_{cc}), if the cross-correlation and the full-spectrum fit uncertainty are plausible ($R_{\epsilon_{vcc}}$ & R_{ϵ_v}) if the full-spectrum fit velocity is agreeing with the expected cluster or foreground velocity and with the cross-correlation (R_v & $R_{v=vcc}$).

First, we consider a minimum SNR of 5 to be reliable:

$$R_{\text{SNR}} = \text{SNR} \geq 5. \quad (4.2)$$

That is, however, not our suggested SNR cut for the whole catalog, which should be higher (Section 4.4.7), but only for the velocity calculation which does not need that high SNR. In addition, we use the FWHM result from our cross-correlation and the r-statistics (Tonry and Davis, 1979) to check the quality of the cross-correlation which gave the initial LOS velocities for the fit with SPEXXY:

$$R_{cc} = r_{cc} \geq 4 \text{ & } FWHM > 10 \text{ \AA}. \quad (4.3)$$

Further, a plausible velocity uncertainty of 0.1 km s^{-1} for the velocity from SPEXXY and from the cross correlation is required:

$$R_{\epsilon_v} = \epsilon_v > 0.1 \text{ km s}^{-1} \quad (4.4)$$

$$R_{\epsilon_{vcc}} = \epsilon_{vcc} > 0.1 \text{ km s}^{-1}. \quad (4.5)$$

Additionally, the velocity output from SPEXXY should be plausible. This means that it should match the velocity of either the cluster or the Galactic field stars. Hence, the values are checked to be within 3σ of the cluster velocity and the cluster dispersion, $v_{cl} = (232.7 \pm 0.2) \text{ km s}^{-1}$ and $\sigma_{cl} = 17.6 \text{ km s}^{-1}$ (Baumgardt and Hilker, 2018), or that they agree with the foreground stars. For the cluster membership, we calculate:

$$R_{v_1} = \frac{|v - v_{cl}|}{\sqrt{\epsilon_v^2 + (\sigma_{cl} + \epsilon_{vcl})^2 + a^2}} \leq 3. \quad (4.6)$$

With a being 30 km s^{-1} which is added to the broadening to account for the orbital motions of binary stars, as their measured velocities would not necessarily be covered by the cluster distribution. For the foreground stars:

$$R_{v_2} = \frac{|v - 0 \text{ km s}^{-1}|}{\sqrt{\epsilon_v^2 + (50 \text{ km s}^{-1})^2}} \leq 3, \quad (4.7)$$

with 50 km s^{-1} being the estimate for the foreground stars from the Besançon model (Robin et al., 2003) used in Section 4.4.4. The total R_v is true if at least one of the $R_{v_{1,2}}$ is true. Similarly, a maximum 3σ difference is allowed between the cross-correlation results and the final SPEXXY results, while allowing a maximal velocity error of 40 km s^{-1} for the cross-correlation:

$$R_{v=vcc} = \frac{|v - v_{cc}|}{\sqrt{\epsilon_v^2 + \epsilon_{cc}^2}} \leq 3. \quad (4.8)$$

We include the total R parameter for all stars in the catalog.

4.4.2 Error Analysis

To get a better understanding and estimate of the errors on our fitted parameters, we use stars with multiple observations (see Section 4.4.3), allowing us to compare the different results we get for the same star, similar to Husser et al. (2016) and Kamann et al. (2018). From that, we can compare the statistical uncertainty we get from the spectral fitting routine with the scatter from the repeat measurements. This allows us to estimate how

Table 4.1: Error Analysis

Dataset Parameter	a	b	Maximum scaling Model/Data	Minimum scaling Model/Data	Maximum fractional residual	Minimal fractional residual
GO [M/H]	0.887	0.007	1.644/1.938	1.401/1.200	0.179	0.226
GO v_{los}	-0.143	0.062	2.819/2.943	1.229/1.351	0.243	0.186
GO T_{eff}	1.791	-0.003	1.639/1.701	1.292/1.213	0.279	0.169
GTO [M/H]	0.866	-0.002	1.359/1.402	1.293/1.246	0.071	0.051
GTO v_{los}	-0.137	0.009	1.354/1.346	0.979/0.982	0.022	0.021
GTO T_{eff}	1.463	-0.014	1.521/1.596	0.976/1.137	0.209	0.125

The dataset and parameter used for the error analysis; column 2, and column 3, are the best fitting parameters for the first order polynomial, $g(x) = a + b \cdot x$, where x the SNR and y the $\sigma^2(\Delta y)$. Columns 4 and 5 are the maximum/minimum scaling we get from our best fit and what the actual data have; columns 6 and 7 are the Maximum and Minimum fractional residuals, which are always under 30 %.

accurate the errors from the spectral fitting routine are, and any scaling factor needed to correct them. We do this analysis for our main results from SPEXXY: the metallicity, line-of-sight velocity, and effective temperature, using only the individual measurements used to compute the mean parameters, as described in the following section (Section 4.4.3), for the error analysis.

We calculate:

$$\Delta y = \frac{y_i - y_j}{\sqrt{\epsilon_i^2 + \epsilon_j^2}}, i \neq j \quad (4.9)$$

where y_i, y_j are the different results we get from SPEXXY (where $y = [\text{M}/\text{H}], v_{\text{los}}$ or T_{eff}) for the same star in two different observations, and ϵ_i, ϵ_j are their SPEXXY errors. Some stars are in more than two observations (maximum in 4 for the GO data, 66 for the GTO data) so we calculate Δy for each combination of different results, giving us 24,216 values for the GO dataset and 2,016,633 for the GTO.

Afterward, we bin all Δy values in SNR bins depending on the mean SNR of the two measurements, SNR_i and SNR_j . We defined the SNR bins so that for the GO and GTO data, the statistics of no SNR bin can be dominated by just one star with multiple measurements if placed in the same bin. In the bottom panel of Figure 4.7 we show the maximum percentage of counts ($f = \max[\text{counts one star}]/\text{total number counts, per bin}$) one star has in each bin, whereas for the GO data it is always below 5 % and for the GTO below 10 %. The distributions of Δy in each of the SNR bins, if the SPEXXY errors are accurately estimated, should be a Gaussian with $\sigma = 1$ and the mean at 0.

In Figure 4.8 we show an example of the cumulative distribution function (CDF) for the metallicity errors before any correction (black solid line) in comparison to a normal distribution (red line). We find that, as in this example for $\text{SNR} > 10$, the SPEXXY errors typically are underestimated relative to the repeat measurements, which are a better estimate of the true errors. We, therefore, multiply the SPEXXY errors by a scaling factor, $\sqrt{1 + g(\text{SNR})}$, to get more accurate errors for each star. After applying the scaling of the errors (see next paragraph), the cumulative distribution of the repeat measurement $\Delta[\text{M}/\text{H}]$ (black dashed line) follows the normal distribution.

If we plot the variance σ^2 (σ calculated as half of the difference between the 15.86 percentile and 84.14 percentile) of this distribution as a function of SNR, we can see that σ^2 is higher than 1 towards larger SNR, see Figure 4.7. We can describe this trend using a simple function, $y = 1 + g(x)$, with $g(x)$ being a linear function, to get an estimate of the error correction needed as a function of SNR. We exclude the SNR bins below 10 for the fitting of the line. In Table 4.1 we list the best fitting parameters for the scaling relation and the values for the maximum and minimum scaling for $\text{SNR} > 10$. To quantify how

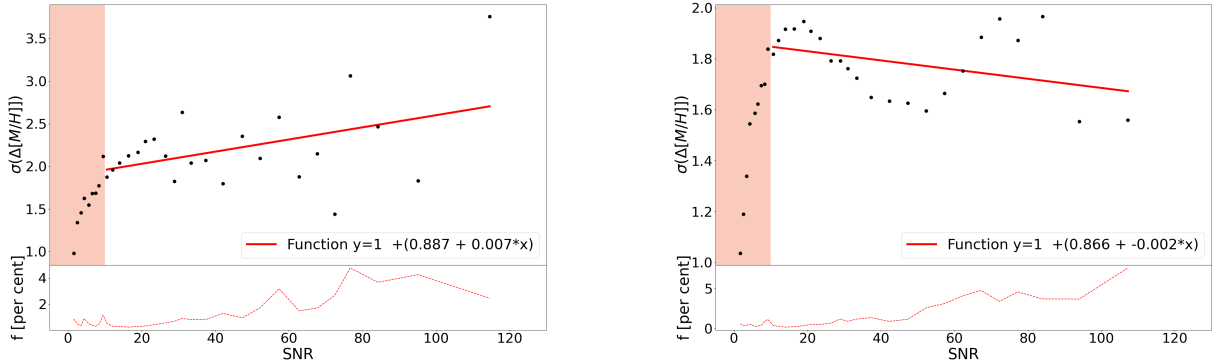


Figure 4.7: Error Analysis Correction. Top panels: The x -axis is the SNR and the y -axis is the σ^2 of the $\Delta[M/H]$ for the GO data on the left and the GTO data on the right. The red line is the best-fitting first-order polynomial, the black dots are our data values, and the light red shaded area is the region below an SNR of 10, which we exclude from the analysis. Bottom panels: The x -axis is the SNR and the maximum percentage of counts one star has in each bin. The red dashed line shows the maximum number of measurements each star can have, which is clearly always below 10 % of the total number of measurements in each bin, making sure the statistics in each bin are not the result of only one star.

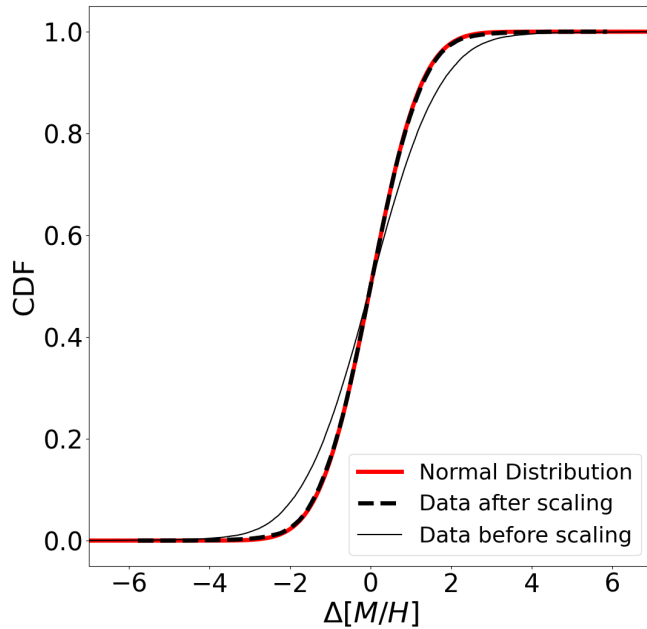


Figure 4.8: Error Analysis CDF. The cumulative distribution of the $\Delta[M/H]$ in black for $\text{SNR} > 10$ for the GO data and in red the distribution if it was a normal distribution. The dashed black line is the distribution after the error correction.

accurately the linear function captures the repeat measurement data, we also include the maximum/minimum fractional residual to this fit (e.g., the fractional error on the point that lies farthest from the line in Figure 4.7).

The derived scaling functions are then applied to all data according to their SNR. The mean scaled errors for $40 < \text{SNR} < 60$ are $\epsilon_{v_{los}} = 3.11 \text{ km s}^{-1}$, $\epsilon_{T_{eff}} = 36 \text{ K}$ and $\epsilon_{M/H} = 0.057 \text{ dex}$. These new, scaled errors are more accurate estimates of the true errors and hence we will always use them in the following analysis.

4.4.3 Combining Multiple Measurements

The next step is to combine measurements for each observed star. Due to the multiple epochs of observations in the GTO data, each star has been observed multiple times, and the spectra were analyzed independently, such that the 795,944 measurements belong to 75,416 unique stars. For the GO data, only stars in the overlap regions of the different pointings (green and yellow regions in Figure 4.2) have been observed more than once, with 303,822 unique stars out of the 356,065 measurements. In addition, there are also overlapping regions in the GTO and GO data where stars are in both datasets.

To combine multiple measurements of stars, we do a mean calculation for both datasets together after scaling the errors. First, we require the measurements to have a successful SPEXXY fit, meaning a fit to the templates could be performed without problems and the final parameters are not close to their limits set for the fit. These cuts leave us with 744,344 GTO measurements and 335,834 GO measurements.

For stars with multiple measurements, we then calculate the mean values using a subset of measurements selected in a procedure based on their reliability value (Section 4.4.1), magnitude accuracy from the spectral extraction, the distance to the edge of the detector, and an SNR cut. We use a threshold reliability value of 0.5, and magnitude accuracy <0.6 (the relative accuracy of the magnitude from the extracted spectrum vs. the *HST* catalog). We continue with measurements that meet these thresholds, or if there are none for a single star, we keep all measurements for the next steps in the combination.

Next, to use comparable measurements in the mean calculation, we first find the highest SNR spectrum and check if it is at least 5 pix ($1''$) away from the edge of the pointing. If it is, we consider it the best measurement for the given star. If it is not, we check the second-highest SNR spectrum and set that as the best measurement or, if it is also too close to the edge, we return to the highest SNR spectrum as the best measurement. Having found the best measurement, we require all remaining measurements to have at least half the SNR of the best measurement or in general higher than 20, at least as good of an extraction quality flag as the best, and if the best measurement was more than 5 pix away from the edge, the other measurements have to be, too. The measurements that pass these tests are in general comparable to the best measurement and are used to calculate the mean measurements for a given star. If there is only one measurement, then that is used as a single entry for that star.

For the mean calculation of [M/H], v_{los} and T_{eff} we calculate the inverse-variance weighted mean, using the scaled errors (see Section 4.4.2):

$$\hat{y} = \frac{\sum_i y_i / \epsilon_{si}^2}{\sum_i 1 / \epsilon_{si}^2} \quad (4.10)$$

$$\epsilon_{sy} = \sqrt{\frac{1}{\sum_i 1 / \epsilon_{si}^2}}. \quad (4.11)$$

ϵ_{sy} is the error to the inverse-variance weighted mean, similarly, we calculate the combined not scaled SPEXXY errors. The scaling factor and SNR are normal unweighted mean values, while for the quality parameters: distance to the edge, magnitude accuracy, extraction quality flag, and reliability parameter, we keep the minimum value (maximum for the extraction quality flag) included in the combined value. For the log(g) parameter we give the unweighted mean value, indicating if it was kept fixed or free during the fit, if we used both free/fixed we give both means.

This leaves us with a combined catalog of 342,796 unique individual stars with physical parameters. We describe recommended quality cuts for using this catalog further in Section 4.4.7. We match this catalog with the *HST* catalog by Anderson and van der Marel (2010), but note that 1432 stars in the GTO data which were extracted using the Anderson et al. (2008) catalog could not be matched; these stars are included in the catalog without Anderson and van der Marel (2010) magnitudes.

4.4.4 Membership

To decide which stars likely belong to ω Cen, we assign the stars a membership probability P_M that we can use to exclude foreground or background stars belonging to the Milky Way. We determine this probability using the python package CLUMPY³ (Kimmig et al., 2015) which is based on Walker et al. (2009). This code can use either radius (r) and velocity only for the estimate or can include another parameter, like the metallicity, to get the membership probability. As a foreground velocity distribution, we use the Besançon model (Robin et al., 2003)⁴ with 1° on each side centered on ω Cen and the model maximum absolute velocities are reaching up to 500 km s^{-1} .

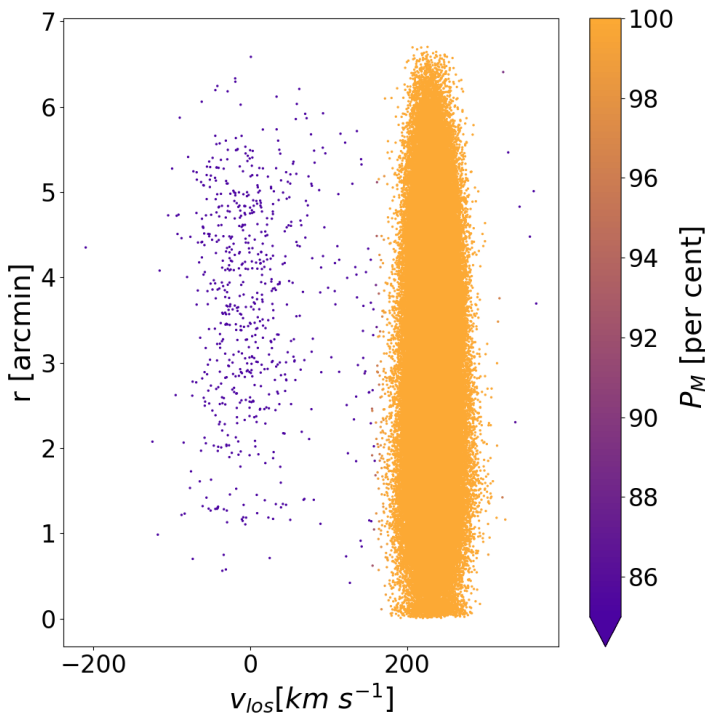


Figure 4.9: Membership Probabilities Using Radius and Velocity for a $\text{SNR} > 10$. The stars' radial distances to the cluster center (r) in arcminutes are plotted against their line-of-sight velocities. The points are color-coded according to their membership probability, yellow being 1.

The package uses an iterative maximization technique to get the probability and the systemic velocity and dispersion. Three separate memberships are going into the total membership probability including information about radius, velocity, and the foreground model: i) the probability of being a member which assumes that the stars follow a Gaussian velocity distribution centered on the mean velocity of the cluster, ii) the non-membership probability including the Besançon model information assuming a velocity dispersion of 20 km s^{-1} , and iii) the probability depending on the radius assuming a radial decrease in membership. After every iteration, the mean velocity, velocity dispersion, and

³<https://github.com/bkimmig/clumpy>

⁴<https://model.obs-besancon.fr/ws/>

probability are updated until they converge. We perform 50 iterations and the initial values are 0.5 for the probabilities and 4 km s^{-1} for the central dispersion of the cluster.

The membership output for $\text{SNR} > 10$ is shown in Figure 4.9 when using only velocity and radius from the center ($RA_c = 13:26:47.24$ and $Dec_c = -47:28:46.45$, Anderson and van der Marel, 2010) as input. We clearly can see the separation between the foreground stars and the members (over 95 % probability) in the velocity radius plane, with 98.8 % (338,531 stars) of stars being members and only 1.2 % (4266 stars) not. We choose to use the membership that does not include metallicity information for the following analysis since the [M/H] distribution of the cluster is too broad and hence not that easily distinguishable from the foreground. We note that 117 stars have no membership probability since their velocity exceeds the 500 km s^{-1} from the foreground model, however, these stars have low SNR (≤ 5).

4.4.5 Atomic Diffusion Correction

In the left panel of Figure 4.10 we show the CMD of our full MUSE catalog with each point colored by its metallicity [M/H]. The stars near the main sequence turn-off (MSTO) seem to be more metal-poor than stars falling directly above and below this region. A similar offset in metallicity was seen by Husser et al. (2016) in NGC 6397, who find a ~ 0.3 dex variation in the mean metallicity along the MS, with the lowest metallicity at the turn-off. Other analyses have also found a decrease in the observed metallicity (up to 0.25 dex, King et al., 1998) (in M92/NGC 6341) compared to stars of the same population along the MS and subgiant branch (SGB).

This shift can be explained by several internal transport processes including atomic diffusion (gravitational settling of heavier elements), thermal diffusion, radiative acceleration, and turbulent mixing (VandenBerg et al., 2002). For stars evolving through the MSTO, heavier elements begin to sink below the outer layers of the star causing them to be undetectable via spectroscopy. The consequence is that the observed metallicity of these stars is lower than the abundance they were originally born with. Once a star enters the SGB, convection in the outer layers begins and heavier elements are then dredged up to the surface where they are once again observable. Therefore, these stars no longer exhibit the offset in metallicity attributed to atomic diffusion. It is also noted in Korn et al. (2007) and Nordlander et al. (2012) that this phenomenon has a larger effect on extremely metal-poor stars, which is where we also see the greatest offset. We note that hereafter we refer to our correction for these effects as an “atomic diffusion correction” (ADC).

To correct for this effect on our metallicity measurements, we use MIST isochrones (Dotter, 2016; Choi et al., 2016), which take into account atomic diffusion. We use the distance modulus for the isochrones and apply extinction and reddening corrections to our photometry. Specifically, we assume $A_v = 0.372 \text{ mag}$ (Harris, 1996; Bellini et al., 2017c) and use the values for A_λ/A_v of 1.34148 and 0.85528 for F435W and F625W respectively⁵, giving us $A_{\lambda,435} = 0.499 \text{ mag}$ and $A_{\lambda,625} = 0.318 \text{ mag}$. We then subtract A_λ from the relevant magnitudes to obtain our corrected photometry.

We use a series of isochrones with Age = 10 Gyr and $-4.0 \text{ dex} < \langle \text{[Fe/H]} \rangle < 0.5 \text{ dex}$. We increase the CMD coverage of the MIST isochrones (which are available in steps of 0.5 to 0.25 dex in metallicity) by interpolating between equivalent evolutionary points to generate isochrones between the given models. We then iterate this process until we

⁵Obtained from <http://stev.oapd.inaf.it/cgi-bin/cmd>, Girardi et al. (2008).

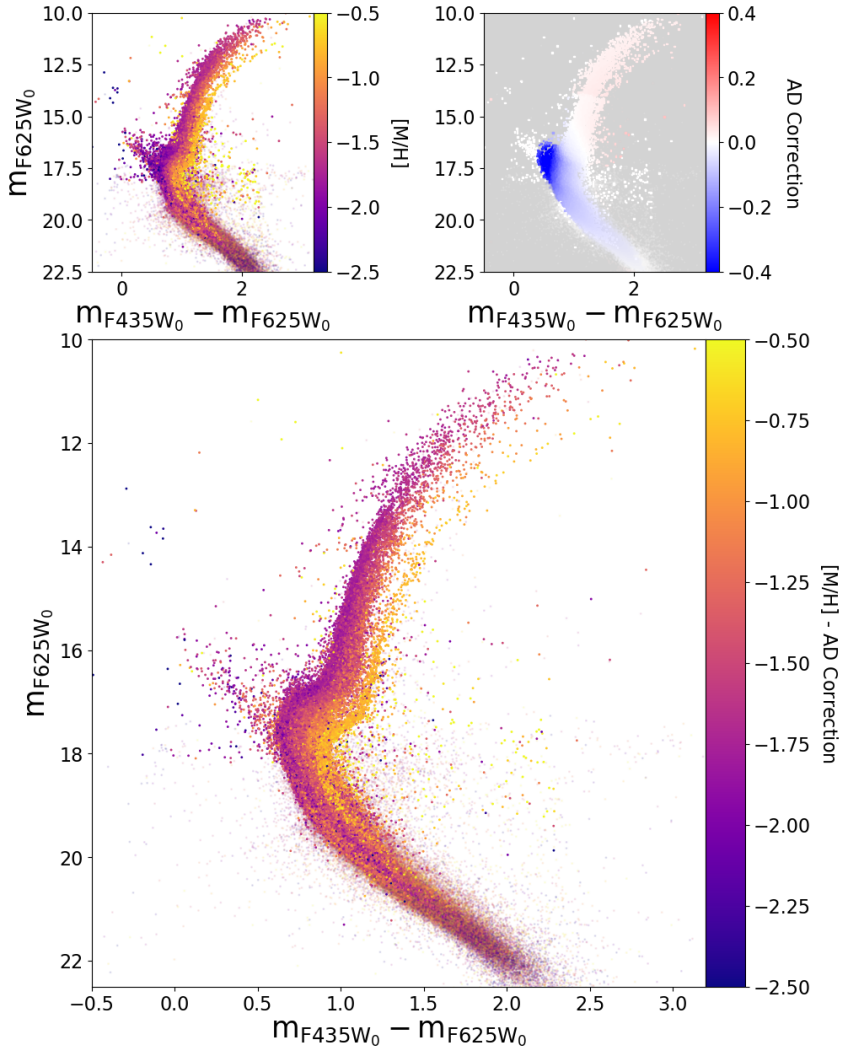


Figure 4.10: Atomic Diffusion Correction. Top left: CMD of all stars with HST photometry colored by their metallicity. Top right: A grid of the median metallicity correction when considering isochrones that model atomic diffusion. Bottom: CMD of all stars from the top left panel, now with the relevant atomic diffusion correction applied. Stars with $\text{SNR} < 10$ and less reliable photometry are plotted with transparency in each panel.

obtain good coverage across the CMD and a metallicity precision of 0.03 to 0.06 dex. For each interpolated isochrone, we calculate the difference between its overall metallicity and the surface metallicity at each point along it. We grid these differences in the CMD using color bins of 0.05 mags and F625W bins of 0.12 mags, finding the median correction in each bin. To derive the atomic diffusion (AD) correction for individual stars, we interpolate within this 2D grid of corrections. The bottom panel of Figure 4.10 shows that these corrections shift the metallicities the most in the MSTO region, while the right panel shows that applying the AD correction narrows the spread in mono-metallic tracks along the full CMD. We also plot the $[M/H]$ distribution of the RGB stars vs. the MSTO (see Figure 4.11). To aid more direct comparison, we also plot the $[M/H]$ of the RGB with "MSTO-like" errors (meaning for each RGB star we randomly sample a MSTO star error then resample the given RGB metallicity from a Gaussian with a sigma equivalent to the new error. Because RGB metallicities are more well-measured, this demonstrates the overall spread in RGB metallicities if they had the same uncertainties as fainter

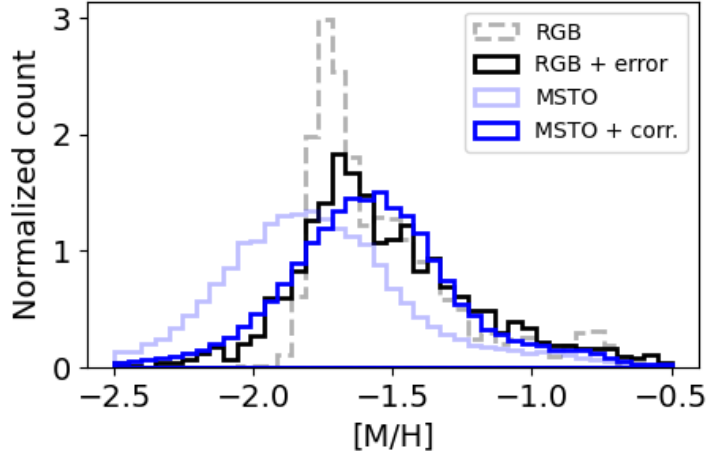


Figure 4.11: $[M/H]$ of RGB vs. MSTO Post AD Correction. The figure shows how the atomic diffusion correction causes the $[M/H]$ distribution to be more consistent between the MSTO and the RGB (when considering both to have MSTO-like errors).

MSTO stars). Before the correction, it is clear that the MSTO stars are shifted to lower metallicities by ~ 0.2 dex while after the correction the distributions are significantly more consistent, as expected.

Using atomic diffusion corrected metallicities allows us to group stars across the CMD by their birth metallicity, not their observed atmospheric metallicity. This enables us to more accurately group stars with similar abundances and better understand the processes that enrich each population. We include both the raw and atomic diffusion corrected values for the metallicities in our catalog and we use the corrected values in all analyses forthcoming.

4.4.6 Perspective rotation

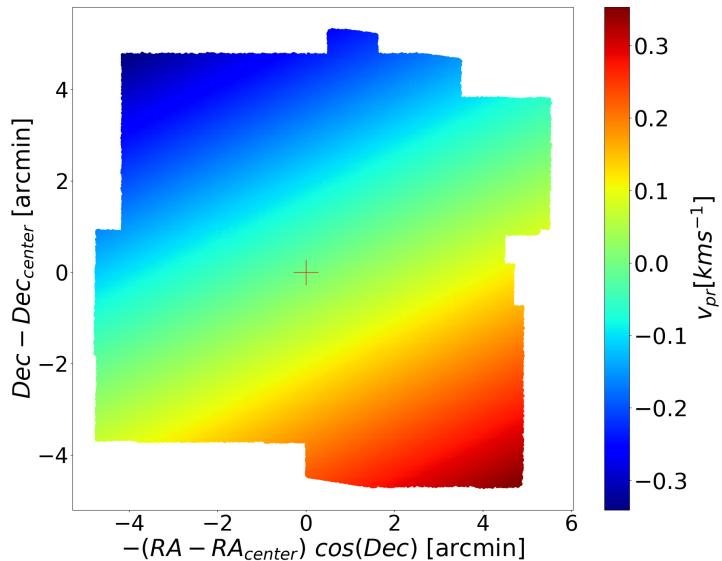


Figure 4.12: Perspective Rotation. The figure shows the position of the data color coded with the perspective rotation value for each star. The red cross indicates the center and the velocity values increase from the bottom left to the top right corner of the plot.

ω Cen takes up a large angle on the plane of the sky. Therefore, there is a non-negligible apparent rotation caused by the different projection of the space motion at different positions in the sky. This is known as perspective rotation (van de Ven et al., 2006a). To correct for it we need to subtract from the line-of-sight velocity the perspective

rotation term:

$$v_{pr} [\text{km s}^{-1}] = 1.3790 \cdot 10^{-3} \cdot D \cdot (-\Delta RA \cdot \cos(Dec) \cdot \mu_{RA}^{sys} + \Delta Dec \cdot \mu_{Dec}^{sys}) \quad (4.12)$$

with the distance to the center of the clusters ΔRA , ΔDec in units of arcmin (RA: right ascension and Dec: declination), distance to the cluster $D = (5.43 \pm 0.05)$ kpc (Baumgardt and Vasiliev, 2021), proper motion in RA $\mu_{RA}^{sys} = (3.25 \pm 0.022)$ mas yr $^{-1}$ and proper motion in Dec $\mu_{Dec}^{sys} = (-6.746 \pm 0.022)$ mas yr $^{-1}$ from Vasiliev and Baumgardt (2021).

The resulting velocity calculated with Section 4.4.6 is shown in Figure 4.12, and the maximum value for the perspective rotation in our dataset is 0.35 km s $^{-1}$.

4.4.7 Catalog

Having performed all the data reduction, stellar spectra extraction, and analysis steps described in Section 4.2, 4.3 and 4.4, we have a final spectroscopic catalog with 342,797 stars (GTO: 58,143, GO: 272,633 and combined GO/GTO: 12,021). All the parameters given in this catalog are described in Appendix 4.E and the SNR of the stars in the CMD is shown in Figure 4.13. The catalog is published together with this work in a machine-readable format.

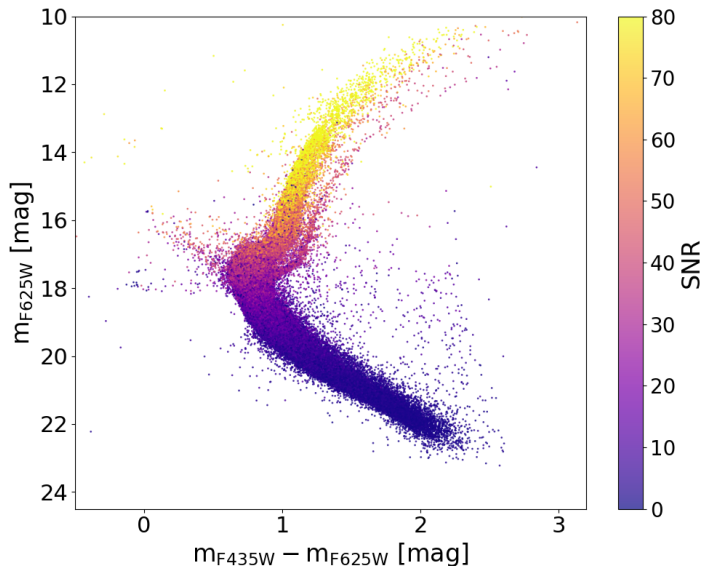


Figure 4.13: SNR in the Catalog.
The CMD of the stars in the catalog color coded with their SNR as calculated from SPEXXY.

Since 1432 GTO stars are not in the Anderson and van der Marel (2010) catalog, they do not have magnitudes in the F625W and F435W filters, and therefore no ADC could be performed. We will update the ADC for these stars in a subsequent paper using a new *HST* catalog (Häberle et al., 2024a) that includes new data acquired under the program GO-16777 (PI: A. Seth).

Our catalog has no quality cuts, as each science case can decide the best cuts for its own purpose. However, the quality cuts we suggest are as follows:

- Membership probability: $P_M > 95\%$
- Magnitude accuracy during extraction with PAMPELMUSE ≥ 0.6

- Reliability: $R \geq 0.5$
- Distance to MUSE IFU edge: ≥ 5 pixel ($1''$)
- Signal-to-Noise ratio: $\text{SNR} > 10$ (see Appendix 4.B and Appendix 4.D).

The above cuts yield 156,871 stars and of these, only 143 GTO stars lack photometry in the [Anderson and van der Marel \(2010\)](#) catalog. These 156,871 stars have a mean metallicity error of 0.15 dex, a median v_{los} error of 6.26 km s^{-1} and a median T_{eff} error of 102 K. In more detail, the mean metallicity error for MS stars ($18 \text{ mag} < \text{mag}_{\text{F625W}} < 22 \text{ mag}$) is 0.174 dex and for RGB stars ($16 \text{ mag} < \text{mag}_{\text{F625W}} < 10 \text{ mag}$) 0.031 dex. We decided on these cuts to have reliable results but still keep as many stars as possible, stricter cuts will give smaller uncertainties. The SNR cut of 10 is consistent with all our tests in Appendix 4.B, Appendix 4.C and Appendix 4.D, which show that below that value biases because of different assumptions and setups can play a role. The distance to the edge is chosen to verify that the stars are not outside or exactly at the edge of the IFU where only part of the starlight can be extracted. The other parameters are reasonable cuts for the extraction accuracy, reliability, and membership, but stricter cuts can be applied for higher precision.

Additionally, the median systemic LOS velocity, corrected for the perspective rotation and sign the above quality cuts, is $v_{\text{los}} = (232.99 \pm 0.06) \text{ km s}^{-1}$ with the error found using bootstrapping and even without the reliability quality cut the result does not change. This value is close to previous values, e.g., $(232.7 \pm 0.2) \text{ km s}^{-1}$ [Baumgardt and Hilker \(2018\)](#) using ESO/VLT, Keck spectra, and literature values, being just slightly out of the 1σ range, while $(234.28 \pm 0.24) \text{ km s}^{-1}$ [Baumgardt et al. \(2019b\)](#) where they used *Gaia* DR2 data, which due to crowding do not have many stars in the central region where we observe, being outside of the 3σ range due to the small errors.

One should note that these are quality cuts based on our spectroscopic analysis, while the photometry and astrometry are added from the *HST* catalogs ([Sarajedini et al., 2007](#); [Anderson and van der Marel, 2010](#)). We are preparing a new astrometric and photometric catalog ([Häberle et al., 2024a](#)) that will provide updated values for the magnitudes and positions.

4.4.8 Literature Comparison

In this subsection, we present a first comparison of our findings with previous works. For the comparison, we use other previous studies that use spectroscopic data and not just photometry.

To compare our [M/H] values from SPEXXY (without AD correction) to literature values for [Fe/H] from RGB stars (e.g.,: [Johnson and Pilachowski, 2010](#); [Johnson et al., 2020](#)) we need to transform [M/H] to [Fe/H] values. We use the following formula ([Salaris et al., 1993](#)):

$$[\text{Fe}/\text{H}] = [\text{M}/\text{H}] - \log(0.638 \cdot 10^{[\alpha/\text{Fe}]} + 0.362) \quad (4.13)$$

with $[\alpha/\text{Fe}]$ set to 0.3 in SPEXXY. This transformation accounts for the contribution of the assumed α enhancement to our assumed [M/H] values, while the literature values derive separate abundances for several α elements ([Johnson and Pilachowski, 2010](#)).

We match the [Johnson and Pilachowski \(2010\)](#); [Johnson et al. \(2020\)](#) catalogs to ours using only the brightest stars ($\text{F625W} < 14 \text{ mag}$) by finding the closest star that is no more than $1''$ away, to find real matches but not have too strict criteria and eliminate

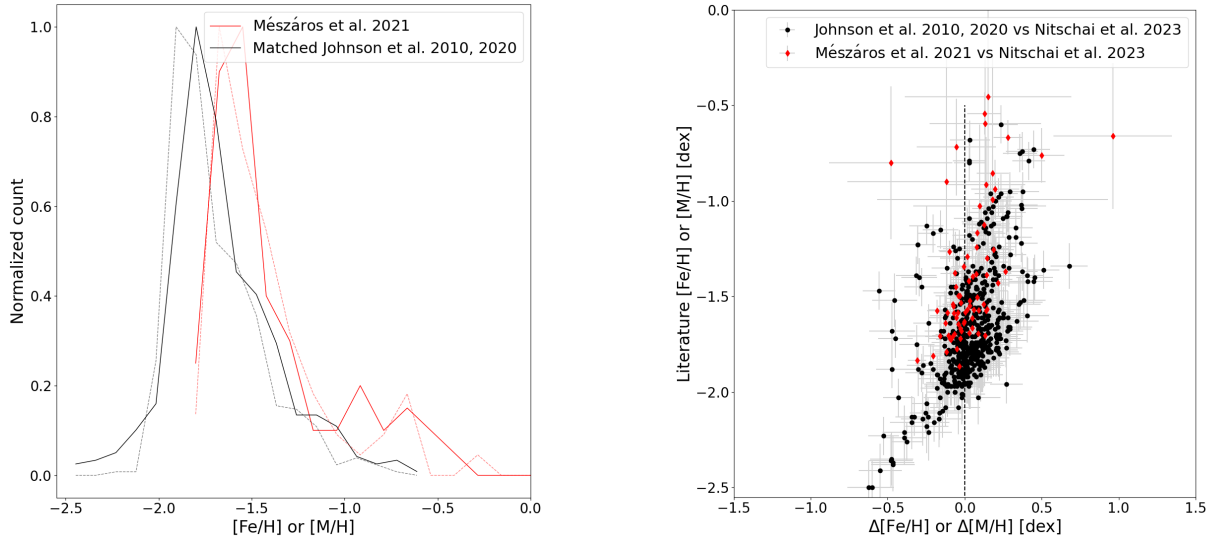


Figure 4.14: Comparison to Literature Values. On the left is the $[\text{Fe}/\text{H}]$ distribution for the Johnson and Pilachowski (2010); Johnson et al. (2020), the black solid line, and from the MUSE results, the black dashed line, for all the matched stars in both catalogs. In red is the $[\text{M}/\text{H}]$ distribution for the matched stars of the Mészáros et al. (2021) data, solid line, and the MUSE data. On the right, we plot the literature values against the difference between the two $[\text{Fe}/\text{H}]$ or $[\text{M}/\text{H}]$ values. The black dashed line indicates where both values agree.

matches due to slight offsets in the coordinates. The $[\text{Fe}/\text{H}]$ of the 524 matched stars are shown in Figure 4.14. The measurements are strongly correlated with a mean offset between them of 0.03 dex and a scatter of 0.17 dex, with the literature values being slightly more metal-rich but still close to zero showing no strong systematic offset and the scatter representing the statistical discrepancy. We note that our matching criteria and differences in astrometry could result in some mismatched stars. Unfortunately, this cannot easily be improved using photometry, as there are no common filters between the catalogs. In addition, we do not find as low metallicity stars as in Johnson et al. (2020), which seem to have the biggest deviation from our data.

Further, we also match our $[\text{M}/\text{H}]$ values to the metallicity from Mészáros et al. (2021) where they used APOGEE measurements. Since, most of the spectroscopic surveys, like *Gaia* and APOGEE, have problems with crowding in the central cluster region where we observe, there is almost no overlap. However, we could match 74 stars, and the results are also shown in Figure 4.14. The measurements have a mean offset between them of 0.06 dex and a scatter of 0.28 dex.

4.5 Conclusion

In this work, we present an extensive catalog of stars obtained with 87 new MUSE pointings plus the already existing 10 WFM and 6 NFM GTO pointings for ω Cen, covering out to the half-light radius.

We describe the data and the analysis steps used to create the final catalog of stars. First, we reduce the data and extract individual spectra of stars using PAMPELMUSE (Kamann et al., 2013). Afterward, we use the spectral fitting routine SPEXXY to measure the LOS velocities, effective temperatures, and metallicities of these stars. We perform multiple tests including exploiting a large number of repeated measurements to verify our

results. We provide several parameters to quantify the reliability of the results and also include several necessary corrections to our measurements. We end up with 342,797 stars after all of our analysis steps without any quality cuts. However, for most use cases we suggest several quality cuts: $\text{SNR} > 10$, membership probability $P_M > 0.95\%$, Magnitude accuracy ≥ 0.6 mag, distance to the IFU edge ≥ 5 and Reliability $R \geq 0.5$. Thus, 156,871 stars meet all these criteria.

Finally, we do a first analysis of the metallicity distribution comparing it to previous works and find that they are consistent with our findings and calculate the median systematic LOS to be $v_{\text{los}} = (232.99 \pm 0.06) \text{ km s}^{-1}$. A more detailed analysis of the metallicities (see Chapter 5) as well as the LOS velocity information (see Section 6.1.1) will be presented in the following chapters.

In the Appendix, we include further information and elaborate on checks we performed on our data.

Appendices

4.A Data Conditions

Since our data were taken over an extended period of longer than a year, the atmospheric conditions were also varying. In Table 4.2 we summarize the conditions and observing date of the individual GO pointings used in this analysis. We requested an airmass less than 1.4 and seeing below $0''.8$, which were almost always fulfilled.

Table 4.2: Observing Conditions

OB	Date	Average Airmass	Average Seeing
1.1	17 February 2021	1.263	0.897
1.2	17 February 2021	1.246	0.777
1.3	17 February 2021	1.204	0.733
1.3 ⁶	2 September 2022	2.144	0.577
2.1	16 March 2021	1.102	1.203
2.2	16 March 2021	1.092	1.133
2.3	16 March 2021	1.087	1.357
3.1	16 March 2021	1.088	1.097
3.2	16 March 2021	1.093	1.127
3.3	16 March 2021	1.103	1.360
4.1	8 April 2021	1.096	0.433
4.2	8 April 2021	1.089	0.500
4.3	8 April 2021	1.086	0.470
5.1	14 March 2021	1.088	1.140
5.2	14 March 2021	1.094	1.110
5.3	14 March 2021	1.103	1.133
5.4	14 March 2021	1.116	1.273
6.1	8 April 2021	1.088	0.503
6.2	8 April 2021	1.093	0.527
6.3	8 April 2021	1.101	0.497

⁶OB 1.3 was observed twice since it had a wrong offset causing a gap in our dataset.

Continued

OB	Date	Average Airmass	Average Seeing
6.4	8 April 2021	1.113	0.547
7.1	18 May 2021	1.209	0.567
7.2	18 May 2021	1.180	0.547
7.3	18 May 2021	1.155	0.553
7.4	18 May 2021	1.135	0.450
8.1	18 May 2021	1.089	0.59
8.2	18 May 2021	1.086	0.573
8.3	18 May 2021	1.087	0.687
9.1	30 June 2021	1.088	0.883
9.2	30 June - 1 July 2021	1.093	0.907
9.3	1 July 2021	1.101	1.147
9.4	1 July 2021	1.113	1.163
10.1	4 July 2021	1.106	0.937
10.2	4 July 2021	1.119	0.877
10.3	4 July 2021	1.119	0.843
10.4	4 July 2021	1.157	0.840
11.1	31 March 2022	1.295	0.62
11.2	31 March 2022	1.253	0.540
11.3	31 March 2022	1.217	0.50
11.4	31 March 2022	1.186	0.4340
12.1	9 February 2022	1.325	0.557
12.2	9 February 2022	1.279	0.677
12.3	9 February 2022	1.239	0.637
12.4	9 February 2022	1.206	0.700
13.1	9 February 2022	1.171	0.507
13.2	9 February 2022	1.148	0.703
13.3	9 February 2022	1.128	0.563
13.4	9 February 2022	1.113	0.693
14.1	9 February 2022	1.099	0.723
14.2	9 February 2022	1.091	1.020
14.3	9 February 2022	1.087	0.650
14.4	9 February 2022	1.085	0.780
15.1	10 February 2022	1.250	0.653
15.2	10 February 2022	1.215	0.727
15.3	10 February 2022	1.184	0.823
15.4	10 February 2022	1.159	0.597
16.1	10 February 2022	1.133	0.740
16.2	10 February 2022	1.117	0.600
16.3	10 February 2022	1.103	0.433
16.4	10 February 2022	1.094	0.897
17.1	27 February 2022	1.358	0.350
17.2	27 February 2022	1.308	0.307
17.3	27 February 2022	1.265	0.293
17.4	27 February 2022	1.228	0.250
18.1	27 February 2022	1.090	0.387
18.2	27 February 2022	1.086	0.413

Continued

OB	Date	Average Airmass	Average Seeing
18.3	27 February 2022	1.086	0.357
18.4	27 February 2022	1.089	0.520
19.1	27 February 2022	1.100	0.437
19.2	27 - 28 February 2022	1.147	0.463
19.3	28 February 2022	1.201	0.500
19.4	28 February 2022	1.173	0.627
20.1	28 February 2022	1.143	0.493
20.2	28 February 2022	1.125	0.397
20.3	28 February 2022	1.110	0.380
20.4	28 February 2022	1.100	0.380
21.1	28 February 2022	1.360	0.413
21.2	28 February 2022	1.087	0.453
21.3	28 February 2022	1.087	0.373
21.4	28 February 2022	1.091	0.307
22.1	2 March 2022	1.379	0.640
22.2	2 March 2022	1.326	0.517
22.3	2 March 2022	1.280	0.567
22.4	2 March 2022	1.241	0.877
23.1	2 March 2022	1.114	0.487
23.2	2 March 2022	1.102	0.493
23.3	2 March 2022	1.094	0.437
23.4	2 March 2022	1.089	0.463

The observing conditions for all GO observations used in our work. OB: the name/numbering of the individual pointings, Date: the date of observation, average airmass: the mean airmass at the start of each of the three rotated exposures, and average seeing: the mean seeing at the start of the three rotated exposures for one OB. OB 1.3 was observed twice since the offset of the pointing was not correct and created a gap in our continuous coverage.

4.B PampelMuse Tests

We verify that slightly changing the PAMPELMUSE setup, does not influence our results for stars with $\text{SNR} > 10$. For these tests, we use two example pointings where a different setting might have been more appropriate. First, we use a round PSF, fixing the ellipticity to 0, for OB 15.3, since the free Moffat PSF we generally use, seems unnecessarily complex as it is round anyway. For the second example, we use OB 21.2 and masked certain layers in the wavelength range that appear to have something wrong with them, bad pixels from the data reduction, since their values drop significantly compared to the rest of the spectrum. The results show no significant difference in the SPEXXY output for an $\text{SNR} > 10$, even though the new setup should be better for these two cases. Therefore, we keep the setup consistent for all OBs as described in Section 4.3.1.

4.C Surface Gravity $\log(g)$

In this section, we investigate the bias we have due to the fixed $\log(g)$ parameter from one single isochrone for most stars (see Section 4.3.3).

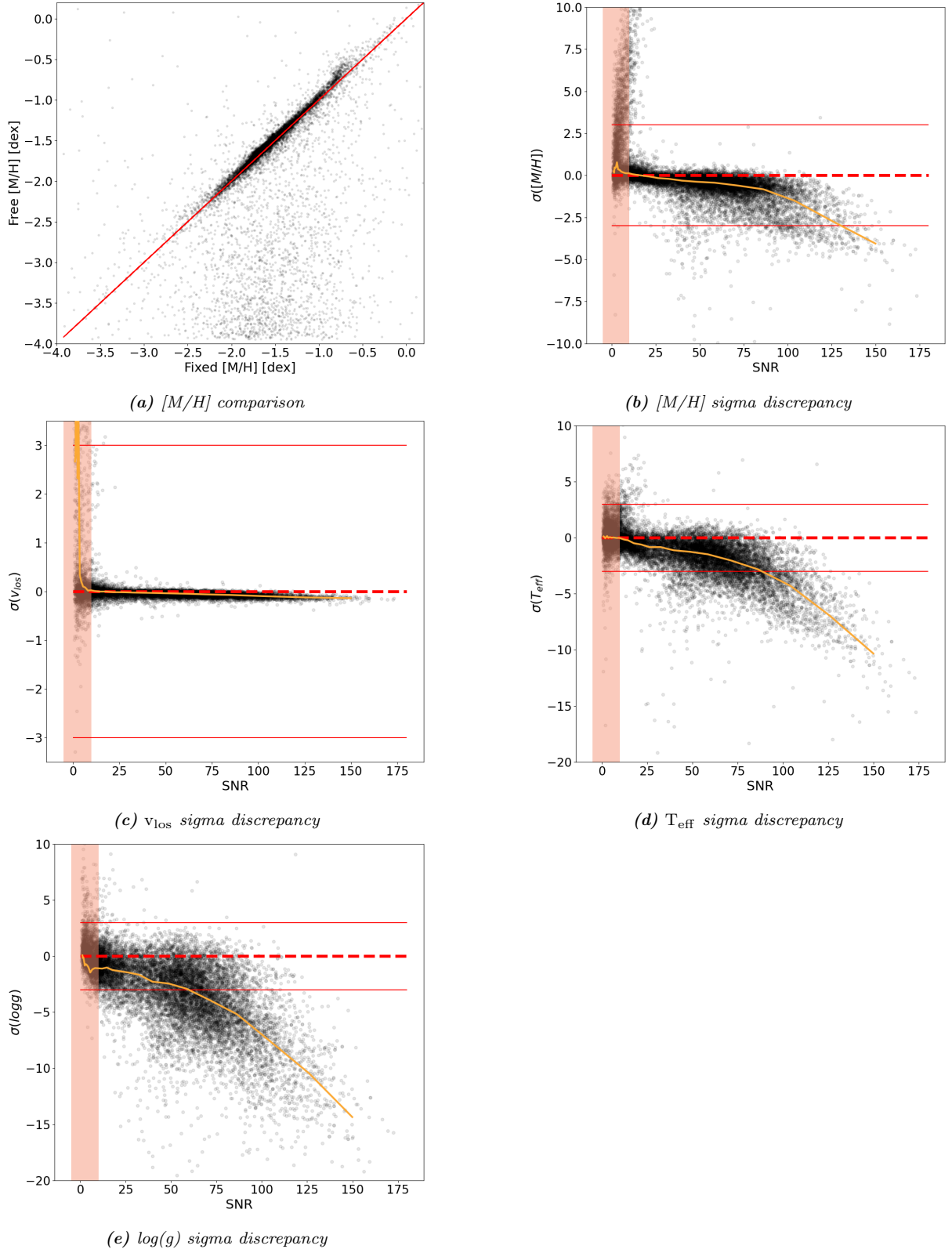


Figure 4.15: Discrepancy between Spectral Parameters with Free and Fixed $\log(g)$. (a.) The one-to-one comparison between the $[M/H]$ values, red line the 1 to 1 ratio, (b.)-(e.); The sigma deviations for $[M/H]$, v_{los} , T_{eff} and $\log(g)$. We divide the difference between the two results with the scale error in our catalog, except for the $\log(g)$ where we take the SPEXXY error for the free $\log(g)$ run. The dashed red line is at 0, the solid red lines at the 3σ limits, and the orange solid line is the median of all stars, while the red shaded area is the SNR limit of 10.

4.C.1 Free log(g)

First, we investigate how allowing $\log(g)$ to vary freely for all stars during the fit with SPEXXY, would change our results. For that, we look at a subset of our data including RGB and MS stars, which gives us a complete representation of the magnitude and SNR range.

The deviations between the free and fixed $\log(g)$ fit are shown in Figure 4.15. Most of the results are within the 3σ range for an $\text{SNR} > 10$. The deviations at high SNR are because of the smaller errors at that level. We can see that all parameters tend to get lower when the $\log(g)$ values are left free, but not as significant for $[\text{M}/\text{H}]$ and v_{los} where they almost all stay within the 3σ range. This also proves that the $\log(g)$ parameter does not affect the metallicity calculation strongly.

4.C.2 Metal Rich Stars

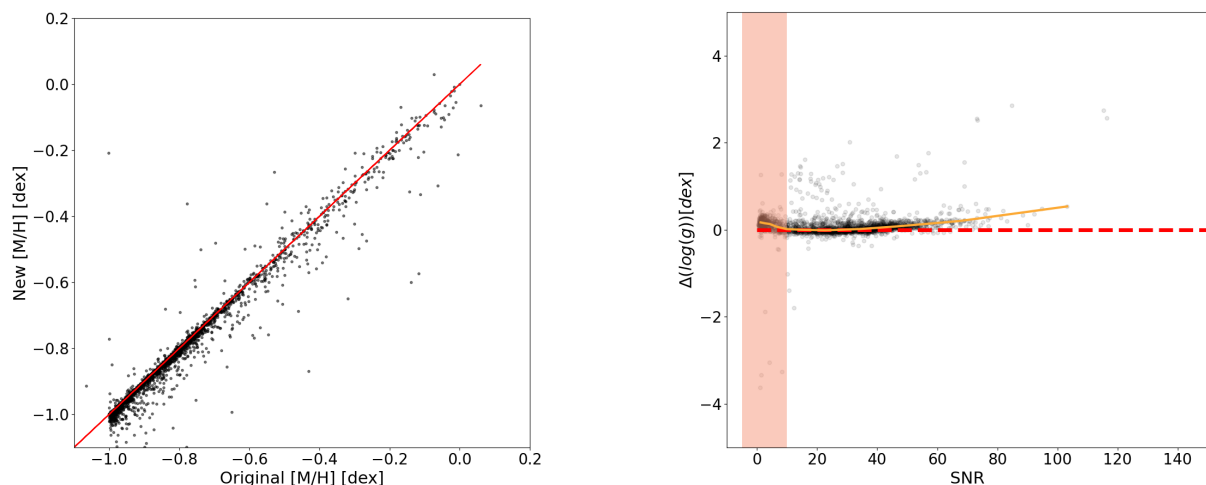


Figure 4.16: Metal Rich. On the left panel, the one-to-one comparison of the $[\text{M}/\text{H}]$ is shown, with the red solid line being the 1 to 1 ratio. On the right is the difference in $\log(g)$ between the two isochrones, with the dashed line indicating no difference at all, the orange line the median difference of our data, and the red shaded area the SNR limit of 10.

Since the cluster is known to have multiple populations, we know that one isochrone for finding the $\log(g)$ is not ideal. To investigate the bias we have because of that, we test one extreme population, the metal rich stars with $[\text{M}/\text{H}] > -1$ dex, and use a different isochrone, more representative for them, and assign them new $\log(g)$ values.

In Figure 4.16 the $[\text{M}/\text{H}]$ results are shown and the difference between the $\log(g)$. In general, there seems to be just a small difference in $\log(g)$ even with a different isochrone and a tight one-to-one correlation between the $[\text{M}/\text{H}]$, reassuring us that the exact isochrone used for the initial guesses and $\log(g)$ values is not that significant.

4.C.3 Literature log(g)

Using the matching between Johnson and Pilachowski (2010); Johnson et al. (2020) and Mészáros et al. (2021) and our catalog, described in Section 4.4.8, we also compare our surface gravity values with the literature. Almost all values are for a fixed $\log(g)$ from the isochrone described in Section 4.3.3.

The $\log(g)$ of the matched stars are shown in Figure 4.17. The measurements have a mean offset between the Johnson and Pilachowski (2010); Johnson et al. (2020) of 0.18 dex and a scatter of 0.26 dex, with the literature values having slightly lower $\log(g)$ values. With the Mészáros et al. (2021) values the mean offset is 0.04 dex and a scatter of 0.46 dex. This shows that even though our initial isochrone is not a perfect match for all stars, because of multiple populations and binaries, it still gives reasonable $\log(g)$ values since they are comparable to previous studies. In addition, the metallicity values also are within the expected literature range (see Section 4.4.8) even though $\log(g)$ is fixed, hence this is another indication that there is no strong effect, as already suggested in Husser et al. (2016), and Kamann et al. (2016) and in Appendix 4.C.1, Appendix 4.C.2.

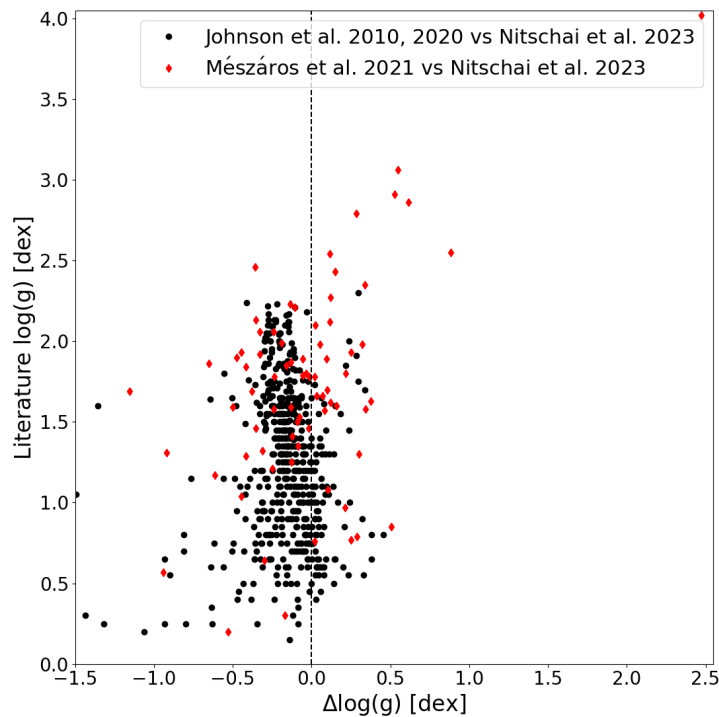


Figure 4.17: Literature Comparison $\log(g)$. We plot the Literature values against the difference between Literature and our $\log(g)$ values.

4.D SNR Test

To make sure that we have no bias in our metallicity and velocity measurements for stars with different SNR, we performed another test, adding different noise values to the spectra and redoing the SPEXXY fit.

We selected randomly 147 spectra with SNR above 28 (being not on the HB) and added Gaussian noise, creating 3999 spectra with SNR between 1 and the original SNR. The difference between the original SPEXXY results and the new ones with more noise increases as expected for lower SNR, and the output errors also increase. The σ difference as a function of the new SNR is shown in Figure 4.18. Almost all results are within the 3σ range for $\text{SNR} > 10$ and we do not see any bias towards higher or lower values for lower SNR.

The σ difference is calculated using the error directly from SPEXXY, if we also apply the error correction as described in Section 4.4.2, the difference even decreases.

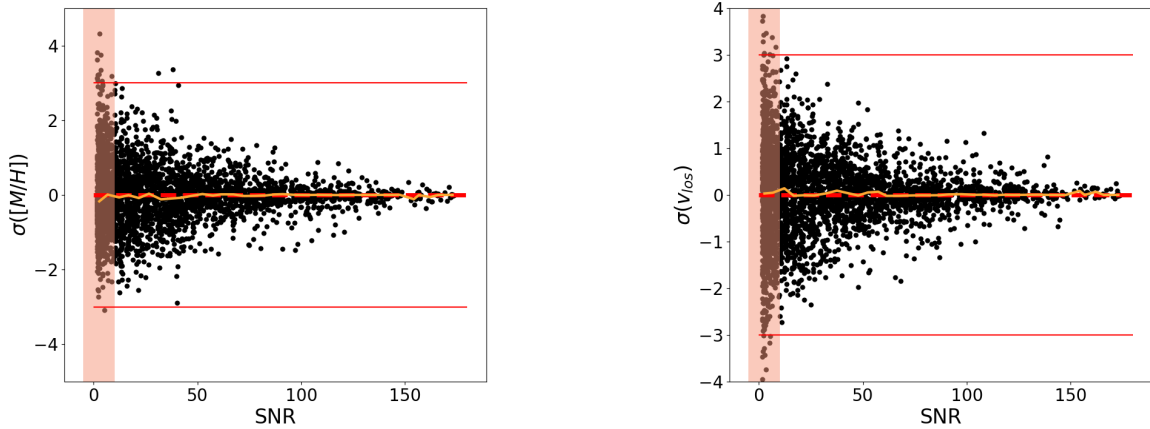


Figure 4.18: SNR Test. The left panel shows on the y-axis the σ difference between the original result and the different $[M/H]$ results after adding noise to the spectra, and the x-axis is the new SNR with the added noise. Similar for the right panel but for the v_{los} values. The light red shaded areas indicate SNR below 10, the red solid horizontal lines are the 3σ difference, the red dashed horizontal lines are at 0, and the orange solid lines are the median values for our measurements of SNR .

4.E Catalog Columns

Table 4.3 lists all parameters given in the spectroscopic catalog described in this work. The entries in the catalog are sorted by increasing radius from the center. The catalog with all the data is publicly available as online material of the published paper [Nitschai et al. \(2023\)](#).

Take away points

- We present an extensive MUSE mosaic with 87 new fields for ω Cen.
- We created a spectroscopic catalog with more than 300,00 stars out to the half-light radius.
- We perform multiple tests of reliability and provide quality parameters to quantify the reliability of the data.
- The mean metallicity error for bright RGB stars is 0.031 dex and for the fainter MS 0.174 dex.
- The mean line-of-sight velocity of the cluster is $(232.99 \pm 0.06) \text{ km s}^{-1}$.
- This is the spectroscopic side of the huge data set (including photometry and astrometry with *HST*) on which future studies for the cluster will be based.

Table 4.3: Catalog Columns

Column Name	Description	More Details	Units
MUSE	Identifier of stars in spectroscopic catalog	SPEXXY output	km s^{-1}
RVel	Line-of-sight velocity (v_{los})	SPEXXY output	km s^{-1}
errRVel	SPEXXY Line-of-sight velocity uncertainty ($\epsilon_{v_{\text{los}}}$)	Section 4.4.2	
sRVel	Scaling factor for $\epsilon_{v_{\text{los}}}$	Section 4.4.2	
e_RVel	Scaled error v_{los}	see Section 4.4.6 and van de Ven et al. (2006a)	km s^{-1}
prv	Perspective rotation	see Section 4.4.6 and van de Ven et al. (2006a)	km s^{-1}
prvRVel	v_{los} corrected for perspective rotation	SPEXXY output	K
Teff	Effective Temperature (T_{eff})	SPEXXY output	K
errTeff	Effective Temperature uncertainty ($\epsilon_{T_{\text{eff}}}$)	Section 4.4.2	
sTeff	Scaling factor for $\epsilon_{T_{\text{eff}}}$	Section 4.4.2	
e_Teff	Scaled error T_{eff}	Isochrone output (Section 4.3.3)	K
logfix	Fixed surface gravity ($\log(g)$)	SPEXXY output	dex
logfree	Fitted surface gravity ($\log(g)$)	SPEXXY output	dex
MH	Metallicity ([M/H])	SPEXXY output	dex
MHadc	Metallicity corrected for AD	see Section 4.4.5	dex
errMH	SPEXXY Metallicity uncertainty ($\epsilon_{[\text{M}/\text{H}]}$)	SPEXXY output	dex
sMH	Scaling factor for $\epsilon_{[\text{M}/\text{H}]}$	Section 4.4.2	
e_MH	Scaled error [M/H]	Section 4.4.2	
SNR	Signal-to-noise ratio (SNR)	SPEXXY output	
fft	Fixed or free $\log(g)$ in SPEXXY	0 free and 1 fixed	
edge	Distance of star to OB edge	PAMELMUSE output	pixel
Magacc	Relative accuracy of recovered magnitude from spectrum extraction	PAMELMUSE output	
SpecFlag	Spectrum extraction quality flag	PAMELMUSE output	
Rel	Reliability Parameter R	Section 4.4.1	
Num	Number of times the star was observed	Section 4.4.3	
Data	Observing program (GO/GTO) the star belongs to	$\sqrt{\frac{\text{GTO, GO or both (GO_GTO)}}{((\text{RA} - \text{RA}_c)\cos(\text{Dec}))^2 + (\text{Dec} - \text{Dec}_c)^2}}$	deg
Bad	Radius from cluster center (r)	Sarajedini et al. (2007) and Anderson et al. (2008),	deg
RAdeg	Right Ascension (RA)	Anderson and van der Marel (2010)	deg

Continued

Column Name	Description	More Details	Units
DEdeg	Declination (Dec)	Sarajedini et al. (2007) and Anderson et al. (2008), Anderson and van der Marel (2010)	deg
435mag	Magnitude in the F435W filter (Vega)	Anderson and van der Marel (2010)	mag
625mag	Magnitude in the F625W filter (Vega)	Anderson and van der Marel (2010)	mag
435magC	F435W-band photometry (Vega)	Anderson and van der Marel (2010)	mag
625magC	F625W-band photometry (Vega)	Anderson and van der Marel (2010)	mag
e_435mag	RMS scatter of single-exposure F435W observation	Anderson and van der Marel (2010)	mag
e_625mag	RMS scatter of single-exposure F625W observation	Anderson and van der Marel (2010)	mag
NBf	Number of F435W images where star was found	Anderson and van der Marel (2010)	
NRf	Number of F625W images where star was found	Anderson and van der Marel (2010)	
probRV	Membership probability	radius and velocity (Section 4.4.4)	
probRVM	Membership probability	radius, velocity and [M/H]	
Flag	Quality Flag	1=True, 0=False, see Section 4.4.7	
HST10Flag	<i>HST</i> quality flag for Anderson and van der Marel (2010)	1=reliable, 0=unreliable photometry/astrometry	

$RA_c = 13:26:47.24$ and $Dec_c = -47^\circ 28' 46.45$ (Anderson and van der Marel, 2010). For the parameters edge, Magacc, SpecFlag, and Rel we provide the minimum (maximum for SpecFlag) value when combining multiple measures, see Section 4.4.3.

Chapter 5

SPATIALLY WELL-MIXED POPULATIONS OF ω CENTAURI

This chapter has been submitted as Nitschai et al. (2024) to ApJ, formatting and small text edits have been made to match this thesis. I conducted the scientific work with the guidance of my supervisor and I wrote all of the text, with suggestions and corrections from co-authors.

Abstract

ω Centauri, the most massive globular cluster in the Milky Way, has long been suspected to be the stripped nucleus of a dwarf galaxy that fell into the Galaxy a long time ago. There is considerable evidence for this scenario including a large spread in metallicity and an unusually large number of distinct subpopulations seen in photometric studies. In this work, we use new MUSE spectroscopic and *HST* photometric catalogs to investigate the underlying metallicity distributions as well as the spatial variations of the populations within the cluster up to its half-light radius. Based on 12,850 member stars, the [M/H] distribution has a median (-1.621 ± 0.003) dex and a large spread of ~ 1.57 dex reaching from -0.66 dex to -2.23 dex for 99.7 % of the stars. In addition, we show the chromosome map of the cluster, which separates the red giant branch stars into different subpopulations, and analyze the subpopulations of the metal-poorest component. Finally, we do not find any metallicity gradient within the half-light radius, and the different subpopulations are well mixed.

Chapter Contents:

5.1	Introduction	88
5.2	Data	89
5.2.1	Spectroscopic Data	89
5.2.2	Photometric Data	90
5.2.3	Quality Cuts	91
5.3	Results	92
5.3.1	Metallicity Distribution	92
5.3.2	Chromosome Map	95
5.3.2.1	Metallicity Dependency	96
5.3.2.2	The Metal-Poor Component and Its Multiple Populations	97

5.3.3	Spatial 2D Metallicity Distribution	98
5.3.4	Metallicity Gradients	100
5.3.4.1	Overall Cluster Gradient	100
5.3.4.2	Spatial Differences between Subpopulations	101
5.3.4.3	Differences in the Two Streams of [M/H] vs $\Delta_{F275W,F814W}$	102
5.4	Conclusion	103
Appendices	104
5.A	Completeness	104
5.B	[M/H] Bias	104
5.C	Details for the Chromosome Map	105
	Take away points	109

5.1 Introduction

The most promising candidate for a stripped nucleus in the Milky Way halo is ω Centauri, due to the complexity of its stellar populations (as mentioned in Chapter 2). It shows multiple sequences in its color-magnitude diagram (e.g., Anderson, 1997; Bedin et al.,

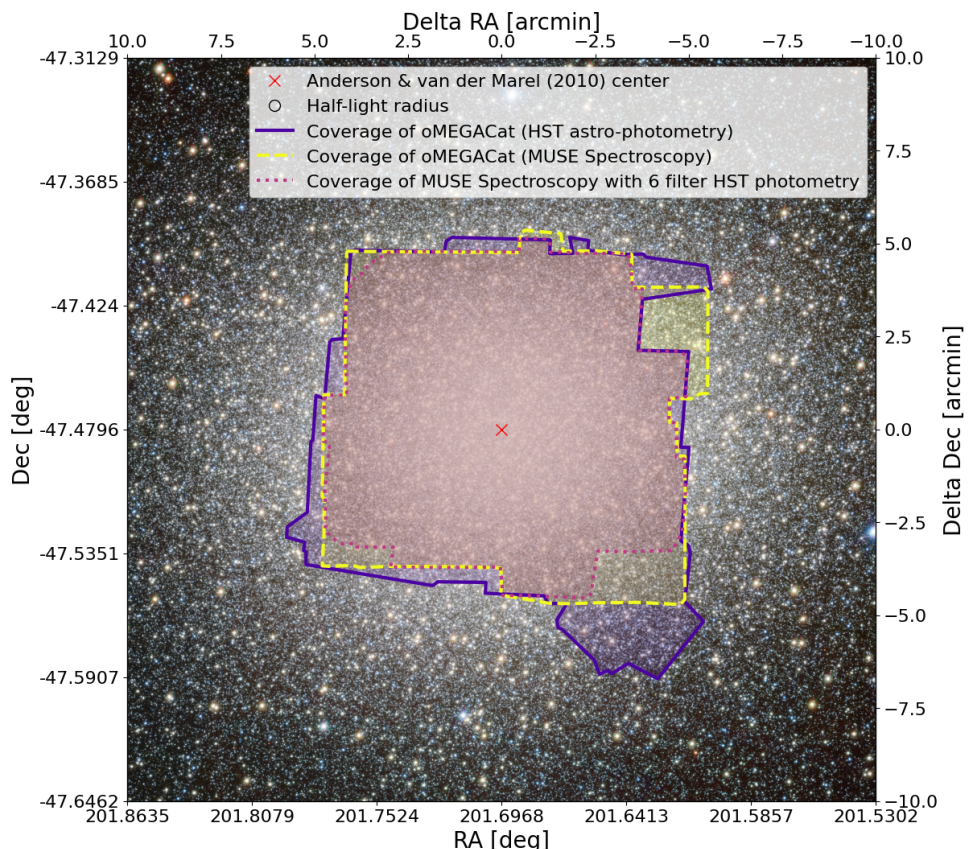


Figure 5.1: Footprint of Data Sets. In dark purple with the solid line is the footprint of the new HST catalog (Häberle et al., 2024a) and in yellow with a dashed line is the MUSE spectroscopic catalog (Nitschai et al., 2023) footprint. The light purple dotted contours show the area where we have a combined catalog with 6 filter photometry from HST. The black circle is the half-light radius at 5' (Harris, 2010) and the red x mark is the Anderson and van der Marel (2010) center. Background: Cut-out of a wide-field image taken with the ESO/VST telescope (Image Credit: ESO/INAF-VST/OmegaCAM. Acknowledgement: A. Grado, L. Limatola/INAF-Capodimonte Observatory, <https://www.eso.org/public/images/eso1119b/>)

2004; Bellini et al., 2010; Milone et al., 2017a) and has a large spread in metallicity (e.g., Freeman and Rodgers, 1975; Johnson and Pilachowski, 2010). In addition, the internal kinematics of the cluster show the presence of a central stellar disk and a bias toward tangential orbits in the outer parts (van de Ven et al., 2006a), counter rotation in the very central region (Pechetti et al., 2024), and fast-moving stars in the inner 3 arcsec (Häberle et al., 2024b) indicating the presence of an intermediate-mass black hole. Further, the orbit of ω Cen has been associated with the *Gaia*-Enceladus merger (Massari et al., 2019; Pfeffer et al., 2021; Callingham et al., 2022; Limberg et al., 2022) ~ 10 Gyr ago (Helmi et al., 2018). The star formation and assembly history of the cluster is still debated and the claims for its populations age span vary from 2 – 3 Gyr (Hilker et al., 2004) up to 4 – 5 Gyr (Villanova et al., 2007). Other studies have found models fully consistent with a shorter star formation of 1 Gyr to 2 Gyr (Joo and Lee, 2013). Finally, tidal material associated with ω Cen is directly seen (e.g., Majewski et al., 2012; Ibata et al., 2019, 2023) which further strengthens the stripped nucleus scenario.

Almost all globular clusters host significant light-element abundance spreads within them, following a basic pattern, a population with abundances akin to field stars, and one or more anomalous populations, with varying enrichment in some elements (e.g., He, N, Na) and depletion in others (e.g., C, O), but the specifics of each cluster are unique (see the review by Bastian and Lardo, 2018). These abundance spreads are typical for old and massive clusters and are known as multiple populations. However, abundance variations in Fe and heavy elements are rare and only have been detected in more complex clusters such as ω Cen (Willman and Strader, 2012).

In our oMEGACat project, we study ω Cen in great detail with the aim of exploring its formation history and interactions with the Galaxy. To do that, we created a spectroscopic catalog (see Chapter 4 and Nitschai et al., 2023) using MUSE, and a photometric and astrometric catalog (Häberle et al., 2024a) using the *HST* up to the half-light radius of the cluster (see Figure 5.1 for the coverage of each catalog). Here, we make use of these data and investigate the metallicity information we have for the stars in ω Cen. In Section 5.2 we summarize the observations used to create the catalogs and describe the quality cuts used in this specific work. Then in Section 5.3, we present the full metallicity distribution, the chromosome map, and we investigate any possible spatial variation of the metallicity. Finally, in Section 5.4 we summarize and discuss our findings.

5.2 Data

5.2.1 Spectroscopic Data

A detailed description of the spectroscopic data used can be found in Nitschai et al. (2023). In summary, the spectroscopic data were acquired with MUSE (Bacon et al., 2010, 2014), a second-generation VLT instrument mounted on the UT4 at the Paranal Observatory in Chile observing in the optical domain (480 nm– 930 nm). The observations were carried out between February 2021 and September 2022 in run 105.20CG.001 (PI: N. Neumayer) and in addition, we also used the complementary MUSE guaranteed time observations (hereafter “GTO data”). These data together have a full coverage out to the half-light radius (4.65' or 7.04 pc, Baumgardt and Hilker, 2018) of the cluster.

For the analysis of the data we first extracted the spectra for the individual stars

using PAMELMUSE¹ (Kamann et al., 2013) and the *HST* catalog from Anderson and van der Marel (2010). Afterward, we used SPEXXY² (Husser et al., 2016) to measure the physical parameters of the stars such as effective temperature, metallicity, and line-of-sight velocity. The observed spectra are compared to synthetic spectra from the Phoenix library (Husser et al., 2013) with varying $\log(g)$, T_{eff} , [M/H] while minimizing the χ^2 difference. During the fit with SPEXXY, $\log(g)$ is fixed to the value provided by the isochrone from the PARSEC database (Marigo et al., 2017) used to estimate the initial guesses, the α -enhancement is kept constant at $[\alpha/\text{Fe}] = 0.3$ dex, while T_{eff} , [Fe/H] and the line-of-sight velocity are determined.

In addition, we performed multiple tests to check for the robustness of our results, which included an error analysis and membership determination, as well as necessary corrections, like the atomic diffusion correction (ADC). For more details and the spectroscopic data themselves, we refer to Nitschai et al. (2023) or Chapter 4.

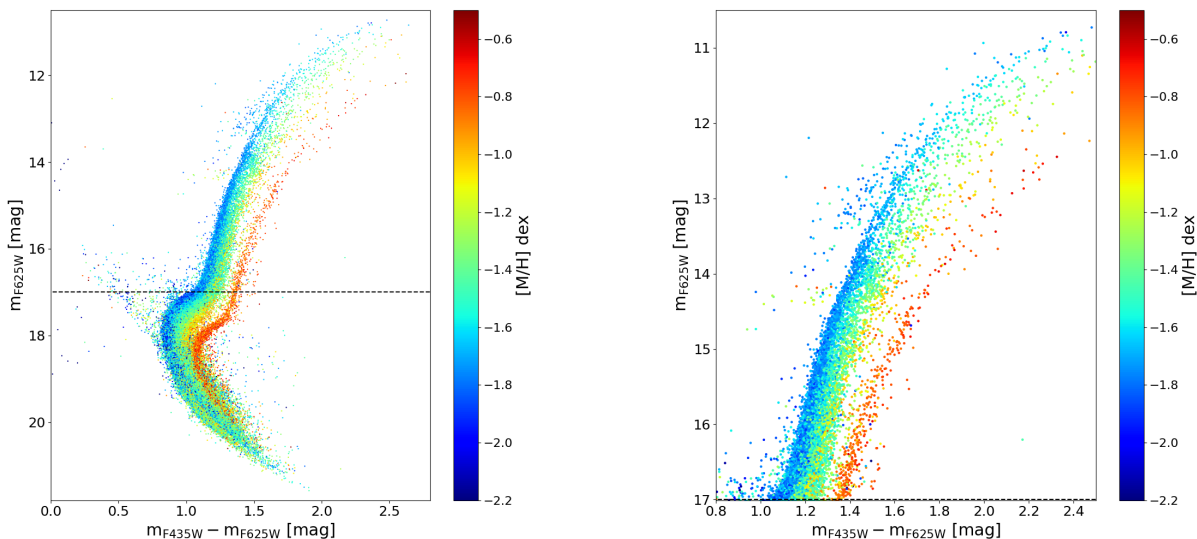


Figure 5.2: Color-Magnitude Diagrams. On the left is the full CMD of our combined data set color-coded with the metallicity (with 145,565 stars). On the right side is a zoom-in on the red giant branch. The black dashed line indicates the magnitude cut at $m_{\text{F}625\text{W}} = 17$ mag, stars above the line will be used in this work. Note we use the new oMEGACat *HST* photometry (Häberle et al., 2024a) in the plot.

5.2.2 Photometric Data

The detailed description of the photometric data is available in Häberle et al. (2024a) (the data have the following DOI: <http://dx.doi.org/10.17909/26qj-g090>) and here we briefly summarize it. The astro-photometric part of the catalog is based on observations with the *HST* spanning over 20 years and using the Advanced Camera for Wide Field Channel (ACS/WFC), and the Wide Field Camera 3 UVIS Channel (WFC3/UVIS). The data was obtained for various general observing and calibration programs, including a new dedicated program (GO-16777, PI: A. Seth) aimed at providing complementary filter coverage out to the half-light radius and additional epochs required for proper motion measurements.

¹<https://pampelmuse.readthedocs.io/en/latest/about.html>

²<https://github.com/thusser/speaxy>

The catalog contains both high-precision photometry spanning from the UV to the near-infrared and proper motions for around 1.4×10^6 stars. The photometric measurements were performed using techniques specifically designed to analyze crowded environments like the cores of GCs (see [Bellini et al. 2017a](#) for details). Six filters have coverage over the full field (ACS/WFC: F435W, F625W, F658N; WFC3/UVIS: F275W, F336W, F814W), in addition, the central region is also covered with multiple epochs of the WFC3/UVIS F606W filter. The proper motions were determined using the technique established and improved in [Bellini et al. \(2014, 2018\)](#); [Libralato et al. \(2018\)](#) and [Libralato et al. \(2022\)](#).

In [Häberle et al. \(2024a\)](#) an empirical correction for spatially dependent photometry variations has been calculated for all seven filters, which is needed due to differential reddening and systematic zero-point variations caused by instrumental effects. When using this *HST* photometry we add the correction for differential reddening and instrumental effects to the magnitudes except where explicitly noted. The coverage for the combined data catalog with 6-filter *HST* photometry is shown in Figure 5.1.

To combine the photometry from [Häberle et al. \(2024a\)](#) with the [M/H] values from [Nitschai et al. \(2023\)](#), we perform an astrometric crossmatch between the two catalogs using a matching radius of 40 mas (equivalent to approximately one WFC3/UVIS pixel). In addition, we require a mag difference in the F625W and F435W filters of $\Delta\text{mag} < 0.1$ between the new photometry and the [Anderson and van der Marel \(2010\)](#) photometry used for the extraction of the spectra. This leaves us with 307,112 matched stars out of the total of 342,797 (or $\sim 90\%$ of the stars) from the catalog published in [Nitschai et al. \(2023\)](#).

5.2.3 Quality Cuts

As default, we assume the quality cuts for the spectroscopic catalog described in [Nitschai et al. \(2023\)](#) (see Section 4.4.7), which are given as an extra flag in the catalog ('Flag'). In summary, we use stars with a minimum SNR of 10, $>95\%$ membership probability, and with a relative accuracy of recovered magnitude from spectrum extraction with PAMPPELMUSE ≥ 0.6 . We also exclude stars near the edge of the field (< 5 pixel) and where the cross-correlation for the velocity is not reliable. These cuts decrease the number of stars from 342,797 to 156,871. The color-magnitude diagram (CMD) in the left panel of Figure 5.2 shows 145,565 stars that fulfill these criteria and are matched to the *HST* photometry as described in the previous section.

As discussed in [Nitschai et al. \(2023\)](#) the above cuts are a compromise that allow us to keep a high number of stars with reliable measurements. Since we want to study the metallicity distribution, chromosome map, and spatial variations of subpopulations we want precise and unbiased [M/H] values over our whole field of view. Hence in addition to the default cuts, we use only stars in the catalog of [Anderson and van der Marel \(2010\)](#) with $m_{\text{F625W}} \leq 17$, a selection that restricts the sample of objects from the spectroscopic catalogs to 12,850 red giant branch (RGB) stars (see the right panel in Figure 5.2). This cut is an extra strict condition to avoid completeness issues of the spectroscopic data set at fainter magnitudes (see Section 5.A), get higher precision on the [M/H] values with a median SNR of ~ 54 , and remove any [M/H] biases between the different original data sets (GTO, GO, NFM, see Section 5.B) that can be caused due to different exposure times. We use the original [Anderson and van der Marel \(2010\)](#) photometry for the magnitude cut unless stated otherwise since it is used for the extraction and the calculation of our

Table 5.1: Data Samples

Name	Number of stars	Description
MUSE QC	156,871	QC of MUSE catalog
MUSE QCM	12,850	QC and $m_{\text{F625W}} \leq 17$ (Anderson and van der Marel, 2010)
<i>HST</i> matched	307,112	MUSE stars matched with catalog presented in Häberle et al. (2024a)
<i>HST</i> QC	145,565	<i>HST</i> matched catalog with QC of MUSE catalog
<i>HST</i> QCM	11,007	QC and $m_{\text{F625W}} \leq 17$ (Häberle et al., 2024a)

QC: quality cuts described in Nitschai et al. (2023) and beginning of Section 5.2.3.

completeness. Additionally, this removes any stars that do not have ADC estimates since these were based on the Anderson and van der Marel (2010) photometry. Note that all metallicities unless otherwise indicated include the ADC correction. The errors used here are the scaled errors as described in Nitschai et al. (2023) or Section 4.4.2.

With these cuts, we get a mean [M/H] error of 0.043 dex. Further, by comparing our MUSE data to the photometric catalog used for the extraction of the spectra (Anderson and van der Marel, 2010) we find a completeness >80 % in all individual cubes, with a median completeness at 17 mag of 97 %. We spatially bin the sample stars and find no significant variation in the mean magnitude with radius or at any point within the field of view. This suggests we can make spatial comparisons with minimal concern about instrumental issues.

In the following section, we will investigate the metallicity information we have for the cluster in detail using the above quality cuts. All the data samples described in this section are summarized in Table 5.1, in Section 5.3 we will use either MUSE QCM or *HST* QCM.

5.3 Results

5.3.1 Metallicity Distribution

First, we analyze the total metallicity distribution of the 156,871 stars (MUSE QC) passing the default criteria, see the left side of Figure 5.3. The additional magnitude-cutoff ($m_{\text{F625W}} \leq 17$ mag) leaves us with 12,850 stars (MUSE QCM) and decreases the more extended tail to lower values (below ~ -2 dex) but also shifts the peak of the distribution to lower values since on average the metal-rich stars have a main-sequence turn-off at fainter F625W magnitudes and hence more metal-rich stars are removed. The cut however ensures that both GTO and GO data sets have a similar distribution and no bias is caused due to different data sets, see Section 5.B. We also used a kernel density estimator (KDE) to estimate the probability density of the distribution, which we normalized to one to plot it onto the same figure. In this distribution multiple peaks are visible and we will identify them later in this section.

The mean [M/H] value is at (-1.558 ± 0.002) dex and the intrinsic standard deviation is (0.260 ± 0.003) dex, which is close to the mean value of the distribution with no magnitude cut (-1.53 dex). The median is (-1.621 ± 0.003) dex with half of the

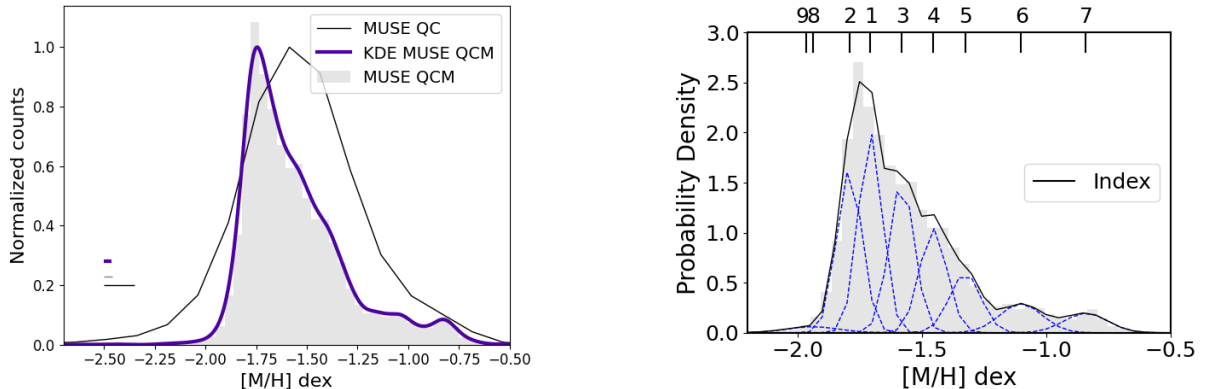


Figure 5.3: Metallicity Distribution. The panel on the left shows the normalized distribution of $[M/H]$ values in the spectroscopic catalog (Nitschai et al., 2023) using the default quality cuts in the black line (MUSE QC), using the extra condition of a minimum brightness of 17 mag in the gray shaded histogram (MUSE QCM) and the purple line is the KDE estimator for that distribution. The small horizontal lines on the left side show the bandwidth (purple short line), 0.035 dex, for the distributions, which are close to the mean error of the $[M/H]$ values (gray and black short line). On the right, we show the same distribution (MUSE QCM) as probability density but fitted with a Gaussian mixture model, shown as a black solid line, with each component (9 in total) shown as a blue dashed line. Note that one component has a small amplitude and is not visible in this plot.

differences between the 16th and 84th percentile being (0.219 ± 0.002) dex. The median of the overall distribution without a magnitude cut is -1.54 dex, which is closer to the mean value since more metal-rich stars are included. All the values and errors (68 %) were calculated with bootstrapping.

The range in metallicity for stars brighter than 17 mag reaches from ~ -2 dex to almost -0.5 dex. In detail, 68 % of the stars are between -1.78 dex and -1.34 dex and 99.7 % between -2.23 dex and -0.66 dex. This huge metallicity spread is, as mentioned previously, an indication of multiple stellar populations, which indeed are visible as distinct sequences in the color-magnitude diagram (CMD, see Figure 5.2).

All our results are comparable to the values in Husser et al. (2020) where in a smaller sample of 1,247 stars they found a mean value of -1.50 dex, a median of -1.65 dex and a range from -1.82 to -1.31 dex for the 1st and 3rd quartiles. However, since our sample is 10 times larger we have even more accurate values with small uncertainties.

We also used a Gaussian Mixture Model to describe our distributions and the result can be seen on the right side of Figure 5.3 and in Table 5.2. We find that the best number of Gaussians to describe the distribution is nine using the Bayes Information Criterion (BIC). However, one component is not visible in the Figure (index 9 in the Table) since it has a very small amplitude compared to the rest and would not count as a separate population but is needed to describe the distribution in the model. Similarly, component 8 is needed for the extended tail towards lower metallicities, but only a few stars contribute to that in the magnitude range we are looking at. Components 1 and 2 are close to each other and not distinguishable by eye in the highest peak of the distribution. Components 6, and 7 can be seen by eye as smaller peaks, and components 3, 4, and 5 are more difficult to distinguish but are still visible.

We have compared our metallicity findings with previous studies already in Nitschai et al. (2023) where we made a one-to-one comparison. Also, the overall distribution agrees with previous studies (e.g., Johnson and Pilachowski, 2010; Mészáros et al., 2021; Alvarez Garay et al., 2024), even though we find more peaks in our distribution. Johnson

Table 5.2: Multi-Gaussian Components of the Metallicity Distribution

index #	Mean [dex]	Intrinsic standard deviation [dex]	Fraction of stars %
1	-1.706	0.048	24.7
2	-1.791	0.050	21.0
3	-1.581	0.051	19.2
4	-1.453	0.055	14.5
5	-1.325	0.063	9.0
6	-1.101	0.086	6.2
7	-0.840	0.087	4.2
8	-1.938	0.106	1.1
9	-1.964	0.934	0.2

The index # is assigned from the highest to the lowest amplitude.

and Pilachowski (2010) find 5 peaks in the distribution at $-1.75, -1.50, -1.15, -1.05$ and -0.75 dex, while Mészáros et al. (2021) and Alvarez Garay et al. (2024) find four peaks, $-1.65, -1.35, -1.05$ and -0.7 dex, and $-1.85, -1.55, -1.15$, and -0.80 dex respectively. All these peaks are in agreement with at least one of our peaks within the 3σ range. The difference in the number of peaks can be explained due to the difference in the data, specifically the amount of data, since it can make it difficult to identify and separate peaks in the distribution with a lower amount of stars. All the above-mentioned studies have stars that reach larger radii than ours, but have fewer than 1,000 stars, while we have more than 10 times their number which allows us to distinguish different metallicity components more easily. However, even in our case, one could reduce the number of components to four or five if one only looks at the distribution by eye, since peaks 1 and 2 can be taken as one, and components 3, 4 and 5 are not that clearly visible peaks in the overall distribution and 8 and 9 are not at all visible. This demonstrates the advantage of our huge data set that allows for much more detailed studies and analysis.

In Husser et al. (2020) they identify nine subpopulations and give their mean metallicity values. Our multi-Gaussian Mixture Model does not separate the stars in different subpopulations, since also photometric analysis needs to be taken into account. However, we can compare their position on the chromosome map in Section 5.3.2 and identify which component belongs to which subpopulation (P) identified in Husser et al. (2020). P1, P2 and P3 (mean $[Fe/H] = -1.83, -1.80, -1.74$ dex) corresponds to our components 1 and 2, P5 (-1.24 dex) to component 5, P8 (-1.50 dex), P6 (-1.47 dex) and P4 (-1.50 dex) to components 4 and 3. Using the chromosome map we can identify component 7 as P7 (-0.18 dex) and component 6 as P9 (-0.72 dex). However, the metallicity values from P7 and P9 disagree the most with our findings, which might be caused by the lower number of stars in these populations in their analysis compared to ours. With our data, they can be much better studied and separated. In the following sections, we investigate a bit further different subpopulations. We do not aim to precisely separate and identify all subpopulations. This will be done in future work including stars of fainter magnitudes (Clontz et al., in prep). Nevertheless, this analysis already shows how our huge data set can improve subpopulation studies.

Lastly, in Johnson et al. (2020) they find two very metal-poor populations, below -2 and -2.25 dex. Our component 8 contains 144 stars at the very low end of the metallicity distribution reaching as low as -2.225 dex being consistent with the -2 dex population in Johnson et al. (2020). However, the even lower population below -2.25 dex is not

found in our data, since our component 9 seems to be broader and contains all stars not belonging to any other Gaussian, with the lowest and highest metallicity stars (reaching almost -4 dex up to -0.1 dex). Also in Johnson et al. (2020) the actual number of very low metallicity stars is low, only 11. These stars could be included in component 9 which has 25 stars in total and 15 stars between -3 dex and -2.25 , corresponding to the range of the Johnson et al. (2020) results. Five stars are above -0.6 dex and the 5 remaining stars are below -3 dex. Both components 8 and 9 are just a tiny fraction of the whole sample and they do not cover the whole CMD range. Specifically, component 9 includes blue stragglers and the stars that most likely are a few remaining horizontal branch stars (see Figure 5.2 at magnitude ~ 14 and color ~ 0) which did not get removed in our initial catalog creation (see Chapter 4), which could explain the extremely low metallicities. Component 8 on the other hand mostly lies on the fainter RGB close to magnitude 17 mag. This indicates that they are not a separate population and are not the same stars as in Johnson et al. (2020) where most of these stars lie on the brighter RGB. They are individual stars with special [M/H] values either due to measurement problems, like horizontal branch stars that need special treatment and do not have accurate [M/H] values the way we calculate them, or they could be captured from the field of the parent galaxy or the metal-rich ones from the Galaxy during a merger. Overall, we can conclude that we do not find the most metal-poor population from Johnson et al. (2020) in our sample, even though we have a few extremely low metallicity stars.

5.3.2 Chromosome Map

In this subsection, we again focus on RGB stars with $m_{\text{F625W}} < 17$ mag, but using the photometry for m_{F625W} from Häberle et al. (2024a). In addition, we require the stars to have accurate photometric measurements in 5 different *HST* filters (F275W, F336W, F435W, F625W, and F814W) in the photometric catalog of Häberle et al. (2024a). These requirements leave us with a sample of 11,007 stars (*HST* QCM). We have excluded some outliers and the blue stragglers in the CMD (see black crosses in Figure 5.17).

The chromosome map is a photometric diagram used to identify multiple stellar populations in globular clusters. It uses multi-color photometric information that is sensitive to element abundance variations to characterize the presence and diversity of multiple populations (Milone et al., 2017b). Many studies have provided accurate investigations of the subpopulations of ω Cen (e.g., Tailo et al., 2016; Latour et al., 2021; Husser et al., 2020). Here, we take advantage of an unprecedented dataset that comprises photometry and spectroscopy of more than 11,000 RGB stars to better investigate them.

To construct the chromosome map, we follow the technique from Milone et al. (2017a) and use the filters F814W, F336W, F275W, and F435W. In Milone et al. (2015a,b) it has been shown that the combination of the pseudo-color $C_{\text{F275W},\text{F336W},\text{F435W}}$ (in our case $C_{\text{F275W},\text{F336W},\text{F435W}}$) (Piotto et al., 2015) with the $m_{\text{F275W}} - m_{\text{F814W}}$ color maximizes the separation between stellar populations along the main sequence and the RGB. We note that we use F435W in our $C_{\text{F275W},\text{F336W},\text{F435W}}$ calculation and here we analyze only the RGB populations, deferring a more comprehensive view of subpopulations and their exact separation in the cluster to a later paper (Clontz et al., in prep.).

The detailed steps to calculate the Δ values can be found in Section 5.C. In general,

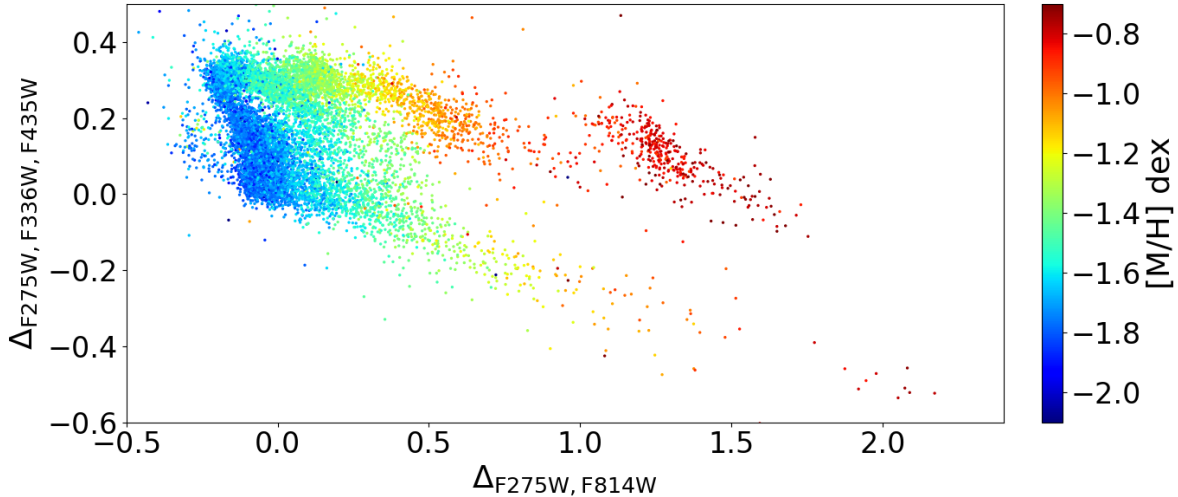


Figure 5.4: *Chromosome Map of ω Cen.* The chromosome map of ω Cen is color-coded with metallicity. One can identify different subpopulations in the map but since we do not aim to separate them precisely in this work we also do not draw the line separating first and second-generation stars as it is usually done in globular clusters.

the following relations are used:

$$\Delta_{F275W,F814W} = W_{F275W,F814W} \cdot \frac{X - X_{fiducialR}}{X_{fiducialR} - X_{fiducialB}} \quad (5.1)$$

and

$$\Delta_{F275W,F336W,F435W} = W_{F275W,F336W,F435W} \cdot \frac{Y_{fiducialR} - Y}{Y_{fiducialR} - Y_{fiducialB}} \quad (5.2)$$

with fiducialR the redder fiducial line and fiducialB the bluer line in color space. Further, $X = m_{F275W} - m_{F814W}$, $Y = C_{F275W,F336W,F435W}$ and the pseudo-color $C_{F275W,F336W,F435W} = (m_{F275W} - m_{F336W}) - (m_{F336W} - m_{F435W})$. The final chromosome map is shown in Figure 5.4.

The x-axis of this chromosome map is mostly sensitive to stellar populations with different helium content and metallicity, whereas the y-axis is mostly efficient in identifying stellar groups of stars with different nitrogen abundance (see e.g., [Marino et al., 2019](#), for details, Figures 25 and 27). In a typical GC, what is known as first (1G) and second-generation (2G) stars would lie around $\Delta_{F275W,F814W} \sim 0$, with 1G being centered at the origin (0,0) and the 2G stars found above ($\Delta_{F275W,F336W,F435W} > 0$). In ω Cen the most metal-poor stars follow this pattern, while higher metallicity stars have different tracks at $\Delta_{F275W,F814W} > 0$. Further abundance studies will help us distinguish the different subpopulations even better.

5.3.2.1 Metallicity Dependency

Since we have the metallicity information for all these stars we can investigate the relationship between the Δ -values and $[M/H]$, see Figure 5.5. $[M/H]$ vs $\Delta_{F275W,F336W,F435W}$ shows as expected a similar structure to the chromosome map since $\Delta_{F275W,F814W}$ tracks

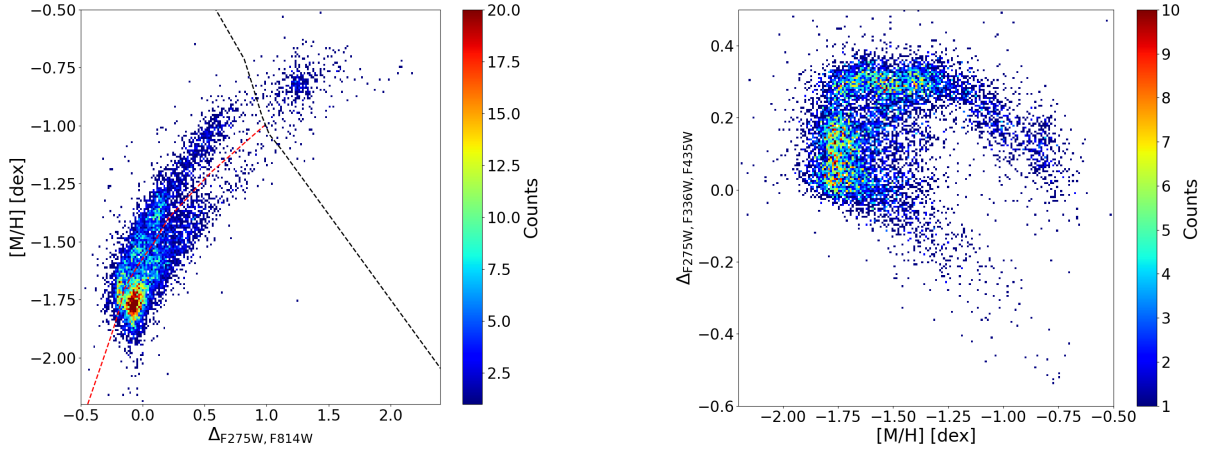


Figure 5.5: Δ Values as a Function of $[M/H]$. The chromosome Δ values, left metallicity against $\Delta_{F275W, F814W}$ and right $\Delta_{F275W, F336W, F435W}$ plotted against metallicity in a density histogram. On the left, the red line separates the two streams visible and the black line indicates the metal-rich stars that are excluded from the analysis in Section 5.3.4.3.

the $[M/H]$ variations. Interestingly, we notice two distinct sequences in the $[M/H]$ vs $\Delta_{F275W, F814W}$ diagram, which correspond to stars with different light-element abundances. Specifically, the upper stream is composed of the most extreme stars in chemical properties, enhanced in $[Na/Fe]$, $[Al/Fe]$ and depleted in $[O/Fe]$ with respect to the lower stream stars with the same metallicity (Marino et al., 2019). Further, Fe enrichment occurs in both streams, the upper has a slightly higher peak (Marino et al., 2019), which we will also show in Section 5.3.2.2 and Section 5.3.4.3.

5.3.2.2 The Metal-Poor Component and Its Multiple Populations

The most metal-poor stars ($[M/H] \lesssim -1.64$ dex) of the cluster follow a similar trend as the stars of mono-metallic globular clusters that separate in the so-called 1G and 2G stars along the $\Delta_{F275W, F336W, F435W}$ axis due to light-element variations.

To identify these metal-poor stars in the chromosome map, we used the same method as in Section 5.C, photometric selection and a high probability of belonging to the component one or two from the Gaussian Mixture Model in Section 5.3.1.

If we only look at those stars, we can see that they also have a metallicity spread reaching from -1.82 to -1.69 dex for 68 % of the stars, see Figure 5.6. With a simple Gaussian Mixture Model fit we identify 3 peaks (using BIC) in the $\Delta_{F275W, F336W, F435W}$ distribution, separating them into three different populations. We see that the third peak (highest $\Delta_{F275W, F336W, F435W}$ values) has the highest metallicity (similar to the findings in Marino et al., 2019) and that all have a significant width. We investigate that further by looking at their metallicity distribution. The yellow peak has the highest mean metallicity at -1.732 dex and an intrinsic standard deviation of $\sigma = 0.056$ dex, the red is at -1.763 dex and $\sigma = 0.056$ dex and the black one is at -1.764 dex and $\sigma = 0.058$ dex. They have similar standard deviations $[M/H]$ but the yellow peak is offset to higher $[M/H]$, with a p-value below 1 % for the Anderson-Darling and Kolmogorov-Smirnov tests. The red and black distributions have higher p-values >25 % meaning that they are consistent to be drawn from the same distribution. Overall, even in this one metallicity component, there is a spread in $[M/H]$ and it rises to higher $[M/H]$ for higher $\Delta_{F275W, F336W, F435W}$ values as seen also in Marino et al. (2019). However, since the difference is small, even though

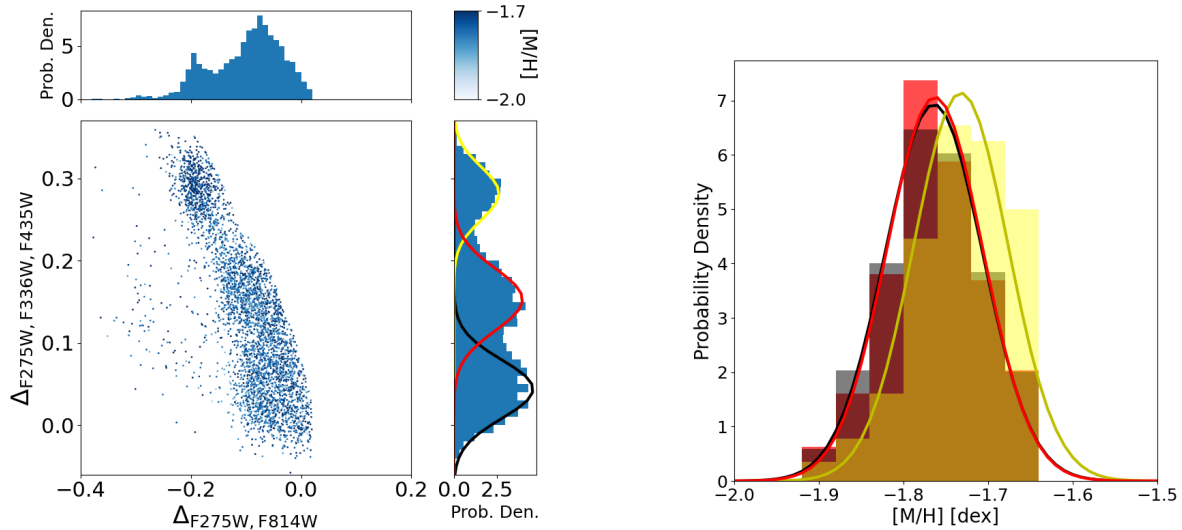


Figure 5.6: Multiple Populations in the Metal-Poor Stars. On the left is the chromosome map only for the metal-poor stars with the probability density histograms of the Δ values. There we can identify 3 peaks in the $\Delta_{\text{F}275\text{W}, \text{F}336\text{W}, \text{F}435\text{W}}$ histogram and plot their metallicity distribution on the right. The metallicity distributions for the populations indicated with the red and black lines are very close, while the population plotted in yellow exhibits a higher metallicity. Stars on the very left side of the chromosome map are lying at the edge of the blue fiducial line in the CMD.

it seems to be significant (see also Figure 5.9), we do not have pure iron abundance but $[\text{M}/\text{H}]$ which could be increased with enrichment in Na and Al which is expected for the red and even stronger for the yellow peak.

Higher $\Delta_{\text{F}275\text{W}, \text{F}336\text{W}, \text{F}435\text{W}}$ also mean more enhanced Na and Al element abundances and depleted in O and Mg, as explained in Section 5.3.2.1 and hence more He-rich stars (Milone et al., 2015b; Milone et al., 2018; Marino et al., 2019). Therefore we will call stars belonging to the black peak Na-poor metal-poor (Na-poor MP) population, the yellow peak Na-rich metal-poor (Na-rich MP) population, and in the red peak are stars with intermediate Na enrichment.

There have been studies identifying subpopulations in ω Cen on the RGB (e.g Lee et al., 1999; Pancino et al., 2000; Sollima et al., 2005; Husser et al., 2020) and the main sequence (MS) (e.g., Bedin et al., 2004; Bellini et al., 2010; Milone et al., 2017a; Bellini et al., 2017d). However, connecting the RGB and main-sequence stars into the same subpopulations is a complex task that has not been done so far since the subpopulations overlap and cross each other below the turnoff point in the CMD. This will be the focus of future studies (Clontz et al., in prep).

5.3.3 Spatial 2D Metallicity Distribution

We analyze the 2D spatial distribution of the metallicity since 2D variations might average each other out in radial bins.

We create smooth maps that still show details using the median of the 200 nearest neighbors (see Figure 5.7) and for visualization only the locally weighted regression (LOESS)³ technique (with a regularization factor $f=0.1$, Cappellari et al., 2013a). We choose 200 nearest neighbors since that gives a smooth map without patches also in the velocity (similar to Pechetti et al., 2024). In Figure 5.7 we can see that indeed there is

³<https://pypi.org/project/loess/>

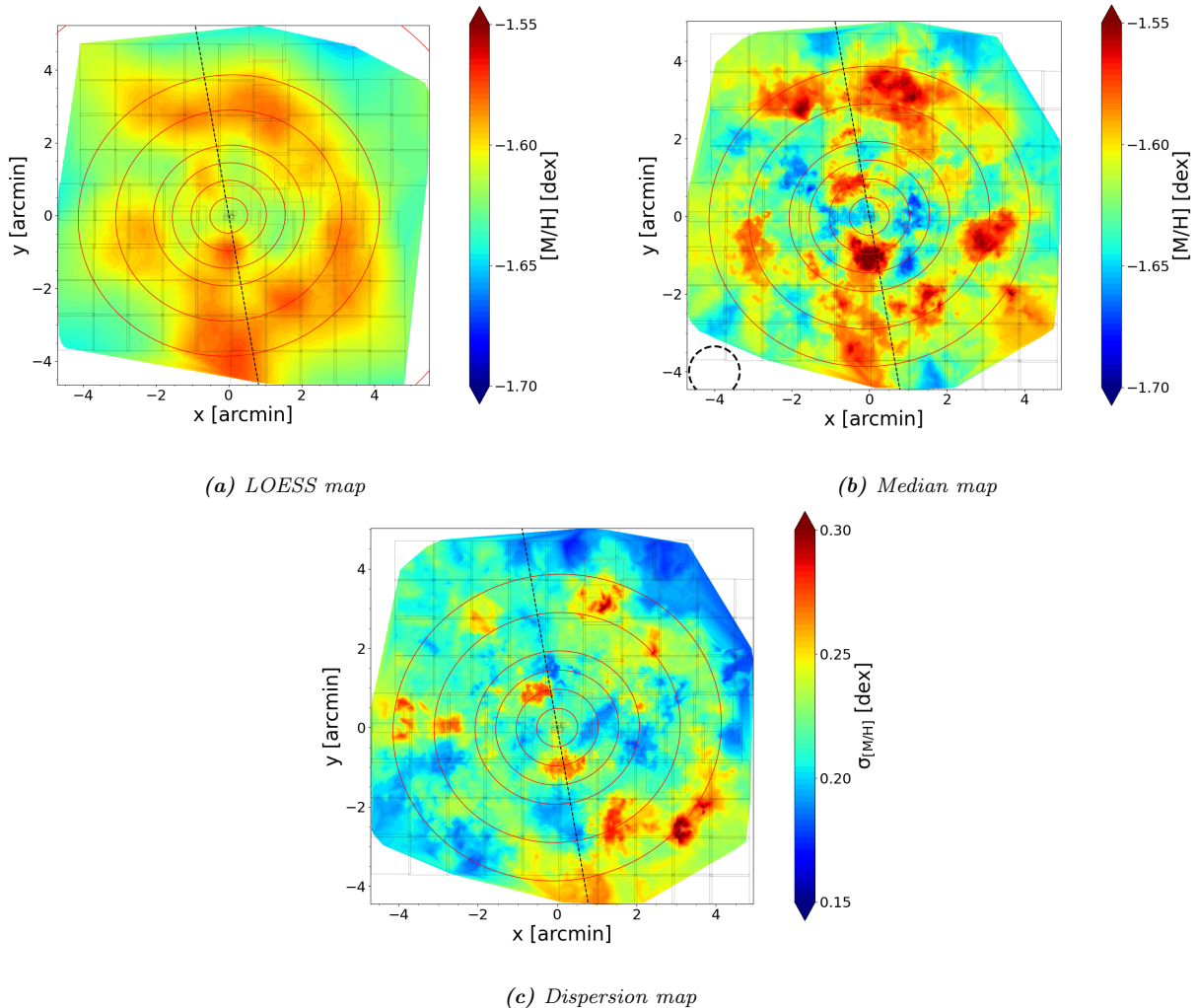


Figure 5.7: Metallicity Maps. (a.) The LOESS smoothed metallicity map for visualization only, (b.) the median map from the 200 nearest neighbors, and (c.) the 68 % dispersion map from the 200 nearest neighbors. In (b.) the black dashed circle in the left corner shows the mean radius of the 200 neighbors. The pointing structure from MUSE is shown with faint squares, the red elliptical annuli are the bin edges used in Section 5.3.4, and the minor axis of the elliptical annuli corresponding to the rotation axis is shown as a black dashed line. The x-axis and y-axis show the distance to the center of the cluster for the right ascension (ΔRa) and declination (ΔDec).

some structure, almost ring-like, consistently visible in both the LOESS and median map. In addition, we also plot half the difference of 68 % of the 200 nearest neighbors as an indication of the dispersion of the [M/H] values. Regions with lower median metallicity in the outskirts of the field have a relatively narrow metallicity distribution, while some of the structures with higher median metallicity also have a higher dispersion. However, there are also regions with moderately high median [M/H] and a narrow [M/H] distribution. In general, the variation in the dispersion map does not perfectly match the ring-like structure of the median metallicity map. Further, the pattern does not follow the MUSE pointing structure, reassuring us that the structure is not caused by calibration differences. We also verified that the structure does not appear if we take the ratio between the redmost RGB branch (metal-rich stars) and the blue RGB (metal-poor stars), which suggests that the structure is not caused by biases in our observations or selection of the sample in specific regions. However, this also indicates that the structure is not caused by

the most metal-rich population but by some other intermediate [M/H] populations that might have been accreted later in its evolution and not yet well mixed.

5.3.4 Metallicity Gradients

5.3.4.1 Overall Cluster Gradient

Since the cluster is elongated in the plane of the sky, we do not use circular radial bins for further analysis but elliptical bins. We use 100° for the position angle (PA) (van de Ven et al., 2006a; Kamann et al., 2018), 0.07 for the ellipticity (median value from Geyer et al., 1983; Pancino et al., 2003; Calamida et al., 2020, inside $5'$) and the equivalent radii for the bins are (0.5, 1, 1.5, 2, 3, 4, 7) arcmin. These bin edges are overplotted in red in Figure 5.7. In all the following analyses we calculate the median circular radius (r) to the center in each of the elliptical bins and show that in the figures.

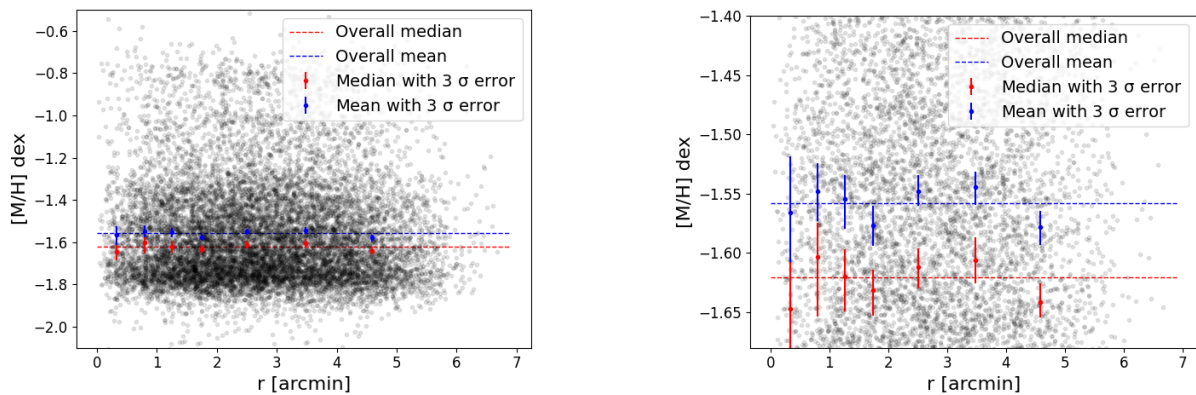


Figure 5.8: Overall Metallicity Gradient. Black are all the stars used for this analysis red is the median value for each bin and blue is the mean value. The dashed lines show the total median or mean value for the whole sample. The left panel shows the whole [M/H] range while the right side is a zoom into metallicities around the mean and median.

In Figure 5.8 we plot the mean and median metallicity value for each bin with the 99.7 % as 3σ error bars, derived with bootstrapping. We can conclude that there is no significant gradient within the half-light radius of the cluster. However, there is an indication of the ring we see in the 2D distribution (Section 5.3.3), in the bins between 2 - 4 arcmin, where the median [M/H] is almost 3σ (99.7 %) above the global median [M/H] of the cluster. Also, the last bin lies 4.8σ below the overall median value. We see these same trends in the mean metallicity profile. The trend is not as strong as in the 2D maps since it is not a perfect ring at some lower and higher [M/H] areas cancel each other out when looking at the radial profile, but the signature is still visible.

Previous studies (e.g., Sollima et al., 2007; Bellini et al., 2009; Calamida et al., 2017, 2020) find spatial differences in subpopulations of the MS and the RGB. The bluer MS (associated with the intermediate metallicity RGB by Piotto et al. 2005), which is thought to be He-enriched (Bedin et al., 2004; Norris, 2004; Piotto et al., 2005) is more centrally concentrated than the red MS (associated to the metal-poor RGB), but increasing towards the outer parts, above 25 arcminutes. While for the RGB the rich and intermediate follow the same distribution and are more centrally concentrated with a decline towards 8 to 10 arcminutes (Bellini et al., 2009). The last bin in our metallicity gradient and lower metallicity towards the outer parts of the 2D map (see Section 5.3.3) indicate a similar

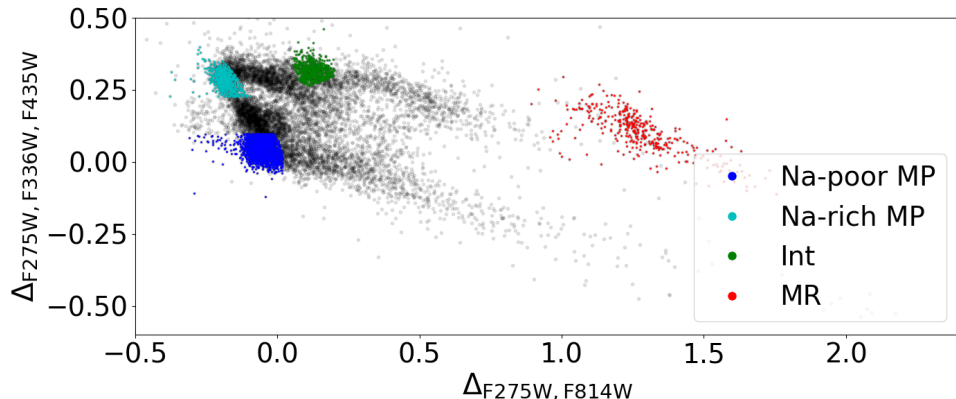


Figure 5.9: Chromosome Map Showing the Four Different Subgroups. Red are the metal-rich stars, green the intermediate population, cyan the metal-poor but Na-rich, and blue the metal- and Na-poor stars.

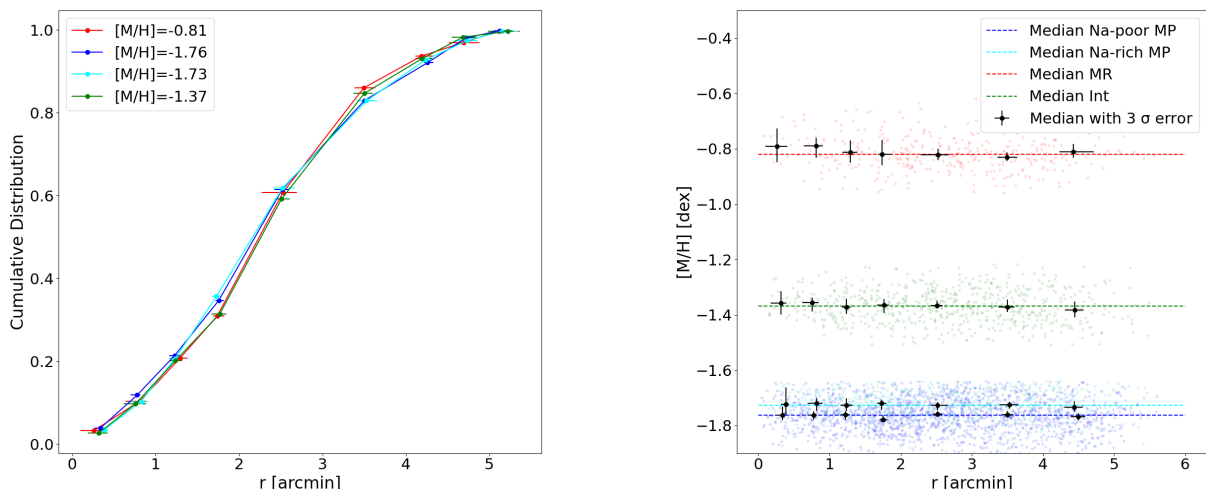


Figure 5.10: Spatial Distribution of the Subgroups. The left side shows the cumulative distribution of the four subgroups, the labels show the median $[M/H]$ value. On the right is their metallicity versus radius.

trend with the more metal-rich or intermediate populations declining at the edge of the half-light radius. In Calamida et al. (2017, 2020) they show that the more metal-poor stars follow the cluster elongation and are more numerous in the northern half, while the more metal-rich are elongated in the northeast-southwest direction and are more numerous in the eastern half. This trend is not visible in our data in the 2D distributions.

In general, for all these previous studies the spatial differences are prominent at the edge or after the half-light radius which is outside of our data range. From our analysis, inside the half-light radius, the subpopulations seem to be well mixed in radial bins.

5.3.4.2 Spatial Differences between Subpopulations

Further, we want to investigate if there is a difference in the spatial distribution of different subpopulations. We use the four different subgroups already identified (see Section 5.C and Section 5.3.2.2), Na-rich but metal-poor (Na-rich MP), Na-poor and metal-poor (Na-poor MP), intermediate metallicity (Int) and the metal-rich population (MR). See Figure 5.9 for their location on the chromosome map.

The cumulative radial distribution and metallicity gradient of each subpopulation is shown in Figure 5.10. The Anderson-Darling test gives a p-value higher than 23 %, so the null hypothesis is not rejected and the subpopulations could have the same underlying distribution. The populations do not show any significant metallicity gradient, see Figure 5.10 right panel. The right panel also confirms our finding in Section 5.3.2.2 that the metallicity difference between Na-rich and Na-poor metal-poor populations is significant (outside the 3σ range) for all radii. The subpopulations, depending on metallicity or Na-enrichment, we selected are all well-mixed.

5.3.4.3 Differences in the Two Streams of $[M/H]$ vs $\Delta_{F275W,F814W}$

In the previous section, we chose four subpopulations with different metallicities and Na-enhancement and found no significant spatial difference. To further check the difference between subpopulations with different enhancement in light elements, we use the two streams seen in $[M/H]$ vs $\Delta_{F275W,F814W}$ (see Section 5.3.2.1 and Figure 5.11). We exclude the metal-rich stars (black line in Section 5.3.2.1) since they lie in between the sequences. The cumulative distribution is shown in the left panel of Figure 5.12 and they do not differ significantly, Kolmogorov-Smirnov and Anderson-Darling tests show 10 % and 8 % p-values confirming that the null hypothesis is not rejected for their spatial distribution. However, the p-values are lower than for the subpopulations indicating that there might be differences that could get stronger towards larger radii (similar to the difference of the blue and red MS [Sollima et al. 2007](#) and [Bellini et al. 2009](#)).

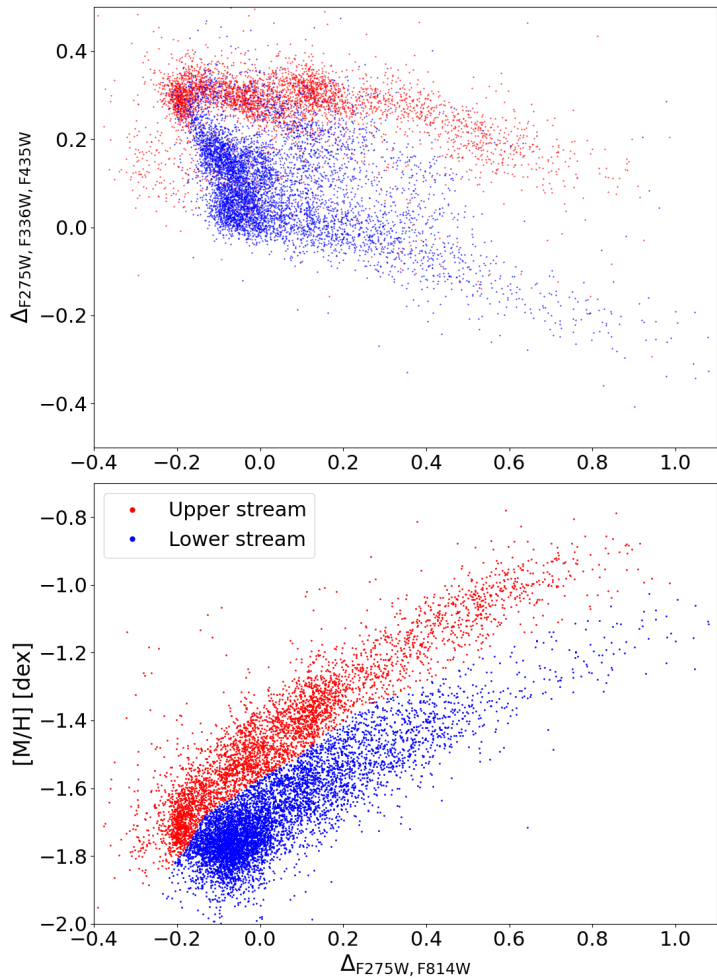


Figure 5.11: The Two Streams in $[M/H]$ vs $\Delta_{F275W,F814W}$. The top panel shows the chromosome map and the bottom panel the $\Delta_{F275W,F814W}$ vs $[M/H]$. We color-coded the stars depending on whether we identified them as belonging to the upper or lower stream in the original Figure 5.5.

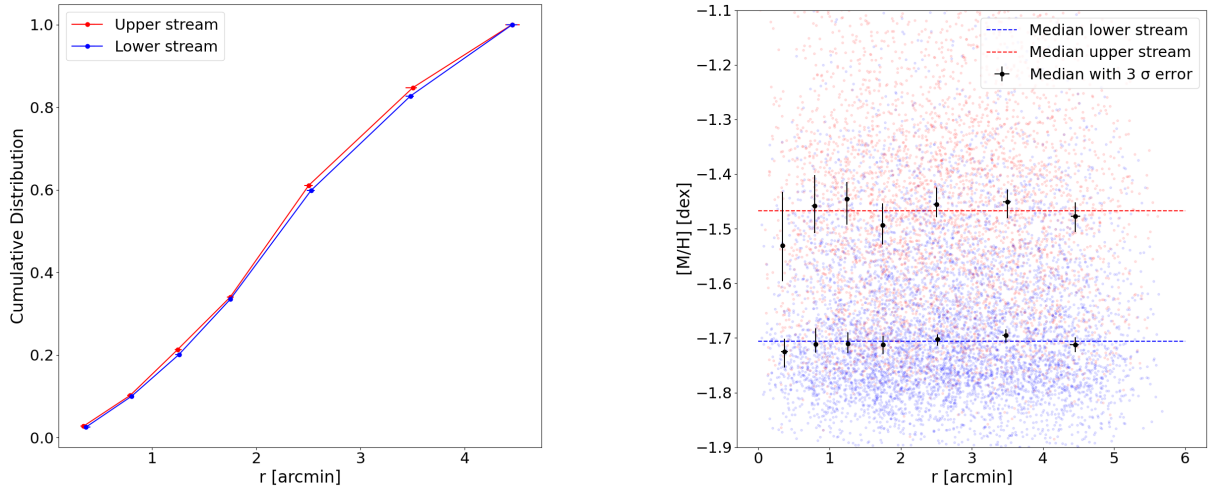


Figure 5.12: Spatial Distribution of the Two Streams in $[M/H]$ vs $b\Delta_{F275W,F814W}$. The left side shows the cumulative distribution of the two sequences. On the right is their metallicity versus radius.

Their metallicity however is different with the lower sequence having a median metallicity higher than the upper sequence. That is not unexpected since most of the metal-richer stars lie on the upper stream and slightly higher iron values are expected in that stream as discussed in Section 5.3.2.1. However, again no significant metallicity gradient is visible (see right panel Figure 5.12).

5.4 Conclusion

We present a detailed study of the metallicity distribution of 12,850 RGB stars in ω Cen with a mean error of 0.043 dex and a median SNR ~ 54 . We find a mean value of -1.577 dex and a median value of -1.621 dex spanning from -0.66 dex to -2.23 dex for 99.7 % of the stars with $m_{F625W} < 17$ mag. Further, we identify multiple peaks in the metallicity distribution indicating different metallicity subgroups.

Additionally, we investigate the chromosome map and its dependencies with metallicity. We looked in detail at the most metal-poor group and identified three populations that show a similar spread in $[M/H] \sim 0.1$ dex while the $[M/H]$ increases for higher $\Delta_{F275W,F336W,F435W}$.

We also studied the 2D spatial distribution of the $[M/H]$ values and created metallicity maps showing a ring-like structure with higher values, while inside and outside the $[M/H]$ values drop. Finally, we check for metallicity gradients and spatial differences in radial bins for different subgroups of stars. There we find no gradient in $[M/H]$ over our field of view.

Overall, the different populations seem to be well mixed and no strong gradient is visible in their radial profiles. However, more information on the abundance might help better separate them and further investigate their differences. In addition, the different subpopulations may be well mixed spatially, but their kinematics may be used to separate them, as it takes longer to erase the stars' memory of their original orbits.

We plan to determine elemental abundances (Di Stefano et al., in prep, Wang et al., in prep), and identify subpopulations (Clontz et al., in prep.) and ages (Clontz et al., in prep), see Chapter 6. This will bring us closer to uncovering the formation history of ω Cen, the nearest nuclear star cluster.

Appendices

5.A Completeness

In Nitschai et al. (2023) we provided the completeness compared to the Anderson and van der Marel (2010) catalog and found that at a magnitude of 18.86 mag in the F625W filter, we have 50 % completeness. For our study, we require higher completeness to avoid biases that could cause gradients or spatial variation in metallicity to vary. A magnitude cut of 17 mag gives us over 80 % completeness for all fields and even reaches 90 % for the majority, see Figure 5.13 left panel.

To further ensure that we do not bias our sample we check the radial dependency of the magnitude, which should be uniform. Indeed Figure 5.13 (right) shows that the mean and median values remain constant over our whole field of view, not showing any crowding effects, for the RGB stars.

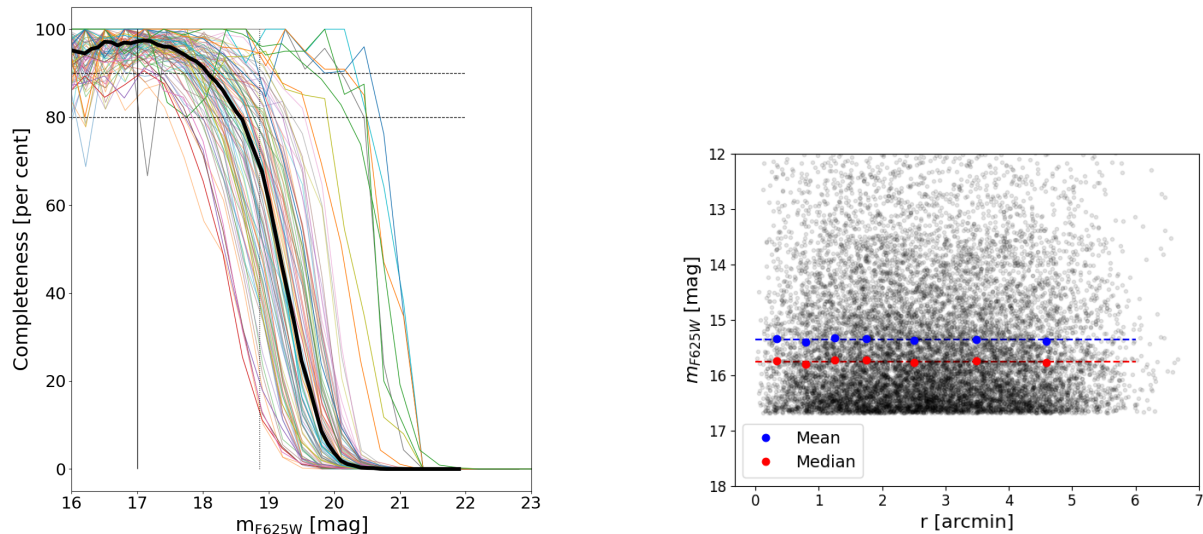


Figure 5.13: Completeness and Magnitude. Left panel: Each line shows the completeness fraction of one pointing compared to the HST catalog from Anderson and van der Marel (2010) and the thick black line shows the median completeness fraction. The vertical solid line is at 17 mag and the dotted one at 18.86 mag (for GO 50 % completeness on average). The dashed horizontal lines are at 80 % and 90 %. Right panel: the magnitude of the stars above 17 mag versus radius, which shows that for our quality cuts, there is no bias or gradient for specific magnitudes.

5.B [M/H] Bias

We noticed a metallicity bias in the different data sets, GO, GTO, NFM, when using all available magnitudes. In Figure 5.14 we can see that the [M/H] has always a trend to go to higher metallicities for lower SNR, but it differs between data sets. In general, the GTO stars with fainter magnitudes have higher [M/H] and lower SNR than the GO, which is likely caused by differences in the observing runs (e.g., different exposure times and number of exposures). However, the trend that stars with higher [M/H] have lower SNR is true for all stars and could be because they are redder, on average fainter (in general lower SNR), and have more absorption lines that make them look noisier to our spectral fitting routine compared to more metal-poor stars. When excluding stars fainter

than 17 mag in the F625W magnitude we remove most of the stars with $\text{SNR} \leq 20$ where the bias is visible, making our sample consistent between GTO and GO observations.

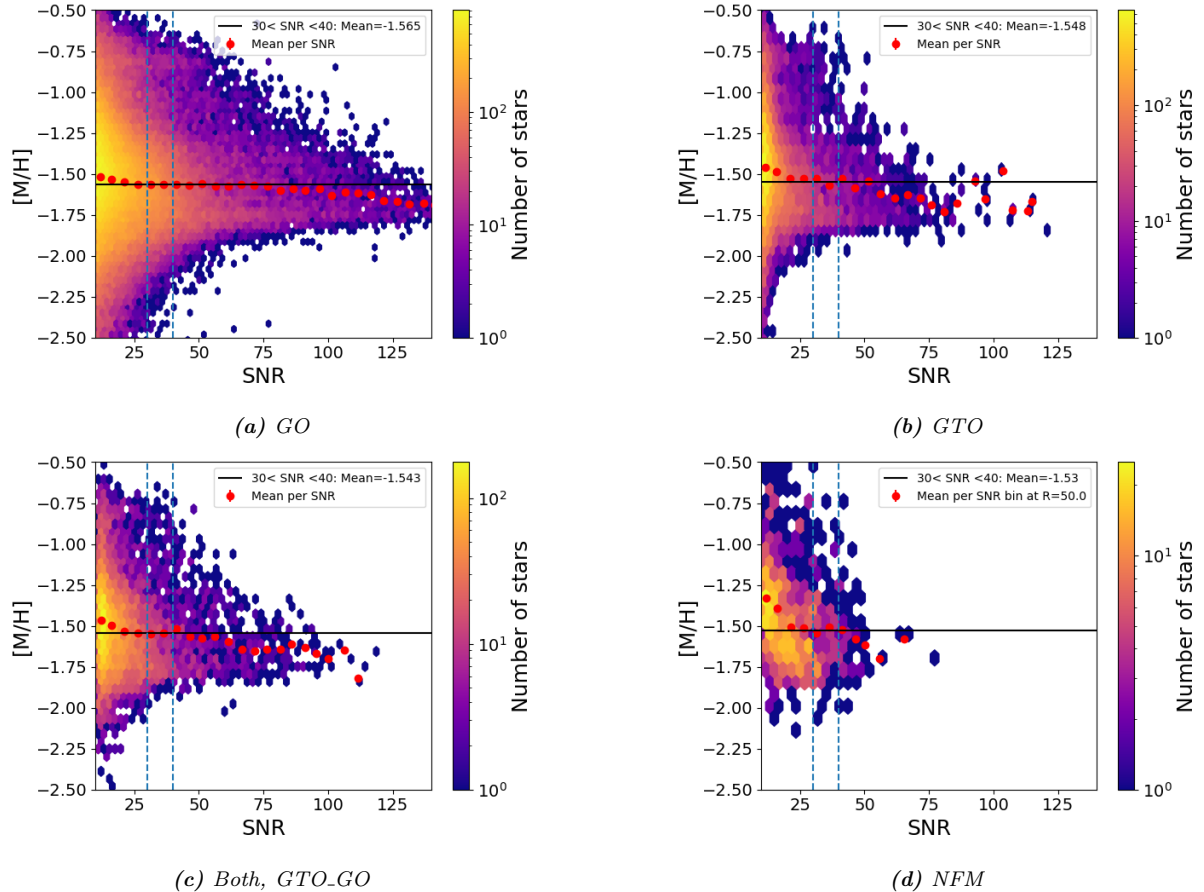


Figure 5.14: Metallicity Bias. We plot the metallicity versus the SNR for the different data sets underlying our spectroscopic catalog. Red dots are the mean values for each bin and the black solid line is the mean value between 30 and 40 SNR (indicated with blue dashed lines).

Additionally, we check if the distribution of the stars in GO and GTO are different, see Figure 5.15. When using all magnitudes the GO distribution is broader reaching lower metallicities which would cause the GTO fields always to be on average more metal-rich. However, when applying the magnitude cut the distributions agree well not having any systematic difference.

5.C Details for the Chromosome Map

Since ω Cen is more complex than typical globular clusters, a more elaborate analysis is needed to create a useful chromosome map. Our method is adapted from the procedure described in Milone et al. (2017a).

In summary, one needs more than just two, red and blue, fiducial lines since there are multiple different populations in ω Cen. Hence, one identifies three subsamples, the metal-poor population that also on its own would look like a chromosome map for typical clusters, an intermediate population, and a metal-rich population (a. Figure 5.16). The process is iterative and we start by identifying the subsamples in $[\text{M}/\text{H}]$ first. Metal-poor stars are those belonging to peaks 1 and 2 of the Gaussian Mixture model in Section 5.3.1,

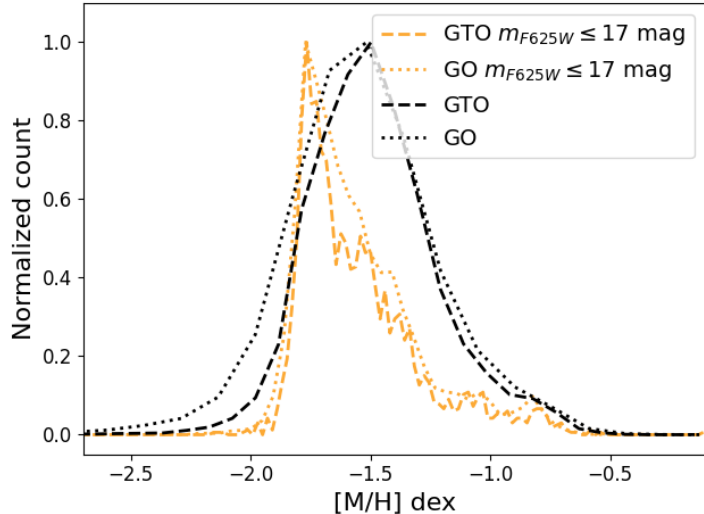


Figure 5.15: Metallicity Distribution GO and GTO. Using all magnitudes the two different data sets have important differences in their distributions. However, with a magnitude cut these disappear and the distributions look almost identical.

metal-rich stars belong to peak 7, and the intermediate population are stars in the fourth and fifth components. We then use slightly adapted fiducial lines from (Milone et al., 2017a) to get an initial chromosome map. Next, we identify the subsamples using the different components identified for the [M/H] distribution and also the photometry as in Milone et al. (2017a). Including the photometry information for the subsamples narrows CMD tracks and we calculate new fiducial lines.

The red and blue fiducial lines correspond to the 96th and 4th percentiles in the CMD and pseudo-CMD. In the $m_{F275W} - m_{F814W}$ CMD (b. Figure 5.16) the red and blue fiducial lines correspond to the metal-poor population. For the intermediate and rich population, one needs to find the median fiducial line. In the CMD with the pseudo-color, $C_{F275W,F336W,F435W}$, (c. Figure 5.16) the populations are more mixed and the intermediate and poor populations can use the same red and blue fiducial lines, while the metal-rich have different 96th and 4th percentiles indicated with the black and cyan lines. For all fiducial lines, we smoothed and corrected by hand for bright magnitudes.

We repeated this process twice refining our subsample selection and fiducial lines. Our final fiducial lines are shown in Figure 5.17 together with the verticalization of the colors for all bright stars.

To get the chromosome map values we calculate the following weights:

$$W_{F275W,F814W_1} = X_{fiducialRed}(15.5 \text{ mag}) - X_{fiducialBlue}(15.5 \text{ mag}) \quad (5.3)$$

$$W_{F275W,F814W_2} = X_{fiducialOrange}(15.5 \text{ mag}) - X_{fiducialRed}(15.5 \text{ mag}) \quad (5.4)$$

$$W_{F275W,F814W_3} = X_{fiducialGreen}(15.5 \text{ mag}) - X_{fiducialOrange}(15.5 \text{ mag}) \quad (5.5)$$

where e.g., $X_{fiducialRed}(15.5 \text{ mag})$ is the color of the fiducial line interpolated at 15.5 magnitude in F814W. Then we can find the respective $\Delta_{F275W,F814W_i}$ values:

$$\Delta_{F275W,F814W_1} = W_{F275W,F814W_1} \frac{X - X_{fiducialRed}}{X_{fiducialRed} - X_{fiducialBlue}} \quad (5.6)$$

$$\Delta_{F275W,F814W_2} = W_{F275W,F814W_2} + W_{F275W,F814W_2} \frac{X - X_{fiducialOrange}}{X_{fiducialOrange} - X_{fiducialRed}} \quad (5.7)$$

$$\begin{aligned} \Delta_{F275W,F814W_3} = & W_{F275W,F814W_2} + W_{F275W,F814W_3} + \\ & W_{F275W,F814W_3} \frac{X - X_{fiducialGreen}}{X_{fiducialGreen} - X_{fiducialOrange}} \end{aligned} \quad (5.8)$$

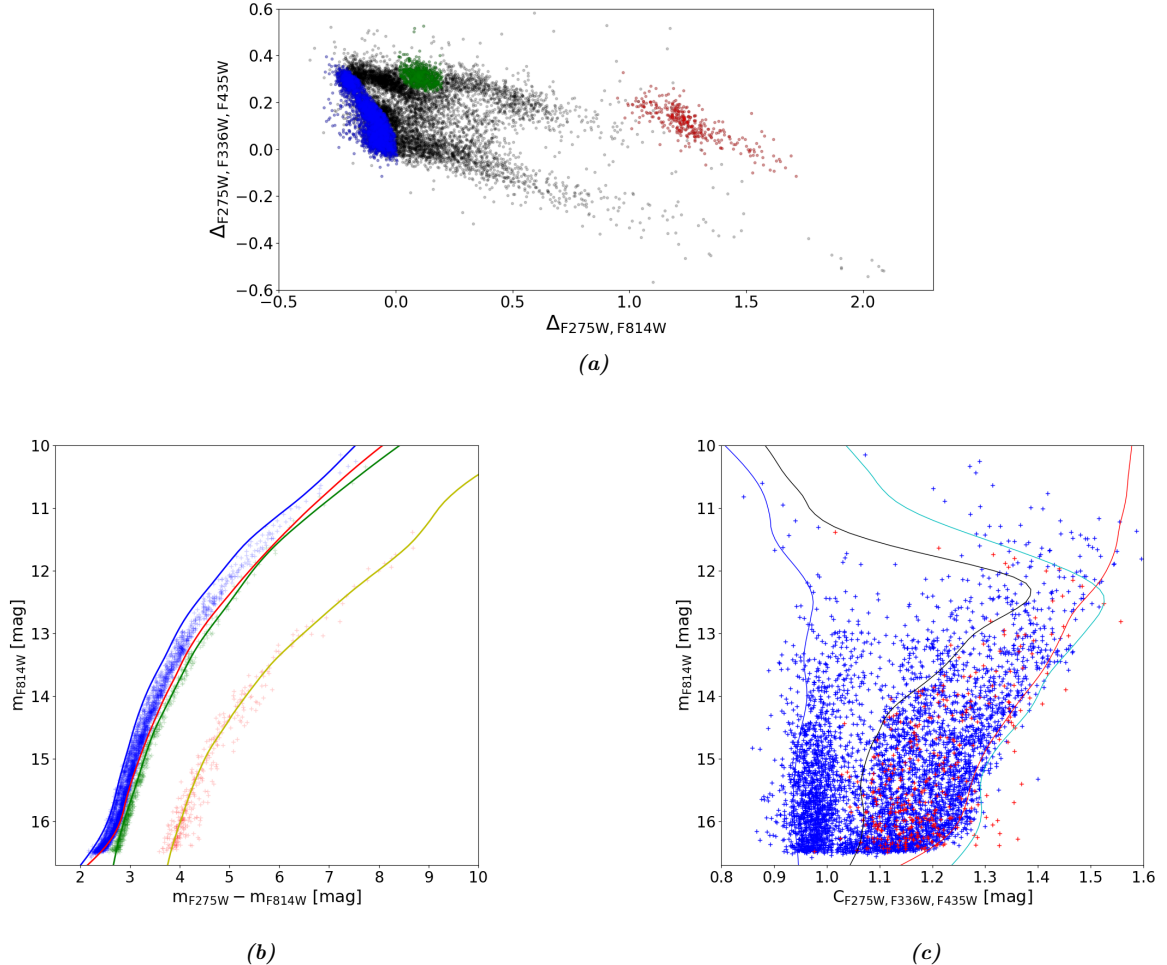


Figure 5.16: The Three Subsamples Used to Calculate the Chromosome Map. (a.) The chromosome map of ω Cen, color-coded with $[M/H]$ only for the stars in the three subsamples. (b.) The CMD of the subsamples with the fiducial lines for each. Blue and red are the 96th and 4th percentile for the poor population (blue crosses), green is the median line for the intermediate (green crosses), and yellow is the median line for the rich population (red crosses). (c.) The pseudo-CMD of the subsamples with blue crosses being the poor and intermediate population and red the rich population. Blue and red lines are the 96 % and 4 % enclosing lines for the blue crosses and black and cyan for the red crosses.

Which of these three $\Delta_{F275W, F814W_i}$ is used for each star depends on its relative position to the different fiducial lines, see Table 5.3 for details.

For the $\Delta_{F275W, F336W, F435W}$ value we calculate:

$$W_{F275W, F336W, F435W_1} = Y_{fiducialRed}(15.5 \text{ mag}) - Y_{fiducialBlue}(15.5 \text{ mag}) \quad (5.9)$$

$$W_{F275W, F336W, F435W_2} = Y_{fiducialRed}(15.5 \text{ mag}) - Y_{fiducialCyan}(15.5 \text{ mag}) \quad (5.10)$$

$$W_{F275W, F336W, F435W_3} = Y_{fiducialCyan}(15.5 \text{ mag}) - Y_{fiducialBlack}(15.5 \text{ mag}) \quad (5.11)$$

and then

$$\Delta_{F275W, F336W, F435W_1} = W_{F275W, F336W, F435W_1} \frac{Y_{fiducialRed} - Y}{Y_{fiducialRed} - Y_{fiducialBlue}} \quad (5.12)$$

$$\begin{aligned} \Delta_{F275W, F336W, F435W_2} &= W_{F275W, F336W, F435W_2} + \\ &W_{F275W, F336W, F435W_3} \frac{Y_{fiducialCyan} - Y}{Y_{fiducialCyan} - Y_{fiducialBlack}}. \end{aligned} \quad (5.13)$$

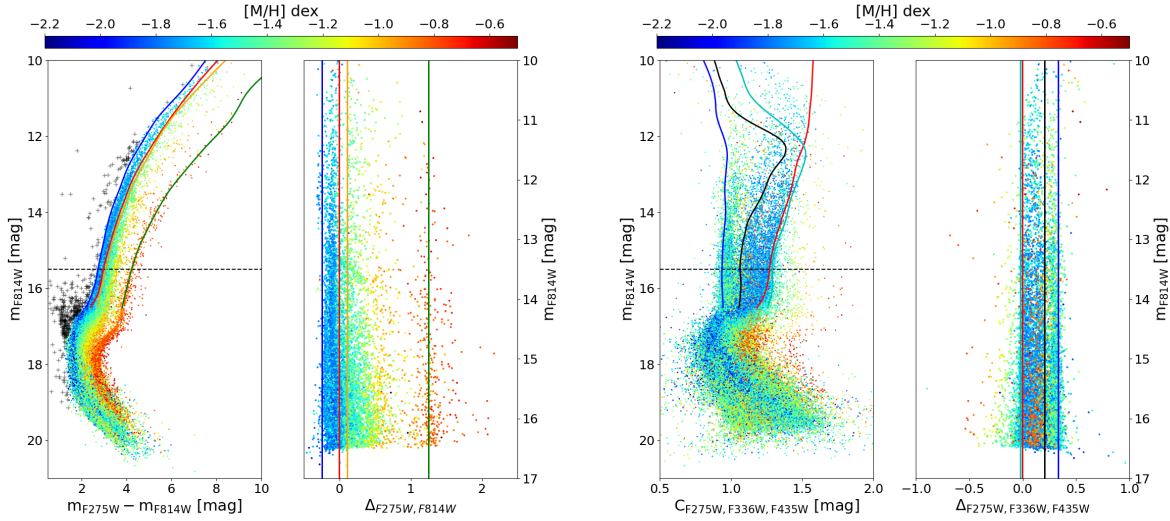


Figure 5.17: Final Fiducial Lines. Left is the CMD and on the right is the pseudo-CMD both color-coded with [M/H] and showing the fiducial lines for stars brighter than 16.3 mag. The black dashed line indicates the 15.5 mag. On the right of each subfigure is the verticalized CMD proving that the subsamples do follow these straight lines.

Depending on each metallicity each star gets assigned either $\Delta_{F275W,F336W,F435W_1}$ or $\Delta_{F275W,F336W,F435W_2}$. The condition is described in Table 5.3.

Finally, we color-coded the final chromosome map with all the components of the Gaussian Mixture model of the [M/H] distribution (Section 5.3.1) in Figure 5.18. All the components are at specific locations on the map depending on their [M/H], separating different subpopulations and showing the complexity of the clusters.

Table 5.3: Final Chromosome Map Values

Final chromosome Δ value	Δ_i value	Condition
$\Delta_{F275W,F814W} =$	$\Delta_{F275W,F814W_1}$	if $\Delta_{F275W,F814W_1} \leq 0$, right of the red fiducial line
	$\Delta_{F275W,F814W_2}$	if $\Delta_{F275W,F814W_1} > 0$ & $\Delta_{F275W,F814W_2} \leq W_{F275W,F814W_2}$, between red and orange fiducial line
	$\Delta_{F275W,F814W_3}$	if $\Delta_{F275W,F814W_3} > W_{F275W,F814W_2}$, right of the orange fiducial line
$\Delta_{F275W,F336W,F435W} =$	$\Delta_{F275W,F336W,F435W_1}$	if star does not belong to the most metal-rich peak (\neq index 7)
	$\Delta_{F275W,F336W,F435W_2}$	if star belongs to metal-rich peak (= index 7)

The metal-rich peak (index 7) is taken from the Gaussian Mixture model Table 5.2 in Section 5.3.1.

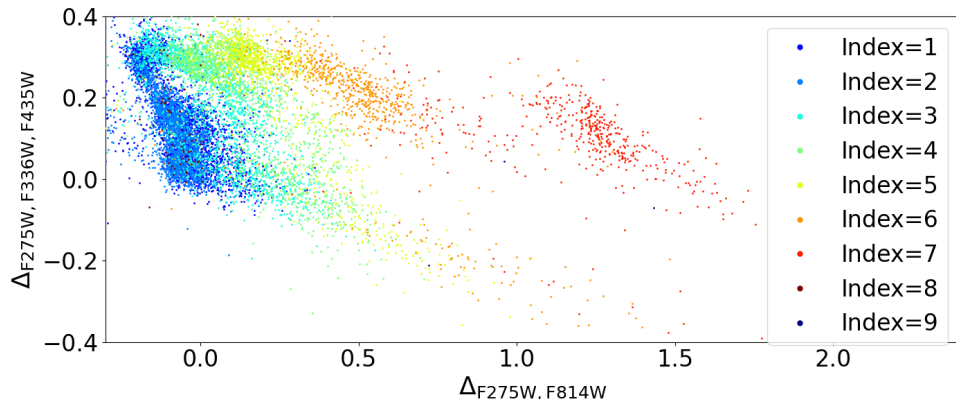


Figure 5.18: Chromosome Map Color-Coded with the Subgroups Identified in the Metallicity Distribution. We use the components of the Multi Gaussian Mixture Model used in Section 5.3.1 and color-coded the stars in the chromosome map with the component (index) they most likely belong to.

Take away points

- We analyze the metallicity distribution of 12,850 RGB stars in ω Cen.
- For stars with $m_{\text{F625W}} < 17$ mag the mean and median metallicities are -1.577 dex and -1.621 dex respectively.
- The spread in metallicity is large, reaching from -0.66 dex to -2.23 dex for 99.7 % of these bright stars.
- We identify multiple peaks in the metallicity distribution indicating different metallicity subgroups.
- We investigate the chromosome map and its dependencies with metallicity.
- The 2D spatial distribution of the [M/H] values shows a ring-like structure of more metal-rich stars.
- We find no gradient in [M/H] over our field of view in radial bins.
- The different populations seem to be well mixed and no strong gradient is visible in their radial profiles.

Chapter 6

OUTLOOK

This chapter includes preliminary work I carried out for the line-of-sight kinematics of ω Cen in Section 6.1, as well as summaries of follow-up work led by close collaborators using the oMEGACat dat. This chapter showcases the science made possible by the oMEGACat data set. It is not meant to present exact methodologies nor final results.

Summary

The new spectroscopic and astro-photometric catalogs for ω Cen provide us with a large amount of data allowing us to investigate various aspects of its formation history as well as its interaction with the Milky Way. We can study the kinematics of the cluster by investigating the overall rotation and individual substructures, down to revealing an IMBH. Further, ages and abundance are helping us to identify subpopulations and analyze their host environment and enrichment histories. In the future, dynamical models will further help us understand the mass distribution of ω Cen, the IMBH, and its formation history.

Chapter Contents:

6.1	Line-of-Sight Kinematics	111
6.1.1	Velocity Maps	113
6.1.2	Kinematic Analysis	113
6.2	Follow up Projects	114
6.2.1	Intermediate Mass Black Hole in ω Cen	114
6.2.2	Ages and Subpopulation Identification	116
6.2.3	Abundance Differences between the Subpopulations	117
6.2.4	Elemental Abundance Catalog for ω Cen	118
6.3	Future Projects	119
6.4	Conclusion	119
	Take away points	120

6.1 Line-of-Sight Kinematics

In Chapter 4 I presented the creation of a spectroscopic catalog for ω Cen and in Chapter 5 I combined that with the photometry from the new *HST* astrometric and photometric catalog (Häberle et al., 2024a). The combination of these catalogs allows us to have 3D

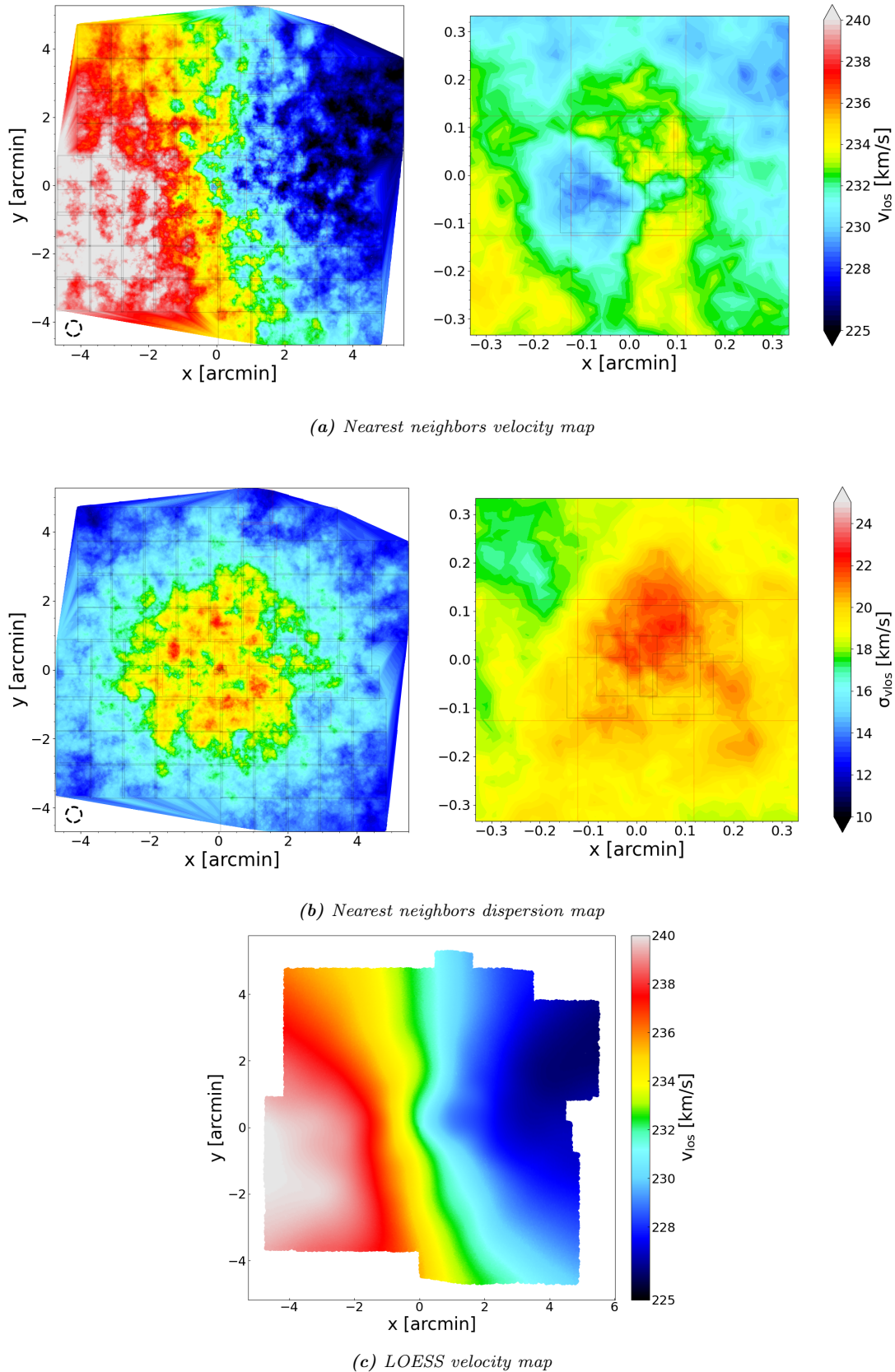


Figure 6.1: Line-of-Sight Velocity Maps. (a.)-(b.) The 300 nearest neighbors maps for the line-of-sight velocity and dispersion, the left panels show the whole field, and the right zoom into the central 20 arcsec where the counterrotation becomes visible (Pechetti et al., 2024). Overplotted are the contours of the individual pointings. (c.) The LOESS v_{los} map. The x -axis and y -axis show the distance to the center of the cluster for the right ascension (ΔRa) and declination (ΔDec)

velocities for hundreds of thousands of stars in the cluster and kinematic and dynamical studies using them will follow, see Section 6.3.

However, using only the line of sight velocities already gives us a lot of insights (e.g., Kamann et al., 2018; Pechetti et al., 2024). Using the new spectroscopic data set (see Chapter 4 and Nitschai et al. 2023) I have performed an initial analysis of the line-of-sight kinematics. Everything I present in this section are first tests and analyses and by no means the final results, but they showcase the amazing data we have and what can be done with them.

6.1.1 Velocity Maps

First, we can study the rotation of the cluster by creating velocity maps. To visually smooth the maps but keep enough details I followed a similar approach as in Pechetti et al. (2024) where the counter-rotation at the center was found. For that, I used 300 neighbors to calculate the mean (biweight_location) and standard deviation (biweight_scale) for the line of sight velocity (Beers et al., 1990, function implemented in ASTROPY), see Figure 6.1 panel (a.) and (b.). Since we use the same data at the very center as Pechetti et al. (2024), we can also see the counterrotation and a slightly offset dispersion peak, in the right panels of the Figure. The rotation and dispersion in the entire MUSE mosaic can be seen on the left, which as expected shows clear rotation with a slightly tilted axis and the dispersion decreasing towards the outer parts of the cluster.

In addition, I also used the locally weighted regression (LOESS) technique (Cappellari et al., 2013b), which determines the mean values in case of noisy data, see Figure 6.1 panel (c.). In that case, fewer substructures are visible and the rotation axis can be followed even better.

6.1.2 Kinematic Analysis

Using the data we also create rotation and dispersion profiles. I radially binned the stars in our data, with each bin consisting of a minimum of 100 stars, and covering a radial range of $\log(r/1'') > 0.15$. I then followed the method used in Kamann et al. (2018) and Pechetti et al. (2024), where a maximum likelihood approach (Pryor and Meylan, 1993) is used in combination with the Markov chain Monte Carlo (MCMC) algorithm emcee (Foreman-Mackey et al., 2013). I used 100 walkers with 500 steps each to derive the profiles shown in Figure 6.2. The rotation increases towards larger radii and the center has high uncertainties. In contrast, the dispersion increases toward the center (it might have a dip at radii of $\sim 20 - 40$ arcsec, but that disappears when one uses only the bright stars and can be caused by small discrepancies between the GTO and GO data sets) and it agrees within the scatter with the values from the globular cluster database in yellow (Holger Baumgardt et al., March 2023¹, data from Watkins et al. 2015b; Baumgardt 2017; Baumgardt and Hilker 2018; Kamann et al. 2018; Vasiliev and Baumgardt 2021). The position angle (PA) of the rotation shows the counter-rotation at the more central region while it is fixed for the outer parts, slightly tilting away from the north axis towards the east. Further, I used the LOESS results for the analysis with the python version of KINEMETRY² (Krajnović et al., 2006). KINEMETRY performs a harmonic expansion of 2-D kinematic moments along a set of best-fitting ellipses on the map. The result can

¹<https://people.smp.uq.edu.au/HolgerBaumgardt/globular/>

²<https://www.aip.de/en/members/davor-krajnovic/kinemetry/>

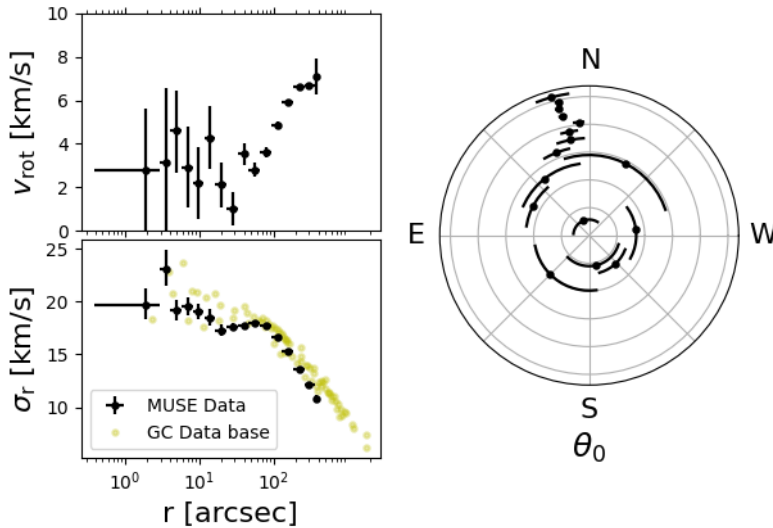


Figure 6.2: Kinematic Profiles. The top left panel shows the rotation of the cluster at each radial bin, with the systematic velocity removed. The bottom left panel shows the dispersion profile in black with the MUSE data and in yellow from the GC database (Holger Baumgardt et al., March 2023, <https://people.smp.uq.edu.au/HolgerBaumgardt/globular/>, data from Watkins et al. 2015b; Baumgardt 2017; Baumgardt and Hilker 2018; Kamann et al. 2018; Vasiliev and Baumgardt 2021) as a comparison. The right panel shows the PA of the rotation for each bin, where the counter-rotation becomes visible in the innermost bin.

be seen in Figure 6.3, we get a median positional angle of $\text{PA} = 103.18^\circ$ and a median systemic velocity of 233.25 km s^{-1} .

As mentioned before, these are the first investigations into the kinematics and further analysis is needed to verify and interpret the results. However, the clear rotation and a PA at $\sim 100^\circ$ is consistent with other studies (e.g van de Ven et al., 2006b; Kamann et al., 2018; Pechetti et al., 2024) and thanks to, the now bigger data set can be studied in greater detail.

6.2 Follow up Projects

The combined spectroscopic (Nitschai et al., 2023) and astro-photometric (Häberle et al., 2024a) catalog created for the oMEGACat project are already enabling a broad range of interesting science. Here I will mention a few of these projects that are in preparation.

6.2.1 Intermediate Mass Black Hole in ω Cen

The work summarized in the following paragraph is led by Maximilian Häberle (Häberle et al., 2024b).

As a massive star cluster and a stripped nucleus, ω Cen has long been suspected to host an intermediate-mass black hole (IMBH). Previous claims of a detection of an IMBH (Noyola et al., 2008, 2010; Baumgardt, 2017) have all been disputed due to their modeling methods and assumptions (Anderson and van der Marel, 2010; van der Marel and Anderson, 2010; Zocchi et al., 2019; Baumgardt et al., 2019a).

Using the oMEGACat proper motion catalog (Häberle et al., 2024a) we find new, strong evidence for an IMBH. We discovered 7 fast-moving stars in the inner 3 arcseconds

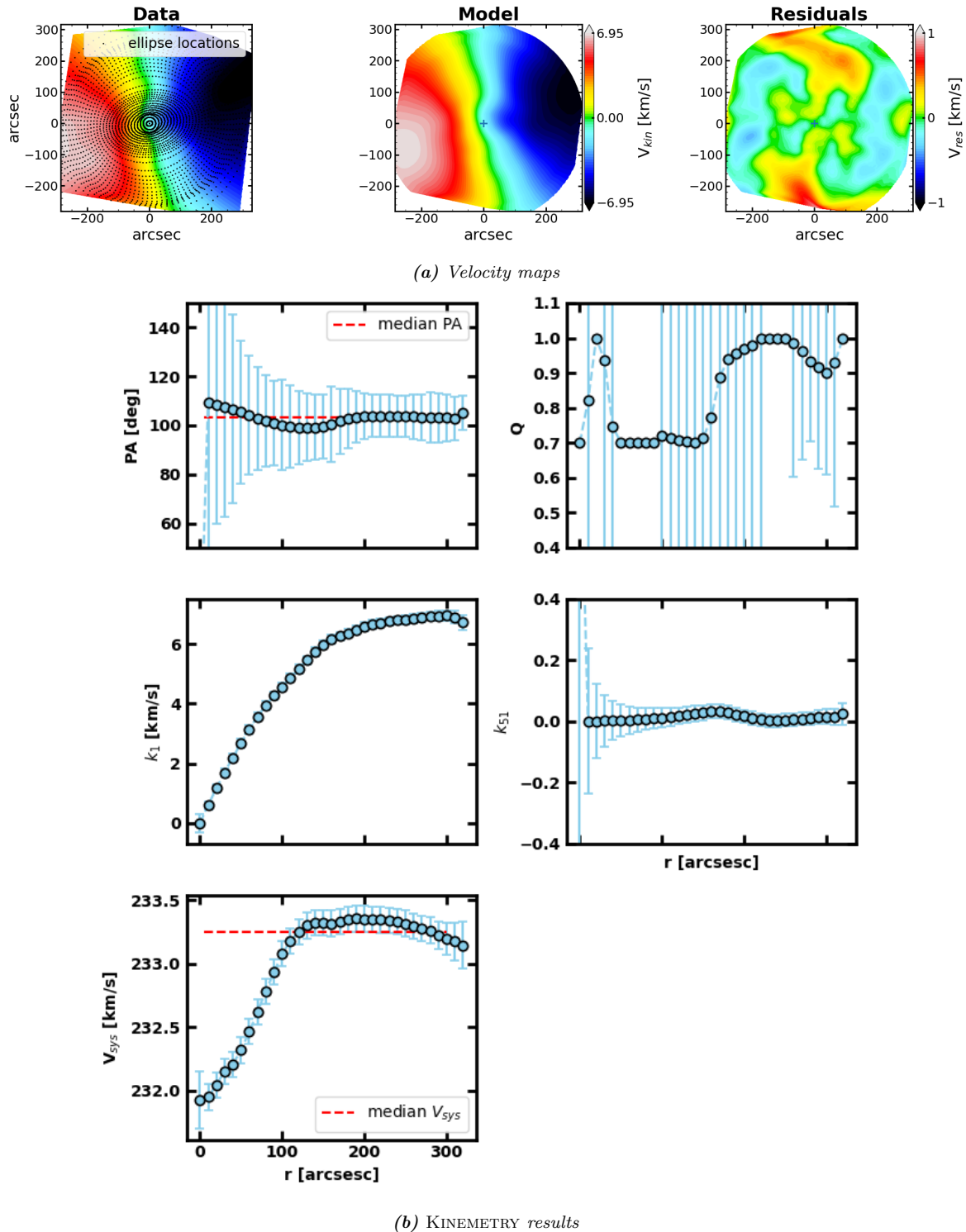


Figure 6.3: Kinemetry Results. (a) Shows the pure rotation velocity ($vel-v_{syst}$), from the data, the model, and their residuals from left to right. (b) The results from the KINEMETRY model, from top to bottom and left to right show the position angle (PA), axial ratio (Q), the coefficient of harmonic expansion k_1 (describes the amplitude of bulk motions), and the ratio between the coefficients k_5/k_1 (k_{51} , with k_5 describing the higher-order deviations from simple rotation and points to complex structures on the maps), and systemic velocity.

that have velocities well above the escape velocity of ω Cen, which can only be explained by IMBH with a minimum mass of $\sim 8,200 M_{\odot}$. N-body models provide us with an upper limit of $\sim 50,000 M_{\odot}$. This black hole is the nearest massive black hole and only the second one where we can observe the orbits of bound stars around it, similar to the S-stars in the Milky Way center (Gillessen et al., 2017).

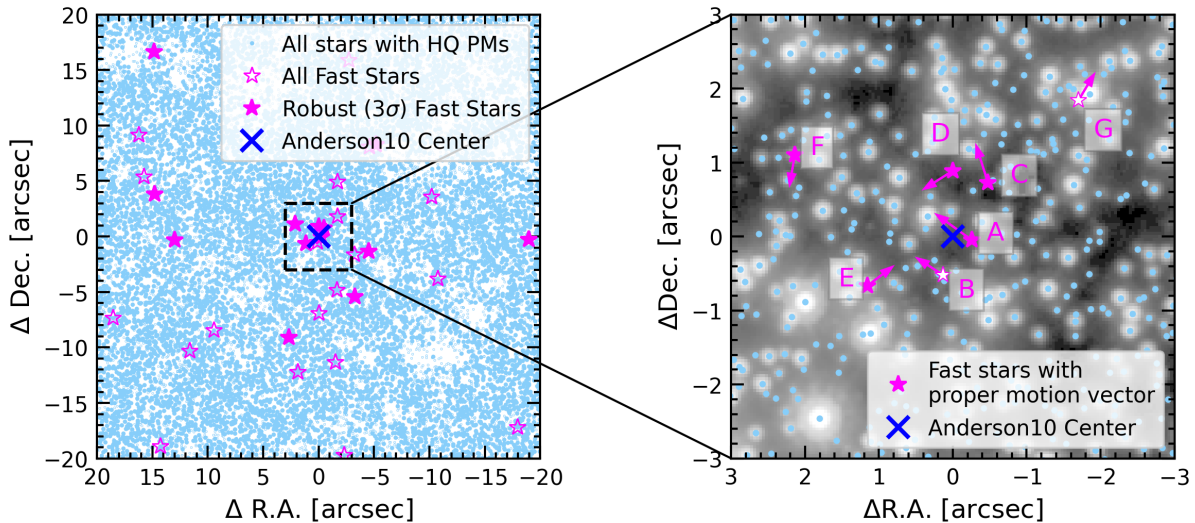


Figure 6.4: Fast Moving Stars in ω Cen. The left panel shows all stars detected in our new proper motion catalog within a $40'' \times 40''$ region around the Anderson and van der Marel (2010) center, with stars with velocities higher than the cluster escape velocity (62 km s^{-1}) marked in pink. Filled markers are for stars that are at least 3σ over the escape velocity. The right panel shows the stacked image of the innermost region of ω Cen in the WFC3/UVIS F606W filter. Stars in the new HST catalog are marked with a light blue dot and the fast-moving stars are shown in pink, together with their proper motion vector (arrows present the predicted stellar motion over 100 years).

Figure Credit: Maximilian Häberle

6.2.2 Ages and Subpopulation Identification

The project to combine the spectroscopic and photometric catalogs to measure accurate ages of individual stars and separate the multiple subpopulations, is led by Callie Clontz (Clontz et al., in prep.).

This project includes the generation of a new set of isochrones specifically tuned to the C+N+O vs. [Fe/H] relation seen in ω Cen. This allows for precise age estimates for individual stars. This study will clarify the age spread, star formation history, and age metallicity relation in the cluster, allowing us to better understand its formation, and assembly history and trace its interaction process with the Milky Way. In Figure 6.5 we show the age spread in different metallicity bins, which seems to increase with metallicity, reaching 1 Gyr in the highest metallicity bin.

Age information (as well as abundances) can be additionally combined with photometry and metallicities to help us parse subpopulations along the full CMD. In previous studies, this has only been possible above and below the MSTO. Our unprecedented data set allows us to parse subpopulations along the full CMD for the first time, giving us the ability to fit isochrones to the MSTO and SGB region. By doing this we hope to constrain the Helium and alpha abundances of each subpopulation. In Figure 6.6 preliminary subpopulations are shown in a CMD, with the mean metallicity value for each subpopulation

indicated. This result will further constrain the formation and evolution of the cluster and its progenitor host galaxy.

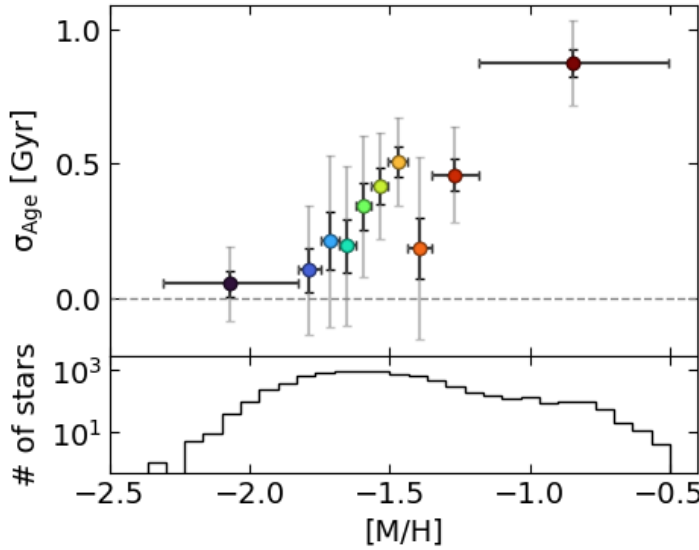


Figure 6.5: Age Spread in ω Cen.
The top panel shows the age spread in the cluster in different metallicity bins. We see an increasing spread with higher $[M/H]$ values. The bottom panel shows the metallicity histogram.

Figure Credit: Callie Clontz

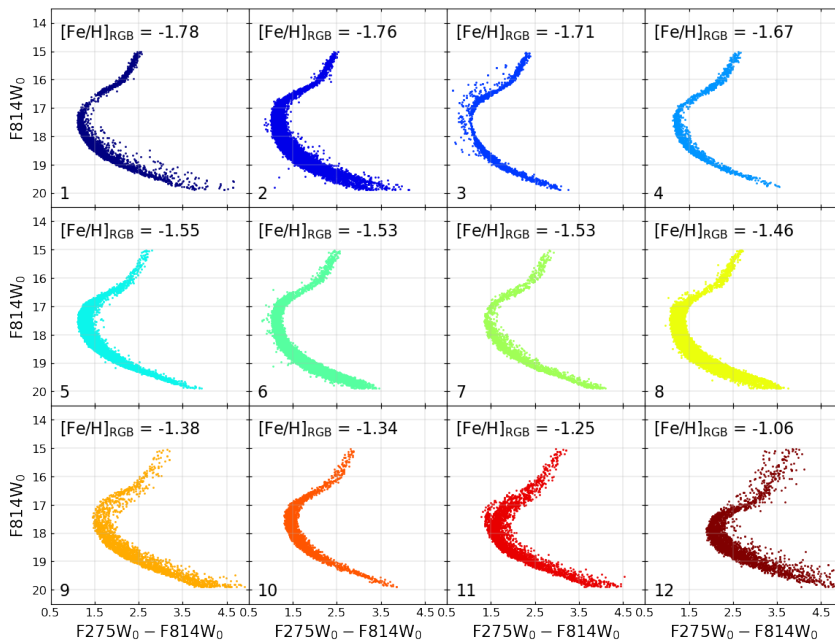


Figure 6.6: Subpopulations in ω Cen. This figure shows CMDs for different subpopulations colored by their cluster assignment, with the metal poorest in the left top corner going to the metal richest in the right bottom corner.

Figure Credit: Callie Clontz

6.2.3 Abundance Differences between the Subpopulations

The first work on abundances in the cluster is led by Simona Di Stefano (Master thesis project and Di Stefano et al., in prep).

Investigating different elemental abundances of the individual subpopulations is important to characterize the differences in enrichment histories between the populations and will eventually help to understand their formation scenarios.

This study is a qualitative analysis of the abundances of predefined subpopulations (in Section 6.2.2 see Figure 6.6). For this, the MUSE spectra of the same subpopulations and in the same magnitude range are stacked together, creating a higher SNR spectrum

for each metallicity and magnitude subgroup. The high-SNR stacked spectra have clearer absorption features than those in individual stellar spectra. Therefore, they are helpful for direct measurements of chemical abundances and the study of their variations between different subpopulations.

Figure 6.7 shows the stacked spectra of the brightest stars for all populations in the wavelength range of the magnesium triplet lines. The different colors represent the different metallicity subpopulations as shown in Figure 6.6 and the general trend is that the populations with higher metallicities exhibit deeper metal lines. This trend does not change in fainter magnitude subgroups of the same populations, confirming that there is no magnitude dependency in the line strength but a [M/H] dependency.

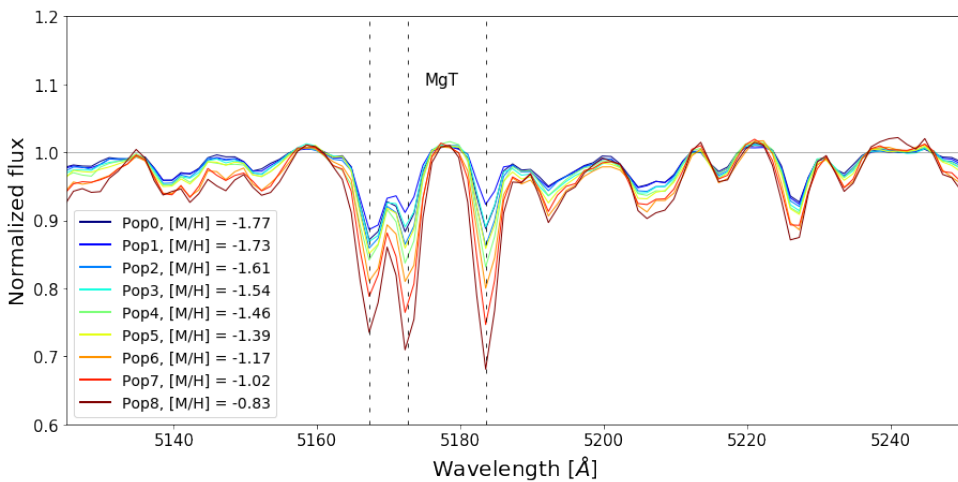


Figure 6.7: Stacked Spectra for Each Subpopulation. The figure shows the combined spectra of the brightest stars ($14.5 \text{ mag} \leq m_{F814W} \leq 15.5 \text{ mag}$) for the different subpopulations (see Section 6.2.2) around the Mg Triplet lines.

Figure Credit: Simona Di Stefano.

6.2.4 Elemental Abundance Catalog for ω Cen

Further work on providing abundances for ω Cen is led by Zixian Wang (Wang et al., in prep.).

Other than the abundance measurements on stacked spectra in Section 6.2.3, we will also measure abundances from individual stellar spectra. This is not only helpful in validating the subpopulation identification (Section 6.2.2) and stacked spectrum abundances (Section 6.2.3), but also in providing additional information to improve the above results. To create such an abundance catalog for ω Cen, the idea is to employ the machine learning model Data-Driven Payne (DD-Payne) and perform full-spectrum fitting for measuring stellar abundances. Detailed development of DD-Payne and its application on MUSE spectra is described in detail in Ting et al. (2017a); Xiang et al. (2019) and Wang et al. (2022). In short, DD-Payne is a neural network model that derives ~ 20 stellar labels from 6 million LAMOST spectra. Some of the [X/Fe] abundances are for C, N, O, Na, Mg, Al, Si, Ca, Ti, Cr, Mn, Fe, Co, Ni and it was trained using spectra from LAMOST DR5 and stellar labels from GALAH DR2 (Buder et al., 2018) and APOGEE-Payne (Ting et al., 2017b).

As for fitting MUSE spectra of ω Cen, we first investigated the reliability of chemical abundances measured by DD-Payne. Figure 6.8 is an example, where it demonstrates the

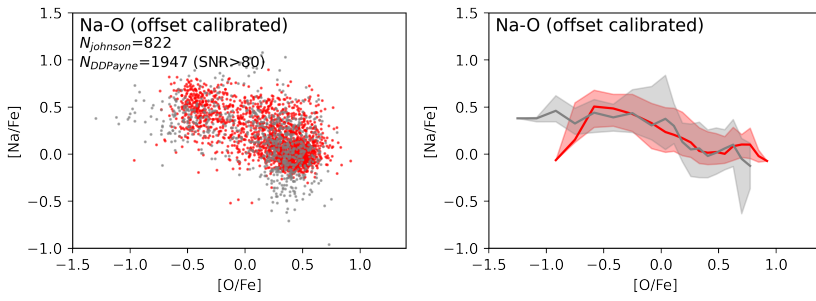


Figure 6.8: Anticorrelation between Na vs O. The plot shows the relation between $[Na/Fe]$ and $[O/Fe]$ for ω Cen, derived from our MUSE Spectra (red) and compared to [Johnson and Pilachowski \(2010\)](#) (gray).

Figure Credit: Zixian Wang

$[Na/Fe]$ - $[O/Fe]$ relation that was also identified from previous studies on other globular clusters. After abundance offsets correction between different datasets, this figure indicates that $[Na/Fe]$ and $[O/Fe]$ can be reasonably recovered by DD-Payne and the trend is consistent with that from [Johnson and Pilachowski \(2010\)](#).

6.3 Future Projects

The goals of future projects include combining new data sets and creating dynamical models for the cluster, constraining for example the overall mass distributions, mass-to-light ratio, and the overall kinematic properties. Since we can infer information for individual stars in ω Cen, we aim to make a detailed dynamical model, including the age, chemical composition, and subpopulations of the stars in the cluster. In addition, we will examine the dynamics and kinematics of individual subpopulations to check if we can find differences that might hint at different formation scenarios. These models will give us more insights into the formation history as well as further constrain the properties of the central IMBH and the amount of stellar mass black holes in the cluster.

For the verification of the existence of an IMBH we will acquire *James Webb Space Telescope* spectroscopic data and have proposed to also obtain even deeper MUSE NFM data for the fast-moving stars at the center found in [Häberle et al. \(2024b\)](#) (see Section 6.2.1). These observations will give us reliable line-of-sight velocities since these stars are too faint, unreliable, or do not exist in our current MUSE data. That will give us three-dimensional velocities for these stars that allow us to constrain even better the motion of the stars, and the mass of the black hole, and do precise dynamical models for them.

Detailed chemistry and kinematics can further tighten the connection of ω Cen with known stellar streams or merger events. Ideally, we would want to identify stars that belonged to its progenitor galaxy to constrain its formation and distribution history. Further projects in preparation include the investigation of the HB stars in ω Cen, finding binary stars, detecting microlensing effects, and even trying to find a radiation signal from the IMBH using instruments such as the Atacama Large Millimeter/Submillimeter Array.

6.4 Conclusion

In summary, the data set created for the oMEGACat project provides a vast amount of information for stars within the half-light radius of ω Cen. The ages and abundances of individual stars will allow us to identify and separate the multiple subpopulations and constrain their formation history. Studying the kinematics can provide further insight

into the formation scenarios and help constrain the mass of the IMBH at the very center of the cluster. Dynamical models are another key part of verifying the presence of an IMBH and they allow us to measure the mass-to-light ratio and mass distribution of the cluster. Dynamical differences in the subpopulations can also hint at different formation scenarios. All of these studies help further disentangle the role of ω Cen and its progenitor galaxy in the assembly history of the Milky Way.

Take away points

- We have an extensive amount of information in the spectroscopic and astrometric/photometric catalogs.
- Detailed kinematics of individual stars have given us evidence for an IMBH.
- Many more studies based on this data set are in preparation: subpopulations, ages, and abundances.
- The next big project will be dynamical models for the cluster.
- We aim to disentangle the formation history of the cluster and the merger with the Milky Way.

Chapter 7

CONCLUSION

In this thesis, I have presented my work on the Galactic disk dynamics and spectroscopic analysis of ω Centauri. Thanks to *Gaia* and other surveys of the Milky Way we can study the Galaxy in great detail and work on disentangling its formation history.

In Chapter 3 I presented a dynamical Jeans model of the Milky Way disk described in Nitschais et al. (2021). The underlying data were based on *Gaia* EDR3, combined with the Hogg et al. (2019) data set, which were combined APOGEE, *Gaia* DR2, 2MASS and WISE data with precise spectrophotometric distance estimates and I made use of the JAM_{sph} code (Cappellari, 2020). This allowed me to probe an area in the range of $5.0 \leq R \leq 19.5$ kpc and $-2.5 \leq z \leq 2.5$ kpc.

The best fit value for the dark matter slope is $\alpha_{\text{DM}} = -1.602 \pm 0.015_{\text{stat}} \pm 0.079_{\text{syst}}$ indicating that a steeper slope than NFW is needed, a circular velocity of $v_{\text{circ}} = (234.7 \pm 0.3_{\text{stat}} \pm 1.7_{\text{syst}})$ km s⁻¹ with a mild decline towards larger radii and total density at the solar radius is $\rho_{\text{tot}}(R_{\odot}) = (0.0672 \pm 0.0006_{\text{stat}} \pm 0.0015_{\text{syst}})$ M_⊙ pc⁻³. All of these values are consistent within the uncertainties with previous works (e.g., McKee et al., 2015; Portail et al., 2017; Cole and Binney, 2017; Eilers et al., 2019; Nitschais et al., 2020a). To test how nonaxisymmetries of the gravitational potential – such as spiral arms, the warp, the Galactic bar, or mergers – change the result, I divided the data into four sectors and remodeled each of them, the results provided systematic uncertainties due to the axisymmetry assumption of the model. Finally, I investigated how a flared disk affects our model and found that it provides a similarly good match to the data. However, a more thorough analysis in the future is needed to better constrain the flaring of the disk given its dynamical properties.

This showed that even a model with many incomplete assumptions can describe the main kinematics of the Galaxy and constrain the mass distribution. Confirming that our understanding of galaxy dynamics and the frameworks we have are correct, even in the case of the Milky Way where we have incredible and detailed amounts of data.

In Chapter 4 I presented an extensive new spectroscopic catalog of stars obtained with 87 new MUSE pointings plus the already existing 10 WFM and 6 NFM GTO pointings for the globular cluster ω Cen, covering out to the half-light radius published in Nitschais et al. (2023). ω Cen has long been suspected to be the stripped nucleus of a dwarf galaxy that fell into the Milky Way a long time ago. Specifically in the last years, it has been associated with the *Gaia*-Enceladus merger (e.g., Majewski et al., 2012; Ibata et al., 2019; Massari et al., 2019; Limberg et al., 2022) which is the last significant merger the Milky Way experienced. This catalog is the largest spectroscopic catalog for the cluster so far and is part of the oMEGACat project, which also provides astrometry and photometry

for millions of stars within the half-light radius.

I described the data and the analysis steps used to create the catalog in detail. First, I reduced the data and extracted individual spectra of stars using PAMELMUSE (Kamann et al., 2013). Then, I used the spectral fitting routine SPEXXY to measure the LOS velocities, effective temperatures, and metallicities of these stars. I performed multiple tests exploiting a large number of repeated measurements to verify the results. Several parameters to quantify the reliability of the results are provided and I included several necessary corrections to the measurements. In the end, I was left with 342,797 stars after all of the analysis steps without any quality cuts. However, for most use cases I suggested several quality cuts: $\text{SNR} > 10$, membership probability $P_M > 95\%$, magnitude accuracy $\geq 0.6 \text{ mag}$, distance to the IFU edge ≥ 5 and Reliability $R \geq 0.5$. Thus, 156,871 stars meet all these criteria. Finally, I did a first analysis of the metallicity distribution comparing it to previous works and found that they are consistent with our findings and calculated the median systematic LOS to be $v_{\text{los}} = (232.99 \pm 0.06) \text{ km s}^{-1}$.

In addition, the new *HST* catalog with proper motions and photometry for millions of stars covering most of the MUSE data was created (Häberle et al., 2024a). I used the combined photometric and spectroscopic catalog in Chapter 5 to present a detailed study of the metallicity distribution of 12,850 RGB stars in ω Cen (submitted as Nitschai et al., 2024). I found a mean metallicity of -1.577 dex (median of -1.621 dex) reaching from -0.66 dex to -2.23 dex for 99.7 % of the bright stars. Further, I identified multiple peaks in the metallicity distribution indicating different metallicity subgroups.

Moreover, I investigated the chromosome map and its dependencies with metallicity. I looked in detail at the most metal-poor group and identified three populations that show a similar spread in $[\text{M}/\text{H}] \sim 0.1 \text{ dex}$ while the $[\text{M}/\text{H}]$ increases for higher $\Delta_{\text{F275W}, \text{F336W}, \text{F435W}}$ which corresponds to enrichment in Na and Al. I also studied the 2D spatial distribution of the $[\text{M}/\text{H}]$ values and created metallicity maps showing a ring-like structure with higher values, while inside and outside the $[\text{M}/\text{H}]$ values decrease, possibly revealing an accreted population that has not been well mixed. Finally, I checked for metallicity gradients and spatial differences in radial bins for different subgroups of stars. There I found no gradient in $[\text{M}/\text{H}]$ over our field of view. Overall, the different $[\text{M}/\text{H}]$ populations seem to be well mixed and no strong gradient is visible in their radial profiles. However, more information on the abundance might help better separate them and further investigate their differences. In addition, the different sub-populations may be well mixed spatially, but their kinematics may be used to separate them, as it takes longer to erase the stars' memory of their original orbits.

Finally in Chapter 6 I showed preliminary results of ongoing projects that showcase the strength of our combined dataset. Combining both the astrometric and spectroscopic catalogs for ω Cen allows us to measure the ages of the stars and identify the subpopulations over the whole magnitude range of the cluster using photometry and metallicity information (Clontz et al., in prep.). Moreover, using the spectroscopic data we can also measure individual abundances by combining spectra of the same population and directly measuring the absorption lines of different elements (Di Stefano et al., in prep.) or use a machine learning model to determine abundances for individual spectra (Wang et al., in prep), which will further constrain the multiple populations and their formation scenario. Combining the information on the stellar populations and kinematics of a large number of stars in ω Cen will provide a clear picture of its formation history.

In summary, the data set created in the oMEGACat project provides us with a massive amount of information for the cluster. Ages and abundances for individual stars will allow

the identification of subpopulations and put constraints on the formation history of the cluster. Studying the kinematics is the first step before doing a dynamical model which will help constrain the IMBH at the center of the cluster, the mass-to-light ratio, and the dynamical differences in the subpopulations caused by different formation scenarios. All of these studies help further tighten ω Cen’s place as a stripped nucleus and part of the last big merger event of the Milky Way.

To summarize in this thesis, I used a very large data set to test our understanding of the galaxy dynamics and constrain the mass distribution and circular velocity of the Milky Way. In addition, I investigated ω Centauri, the stripped nucleus of the last significant big merger the Galaxy experienced, and provided an extensive spectroscopic catalog for stars within its half-light radius. Based on that and a new photometric catalog I further analyzed the subpopulations on the RGB and the broad metallicity distribution. Finally, I showed preliminary results in our endeavor to understand the cluster’s formation history and tie it to the assembly history of the Milky Way.

Data and Software Acknowledgements

In each chapter, the data and most important software packages are described and referenced therein. Here I acknowledge the facilities directly used in the thesis and provide a list of all software packages I made use of.

Data

This work has made use of data from the European Space Agency (ESA) mission *Gaia* (<https://www.cosmos.esa.int/gaia>, Gaia Collaboration et al., 2016), processed by the *Gaia* Data Processing and Analysis Consortium (DPAC, <https://www.cosmos.esa.int/web/gaia/dpac/consortium>). Funding for the DPAC has been provided by national institutions, in particular, the institutions participating in the *Gaia* Multilateral Agreement. Further, the work is based on observations collected at the European Southern Observatory under ESO program 105.20CG.001 and GTO with program IDs: 094.D-0142, 095.D-0629, 096.D-0175, 097.D-0295, 098.D-0148, 099.D-0019, 0100.D-0161, 0101.D-0268, 0102.D-0270, 0103.D-0204, 0104.D-0257, 105.20CR, and 109.23DV. Lastly, it is based on observations made with the NASA/ESA Hubble Space Telescope, obtained from the data archive at the Space Telescope Science Institute (STScI). STScI is operated by the Association of Universities for Research in Astronomy, Inc. under NASA contract NAS 5-26555. This research made use of NASA's Astrophysics Data System.

Facilities: *Gaia*, VLT Yepun (MUSE), *HST* (ACS/WFC, WFC3/UVIS),

Software

Python packages: ASTROPY (Astropy Collaboration et al., 2013, 2018, 2022), CLUMPY (Kimmig et al., 2015), EMCEE Foreman-Mackey et al. (2013), JAMPY (Cappellari, 2008, 2020), KINEMETRY (Krajnović et al., 2006), LOESS (Cappellari et al., 2013b), MATPLOTLIB (Hunter, 2007; Caswell et al., 2023), MGEFIT (Cappellari, 2002), NUMPY (Harris et al., 2020), PANDAS (Wes McKinney, 2010; The pandas development team, 2023), PLOTBIN (<https://pypi.org/project/plotbin/>), SCIKIT-LEARN (Pedregosa et al., 2011), SCIPY (Virtanen et al., 2020), SPEXXY <https://github.com/thusser/spexxy> (Husser et al., 2016), VORBIN (Cappellari and Copin, 2003)

Other: PAMPELMUSE (Kamann et al., 2013), MUSE pipeline v2.8.3 (Weilbacher et al., 2016, 2020).

Acknowledgements

Words cannot express my gratitude to my supervisor Dr. Nadine Neumayer for her time, feedback, and support during the entirety of my studies. I am really happy that I had you as a supervisor! My Ph.D. project could not have been possible without Prof. Dr. Anil Seth, who is one of the key members of our collaboration. To the biweekly meeting group, with Nadine, Anil, Max, and Callie, I am very grateful for your feedback, your help, and the useful discussions on how to move forward in the overall project. I am extremely thankful to the whole Collaboration, specifically Dr. Sebastian Kamann and Dr. Tim-Oliver Husser, for their help and support with my questions during the data reduction and analysis phase.

Further, I am deeply indebted to my thesis committee, Prof. Dr. Hans-Walter Rix and Prof. Dr. ir. Saskia Hekker, who took the time to meet regularly during the four years and give helpful feedback and counsel. I also want to thank the referees (Dr. Nadine Neumayer and Prof. Dr. Michela Mapelli) and the examiners (Prof. Dr. Hans-Walter Rix and Prof. Dr. Luca Amendola) for taking the time to read my work.

Thanks should also go to IMPRS which organizes and supports the Ph.D. program, but also allows for some fun activities and social events that are equally important. Many thanks, to my whole IMPRS generation for the fun times and the feeling that there are always people in the same situation who can help each other. To the Galactic Nuclei Research Group thank you so much for the super friendly and collaborative atmosphere we always have, I cannot think of a better Group. A big thank you also to the proofreaders of the thesis: Ari, Molly, Max, Callie, and Eric, and the feedback and input from Zixian (Purmortal) and Simona on the outlook chapter.

To all my friends who listened to my problems and encouraged me, thank you very much! It was immensely important to have you. No words will ever express all the support and love I get from Tim, thank you for being there! Lastly, to my family, nothing would have been possible without your support and encouragement. Thank you for believing in me and supporting me in whatever I do.

List of Publications

A list of all the submitted or accepted publications I am an author of. The thesis is based on the first-author publications 1, 2 and 3, while the two publications as co-author are mentioned in the thesis.

First Author Publications

1. M. S. Nitschai, N. Neumayer, M. Häberle, C. Clontz, A. C. Seth, A. P. Milone, M. Alfaro-Cuello, A. Bellini, S. Dreizler, T. O. Feldmeier-Krause, Husser, N. Kacharov, S. Kamann, A., M. Latour, M. Libralato, G. van de Ven, K. Voggel, and Z. Wang. oMEGACat III. Multi-band photometry and metallicities reveal spatially well-mixed populations within ω Centauri's half-light radius. *submitted to ApJ*, 2024
2. M. S. Nitschai, N. Neumayer, C. Clontz, M. Häberle, A. C. Seth, T. O. Husser, S. Kamann, M. Alfaro-Cuello, N. Kacharov, A. Bellini, A. Dotter, S. Dreizler, A. Feldmeier-Krause, M. Latour, M. Libralato, A. P. Milone, R. Pechetti, G. van de Ven, K. Voggel, and D. R. Weisz. oMEGACat. I. MUSE Spectroscopy of 300,000 Stars within the Half-light Radius of ω Centauri. *ApJ*, 958(1):8, Nov. 2023. doi: [10.3847/1538-4357/acf5db](https://doi.org/10.3847/1538-4357/acf5db)
3. M. S. Nitschai, A.-C. Eilers, N. Neumayer, M. Cappellari, and H.-W. Rix. Dynamical Model of the Milky Way Using APOGEE and Gaia Data. *ApJ*, 916(2):112, Aug. 2021. doi: [10.3847/1538-4357/ac04b5](https://doi.org/10.3847/1538-4357/ac04b5)
4. M. S. Nitschai, M. Cappellari, and N. Neumayer. First Gaia dynamical model of the Milky Way disc with six phase space coordinates: a test for galaxy dynamics. *MNRAS*, 494(4):6001–6011, Apr. 2020a. doi: [10.1093/mnras/staa1128](https://doi.org/10.1093/mnras/staa1128)
5. M. S. Nitschai, N. Neumayer, and A. Feldmeier-Krause. Three-dimensional Analysis of the Minispiral at the Galactic Center: Orbital Parameters, Periods, and the Mass of the Black Hole. *ApJ*, 896(1):68, June 2020b. doi: [10.3847/1538-4357/ab8ea8](https://doi.org/10.3847/1538-4357/ab8ea8)

Publications as Contributing Author

- M. Häberle, N. Neumayer, A. Bellini, M. Libralato, C. Clontz, A. C. Seth, M. S. Nitschai, S. Kamann, M. Alfaro-Cuello, J. Anderson, S. Dreizler, A. Feldmeier-Krause, N. Kacharov, M. Latour, A. Milone, R. Pechetti, G. van de Ven, and

K. Voggel. oMEGACat II – Photometry and proper motions for 1.4 million stars in Omega Centauri and its rotation in the plane of the sky. *arXiv e-prints*, art. arXiv:2404.03722, Apr. 2024a. URL <https://arxiv.org/abs/2404.03722>

- M. Häberle, N. Neumayer, A. Seth, A. Bellini, M. Libralato, H. Baumgardt, M. Whitaker, A. Dumont, M. Alfaro-Cuello, A. J., C. Clontz, K. N., S. Kamann, A. Feldmeier-Krause, A. P. Milone, M. S. Nitschai, R. Pechetti, and G. van de Ven. Fast-moving stars around an intermediate-mass black hole in ω Centauri. *under review*, 2024b

Bibliography

B. Abolfathi, D. S. Aguado, G. Aguilar, C. Allende Prieto, A. Almeida, T. T. Ananna, F. Anders, S. F. Anderson, B. H. Andrews, B. Anguiano, A. Aragón-Salamanca, M. Argudo-Fernández, E. Armengaud, M. Ata, E. Aubourg, V. Avila-Reese, C. Badenes, S. Bailey, C. Balland, K. A. Barger, J. Barrera-Ballesteros, C. Bartosz, F. Bastien, D. Bates, F. Baumgarten, J. Bautista, R. Beaton, T. C. Beers, F. Belfiore, C. F. Bender, M. Bernardi, M. A. Bershadsky, F. Beutler, J. C. Bird, D. Bizyaev, G. A. Blanc, M. R. Blanton, M. Blomqvist, A. S. Bolton, M. Boquien, J. Borissova, J. Bovy, C. A. Bradna Diaz, W. N. Brandt, J. Brinkmann, J. R. Brownstein, K. Bundy, A. J. Burgasser, E. Burtin, N. G. Busca, C. I. Cañas, M. Cano-Díaz, M. Cappellari, R. Carrera, A. R. Casey, B. Cervantes Sodi, Y. Chen, B. Cherinka, C. Chiappini, P. D. Choi, D. Chojnowski, C.-H. Chuang, H. Chung, N. Clerc, R. E. Cohen, J. M. Comerford, J. Comparat, J. Correa do Nascimento, L. da Costa, M.-C. Cousinou, K. Covey, J. D. Crane, I. Cruz-Gonzalez, K. Cunha, G. da Silva Ilha, G. J. Damke, J. Darling, J. Davidson, James W., K. Dawson, M. A. C. de Icaza Lizaola, A. de la Macorra, S. de la Torre, N. De Lee, V. de Sainte Agathe, A. Deconto Machado, F. Dell'Agli, T. Delubac, A. M. Diamond-Stanic, J. Donor, J. J. Downes, N. Drory, H. du Mas des Bourboux, C. J. Duckworth, T. Dwelly, J. Dyer, G. Ebelke, A. Davis Eigenbrot, D. J. Eisenstein, Y. P. Elsworth, E. Emsellem, M. Eracleous, G. Erfanianfar, S. Escoffier, X. Fan, E. Fernández Alvar, J. G. Fernandez-Trincado, R. Fernand o Cirolini, D. Feuillet, A. Finoguenov, S. W. Fleming, A. Font-Ribera, G. Freischlad, P. Frinchaboy, H. Fu, Y. Gómez Maqueo Chew, L. Galbany, A. E. García Pérez, R. Garcia-Dias, D. A. García-Hernández, L. A. Garma Oehmichen, P. Gaulme, J. Gelfand, H. Gil-Marín, B. A. Gillespie, D. Goddard, J. I. González Hernández, V. Gonzalez-Perez, K. Grabowski, P. J. Green, C. J. Grier, A. Gueguen, H. Guo, J. Guy, A. Hagen, P. Hall, P. Harding, S. Hasselquist, S. Hawley, C. R. Hayes, F. Hearty, S. Hekker, J. Hernández, H. Hernandez Toledo, D. W. Hogg, K. Holley-Bockelmann, J. A. Holtzman, J. Hou, B.-C. Hsieh, J. A. S. Hunt, T. A. Hutchinson, H. S. Hwang, C. E. Jimenez Angel, J. A. Johnson, A. Jones, H. Jönsson, E. Jullo, F. S. Khan, K. Kinemuchi, D. Kirkby, I. Kirkpatrick, Charles C., F.-S. Kitaura, G. R. Knapp, J.-P. Kneib, J. A. Kollmeier, I. Lacerna, R. R. Lane, D. Lang, D. R. Law, J.-M. Le Goff, Y.-B. Lee, H. Li, C. Li, J. Lian, Y. Liang, M. Lima, L. Lin, D. Long, S. Lucatello, B. Lundgren, J. T. Mackereth, C. L. MacLeod, S. Mahadevan, M. A. G. Maia, S. Majewski, A. Manchado, C. Maraston, V. Mariappan, R. Marques-Chaves, T. Masseron, K. L. Masters, R. M. McDermid, I. D. McGreer, M. Melendez, S. Meneses-Goytia, A. Merloni, M. R. Merrifield, S. Meszaros, A. Meza, I. Minchev, D. Minniti, E.-M. Mueller, F. Muller-Sánchez, D. Muna, R. R. Muñoz, A. D. Myers, P. Nair, K. Nand ra, M. Ness, J. A.

Newman, R. C. Nichol, D. L. Nidever, C. Nitschelm, P. Noterdaeme, J. O'Connell, R. J. Oelkers, A. Oravetz, D. Oravetz, E. A. Ortíz, Y. Osorio, Z. Pace, N. Padilla, N. Palanque-Delabrouille, P. A. Palicio, H.-A. Pan, K. Pan, T. Parikh, I. Pâris, C. Park, S. Peirani, M. Pellejero-Ibanez, S. Penny, W. J. Percival, I. Perez-Fournon, P. Petitjean, M. M. Pieri, M. Pinsonneault, A. Pisani, F. Prada, A. Prakash, A. B. d. A. Queiroz, M. J. Raddick, A. Raichoor, S. Barboza Rembold, H. Richstein, R. A. Riffel, R. Riffel, H.-W. Rix, A. C. Robin, S. Rodríguez Torres, C. Román-Zúñiga, A. J. Ross, G. Rossi, J. Ruan, R. Ruggeri, J. Ruiz, M. Salvato, A. G. Sánchez, S. F. Sánchez, J. Sanchez Almeida, J. R. Sánchez-Gallego, F. A. Santana Rojas, B. X. Santiago, R. P. Schiavon, J. S. Schimoia, E. Schlafly, D. Schlegel, D. P. Schneider, W. J. Schuster, A. Schwope, H.-J. Seo, A. Serenelli, S. Shen, Y. Shen, M. Shetrone, M. Shull, V. Silva Aguirre, J. D. Simon, M. Skrutskie, A. Slosar, R. Smethurst, V. Smith, J. Sobeck, G. Somers, B. J. Souter, D. Souto, A. Spindler, D. V. Stark, K. Stassun, M. Steinmetz, D. Stello, T. Storchi-Bergmann, A. Streblyanska, G. S. Stringfellow, G. Suárez, J. Sun, L. Szigeti, M. Taghizadeh-Popp, M. S. Talbot, B. Tang, C. Tao, J. Tayar, M. Tembe, J. Teske, A. R. Thakar, D. Thomas, P. Tissera, R. Tojeiro, C. Tremonti, N. W. Troup, M. Urry, O. Valenzuela, R. van den Bosch, J. Vargas-González, M. Vargas-Magaña, J. A. Vazquez, S. Villanova, N. Vogt, D. Wake, Y. Wang, B. A. Weaver, A.-M. Weijmans, D. H. Weinberg, K. B. Westfall, D. G. Whelan, E. Wilcots, V. Wild, R. A. Williams, J. Wilson, W. M. Wood-Vasey, D. Wylezalek, T. Xiao, R. Yan, M. Yang, J. E. Ybarra, C. Yèche, N. Zakamska, O. Zamora, P. Zarrouk, G. Zasowski, K. Zhang, C. Zhao, G.-B. Zhao, Z. Zheng, Z. Zheng, Z.-M. Zhou, G. Zhu, J. C. Zinn, and H. Zou. The Fourteenth Data Release of the Sloan Digital Sky Survey: First Spectroscopic Data from the Extended Baryon Oscillation Spectroscopic Survey and from the Second Phase of the Apache Point Observatory Galactic Evolution Experiment. *ApJS*, 235(2): 42, Apr. 2018. doi: [10.3847/1538-4365/aa9e8a](https://doi.org/10.3847/1538-4365/aa9e8a).

A. Adamo, L. D. Bradley, E. Vanzella, A. Claeysens, B. Welch, J. M. Diego, G. Mahler, M. Oguri, K. Sharon, Abdurro'uf, T. Y.-Y. Hsiao, M. Messa, E. Zackrisson, G. Brammer, D. Coe, V. Kokorev, M. Ricotti, A. Zitrin, S. Fujimoto, A. K. Inoue, T. Resseguier, J. R. Rigby, Y. Jiménez-Teja, R. A. Windhorst, and X. Xu. The discovery of bound star clusters 460 Myr after the Big Bang. *arXiv e-prints*, art. arXiv:2401.03224, Jan. 2024. doi: [10.48550/arXiv.2401.03224](https://doi.org/10.48550/arXiv.2401.03224).

A. V. Afanasiev, I. V. Chilingarian, S. Mieske, K. T. Voggel, A. Picotti, M. Hilker, A. Seth, N. Neumayer, M. Frank, A. J. Romanowsky, G. Hau, H. Baumgardt, C. Ahn, J. Strader, M. den Brok, R. McDermid, L. Spitler, J. Brodie, and J. L. Walsh. A 3.5 million Solar masses black hole in the centre of the ultracompact dwarf galaxy fornax UCD3. *MNRAS*, 477(4):4856–4865, July 2018. doi: [10.1093/mnras/sty913](https://doi.org/10.1093/mnras/sty913).

C. Alard. Flaring and warping of the Milky Way disk: not only in the gas. *arXiv e-prints*, art. astro-ph/0007013, July 2000. doi: [10.48550/arXiv.astro-ph/0007013](https://doi.org/10.48550/arXiv.astro-ph/0007013).

M. Alfaro-Cuello, N. Kacharov, N. Neumayer, N. Lützgendorf, A. C. Seth, T. Böker, S. Kamann, R. Leaman, G. van de Ven, P. Bianchini, L. L. Watkins, and M. Lyubenova. A Deep View into the Nucleus of the Sagittarius Dwarf Spheroidal Galaxy with MUSE. I. Data and Stellar Population Characterization. *ApJ*, 886(1):57, Nov. 2019. doi: [10.3847/1538-4357/ab1b2c](https://doi.org/10.3847/1538-4357/ab1b2c).

M. Alfaro-Cuello, N. Kacharov, N. Neumayer, P. Bianchini, A. Mastrobuono-Battisti,

- N. Lützgendorf, A. C. Seth, T. Böker, S. Kamann, R. Leaman, L. L. Watkins, and G. van de Ven. A Deep View into the Nucleus of the Sagittarius Dwarf Spheroidal Galaxy with MUSE. II. Kinematic Characterization of the Stellar Populations. *ApJ*, 892(1):20, Mar. 2020. doi: [10.3847/1538-4357/ab77bb](https://doi.org/10.3847/1538-4357/ab77bb).
- C. Allende Prieto, S. R. Majewski, R. Schiavon, K. Cunha, P. Frinchaboy, J. Holtzman, K. Johnston, M. Shetrone, M. Skrutskie, V. Smith, and J. Wilson. APOGEE: The Apache Point Observatory Galactic Evolution Experiment. *Astronomische Nachrichten*, 329:1018, Dec 2008. doi: [10.1002/asna.200811080](https://doi.org/10.1002/asna.200811080).
- D. A. Alvarez Garay, A. Mucciarelli, M. Bellazzini, C. Lardo, and P. Ventura. MgAl burning chain in ω Centauri. *A&A*, 681:A54, Jan. 2024. doi: [10.1051/0004-6361/202347834](https://doi.org/10.1051/0004-6361/202347834).
- F. Anders, A. Khalatyan, C. Chiappini, A. B. Queiroz, B. X. Santiago, C. Jordi, L. Giarradi, A. G. A. Brown, G. Matijević, G. Monari, T. Cantat-Gaudin, M. Weiler, S. Khan, A. Miglio, I. Carrillo, M. Romero-Gómez, I. Minchev, R. S. de Jong, T. Antoja, P. Ramos, M. Steinmetz, and H. Enke. Photo-astrometric distances, extinctions, and astrophysical parameters for Gaia DR2 stars brighter than $G = 18$. *A&A*, 628:A94, Aug. 2019. doi: [10.1051/0004-6361/201935765](https://doi.org/10.1051/0004-6361/201935765).
- A. J. Anderson. *Mass Segregation in Globular Clusters M92, 47 Tucanae, and Omega Centauri*. PhD thesis, University of California, Berkeley, Jan. 1997.
- J. Anderson and R. P. van der Marel. New Limits on an Intermediate-Mass Black Hole in Omega Centauri. I. Hubble Space Telescope Photometry and Proper Motions. *ApJ*, 710(2):1032–1062, Feb. 2010. doi: [10.1088/0004-637X/710/2/1032](https://doi.org/10.1088/0004-637X/710/2/1032).
- J. Anderson, A. Sarajedini, L. R. Bedin, I. R. King, G. Piotto, I. N. Reid, M. Siegel, S. R. Majewski, N. E. Q. Paust, A. Aparicio, A. P. Milone, B. Chaboyer, and A. Rosenberg. The Acs Survey of Globular Clusters. V. Generating a Comprehensive Star Catalog for each Cluster. *AJ*, 135(6):2055–2073, June 2008. doi: [10.1088/0004-6256/135/6/2055](https://doi.org/10.1088/0004-6256/135/6/2055).
- T. Antoja, S. Roca-Fàbrega, J. de Bruijne, and T. Prusti. Kinematics of symmetric Galactic longitudes to probe the spiral arms of the Milky Way with Gaia. *A&A*, 589:A13, May 2016. doi: [10.1051/0004-6361/201628200](https://doi.org/10.1051/0004-6361/201628200).
- T. Antoja, A. Helmi, M. Romero-Gómez, D. Katz, C. Babusiaux, R. Drimmel, D. W. Evans, F. Figueras, E. Poggio, C. Reylé, A. C. Robin, G. Seabroke, and C. Soubiran. A dynamically young and perturbed Milky Way disk. *Nature*, 561:360–362, Sept. 2018. doi: [10.1038/s41586-018-0510-7](https://doi.org/10.1038/s41586-018-0510-7).
- F. Antonini, M. Gieles, and A. Gualandris. Black hole growth through hierarchical black hole mergers in dense star clusters: implications for gravitational wave detections. *MNRAS*, 486(4):5008–5021, July 2019. doi: [10.1093/mnras/stz1149](https://doi.org/10.1093/mnras/stz1149).
- R. Arsenault, P. Y. Madec, N. Hubin, S. Stroebele, J. Paufique, E. Vernet, W. Hackenberg, J. F. Pirard, L. Jochum, A. Glindemann, A. Jost, R. Conzelmann, M. Kiekebusch, S. Tordo, J. L. Lizon, R. Donaldson, E. Fedrigo, C. Soenke, M. Duchateau, A. Bruton, B. Delabre, M. Downing, J. Reyes, J. Kolb, C. Bechet, M. Lelouarn, D. Bonaccini Calia, M. Quattri, I. Guidolin, B. Buzzoni, C. Dupuy, R. Guzman, M. Comin, A. Silber, J. Quentin, P. La Penna, A. Manescau, P. Jolley, V. Heinz, P. Duhoux, J. Argomedo, D. Gallieni, P. Lazzarini, R. Biasi, M. Andrijhettoni, G. Angerer, D. Pescoller, R. Stuik,

and A. Deep. Manufacturing of the ESO adaptive optics facility. In *Adaptive Optics Systems II*, volume 7736 of *Society of Photo-Optical Instrumentation Engineers (SPIE) Conference Series*, page 77360L, July 2010. doi: [10.1117/12.857973](https://doi.org/10.1117/12.857973).

Astropy Collaboration, T. P. Robitaille, E. J. Tollerud, P. Greenfield, M. Droettboom, E. Bray, T. Aldcroft, M. Davis, A. Ginsburg, A. M. Price-Whelan, W. E. Kerzendorf, A. Conley, N. Crighton, K. Barbary, D. Muna, H. Ferguson, F. Grollier, M. M. Parikh, P. H. Nair, H. M. Unther, C. Deil, J. Woillez, S. Conseil, R. Kramer, J. E. H. Turner, L. Singer, R. Fox, B. A. Weaver, V. Zabalza, Z. I. Edwards, K. Azalee Bostroem, D. J. Burke, A. R. Casey, S. M. Crawford, N. Dencheva, J. Ely, T. Jenness, K. Labrie, P. L. Lim, F. Pierfederici, A. Pontzen, A. Ptak, B. Refsdal, M. Servillat, and O. Streicher. Astropy: A community Python package for astronomy. *A&A*, 558:A33, Oct. 2013. doi: [10.1051/0004-6361/201322068](https://doi.org/10.1051/0004-6361/201322068).

Astropy Collaboration, A. M. Price-Whelan, B. M. Sipőcz, H. M. Günther, P. L. Lim, S. M. Crawford, S. Conseil, D. L. Shupe, M. W. Craig, N. Dencheva, A. Ginsburg, J. T. VanderPlas, L. D. Bradley, D. Pérez-Suárez, M. de Val-Borro, T. L. Aldcroft, K. L. Cruz, T. P. Robitaille, E. J. Tollerud, C. Ardelean, T. Babej, Y. P. Bach, M. Bachetti, A. V. Bakanov, S. P. Bamford, G. Barentsen, P. Barmby, A. Baumbach, K. L. Berry, F. Biscani, M. Boquien, K. A. Bostroem, L. G. Bouma, G. B. Brammer, E. M. Bray, H. Breytenbach, H. Buddelmeijer, D. J. Burke, G. Calderone, J. L. Cano Rodríguez, M. Cara, J. V. M. Cardoso, S. Cheedella, Y. Copin, L. Corrales, D. Crichton, D. D'Avella, C. Deil, É. Depagne, J. P. Dietrich, A. Donath, M. Droettboom, N. Earl, T. Erben, S. Fabbro, L. A. Ferreira, T. Finethy, R. T. Fox, L. H. Garrison, S. L. J. Gibbons, D. A. Goldstein, R. Gommers, J. P. Greco, P. Greenfield, A. M. Groener, F. Grollier, A. Hagen, P. Hirst, D. Homeier, A. J. Horton, G. Hosseinzadeh, L. Hu, J. S. Hunkeler, Ž. Ivezić, A. Jain, T. Jenness, G. Kanarek, S. Kendrew, N. S. Kern, W. E. Kerzendorf, A. Khvalko, J. King, D. Kirkby, A. M. Kulkarni, A. Kumar, A. Lee, D. Lenz, S. P. Littlefair, Z. Ma, D. M. Macleod, M. Mastropietro, C. McCully, S. Montagnac, B. M. Morris, M. Mueller, S. J. Mumford, D. Muna, N. A. Murphy, S. Nelson, G. H. Nguyen, J. P. Ninan, M. Nöthe, S. Ogaz, S. Oh, J. K. Parejko, N. Parley, S. Pascual, R. Patil, A. A. Patil, A. L. Plunkett, J. X. Prochaska, T. Rastogi, V. Reddy Janga, J. Sabater, P. Sakurikar, M. Seifert, L. E. Sherbert, H. Sherwood-Taylor, A. Y. Shih, J. Sick, M. T. Silbiger, S. Singanamalla, L. P. Singer, P. H. Sladen, K. A. Sooley, S. Sornarajah, O. Streicher, P. Teuben, S. W. Thomas, G. R. Tremblay, J. E. H. Turner, V. Terrón, M. H. van Kerkwijk, A. de la Vega, L. L. Watkins, B. A. Weaver, J. B. Whitmore, J. Woillez, V. Zabalza, and Astropy Contributors. The Astropy Project: Building an Open-science Project and Status of the v2.0 Core Package. *AJ*, 156(3):123, Sept. 2018. doi: [10.3847/1538-3881/aabc4f](https://doi.org/10.3847/1538-3881/aabc4f).

Astropy Collaboration, A. M. Price-Whelan, P. L. Lim, N. Earl, N. Starkman, L. Bradley, D. L. Shupe, A. A. Patil, L. Corrales, C. E. Brasseur, M. Nøthe, A. Donath, E. Tollerud, B. M. Morris, A. Ginsburg, E. Vaher, B. A. Weaver, J. Tocknell, W. Jamieson, M. H. van Kerkwijk, T. P. Robitaille, B. Merry, M. Bachetti, H. M. Günther, T. L. Aldcroft, J. A. Alvarado-Montes, A. M. Archibald, A. B'odi, S. Bapat, G. Barentsen, J. Baz'an, M. Biswas, M. Boquien, D. J. Burke, D. Cara, M. Cara, K. E. Conroy, S. Conseil, M. W. Craig, R. M. Cross, K. L. Cruz, F. D'Eugenio, N. Dencheva, H. A. R. Devillepoix, J. P. Dietrich, A. D. Eigenbrot, T. Erben, L. Ferreira, D. Foreman-Mackey, R. Fox, N. Freij, S. Garg, R. Geda, L. Glattly, Y. Gondhalekar, K. D. Gordon,

D. Grant, P. Greenfield, A. M. Groener, S. Guest, S. Gurovich, R. Handberg, A. Hart, Z. Hatfield-Dodds, D. Homeier, G. Hosseinzadeh, T. Jenness, C. K. Jones, P. Joseph, J. B. Kalmbach, E. Karamehmetoglu, M. Kaluszy’nski, M. S. P. Kelley, N. Kern, W. E. Kerzendorf, E. W. Koch, S. Kulumani, A. Lee, C. Ly, Z. Ma, C. MacBride, J. M. Maljaars, D. Muna, N. A. Murphy, H. Norman, R. O’Steen, K. A. Oman, C. Pacifici, S. Pascual, J. Pascual-Granado, R. R. Patil, G. I. Perren, T. E. Pickering, T. Rastogi, B. R. Roulston, D. F. Ryan, E. S. Rykoff, J. Sabater, P. Sakurikar, J. Salgado, A. Sanghi, N. Saunders, V. Savchenko, L. Schwardt, M. Seifert-Eckert, A. Y. Shih, A. S. Jain, G. Shukla, J. Sick, C. Simpson, S. Singanamalla, L. P. Singer, J. Singhal, M. Sinha, B. M. SipHocz, L. R. Spitzer, D. Stansby, O. Streicher, J. Sumak, J. D. Swinbank, D. S. Taranu, N. Tewary, G. R. Tremblay, M. d. Val-Borro, S. J. Van Kooten, Z. Vasovi’c, S. Verma, J. V. de Miranda Cardoso, P. K. G. Williams, T. J. Wilson, B. Winkel, W. M. Wood-Vasey, R. Xue, P. Yoachim, C. Zhang, A. Zonca, and Astropy Project Contributors. The Astropy Project: Sustaining and Growing a Community-oriented Open-source Project and the Latest Major Release (v5.0) of the Core Package. *apj*, 935(2):167, Aug. 2022. doi: [10.3847/1538-4357/ac7c74](https://doi.org/10.3847/1538-4357/ac7c74).

R. Bacon. Anisotropic models of elliptical galaxies. II. The case of flattened isophotes. *A&A*, 143:84–93, Feb 1985. URL <https://ui.adsabs.harvard.edu/abs/1985A&A...143...84B>.

R. Bacon, F. Simien, and G. Monnet. Anisotropic models of elliptical galaxies. *A&A*, 128: 405–410, Dec 1983. URL <https://ui.adsabs.harvard.edu/abs/1983A&A...128..405B>.

R. Bacon, M. Accardo, L. Adjali, H. Anwand, S. Bauer, I. Biswas, J. Blaizot, D. Boudon, S. Brau-Nogue, J. Brinchmann, P. Caillier, L. Capoani, C. M. Carollo, T. Contini, P. Couderc, E. Daguisé, S. Deiries, B. Delabre, S. Dreizler, J. Dubois, M. Dupieux, C. Dupuy, E. Emsellem, T. Fechner, A. Fleischmann, M. François, G. Gallou, T. Gharsa, A. Glindemann, D. Gojak, B. Guiderdoni, G. Hansali, T. Hahn, A. Jarno, A. Kelz, C. Koehler, J. Kosmalski, F. Laurent, M. Le Floch, S. J. Lilly, J. L. Lizon, M. Loupias, A. Manescau, C. Monstein, H. Nicklas, J. C. Olaya, L. Pares, L. Pasquini, A. Pécontal-Rousset, R. Pelló, C. Petit, E. Popow, R. Reiss, A. Remillieux, E. Renault, M. Roth, G. Rupprecht, D. Serre, J. Schaye, G. Soucail, M. Steinmetz, O. Streicher, R. Stuik, H. Valentin, J. Vernet, P. Weilbacher, L. Wisotzki, and N. Yerle. The MUSE second-generation VLT instrument. In *Ground-based and Airborne Instrumentation for Astronomy III*, volume 7735 of *Society of Photo-Optical Instrumentation Engineers (SPIE) Conference Series*, page 773508, July 2010. doi: [10.1117/12.856027](https://doi.org/10.1117/12.856027).

R. Bacon, J. Vernet, E. Borisova, N. Bouché, J. Brinchmann, M. Carollo, D. Carton, J. Caruana, S. Cerda, T. Contini, M. Franx, M. Girard, A. Guerou, N. Haddad, G. Hau, C. Herenz, J. C. Herrera, B. Husemann, T. O. Husser, A. Jarno, S. Kammann, D. Krajnovic, S. Lilly, V. Mainieri, T. Martinsson, R. Palsa, V. Patricio, A. Pécontal, R. Pello, L. Piqueras, J. Richard, C. Sandin, I. Schroetter, F. Selman, M. Shirazi, A. Smette, K. Soto, O. Streicher, T. Urrutia, P. Weilbacher, L. Wisotzki, and G. Zins. MUSE Commissioning. *The Messenger*, 157:13–16, Sept. 2014. URL <https://ui.adsabs.harvard.edu/abs/2014Msngr.157...13B>.

C. A. L. Bailer-Jones, J. Rybizki, M. Fouesneau, M. Demleitner, and R. Andrae. Estimating Distances from Parallaxes. V. Geometric and Photogeometric Distances to

- 1.47 Billion Stars in Gaia Early Data Release 3. AJ, 161(3):147, Mar. 2021. doi: [10.3847/1538-3881/abd806](https://doi.org/10.3847/1538-3881/abd806).
- N. Bastian and C. Lardo. Multiple Stellar Populations in Globular Clusters. ARA&A, 56:83–136, Sept. 2018. doi: [10.1146/annurev-astro-081817-051839](https://doi.org/10.1146/annurev-astro-081817-051839).
- H. Baumgardt. N -body modelling of globular clusters: masses, mass-to-light ratios and intermediate-mass black holes. MNRAS, 464(2):2174–2202, Jan. 2017. doi: [10.1093/mnras/stw2488](https://doi.org/10.1093/mnras/stw2488).
- H. Baumgardt and M. Hilker. A catalogue of masses, structural parameters, and velocity dispersion profiles of 112 Milky Way globular clusters. MNRAS, 478(2):1520–1557, Aug. 2018. doi: [10.1093/mnras/sty1057](https://doi.org/10.1093/mnras/sty1057).
- H. Baumgardt and E. Vasiliev. Accurate distances to Galactic globular clusters through a combination of Gaia EDR3, HST, and literature data. MNRAS, 505(4):5957–5977, Aug. 2021. doi: [10.1093/mnras/stab1474](https://doi.org/10.1093/mnras/stab1474).
- H. Baumgardt, C. He, S. M. Sweet, M. Drinkwater, A. Sollima, J. Hurley, C. Usher, S. Kamann, H. Dagleish, S. Dreizler, and T. O. Husser. No evidence for intermediate-mass black holes in the globular clusters ω Cen and NGC 6624. MNRAS, 488(4):5340–5351, Oct. 2019a. doi: [10.1093/mnras/stz2060](https://doi.org/10.1093/mnras/stz2060).
- H. Baumgardt, M. Hilker, A. Sollima, and A. Bellini. Mean proper motions, space orbits, and velocity dispersion profiles of Galactic globular clusters derived from Gaia DR2 data. MNRAS, 482(4):5138–5155, Feb. 2019b. doi: [10.1093/mnras/sty2997](https://doi.org/10.1093/mnras/sty2997).
- E. E. Becklin and G. Neugebauer. Infrared Observations of the Galactic Center. ApJ, 151:145, Jan. 1968. doi: [10.1086/149425](https://doi.org/10.1086/149425).
- L. R. Bedin, G. Piotto, J. Anderson, S. Cassisi, I. R. King, Y. Momany, and G. Carraro. ω Centauri: The Population Puzzle Goes Deeper. ApJ, 605(2):L125–L128, Apr. 2004. doi: [10.1086/420847](https://doi.org/10.1086/420847).
- T. C. Beers, K. Flynn, and K. Gebhardt. Measures of Location and Scale for Velocities in Clusters of Galaxies—A Robust Approach. AJ, 100:32, July 1990. doi: [10.1086/115487](https://doi.org/10.1086/115487).
- M. C. Begelman and M. J. Rees. The fate of dense stellar systems. MNRAS, 185:847–860, Dec. 1978. doi: [10.1093/mnras/185.4.847](https://doi.org/10.1093/mnras/185.4.847).
- M. C. Begelman, M. Volonteri, and M. J. Rees. Formation of supermassive black holes by direct collapse in pre-galactic haloes. MNRAS, 370(1):289–298, July 2006. doi: [10.1111/j.1365-2966.2006.10467.x](https://doi.org/10.1111/j.1365-2966.2006.10467.x).
- K. Bekki and K. C. Freeman. Formation of ω Centauri from an ancient nucleated dwarf galaxy in the young Galactic disc. MNRAS, 346(2):L11–L15, Dec. 2003. doi: [10.1046/j.1365-2966.2003.07275.x](https://doi.org/10.1046/j.1365-2966.2003.07275.x).
- A. Bellini, G. Piotto, L. R. Bedin, I. R. King, J. Anderson, A. P. Milone, and Y. Momany. Radial distribution of the multiple stellar populations in ω Centauri. A&A, 507(3):1393–1408, Dec. 2009. doi: [10.1051/0004-6361/200912757](https://doi.org/10.1051/0004-6361/200912757).

- A. Bellini, L. R. Bedin, G. Piotto, A. P. Milone, A. F. Marino, and S. Villanova. New Hubble Space Telescope WFC3/UVIS Observations Augment the Stellar-population Complexity of ω Centauri. *AJ*, 140(2):631–641, Aug. 2010. doi: [10.1088/0004-6256/140/2/631](https://doi.org/10.1088/0004-6256/140/2/631).
- A. Bellini, J. Anderson, R. P. van der Marel, L. L. Watkins, I. R. King, P. Bianchini, J. Chanamé, R. Chandar, A. M. Cool, F. R. Ferraro, H. Ford, and D. Massari. Hubble Space Telescope Proper Motion (HSTPROMO) Catalogs of Galactic Globular Clusters. I. Sample Selection, Data Reduction, and NGC 7078 Results. *ApJ*, 797(2):115, Dec. 2014. doi: [10.1088/0004-637X/797/2/115](https://doi.org/10.1088/0004-637X/797/2/115).
- A. Bellini, J. Anderson, L. R. Bedin, I. R. King, R. P. van der Marel, G. Piotto, and A. Cool. The State-of-the-art HST Astro-photometric Analysis of the Core of ω Centauri. I. The Catalog. *ApJ*, 842(1):6, June 2017a. doi: [10.3847/1538-4357/aa7059](https://doi.org/10.3847/1538-4357/aa7059).
- A. Bellini, J. Anderson, L. R. Bedin, I. R. King, R. P. van der Marel, G. Piotto, and A. Cool. The State-of-the-art HST Astro-photometric Analysis of the Core of ω Centauri. I. The Catalog. *ApJ*, 842(1):6, June 2017b. doi: [10.3847/1538-4357/aa7059](https://doi.org/10.3847/1538-4357/aa7059).
- A. Bellini, J. Anderson, R. P. van der Marel, I. R. King, G. Piotto, and L. R. Bedin. The State-of-the-art HST Astro-photometric Analysis of the Core of ω Centauri. II. Differential-reddening Map. *ApJ*, 842(1):7, June 2017c. doi: [10.3847/1538-4357/aa705f](https://doi.org/10.3847/1538-4357/aa705f).
- A. Bellini, A. P. Milone, J. Anderson, A. F. Marino, G. Piotto, R. P. van der Marel, L. R. Bedin, and I. R. King. The State-of-the-art HST Astro-photometric Analysis of the Core of ω Centauri. III. The Main Sequence’s Multiple Populations Galore. *ApJ*, 844(2):164, Aug. 2017d. doi: [10.3847/1538-4357/aa7b7e](https://doi.org/10.3847/1538-4357/aa7b7e).
- A. Bellini, M. Libralato, L. R. Bedin, A. P. Milone, R. P. van der Marel, J. Anderson, D. Apai, A. J. Burgasser, A. F. Marino, and J. M. Rees. The HST Large Programme on ω Centauri. II. Internal Kinematics. *ApJ*, 853(1):86, Jan. 2018. doi: [10.3847/1538-4357/aaa3ec](https://doi.org/10.3847/1538-4357/aaa3ec).
- V. Belokurov, D. Erkal, N. W. Evans, S. E. Koposov, and A. J. Deason. Co-formation of the disc and the stellar halo. *MNRAS*, 478(1):611–619, July 2018. doi: [10.1093/mnras/sty982](https://doi.org/10.1093/mnras/sty982).
- T. Bensby, S. Feltzing, and M. S. Oey. Exploring the Milky Way stellar disk. A detailed elemental abundance study of 714 F and G dwarf stars in the solar neighbourhood. *A&A*, 562:A71, Feb. 2014. doi: [10.1051/0004-6361/201322631](https://doi.org/10.1051/0004-6361/201322631).
- J. Binney. More dynamical models of our Galaxy. *MNRAS*, 426(2):1328–1337, Oct 2012. doi: [10.1111/j.1365-2966.2012.21692.x](https://doi.org/10.1111/j.1365-2966.2012.21692.x).
- J. Binney and P. McMillan. Models of our Galaxy - II. *MNRAS*, 413(3):1889–1898, May 2011. doi: [10.1111/j.1365-2966.2011.18268.x](https://doi.org/10.1111/j.1365-2966.2011.18268.x).
- J. Binney and S. Tremaine. *Galactic Dynamics: Second Edition*. Princeton: Princeton University Press, Princeton, NJ, 2008. ISBN 9780691130279. doi: <https://doi.org/10.1515/9781400828722>.

- J. Binney, O. E. Gerhard, A. A. Stark, J. Bally, and K. I. Uchida. Understanding the kinematics of Galactic Centre gas. MNRAS, 252:210, Sept. 1991. doi: [10.1093/mnras/252.2.210](https://doi.org/10.1093/mnras/252.2.210).
- N. Bissantz and O. Gerhard. Spiral arms, bar shape and bulge microlensing in the Milky Way. MNRAS, 330:591–608, Mar. 2002. doi: [10.1046/j.1365-8711.2002.05116.x](https://doi.org/10.1046/j.1365-8711.2002.05116.x).
- J. Bland-Hawthorn and O. Gerhard. The Galaxy in Context: Structural, Kinematic, and Integrated Properties. ARA&A, 54:529–596, Sept. 2016. doi: [10.1146/annurev-astro-081915-023441](https://doi.org/10.1146/annurev-astro-081915-023441).
- J. Bland-Hawthorn, S. Sharma, T. Tepper-Garcia, J. Binney, K. C. Freeman, M. R. Hayden, J. Kos, G. M. De Silva, S. Ellis, G. F. Lewis, M. Asplund, S. Buder, A. R. Casey, V. D’Orazi, L. Duong, S. Khanna, J. Lin, K. Lind, S. L. Martell, M. K. Ness, J. D. Simpson, D. B. Zucker, T. Zwitter, P. R. Kafle, A. C. Quillen, Y.-S. Ting, and R. F. G. Wyse. The GALAH survey and Gaia DR2: dissecting the stellar disc’s phase space by age, action, chemistry, and location. MNRAS, 486(1):1167–1191, June 2019. doi: [10.1093/mnras/stz217](https://doi.org/10.1093/mnras/stz217).
- D. Boubert and A. Everall. Completeness of the Gaia verse II: what are the odds that a star is missing from Gaia DR2? MNRAS, 497(4):4246–4261, Aug. 2020. doi: [10.1093/mnras/staa2305](https://doi.org/10.1093/mnras/staa2305).
- D. Boubert, A. Everall, and B. Holl. Completeness of the Gaia-verse - I. When and where were Gaia’s eyes on the sky during DR2? MNRAS, 497(2):1826–1841, July 2020. doi: [10.1093/mnras/staa2050](https://doi.org/10.1093/mnras/staa2050).
- J. Bovy and H.-W. Rix. A Direct Dynamical Measurement of the Milky Way’s Disk Surface Density Profile, Disk Scale Length, and Dark Matter Profile at 4 kpc $\sim R$ <math>\sim 9</math> kpc. ApJ, 779(2):115, Dec 2013. doi: [10.1088/0004-637X/779/2/115](https://doi.org/10.1088/0004-637X/779/2/115).
- J. Bovy and S. Tremaine. On the Local Dark Matter Density. ApJ, 756(1):89, Sept. 2012. doi: [10.1088/0004-637X/756/1/89](https://doi.org/10.1088/0004-637X/756/1/89).
- J. Bovy, D. L. Nidever, H.-W. Rix, L. Girardi, G. Zasowski, S. D. Chojnowski, J. Holtzman, C. Epstein, P. M. Frinchaboy, M. R. Hayden, T. S. Rodrigues, S. R. Majewski, J. A. Johnson, M. H. Pinsonneault, D. Stello, C. Allende Prieto, B. Andrews, S. Basu, T. C. Beers, D. Bizyaev, A. Burton, W. J. Chaplin, K. Cunha, Y. Elsworth, R. A. García, D. A. García-Hernández, A. E. García Pérez, F. R. Hearty, S. Hekker, T. Kallinger, K. Kinemuchi, L. Koesterke, S. Mészáros, B. Mosser, R. W. O’Connell, D. Oravetz, K. Pan, A. C. Robin, R. P. Schiavon, D. P. Schneider, M. Schultheis, A. Serenelli, M. Shetrone, V. Silva Aguirre, A. Simmons, M. Skrutskie, V. V. Smith, K. Stassun, D. H. Weinberg, J. C. Wilson, and O. Zamora. The APOGEE Red-clump Catalog: Precise Distances, Velocities, and High-resolution Elemental Abundances over a Large Area of the Milky Way’s Disk. ApJ, 790(2):127, Aug. 2014. doi: [10.1088/0004-637X/790/2/127](https://doi.org/10.1088/0004-637X/790/2/127).
- J. Bovy, H. W. Leung, J. A. S. Hunt, J. T. Mackereth, D. A. García-Hernández, and A. Roman-Lopes. Life in the fast lane: a direct view of the dynamics, formation, and evolution of the Milky Way’s bar. MNRAS, 490(4):4740–4747, Dec 2019. doi: [10.1093/mnras/stz2891](https://doi.org/10.1093/mnras/stz2891).

- J. P. Brodie and J. Strader. Extragalactic Globular Clusters and Galaxy Formation. *ARA&A*, 44(1):193–267, Sept. 2006. doi: [10.1146/annurev.astro.44.051905.092441](https://doi.org/10.1146/annurev.astro.44.051905.092441).
- J. P. Brodie, A. J. Romanowsky, J. Strader, and D. A. Forbes. The Relationships among Compact Stellar Systems: A Fresh View of Ultracompact Dwarfs. *AJ*, 142(6):199, Dec. 2011. doi: [10.1088/0004-6256/142/6/199](https://doi.org/10.1088/0004-6256/142/6/199).
- V. Bromm and A. Loeb. Formation of the First Supermassive Black Holes. *ApJ*, 596(1):34–46, Oct. 2003. doi: [10.1086/377529](https://doi.org/10.1086/377529).
- S. Buder, M. Asplund, L. Duong, J. Kos, K. Lind, M. K. Ness, S. Sharma, J. Bland-Hawthorn, A. R. Casey, G. M. de Silva, V. D’Orazi, K. C. Freeman, G. F. Lewis, J. Lin, S. L. Martell, K. J. Schlesinger, J. D. Simpson, D. B. Zucker, T. Zwitter, A. M. Amarsi, B. Anguiano, D. Carollo, L. Casagrande, K. Čotar, P. L. Cottrell, G. da Costa, X. D. Gao, M. R. Hayden, J. Horner, M. J. Ireland, P. R. Kafle, U. Munari, D. M. Nataf, T. Nordlander, D. Stello, Y.-S. Ting, G. Traven, F. Watson, R. A. Wittenmyer, R. F. G. Wyse, D. Yong, J. C. Zinn, M. Žerjal, and Galah Collaboration. The GALAH Survey: second data release. *MNRAS*, 478(4):4513–4552, Aug. 2018. doi: [10.1093/mnras/sty1281](https://doi.org/10.1093/mnras/sty1281).
- A. Calamida, G. Strampelli, A. Rest, G. Bono, I. Ferraro, A. Saha, G. Iannicola, D. Scolnic, D. James, C. Smith, and A. Zenteno. The Not So Simple Globular Cluster ω Cen. I. Spatial Distribution of the Multiple Stellar Populations. *AJ*, 153(4):175, Apr. 2017. doi: [10.3847/1538-3881/aa6397](https://doi.org/10.3847/1538-3881/aa6397).
- A. Calamida, A. Zocchi, G. Bono, I. Ferraro, A. Mastrobuono-Battisti, A. Saha, G. Iannicola, A. Rest, G. Strampelli, and A. Zenteno. The Not So Simple Stellar System ω Cen. II. Evidence in Support of a Merging Scenario. *ApJ*, 891(2):167, Mar. 2020. doi: [10.3847/1538-4357/ab77c0](https://doi.org/10.3847/1538-4357/ab77c0).
- T. M. Callingham, M. Cautun, A. J. Deason, C. S. Frenk, R. J. J. Grand, and F. Marinacci. The chemo-dynamical groups of Galactic globular clusters. *MNRAS*, 513(3):4107–4129, July 2022. doi: [10.1093/mnras/stac1145](https://doi.org/10.1093/mnras/stac1145).
- M. Cappellari. Efficient multi-Gaussian expansion of galaxies. *MNRAS*, 333:400–410, June 2002. doi: [10.1046/j.1365-8711.2002.05412.x](https://doi.org/10.1046/j.1365-8711.2002.05412.x).
- M. Cappellari. Measuring the inclination and mass-to-light ratio of axisymmetric galaxies via anisotropic Jeans models of stellar kinematics. *MNRAS*, 390:71–86, Oct. 2008. doi: [10.1111/j.1365-2966.2008.13754.x](https://doi.org/10.1111/j.1365-2966.2008.13754.x).
- M. Cappellari. Structure and kinematics of early-type galaxies from integral field spectroscopy. *ARA&A*, 54(1):597–665, 2016. doi: [10.1146/annurev-astro-082214-122432](https://doi.org/10.1146/annurev-astro-082214-122432).
- M. Cappellari. Efficient solution of the anisotropic spherically aligned axisymmetric Jeans equations of stellar hydrodynamics for galactic dynamics. *MNRAS*, 494(4):4819–4837, Apr. 2020. doi: [10.1093/mnras/staa959](https://doi.org/10.1093/mnras/staa959).
- M. Cappellari and Y. Copin. Adaptive spatial binning of integral-field spectroscopic data using Voronoi tessellations. *MNRAS*, 342(2):345–354, June 2003. doi: [10.1046/j.1365-8711.2003.06541.x](https://doi.org/10.1046/j.1365-8711.2003.06541.x).

M. Cappellari, R. Bacon, M. Bureau, M. C. Damen, R. L. Davies, P. T. de Zeeuw, E. Emsellem, J. Falcón-Barroso, D. Krajnović, H. Kuntschner, R. M. McDermid, R. F. Peletier, M. Sarzi, R. C. E. van den Bosch, and G. van de Ven. The sauron project - iv. the mass-to-light ratio, the virial mass estimator and the fundamental plane of elliptical and lenticular galaxies. *MNRAS*, 366:1126–1150, Mar. 2006. doi: [10.1111/j.1365-2966.2005.09981.x](https://doi.org/10.1111/j.1365-2966.2005.09981.x).

M. Cappellari, R. M. McDermid, K. Alatalo, L. Blitz, M. Bois, F. Bournaud, M. Bureau, A. F. Crocker, R. L. Davies, T. A. Davis, P. T. de Zeeuw, P.-A. Duc, E. Emsellem, S. Khochfar, D. Krajnović, H. Kuntschner, R. Morganti, T. Naab, T. Oosterloo, M. Sarzi, N. Scott, P. Serra, A.-M. Weijmans, and L. M. Young. The ATLAS^{3D} project - XX. Mass-size and mass- σ distributions of early-type galaxies: bulge fraction drives kinematics, mass-to-light ratio, molecular gas fraction and stellar initial mass function. *MNRAS*, 432(3):1862–1893, July 2013a. doi: [10.1093/mnras/stt644](https://doi.org/10.1093/mnras/stt644).

M. Cappellari, N. Scott, K. Alatalo, L. Blitz, M. Bois, F. Bournaud, M. Bureau, A. F. Crocker, R. L. Davies, T. A. Davis, P. T. de Zeeuw, P.-A. Duc, E. Emsellem, S. Khochfar, D. Krajnović, H. Kuntschner, R. M. McDermid, R. Morganti, T. Naab, T. Oosterloo, M. Sarzi, P. Serra, A.-M. Weijmans, and L. M. Young. The ATLAS^{3D} project - XV. Benchmark for early-type galaxies scaling relations from 260 dynamical models: mass-to-light ratio, dark matter, Fundamental Plane and Mass Plane. *MNRAS*, 432: 1709–1741, July 2013b. doi: [10.1093/mnras/stt562](https://doi.org/10.1093/mnras/stt562).

M. Cappellari, A. J. Romanowsky, J. P. Brodie, D. A. Forbes, J. Strader, C. Foster, S. S. Kartha, N. Pastorello, V. Pota, L. R. Spitler, C. Usher, and J. A. Arnold. Small Scatter and Nearly Isothermal Mass Profiles to Four Half-light Radii from Two-dimensional Stellar Dynamics of Early-type Galaxies. *ApJ*, 804:L21, May 2015. doi: [10.1088/2041-8205/804/1/L21](https://doi.org/10.1088/2041-8205/804/1/L21).

B. W. Carney and P. Seitzer. Optical detection of the Galaxy’s Southern Stellar Warp and Outer Disk. *AJ*, 105:2127, June 1993. doi: [10.1086/116591](https://doi.org/10.1086/116591).

G. Carraro, R. A. Vázquez, E. Costa, J. A. Ahumada, and E. E. Giorgi. The Thickening of the Thin Disk in the Third Galactic Quadrant. *AJ*, 149(1):12, Jan. 2015. doi: [10.1088/0004-6256/149/1/12](https://doi.org/10.1088/0004-6256/149/1/12).

B. W. Carroll and D. A. Ostlie. *An Introduction to Modern Astrophysics*. Cambridge University Press, 2 edition, 2017. ISBN 9781108422161. doi: [10.1017/9781108380980](https://doi.org/10.1017/9781108380980).

D. J. Carson, A. J. Barth, A. C. Seth, M. den Brok, M. Cappellari, J. E. Greene, L. C. Ho, and N. Neumayer. The Structure of Nuclear Star Clusters in Nearby Late-type Spiral Galaxies from Hubble Space Telescope Wide Field Camera 3 Imaging. *AJ*, 149 (5):170, May 2015. doi: [10.1088/0004-6256/149/5/170](https://doi.org/10.1088/0004-6256/149/5/170).

T. A. Caswell, A. Lee, E. Sales de Andrade, M. Droettboom, T. Hoffmann, J. Klymak, J. Hunter, E. Firing, D. Stansby, N. Varoquaux, J. Hedegaard Nielsen, B. Root, R. May, O. Gustafsson, P. Elson, J. K. Seppänen, J.-J. Lee, D. Dale, hannah, D. McDougall, A. Straw, P. Hobson, K. Sundén, G. Lucas, C. Gohlke, A. F. Vincent, T. S. Yu, E. Ma, S. Silvester, and C. Moad. matplotlib/matplotlib: Rel: v3.7.1, 2023. URL <https://doi.org/10.5281/zenodo.7697899>.

- J. Choi, A. Dotter, C. Conroy, M. Cantiello, B. Paxton, and B. D. Johnson. Mesa Isochrones and Stellar Tracks (MIST). I. Solar-scaled Models. *ApJ*, 823(2):102, June 2016. doi: [10.3847/0004-637X/823/2/102](https://doi.org/10.3847/0004-637X/823/2/102).
- E. Churchwell, B. L. Babler, M. R. Meade, B. A. Whitney, R. Benjamin, R. Indebetouw, C. Cyganowski, T. P. Robitaille, M. Povich, C. Watson, and S. Bracker. The Spitzer/GLIMPSE Surveys: A New View of the Milky Way. *PASP*, 121(877):213, Mar. 2009. doi: [10.1086/597811](https://doi.org/10.1086/597811).
- D. R. Cole and J. Binney. A centrally heated dark halo for our Galaxy. *MNRAS*, 465: 798–810, Feb. 2017. doi: [10.1093/mnras/stw2775](https://doi.org/10.1093/mnras/stw2775).
- F. de Lorenzi, O. Gerhard, L. Coccato, M. Arnaboldi, M. Capaccioli, N. G. Douglas, K. C. Freeman, K. Kuijken, M. R. Merrifield, N. R. Napolitano, E. Noordermeer, A. J. Romanowsky, and V. P. Debattista. Dearth of dark matter or massive dark halo? Mass-shape-anisotropy degeneracies revealed by NMAGIC dynamical models of the elliptical galaxy NGC 3379. *MNRAS*, 395:76–96, May 2009. doi: [10.1111/j.1365-2966.2009.14553.x](https://doi.org/10.1111/j.1365-2966.2009.14553.x).
- W. Dehnen. Tailoring triaxial N-body models via a novel made-to-measure method. *MNRAS*, 395(2):1079–1086, May 2009. doi: [10.1111/j.1365-2966.2009.14603.x](https://doi.org/10.1111/j.1365-2966.2009.14603.x).
- S. Derriere and A. C. Robin. Near-infrared Surveys and the Shape of the Galactic Disc. In R. Clowes, A. Adamson, and G. Bromage, editors, *The New Era of Wide Field Astronomy*, volume 232 of *Astronomical Society of the Pacific Conference Series*, page 229, Jan. 2001. URL <https://ui.adsabs.harvard.edu/abs/2001ASPC..232..229D>.
- M. I. P. Dierickx and A. Loeb. Predicted Extension of the Sagittarius Stream to the Milky Way Virial Radius. *ApJ*, 836(1):92, Feb. 2017. doi: [10.3847/1538-4357/836/1/92](https://doi.org/10.3847/1538-4357/836/1/92).
- A. Dotter. MESA Isochrones and Stellar Tracks (MIST) 0: Methods for the Construction of Stellar Isochrones. *ApJS*, 222(1):8, Jan. 2016. doi: [10.3847/0067-0049/222/1/8](https://doi.org/10.3847/0067-0049/222/1/8).
- M. J. Drinkwater, M. D. Gregg, M. Hilker, K. Bekki, W. J. Couch, H. C. Ferguson, J. B. Jones, and S. Phillipps. A class of compact dwarf galaxies from disruptive processes in galaxy clusters. *Nature*, 423(6939):519–521, May 2003. doi: [10.1038/nature01666](https://doi.org/10.1038/nature01666).
- J. Dunlop. A Catalogue of Nebulae and Clusters of Stars in the Southern Hemisphere, Observed at Paramatta in New South Wales. *Philosophical Transactions of the Royal Society of London Series I*, 118:113–151, Jan. 1828. doi: [10.1098/rstl.1828.0010](https://doi.org/10.1098/rstl.1828.0010).
- A. Eckart, R. Genzel, R. Hofmann, B. J. Sams, and L. E. Tacconi-Garman. High Angular Resolution Spectroscopic and Polarimetric Imaging of the Galactic Center in the Near-Infrared. *ApJ*, 445:L23, May 1995. doi: [10.1086/187880](https://doi.org/10.1086/187880).
- B. Efron and R. J. Tibshirani. *An Introduction to the Bootstrap*. Number 57 in Monographs on Statistics and Applied Probability. Chapman & Hall/CRC, 1993.
- A.-C. Eilers, D. W. Hogg, H.-W. Rix, and M. K. Ness. The Circular Velocity Curve of the Milky Way from 5 to 25 kpc. *ApJ*, 871:120, Jan. 2019. doi: [10.3847/1538-4357/aaf648](https://doi.org/10.3847/1538-4357/aaf648).

- A.-C. Eilers, D. W. Hogg, H.-W. Rix, N. Frankel, J. A. S. Hunt, J.-B. Fouvry, and T. Buck. The Strength of the Dynamical Spiral Perturbation in the Galactic Disk. *ApJ*, 900(2):186, Sept. 2020. doi: [10.3847/1538-4357/abac0b](https://doi.org/10.3847/1538-4357/abac0b).
- R. A. W. Elson, G. F. Gilmore, B. X. Santiago, and S. Casertano. HST Observations of the Stellar Population of the Globular Cluster W CEN. *AJ*, 110:682, Aug. 1995. doi: [10.1086/117553](https://doi.org/10.1086/117553).
- E. Emsellem, G. Monnet, and R. Bacon. The multi-gaussian expansion method: a tool for building realistic photometric and kinematical models of stellar systems I. The formalism. *A&A*, 285:723–738, May 1994.
- ESO CPL Development Team. EsoRex: ESO Recipe Execution Tool, Apr. 2015. URL <https://ascl.net/1504.003>.
- A. Everall, N. W. Evans, V. Belokurov, and R. Schönrich. The Tilt of the Local Velocity Ellipsoid as seen by Gaia. *MNRAS*, 489:910–918, Aug 2019. doi: [10.1093/mnras/stz2217](https://doi.org/10.1093/mnras/stz2217).
- E. A. Evstigneева, M. D. Gregg, M. J. Drinkwater, and M. Hilker. Internal Properties of Ultracompact Dwarf Galaxies in the Virgo Cluster. *AJ*, 133(4):1722–1740, Apr. 2007. doi: [10.1086/511958](https://doi.org/10.1086/511958).
- K. Fahrion, M. Lyubenova, G. van de Ven, M. Hilker, R. Leaman, J. Falcón-Barroso, A. Bittner, L. Coccato, E. M. Corsini, D. A. Gadotti, E. Iodice, R. M. McDermid, I. Martín-Navarro, F. Pinna, A. Poci, M. Sarzi, P. T. de Zeeuw, and L. Zhu. Diversity of nuclear star cluster formation mechanisms revealed by their star formation histories. *A&A*, 650:A137, June 2021. doi: [10.1051/0004-6361/202140644](https://doi.org/10.1051/0004-6361/202140644).
- K. Fahrion, R. Leaman, M. Lyubenova, and G. van de Ven. Disentangling the formation mechanisms of nuclear star clusters. *A&A*, 658:A172, Feb. 2022. doi: [10.1051/0004-6361/202039778](https://doi.org/10.1051/0004-6361/202039778).
- O. Fakhouri and C.-P. Ma. The nearly universal merger rate of dark matter haloes in Λ CDM cosmology. *MNRAS*, 386(2):577–592, May 2008. doi: [10.1111/j.1365-2966.2008.13075.x](https://doi.org/10.1111/j.1365-2966.2008.13075.x).
- M. A. Fardal, R. P. van der Marel, D. R. Law, S. T. Sohn, B. Sesar, N. Hernitschek, and H.-W. Rix. Connecting the Milky Way potential profile to the orbital time-scales and spatial structure of the Sagittarius Stream. *MNRAS*, 483(4):4724–4741, Mar. 2019. doi: [10.1093/mnras/sty3428](https://doi.org/10.1093/mnras/sty3428).
- A. Fattahi, V. Belokurov, A. J. Deason, C. S. Frenk, F. A. Gómez, R. J. J. Grand, F. Marinacci, R. Pakmor, and V. Springel. The origin of galactic metal-rich stellar halo components with highly eccentric orbits. *MNRAS*, 484(4):4471–4483, Apr. 2019. doi: [10.1093/mnras/stz159](https://doi.org/10.1093/mnras/stz159).
- C. Flynn, J. Holmberg, L. Portinari, B. Fuchs, and H. Jahreiß. On the mass-to-light ratio of the local Galactic disc and the optical luminosity of the Galaxy. *MNRAS*, 372:1149–1160, Nov. 2006. doi: [10.1111/j.1365-2966.2006.10911.x](https://doi.org/10.1111/j.1365-2966.2006.10911.x).
- D. A. Forbes and T. Bridges. Accreted versus in situ Milky Way globular clusters. *MNRAS*, 404(3):1203–1214, May 2010. doi: [10.1111/j.1365-2966.2010.16373.x](https://doi.org/10.1111/j.1365-2966.2010.16373.x).

- D. Foreman-Mackey, D. W. Hogg, D. Lang, and J. Goodman. emcee: The MCMC Hammer. *PASP*, 125(925):306, Mar. 2013. doi: [10.1086/670067](https://doi.org/10.1086/670067).
- K. C. Freeman and A. W. Rodgers. The Chemical Inhomogeneity of Omega Centauri. *ApJ*, 201:L71, Oct. 1975. doi: [10.1086/181945](https://doi.org/10.1086/181945).
- M. Freitag, M. A. Gürkan, and F. A. Rasio. Runaway collisions in young star clusters - II. Numerical results. *MNRAS*, 368(1):141–161, May 2006a. doi: [10.1111/j.1365-2966.2006.10096.x](https://doi.org/10.1111/j.1365-2966.2006.10096.x).
- M. Freitag, F. A. Rasio, and H. Baumgardt. Runaway collisions in young star clusters - I. Methods and tests. *MNRAS*, 368(1):121–140, May 2006b. doi: [10.1111/j.1365-2966.2006.10095.x](https://doi.org/10.1111/j.1365-2966.2006.10095.x).
- C. L. Fryer, S. E. Woosley, and A. Heger. Pair-Instability Supernovae, Gravity Waves, and Gamma-Ray Transients. *ApJ*, 550(1):372–382, Mar. 2001. doi: [10.1086/319719](https://doi.org/10.1086/319719).
- Gaia Collaboration, T. Prusti, J. H. J. de Bruijne, A. G. A. Brown, A. Vallenari, C. Babusiaux, C. A. L. Bailer-Jones, U. Bastian, M. Biermann, D. W. Evans, and et al. The Gaia mission. *A&A*, 595:A1, Nov. 2016. doi: [10.1051/0004-6361/201629272](https://doi.org/10.1051/0004-6361/201629272).
- Gaia Collaboration, A. G. A. Brown, A. Vallenari, T. Prusti, J. H. J. de Bruijne, C. Babusiaux, C. A. L. Bailer-Jones, M. Biermann, D. W. Evans, L. Eyer, and et al. Gaia Data Release 2. Summary of the contents and survey properties. *A&A*, 616:A1, Aug. 2018a. doi: [10.1051/0004-6361/201833051](https://doi.org/10.1051/0004-6361/201833051).
- Gaia Collaboration, D. Katz, T. Antoja, M. Romero-Gómez, R. Drimmel, C. Reylé, G. M. Seabroke, C. Soubiran, C. Babusiaux, P. Di Matteo, F. Figueras, E. Poggio, A. C. Robin, D. W. Evans, A. G. A. Brown, A. Vallenari, T. Prusti, J. H. J. de Bruijne, C. A. L. Bailer-Jones, M. Biermann, L. Eyer, F. Jansen, C. Jordi, S. A. Klioner, U. Lammers, L. Lindegren, X. Luri, F. Mignard, C. Panem, D. Pourbaix, S. Randich, P. Sartoretti, H. I. Siddiqui, F. van Leeuwen, N. A. Walton, F. Arenou, U. Bastian, M. Cropper, M. G. Lattanzi, J. Bakker, C. Cacciari, J. Casta n, L. Chaoul, N. Cheek, F. De Angeli, C. Fabricius, R. Guerra, B. Holl, E. Masana, R. Messineo, N. Mowlavi, K. Nienartowicz, P. Panuzzo, J. Portell, M. Riello, P. Tanga, F. Thévenin, G. Gracia-Abril, G. Comoretto, M. Garcia-Reinaldos, D. Teyssier, M. Altmann, R. Andrae, M. Audard, I. Bellas-Velidis, K. Benson, J. Berthier, R. Blomme, P. Burgess, G. Busso, B. Carry, A. Cellino, G. Clementini, M. Clotet, O. Creevey, M. Davidson, J. De Ridder, L. Delchambre, A. Dell’Oro, C. Ducourant, J. Fernández-Hernández, M. Fouesneau, Y. Frémat, L. Galluccio, M. García-Torres, J. González-Núñez, J. J. González-Vidal, E. Gosset, L. P. Guy, J. L. Halbwachs, N. C. Hambly, D. L. Harrison, J. Hernández, D. Hestroffer, S. T. Hodgkin, A. Hutton, G. Jasniewicz, A. Jean-Antoine-Piccolo, S. Jordan, A. J. Korn, A. Krone-Martins, A. C. Lanzafame, T. Lebzelter, W. Löffler, M. Manteiga, P. M. Marrese, J. M. Martín-Fleitas, A. Moitinho, A. Mora, K. Muinonen, J. Osinde, E. Pancino, T. Pauwels, J. M. Petit, A. Recio-Blanco, P. J. Richards, L. Rimoldini, L. M. Sarro, C. Siopis, M. Smith, A. Sozzetti, M. Süveges, J. Torra, W. van Reeven, U. Abbas, A. Abreu Aramburu, S. Accart, C. Aerts, G. Altavilla, M. A. Álvarez, R. Alvarez, J. Alves, R. I. Anderson, A. H. Andrei, E. Anglada Varela, E. Antiche, B. Arcay, T. L. Astraatmadja, N. Bach, S. G. Baker, L. Balaguer-Núñez, P. Balm, C. Barache, C. Barata, D. Barbato, F. Barblan, P. S. Barklem, D. Barraido, M. Barros, M. A. Barstow, L. Bartholomé Muñoz, J. L. Bassilana, U. Becciani,

M. Bellazzini, A. Berihuete, S. Bertone, L. Bianchi, O. Bienaymé, S. Blanco-Cuaresma, T. Boch, C. Boeche, A. Bombrun, R. Borrachero, D. Bossini, S. Bouquillon, G. Bourda, A. Bragaglia, L. Bramante, M. A. Breddels, A. Bressan, N. Brouillet, T. Brüsemeister, E. Brugaletta, B. Bucciarelli, A. Burlacu, D. Busonero, A. G. Butkevich, R. Buzzi, E. Caffau, R. Cancelliere, G. Cannizzaro, T. Cantat-Gaudin, R. Carballo, T. Carrucci, J. M. Carrasco, L. Casamiquela, M. Castellani, A. Castro-Ginard, P. Charlot, L. Chemin, A. Chiavassa, G. Cocozza, G. Costigan, S. Cowell, F. Crifo, M. Crosta, C. Crowley, J. Cuypers, C. Dafonte, Y. Damerdji, A. Dapergolas, P. David, M. David, P. de Laverny, F. De Luise, R. De March, R. de Souza, A. de Torres, J. Debosscher, E. del Pozo, M. Delbo, A. Delgado, H. E. Delgado, S. Diakite, C. Diener, E. Distefano, C. Dolding, P. Drazinos, J. Durán, B. Edvardsson, H. Enke, K. Eriksson, P. Esquej, G. Eynard Bontemps, C. Fabre, M. Fabrizio, S. Faigler, A. J. Falc a, M. Farràs Casas, L. Federici, G. Fedorets, P. Fernique, F. Filippi, K. Findeisen, A. Fonti, E. Fraile, M. Fraser, B. Frézouls, M. Gai, S. Galleti, D. Garabato, F. García-Sedano, A. Garofalo, N. Garralda, A. Gavel, P. Gavras, J. Gerssen, R. Geyer, P. Giacobbe, G. Gilmore, S. Girona, G. Giuffrida, F. Glass, M. Gomes, M. Granvik, A. Gueguen, A. Guerrier, J. Guiraud, R. Gutié, R. Haigron, D. Hatzidimitriou, M. Hauser, M. Haywood, U. Heiter, A. Helmi, J. Heu, T. Hilger, D. Hobbs, W. Hofmann, G. Holland, H. E. Huckle, A. Hypki, V. Icardi, K. Janßen, G. Jevardat de Fombelle, P. G. Jonker, Á. L. Juhász, F. Julbe, A. Karampelas, A. Kewley, J. Klar, A. Kochoska, R. Kohley, K. Kolenberg, M. Kontizas, E. Kontizas, S. E. Koposov, G. Kordopatis, Z. Kostrzewa-Rutkowska, P. Koubsky, S. Lambert, A. F. Lanza, Y. Lasne, J. B. Lavigne, Y. Le Fustec, C. Le Poncin-Lafitte, Y. Lebreton, S. Leccia, N. Leclerc, I. Lecoeur-Taibi, H. Lenhardt, F. Leroux, S. Liao, E. Licata, H. E. P. Lindstrøm, T. A. Lister, E. Livanou, A. Lobel, M. López, S. Managau, R. G. Mann, G. Mantelet, O. Marchal, J. M. Marchant, M. Marconi, S. Marinoni, G. Marschalkó, D. J. Marshall, M. Martino, G. Marton, N. Mary, D. Massari, G. Matijević, T. Mazeh, P. J. McMillan, S. Messina, D. Michalik, N. R. Millar, D. Molina, R. Molinaro, L. Molnár, P. Montegriffo, R. Mor, R. Morbidelli, T. Morel, D. Morris, A. F. Mulone, T. Muraveva, I. Musella, G. Nelemans, L. Nicastro, L. Noval, W. O'Mullane, C. Ordénovic, D. Ordóñez-Blanco, P. Osborne, C. Pagani, I. Pagano, F. Pailler, H. Palacin, L. Palaversa, A. Panahi, M. Pawlak, A. M. Piersimoni, F. X. Pineau, E. Plachy, G. Plum, E. Poujoulet, A. Prša, L. Pulone, E. Racero, S. Ragaini, N. Rambaux, M. Ramos-Lerate, S. Regibo, F. Riclet, V. Ripepi, A. Riva, A. Rivard, G. Rixon, T. Roegiers, M. Roelens, N. Rowell, F. Royer, L. Ruiz-Dern, G. Sadowski, T. Sagristà Sellés, J. Sahlmann, J. Salgado, E. Salguero, N. Sanna, T. Santana-Ros, M. Sarasso, H. Savietto, M. Schultheis, E. Sciacca, M. Segol, J. C. Segovia, D. Ségransan, I. C. Shih, L. Siltala, A. F. Silva, R. L. Smart, K. W. Smith, E. Solano, F. Solitro, R. Sordo, S. Soria Nieto, J. Souchay, A. Spagna, F. Spoto, U. Stampa, I. A. Steele, H. Steidelmüller, C. A. Stephenson, H. Stoev, F. F. Suess, J. Surdej, L. Szabados, E. Szegedi-Elek, D. Tapiador, F. Taris, G. Tauran, M. B. Taylor, R. Teixeira, D. Terrett, P. Teyssandier, W. Thuillot, A. Titarenko, F. Torra Clotet, C. Turon, A. Ulla, E. Utrilla, S. Uzzi, M. Vaillant, G. Valentini, V. Valette, A. van Elteren, E. Van Hemelryck, M. van Leeuwen, M. Vaschetto, A. Vecchiato, J. Veljanoski, Y. Viala, D. Vicente, S. Vogt, C. von Essen, H. Voss, V. Votruba, S. Voutsinas, G. Walmsley, M. Weiler, O. Wertz, T. Wevers, Ł. Wyrzykowski, A. Yoldas, M. Žerjal, H. Ziaeepour, J. Zorec, S. Zschocke, S. Zucker, C. Zurbach, and T. Zwitter. Gaia Data Release 2. Mapping the Milky Way disc kinematics. *A&A*, 616:A11, Aug. 2018b. doi: [10.1051/0004-6361/201832865](https://doi.org/10.1051/0004-6361/201832865).

Gaia Collaboration, A. G. A. Brown, A. Vallenari, T. Prusti, J. H. J. de Bruijne, C. Babusiaux, M. Biermann, O. L. Creevey, D. W. Evans, L. Eyer, A. Hutton, F. Jansen, C. Jordi, S. A. Klioner, U. Lammers, L. Lindegren, X. Luri, F. Mignard, C. Panem, D. Pourbaix, S. Randich, P. Sartoretti, C. Soubiran, N. A. Walton, F. Arenou, C. A. L. Bailer-Jones, U. Bastian, M. Cropper, R. Drimmel, D. Katz, M. G. Lattanzi, F. van Leeuwen, J. Bakker, C. Cacciari, J. Castañeda, F. De Angeli, C. Ducourant, C. Fabricius, M. Fouesneau, Y. Frémat, R. Guerra, A. Guerrier, J. Guiraud, A. Jean-Antoine Piccolo, E. Masana, R. Messineo, N. Mowlavi, C. Nicolas, K. Nienartowicz, F. Pailler, P. Panuzzo, F. Riclet, W. Roux, G. M. Seabroke, R. Sordo, P. Tanga, F. Thévenin, G. Gracia-Abril, J. Portell, D. Teyssier, M. Altmann, R. Andrae, I. Bellas-Velidis, K. Benson, J. Berthier, R. Blomme, E. Brugaletta, P. W. Burgess, G. Busso, B. Carry, A. Cellino, N. Cheek, G. Clementini, Y. Damerdji, M. Davidson, L. Delchambre, A. Dell’Oro, J. Fernández-Hernández, L. Galluccio, P. García-Lario, M. Garcia-Reinaldos, J. González-Núñez, E. Gosset, R. Haigron, J. L. Halbwachs, N. C. Hambley, D. L. Harrison, D. Hatzidimitriou, U. Heiter, J. Hernández, D. Hestroffer, S. T. Hodgkin, B. Holl, K. Janßen, G. Jevardat de Fombelle, S. Jordan, A. Krone-Martins, A. C. Lanzafame, W. Löffler, A. Lorca, M. Manteiga, O. Marchal, P. M. Marrese, A. Moitinho, A. Mora, K. Muinonen, P. Osborne, E. Pancino, T. Pauwels, J. M. Petit, A. Recio-Blanco, P. J. Richards, M. Riello, L. Rimoldini, A. C. Robin, T. Roegiers, J. Rybizki, L. M. Sarro, C. Siopis, M. Smith, A. Sozzetti, A. Ulla, E. Utrilla, M. van Leeuwen, W. van Reeven, U. Abbas, A. Abreu Aramburu, S. Accart, C. Aerts, J. J. Aguado, M. Ajaj, G. Altavilla, M. A. Álvarez, J. Álvarez Cid-Fuentes, J. Alves, R. I. Anderson, E. Anglada Varela, T. Antoja, M. Audard, D. Baines, S. G. Baker, L. Balaguer-Núñez, E. Balbinot, Z. Balog, C. Barache, D. Barbato, M. Barros, M. A. Barstow, S. Bartolomé, J. L. Bassilana, N. Bauchet, A. Baudesson-Stella, U. Becciani, M. Bellazzini, M. Bernet, S. Bertone, L. Bianchi, S. Blanco-Cuaresma, T. Boch, A. Bombrun, D. Bossini, S. Bouquillon, A. Bragaglia, L. Bramante, E. Breedt, A. Bressan, N. Brouillet, B. Bucciarelli, A. Burlacu, D. Busonero, A. G. Butkevich, R. Buzzi, E. Caffau, R. Cancelliere, H. Cánovas, T. Cantat-Gaudin, R. Carballo, T. Carlucci, M. I. Carnerero, J. M. Carrasco, L. Casamiquela, M. Castellani, A. Castro-Ginard, P. Castro Sampol, L. Chaoul, P. Charlot, L. Chemin, A. Chiavassa, M. R. L. Cioni, G. Comoretto, W. J. Cooper, T. Cornez, S. Cowell, F. Crifo, M. Crosta, C. Crowley, C. Dafonte, A. Dapergolas, M. David, P. David, P. de Laverny, F. De Luise, R. De March, J. De Ridder, R. de Souza, P. de Teodoro, A. de Torres, E. F. del Peloso, E. del Pozo, M. Delbo, A. Delgado, H. E. Delgado, J. B. Delisle, P. Di Matteo, S. Diakite, C. Diener, E. Distefano, C. Dolding, D. Eappachen, B. Edvardsson, H. Enke, P. Esquej, C. Fabre, M. Fabrizio, S. Faigler, G. Fedorets, P. Fernique, A. Fienga, F. Figueras, C. Fouron, F. Frakoudi, E. Fraile, F. Franke, M. Gai, D. Garabato, A. García-Gutierrez, M. García-Torres, A. Garofalo, P. Gavras, E. Gerlach, R. Geyer, P. Giacobbe, G. Gilmore, S. Girona, G. Giuffrida, R. Gomel, A. Gomez, I. Gonzalez-Santamaria, J. J. González-Vidal, M. Granvik, R. Gutiérrez-Sánchez, L. P. Guy, M. Hauser, M. Haywood, A. Helmi, S. L. Hidalgo, T. Hilger, N. Hładczuk, D. Hobbs, G. Holland, H. E. Huckle, G. Jasniewicz, P. G. Jonker, J. Juaristi Campillo, F. Julbe, L. Karbevska, P. Kervella, S. Khanna, A. Kochoska, M. Kontizas, G. Kordopatis, A. J. Korn, Z. Kostrzewa-Rutkowska, K. Kruszynska, S. Lambert, A. F. Lanza, Y. Lasne, J. F. Le Campion, Y. Le Fustec, Y. Lebreton, T. Lebzelter, S. Leccia, N. Leclerc, I. Lecoeur-Taibi, S. Liao, E. Licata, E. P. Lindstrøm, T. A. Lister, E. Livanou, A. Lobel, P. Madrero Pardo, S. Managau, R. G. Mann, J. M. Marchant, M. Marconi, M. M. S. Marcos Santos, S. Marinoni,

F. Marocco, D. J. Marshall, L. Martin Polo, J. M. Martín-Fleitas, A. Masip, D. Massari, A. Mastrobuono-Battisti, T. Mazeh, P. J. McMillan, S. Messina, D. Michalik, N. R. Millar, A. Mints, D. Molina, R. Molinaro, L. Molnár, P. Montegriffo, R. Mor, R. Morbidelli, T. Morel, D. Morris, A. F. Mulone, D. Munoz, T. Muraveva, C. P. Murphy, I. Musella, L. Noval, C. Ordénovic, G. Orrù, J. Osinde, C. Pagani, I. Pagano, L. Palaversa, P. A. Palicio, A. Panahi, M. Pawlak, X. Peñalosa Esteller, A. Penttilä, A. M. Piersimoni, F. X. Pineau, E. Plachy, G. Plum, E. Poggio, E. Poretti, E. Poujoulet, A. Prša, L. Pulone, E. Racero, S. Ragaini, M. Rainer, C. M. Raiteri, N. Rambaux, P. Ramos, M. Ramos-Lerate, P. Re Fiorentin, S. Regibo, C. Reydé, V. Ripepi, A. Riva, G. Rixon, N. Robichon, C. Robin, M. Roelens, L. Rohrbasser, M. Romero-Gómez, N. Rowell, F. Royer, K. A. Rybicki, G. Sadowski, A. Sagristà Sellés, J. Sahlmann, J. Salgado, E. Salguero, N. Samaras, V. Sanchez Gimenez, N. Sanna, R. Santoveña, M. Sarasso, M. Schultheis, E. Sciacca, M. Segol, J. C. Segovia, D. Ségransan, D. Semeux, S. Shahaf, H. I. Siddiqui, A. Siebert, L. Siltala, E. Slezak, R. L. Smart, E. Solano, F. Solitro, D. Souami, J. Souchay, A. Spagna, F. Spoto, I. A. Steele, H. Steidelmüller, C. A. Stephenson, M. Süveges, L. Szabados, E. Szegedi-Elek, F. Taris, G. Tauran, M. B. Taylor, R. Teixeira, W. Thuillot, N. Tonello, F. Torra, J. Torra, C. Turon, N. Unger, M. Vaillant, E. van Dillen, O. Vanel, A. Vecchiato, Y. Viala, D. Vicente, S. Voutsinas, M. Weiler, T. Wevers, Ł. Wyrzykowski, A. Yoldas, P. Yvard, H. Zhao, J. Zorec, S. Zucker, C. Zurbach, and T. Zwitter. Gaia Early Data Release 3. Summary of the contents and survey properties. *A&A*, 649:A1, May 2021. doi: [10.1051/0004-6361/202039657](https://doi.org/10.1051/0004-6361/202039657).

Gaia Collaboration, R. Drimmel, M. Romero-Gómez, L. Chemin, P. Ramos, E. Poggio, V. Ripepi, R. Andrae, R. Blomme, T. Cantat-Gaudin, A. Castro-Ginard, G. Clementini, F. Figueras, M. Fouesneau, Y. Frémat, K. Jardine, S. Khanna, A. Lobel, D. J. Marshall, T. Muraveva, A. G. A. Brown, A. Vallenari, T. Prusti, J. H. J. de Bruijne, F. Arenou, C. Babusiaux, M. Biermann, O. L. Creevey, C. Ducourant, D. W. Evans, L. Eyer, R. Guerra, A. Hutton, C. Jordi, S. A. Klioner, U. L. Lammers, L. Lindegren, X. Luri, F. Mignard, C. Panem, D. Pourbaix, S. Randich, P. Sartoretti, C. Soubiran, P. Tanga, N. A. Walton, C. A. L. Bailer-Jones, U. Bastian, F. Jansen, D. Katz, M. G. Lattanzi, F. van Leeuwen, J. Bakker, C. Cacciari, J. Castañeda, F. De Angeli, C. Fabricius, L. Galluccio, A. Guerrier, U. Heiter, E. Masana, R. Messineo, N. Mowlavi, C. Nicolas, K. Nienartowicz, F. Pailler, P. Panuzzo, F. Riclet, W. Roux, G. M. Seabroke, R. Sordo, F. Thévenin, G. Gracia-Abril, J. Portell, D. Teyssier, M. Altmann, M. Audard, I. Bellas-Velidis, K. Benson, J. Berthier, P. W. Burgess, D. Busonero, G. Busso, H. Cánovas, B. Carry, A. Cellino, N. Cheek, Y. Damerdji, M. Davidson, P. de Teodoro, M. Nuñez Campos, L. Delchambre, A. Dell’Oro, P. Esquej, J. Fernández-Hernández, E. Fraile, D. Garabato, P. García-Lario, E. Gosset, R. Haigron, J. L. Halbwachs, N. C. Hambly, D. L. Harrison, J. Hernández, D. Hestroffer, S. T. Hodgkin, B. Holl, K. Janßen, G. Jevardat de Fombelle, S. Jordan, A. Krone-Martins, A. C. Lanzafame, W. Löffler, O. Marchal, P. M. Marrese, A. Moitinho, K. Muinonen, P. Osborne, E. Pancino, T. Pauwels, A. Recio-Blanco, C. Reydé, M. Riello, L. Rimoldini, T. Roegiers, J. Rybizki, L. M. Sarro, C. Siopis, M. Smith, A. Sozzetti, E. Utrilla, M. van Leeuwen, U. Abbas, P. Ábrahám, A. Abreu Aramburu, C. Aerts, J. J. Aguado, M. Ajaj, F. Aldea-Montero, G. Altavilla, M. A. Álvarez, J. Alves, F. Anders, R. I. Anderson, E. Anglada Varela, T. Antoja, D. Baines, S. G. Baker, L. Balaguer-Núñez, E. Balbinot, Z. Balog, C. Barache, D. Barbato, M. Barros, M. A. Barstow, S. Bartolomé, J. L. Bassilana, N. Bauchet, U. Becciani, M. Bellazzini, A. Berihuete, M. Bernet, S. Bertone, L. Bianchi, A. Binnenfeld, S. Blanco-Cuaresma, T. Boch, A. Bom-

brun, D. Bossini, S. Bouquillon, A. Bragaglia, L. Bramante, E. Breedt, A. Bressan, N. Brouillet, E. Brugaletta, B. Bucciarelli, A. Burlacu, A. G. Butkevich, R. Buzzi, E. Caffau, R. Cancelliere, R. Carballo, T. Carlucci, M. I. Carnerero, J. M. Carrasco, L. Casamiquela, M. Castellani, L. Chaoul, P. Charlot, V. Chiaramida, A. Chiavassa, N. Chornay, G. Comoretto, G. Contursi, W. J. Cooper, T. Cornez, S. Cowell, F. Crifo, M. Cropper, M. Crosta, C. Crowley, C. Dafonte, A. Dapergolas, P. David, P. de Laverny, F. De Luise, R. De March, J. De Ridder, R. de Souza, A. de Torres, E. F. del Peloso, E. del Pozo, M. Delbo, A. Delgado, J. B. Delisle, C. Demouchy, T. E. Dharmawardena, P. Di Matteo, S. Diakite, C. Diener, E. Distefano, C. Dolding, H. Enke, C. Fabre, M. Fabrizio, S. Faigler, G. Fedorets, P. Fernique, Y. Fournier, C. Fouron, F. Fragkoudi, M. Gai, A. Garcia-Gutierrez, M. Garcia-Reinaldos, M. García-Torres, A. Garofalo, A. Gavel, P. Gavras, E. Gerlach, R. Geyer, P. Giacobbe, G. Gilmore, S. Girona, G. Giuffrida, R. Gomel, A. Gomez, J. González-Núñez, I. González-Santamaría, J. J. González-Vidal, M. Granvik, P. Guillout, J. Guiraud, R. Gutiérrez-Sánchez, L. P. Guy, D. Hatzidimitriou, M. Hauser, M. Haywood, A. Helmer, A. Helmi, M. H. Sarmiento, S. L. Hidalgo, N. Hładcuk, D. Hobbs, G. Holland, H. E. Huckle, G. Jasniewicz, A. Jean-Antoine Piccolo, Ó. Jiménez-Arranz, J. Juaristi Campillo, F. Julbe, L. Karbevska, P. Kervella, G. Kordopatis, A. J. Korn, Á. Kóspál, Z. Kostrzewska-Rutkowska, K. Kruszyńska, M. Kun, P. Laizeau, S. Lambert, A. F. Lanza, Y. Lasne, J. F. Le Campion, Y. Lebreton, T. Lebzelter, S. Leccia, N. Leclerc, I. Lecoeur-Taibi, S. Liao, E. L. Licata, H. E. P. Lindstrøm, T. A. Lister, E. Livanou, A. Lorca, C. Loup, P. Madrero Pardo, A. Magdaleno Romeo, S. Managau, R. G. Mann, M. Manteiga, J. M. Marchant, M. Marconi, J. Marcos, M. M. S. Marcos Santos, D. Marín Pina, S. Marinoni, F. Marocco, L. Martin Polo, J. M. Martín-Fleitas, G. Marton, N. Mary, A. Masip, D. Massari, A. Mastrobuono-Battisti, T. Mazeh, P. J. McMillan, S. Messina, D. Michalik, N. R. Millar, A. Mints, D. Molina, R. Molinaro, L. Molnár, G. Monari, M. Monguió, P. Montegriffo, A. Montero, R. Mor, A. Mora, R. Morbidelli, T. Morel, D. Morris, C. P. Murphy, I. Musella, Z. Nagy, L. Noval, F. Ocaña, A. Ogden, C. Ordenvovic, J. O. Osinde, C. Pagani, I. Pagano, L. Palaversa, P. A. Palicio, L. Pallas-Quintela, A. Panahi, S. Payne-Wardenaar, X. Peñalosa Esteller, A. Penttilä, B. Pichon, A. M. Piersimoni, F. X. Pineau, E. Plachy, G. Plum, A. Prša, L. Pulone, E. Racero, S. Ragagni, M. Rainer, C. M. Raiteri, M. Ramos-Lerate, P. Re Fiorentin, S. Regibo, P. J. Richards, C. Rios Diaz, A. Riva, H. W. Rix, G. Rixon, N. Robichon, A. C. Robin, C. Robin, M. Roelens, H. R. O. Rogues, L. Rohrbasser, N. Rowell, F. Royer, D. Ruz Mieres, K. A. Rybicki, G. Sadowski, A. Sáez Núñez, A. Sagristà Sellés, J. Sahlmann, E. Salguero, N. Samaras, V. Sanchez Gimenez, N. Sanna, R. Santovenia, M. Sarasso, M. S. Schultheis, E. Sciacca, M. Segol, J. C. Segovia, D. Ségransan, D. Semeux, S. Shahaf, H. I. Siddiqui, A. Siebert, L. Siltala, A. Silvelo, E. Slezak, I. Slezak, R. L. Smart, O. N. Snaith, E. Solano, F. Solitro, D. Souami, J. Souchay, A. Spagna, L. Spina, F. Spoto, I. A. Steele, H. Steidelmüller, C. A. Stephenson, M. Süveges, J. Surdej, L. Szabados, E. Szegedi-Elek, F. Taris, M. B. Taylor, R. Teixeira, L. Tolomei, N. Tonello, F. Torra, J. Torra, G. Torralba Elipe, M. Trabucchi, A. T. Tsounis, C. Turon, A. Ulla, N. Unger, M. V. Vaillant, E. van Dillen, W. van Reeven, O. Vanel, A. Vecchiato, Y. Viala, D. Vicente, S. Voutsinas, M. Weiler, T. Wevers, L. Wyrzykowski, A. Yoldas, P. Yvard, H. Zhao, J. Zorec, S. Zucker, and T. Zwitter. Gaia Data Release 3. Mapping the asymmetric disc of the Milky Way. *A&A*, 674:A37, June 2023a. doi: [10.1051/0004-6361/202243797](https://doi.org/10.1051/0004-6361/202243797).

M. Davidson, F. De Angeli, J. Hernández, F. Torra, M. Ramos-Lerate, C. Babusiaux, M. Biermann, C. Crowley, D. W. Evans, L. Lindegren, J. M. Martín-Fleitas, L. Palaversa, D. Ruz Mieres, K. Tisanić, A. G. A. Brown, A. Vallenari, T. Prusti, J. H. J. de Bruijne, F. Arenou, A. Barbier, O. L. Creevey, C. Ducourant, L. Eyer, R. Guerra, A. Hutton, C. Jordi, S. A. Klioner, U. Lammers, X. Luri, F. Mignard, S. Randich, P. Sartoretti, R. Smiljanic, P. Tanga, N. A. Walton, C. A. L. Bailer-Jones, U. Bastian, M. Cropper, R. Drimmel, D. Katz, C. Soubiran, F. van Leeuwen, M. Audard, J. Bakker, R. Blomme, C. Fabricius, M. Fouesneau, Y. Frémat, L. Galluccio, A. Guerrier, E. Masana, R. Messineo, C. Nicolas, K. Nienartowicz, F. Pailler, P. Panuzzo, F. Riclet, W. Roux, G. M. Seabroke, R. Sordo, F. Thévenin, G. Gracia-Abril, J. Portell, D. Teyssier, M. Altmann, K. Benson, J. Berthier, P. W. Burgess, D. Busonero, G. Busso, H. Cánovas, B. Carry, N. Cheek, G. Clementini, Y. Damerdji, P. de Teodoro, L. Delchambre, A. Dell’Oro, E. Fraile Garcia, D. Garabato, P. García-Lario, N. Garralda Torres, P. Gavras, R. Haigron, N. C. Hambly, D. L. Harrison, D. Hatzidimitriou, S. T. Hodgkin, B. Holl, S. Jamal, S. Jordan, A. Krone-Martins, A. C. Lanzafame, W. Löffler, A. Lorca, O. Marchal, P. M. Marrese, A. Moitinho, K. Muinonen, M. Nuñez Campos, I. Oreshina-Slezak, P. Osborne, E. Pancino, T. Pauwels, A. Recio-Blanco, M. Riello, L. Rimoldini, A. C. Robin, T. Roegiers, L. M. Sarro, M. Schultheis, C. Siopis, M. Smith, A. Sozzetti, E. Utrilla, M. van Leeuwen, U. Abbas, P. Ábrahám, A. Abreu Aramburu, C. Aerts, G. Altavilla, M. A. Álvarez, J. Alves, F. Anders, R. I. Anderson, T. Antoja, D. Baines, S. G. Baker, Z. Balog, C. Barache, D. Barbato, M. Barros, M. A. Barstow, S. Bartolomé, D. Bashi, N. Bauchet, N. Baudeau, U. Becciani, L. R. Bedin, I. Bellas-Velidis, M. Bellazzini, W. Beordo, A. Berihuete, M. Bernet, C. Bertolotto, S. Bertone, L. Bianchi, A. Binnenfeld, A. Blazere, T. Boch, A. Bombrun, S. Bouquillon, A. Bragaglia, J. Braine, L. Bramante, E. Breedt, A. Bressan, N. Brouillet, E. Brugalette, B. Bucciarelli, A. G. Butkevich, R. Buzzi, E. Caffau, R. Cancelliere, S. Cannizzo, T. Cantat-Gaudin, R. Carballo, T. Carlucci, M. I. Carnerero, J. M. Carrasco, J. Carretero, S. Carton, L. Casamiquela, M. Castellani, A. Castro-Ginard, V. Cesare, P. Charlot, L. Chemin, V. Chiaramida, A. Chiavassa, N. Chornay, R. Collins, G. Contursi, W. J. Cooper, T. Cornez, M. Crosta, C. Dafonte, P. de Laverny, F. De Luise, R. De March, R. de Souza, A. de Torres, E. F. del Peloso, M. Delbo, A. Delgado, T. E. Dharmawardena, S. Diakite, C. Diener, E. Distefano, C. Dolding, K. Dsilva, J. Durán, H. Enke, P. Esquej, C. Fabre, M. Fabrizio, S. Faigler, M. Fatović, G. Fedorets, J. Fernández-Hernández, P. Fernique, F. Figueras, Y. Fournier, C. Fouron, M. Gai, M. Galinier, A. Garcia-Gutierrez, M. García-Torres, A. Garofalo, E. Gerlach, R. Geyer, P. Giacobbe, G. Gilmore, S. Girona, G. Giuffrida, R. Gomel, A. Gomez, J. González-Núñez, I. González-Santamaría, E. Gosset, M. Granvik, V. Gregori Barrera, R. Gutiérrez-Sánchez, M. Haywood, A. Helmer, A. Helmi, K. Henares, S. L. Hidalgo, T. Hilger, D. Hobbs, C. Hottier, H. E. Huckle, M. Jabłońska, F. Jansen, Ó. Jiménez-Arranz, J. Juaristi Campillo, S. Khanna, G. Kordopatis, Á. Kóspál, M. Kun, S. Lambert, A. F. Lanza, J. F. Le Campion, Y. Lebreton, T. Lebzelter, S. Leccia, I. Lecoeur-Taibi, G. Lecoutre, S. Liao, L. Liberato, E. Licata, H. E. P. Lindstrøm, T. A. Lister, E. Livanou, A. Lobel, C. Loup, L. Mahy, R. G. Mann, M. Manteiga, J. M. Marchant, M. Marconi, D. Marín Pina, S. Marinoni, D. J. Marshall, J. Martín Lozano, G. Marton, N. Mary, A. Masip, D. Massari, A. Mastrobuono-Battisti, T. Mazeh, P. J. McMillan, J. Meichsner, S. Messina, D. Michalik, N. R. Millar, D. Molina, R. Molinaro, L. Molnár, G. Monari, M. Monguió, P. Montegriffo, A. Montero, R. Mor, A. Mora, R. Morbidelli, T. Morel, D. Morris, N. Mowlavi, D. Munoz, T. Muraveva, C. P. Murphy, I. Musella,

Z. Nagy, S. Nieto, L. Noval, A. Ogden, C. Ordenovic, C. Pagani, I. Pagano, P. A. Palicio, L. Pallas-Quintela, A. Panahi, C. Panem, S. Payne-Wardenaar, L. Pegoraro, A. Penttilä, P. Pesciullesi, A. M. Piersimoni, M. Pinamonti, F. X. Pineau, E. Plachy, G. Plum, E. Poggio, D. Pourbaix, A. Prša, L. Pulone, E. Racero, M. Rainer, C. M. Raiteri, P. Ramos, M. Ratajczak, P. Re Fiorentin, S. Regibo, C. Reylé, V. Ripepi, A. Riva, H. W. Rix, G. Rixon, N. Robichon, C. Robin, M. Romero-Gómez, N. Rowell, F. Royer, K. A. Rybicki, G. Sadowski, A. Sáez Núñez, A. Sagristà Sellés, J. Sahlmann, V. Sanchez Gimenez, N. Sanna, R. Santoveña, M. Sarasso, C. Sarrate Riera, E. Sciaccia, J. C. Segovia, D. Ségransan, S. Shahaf, A. Siebert, L. Siltala, E. Slezak, R. L. Smart, O. N. Snaith, E. Solano, F. Solitro, D. Souami, J. Souchay, L. Spina, E. Spitoni, F. Spoto, L. A. Squillante, I. A. Steele, H. Steidelmüller, J. Surdej, L. Szabados, F. Taris, M. B. Taylor, R. Teixeira, L. Tolomei, G. Torralba Elipe, M. Trabucchi, M. Tsantaki, A. Ulla, N. Unger, O. Vanel, A. Vecchiato, D. Vicente, S. Voutsinas, M. Weiler, Ł. Wyrzykowski, H. Zhao, J. Zorec, T. Zwitter, L. Balaguer-Núñez, N. Leclerc, S. Morgenthaler, G. Robert, and S. Zucker. Gaia Focused Product Release: Sources from Service Interface Function image analysis. Half a million new sources in omega Centauri. *A&A*, 680:A35, Dec. 2023b. doi: [10.1051/0004-6361/202347203](https://doi.org/10.1051/0004-6361/202347203).

K. Gebhardt, D. Richstone, J. Kormendy, T. R. Lauer, E. A. Ajhar, R. Bender, A. Dressler, S. M. Faber, C. Grillmair, J. Magorrian, and S. Tremaine. Axisymmetric, Three-Integral Models of Galaxies: A Massive Black Hole in NGC 3379. *AJ*, 119: 1157–1171, Mar. 2000. doi: [10.1086/301240](https://doi.org/10.1086/301240).

I. Y. Georgiev and T. Böker. Nuclear star clusters in 228 spiral galaxies in the HST/WFPC2 archive: catalogue and comparison to other stellar systems. *MNRAS*, 441(4):3570–3590, July 2014. doi: [10.1093/mnras/stu797](https://doi.org/10.1093/mnras/stu797).

E. H. Geyer, U. Hopp, and B. Nelles. Ellipticity variations within some globular clusters of the galaxy and the Magellanic Clouds. *A&A*, 125:359–367, Sept. 1983. URL <https://ui.adsabs.harvard.edu/abs/1983A&A...125..359G>.

B. Giesers, S. Kamann, S. Dreizler, T.-O. Husser, A. Askar, F. Göttgens, J. Brinchmann, M. Latour, P. M. Weilbacher, M. Wendt, and M. M. Roth. A stellar census in globular clusters with MUSE: Binaries in NGC 3201. *A&A*, 632:A3, Dec. 2019. doi: [10.1051/0004-6361/201936203](https://doi.org/10.1051/0004-6361/201936203).

S. Gillessen, P. M. Plewa, F. Eisenhauer, R. Sari, I. Waisberg, M. Habibi, O. Pfuhl, E. George, J. Dexter, S. von Fellenberg, T. Ott, and R. Genzel. An Update on Monitoring Stellar Orbits in the Galactic Center. *ApJ*, 837(1):30, Mar. 2017. doi: [10.3847/1538-4357/aa5c41](https://doi.org/10.3847/1538-4357/aa5c41).

L. Girardi, J. Dalcanton, B. Williams, R. de Jong, C. Gallart, M. Monelli, M. A. T. Groenewegen, J. A. Holtzman, K. A. G. Olsen, A. C. Seth, D. R. Weisz, and ANGST/ANGRRR Collaboration. Revised Bolometric Corrections and Interstellar Extinction Coefficients for the ACS and WFPC2 Photometric Systems. *PASP*, 120(867):583, May 2008. doi: [10.1086/588526](https://doi.org/10.1086/588526).

J. Goodman and J. Weare. Ensemble samplers with affine invariance. *Communications in Applied Mathematics and Computational Science*, 5(1):65–80, Jan. 2010. doi: [10.2140/camcos.2010.5.65](https://doi.org/10.2140/camcos.2010.5.65).

D. A. Grabelsky, R. S. Cohen, L. Bronfman, P. Thaddeus, and J. May. Molecular Clouds in the Carina Arm: Large-Scale Properties of Molecular Gas and Comparison with H i. *ApJ*, 315:122, Apr. 1987. doi: [10.1086/165118](https://doi.org/10.1086/165118).

Gravity Collaboration, R. Abuter, A. Amorim, N. Anugu, M. Bauböck, M. Benisty, J. P. Berger, N. Blind, H. Bonnet, W. Brandner, A. Buron, C. Collin, F. Chapron, Y. Clénet, V. Coudé Du Foresto, P. T. de Zeeuw, C. Deen, F. Delplancke-Ströbele, R. Dembet, J. Dexter, G. Duvert, A. Eckart, F. Eisenhauer, G. Finger, N. M. Förster Schreiber, P. Fédou, P. Garcia, R. Garcia Lopez, F. Gao, E. Gendron, R. Genzel, S. Gillessen, P. Gordo, M. Habibi, X. Haubois, M. Haug, F. Haußmann, T. Henning, S. Hippler, M. Horrobin, Z. Hubert, N. Hubin, A. Jimenez Rosales, L. Jochum, K. Jocou, A. Kaufer, S. Kellner, S. Kendrew, P. Kervella, Y. Kok, M. Kulas, S. Lacour, V. Lapeyrère, B. Lazareff, J. B. Le Bouquin, P. Léna, M. Lippa, R. Lenzen, A. Mérand, E. Müller, U. Neumann, T. Ott, L. Palanca, T. Paumard, L. Pasquini, K. Perraut, G. Perrin, O. Pfuhl, P. M. Plewa, S. Rabien, A. Ramírez, J. Ramos, C. Rau, G. Rodríguez-Coira, R. R. Rohloff, G. Rousset, J. Sanchez-Bermudez, S. Scheithauer, M. Schöller, N. Schuler, J. Spyromilio, O. Straub, C. Straubmeier, E. Sturm, L. J. Tacconi, K. R. W. Tristram, F. Vincent, S. von Fellenberg, I. Wank, I. Waisberg, F. Widmann, E. Wieprecht, M. Wiest, E. Wiezorek, J. Woillez, S. Yazici, D. Ziegler, and G. Zins. Detection of the gravitational redshift in the orbit of the star S2 near the Galactic centre massive black hole. *A&A*, 615:L15, July 2018. doi: [10.1051/0004-6361/201833718](https://doi.org/10.1051/0004-6361/201833718).

Gravity Collaboration, R. Abuter, A. Amorim, M. Bauböck, J. P. Berger, H. Bonnet, W. Brandner, Y. Clénet, V. Coudé Du Foresto, P. T. de Zeeuw, J. Dexter, G. Duvert, A. Eckart, F. Eisenhauer, N. M. Förster Schreiber, P. Garcia, F. Gao, E. Gendron, R. Genzel, O. Gerhard, S. Gillessen, M. Habibi, X. Haubois, T. Henning, S. Hippler, M. Horrobin, A. Jiménez-Rosales, L. Jocou, P. Kervella, S. Lacour, V. Lapeyrère, J. B. Le Bouquin, P. Léna, T. Ott, T. Paumard, K. Perraut, G. Perrin, O. Pfuhl, S. Rabien, G. Rodriguez Coira, G. Rousset, S. Scheithauer, A. Sternberg, O. Straub, C. Straubmeier, E. Sturm, L. J. Tacconi, F. Vincent, S. von Fellenberg, I. Waisberg, F. Widmann, E. Wieprecht, E. Wiezorek, J. Woillez, and S. Yazici. A geometric distance measurement to the Galactic center black hole with 0.3% uncertainty. *A&A*, 625:L10, May 2019. doi: [10.1051/0004-6361/201935656](https://doi.org/10.1051/0004-6361/201935656).

J. E. Greene, J. Strader, and L. C. Ho. Intermediate-Mass Black Holes. *ARA&A*, 58: 257–312, Aug. 2020. doi: [10.1146/annurev-astro-032620-021835](https://doi.org/10.1146/annurev-astro-032620-021835).

G. Gyuk, C. Flynn, and N. W. Evans. Star Counts and the Warped and Flaring Milky Way Disk. *ApJ*, 521(1):190–193, Aug. 1999. doi: [10.1086/307542](https://doi.org/10.1086/307542).

M. Häberle, N. Neumayer, A. Bellini, M. Libralato, C. Clontz, A. C. Seth, M. S. Nitschai, S. Kamann, M. Alfaro-Cuello, J. Anderson, S. Dreizler, A. Feldmeier-Krause, N. Kacharov, M. Latour, A. Milone, R. Pechetti, G. van de Ven, and K. Voggel. oMEGACat II – Photometry and proper motions for 1.4 million stars in Omega Centauri and its rotation in the plane of the sky. *arXiv e-prints*, art. arXiv:2404.03722, Apr. 2024a. URL <https://arxiv.org/abs/2404.03722>.

M. Häberle, N. Neumayer, A. Seth, A. Bellini, M. Libralato, H. Baumgardt, M. Whitaker, A. Dumont, M. Alfaro-Cuello, A. J., C. Clontz, K. N., S. Kamann, A. Feldmeier-Krause,

- A. P. Milone, M. S. Nitschai, R. Pechetti, and G. van de Ven. Fast-moving stars around an intermediate-mass black hole in ω Centauri. *under review*, 2024b.
- J. H. J. Hagen, A. Helmi, P. T. de Zeeuw, and L. Posti. The tilt of the velocity ellipsoid in the Milky Way with Gaia DR2. *A&A*, 629:A70, Feb. 2019. doi: [10.1051/0004-6361/201935264](https://doi.org/10.1051/0004-6361/201935264).
- E. Halley. An Account of several Nebulae or lucid Spots like Clouds, lately discovered among the Fixt Stars by help of the Telescope. *Philosophical Transactions of the Royal Society of London Series I*, 29(347):390–392, Jan. 1715. doi: [10.1098/rstl.1714.0046](https://doi.org/10.1098/rstl.1714.0046).
- J. J. Han, C. Conroy, and L. Hernquist. A tilted dark halo origin of the Galactic disk warp and flare. *Nature Astronomy*, 7:1481–1485, Dec. 2023. doi: [10.1038/s41550-023-02076-9](https://doi.org/10.1038/s41550-023-02076-9).
- C. R. Harris, K. J. Millman, S. J. van der Walt, R. Gommers, P. Virtanen, D. Cournapeau, E. Wieser, J. Taylor, S. Berg, N. J. Smith, R. Kern, M. Picus, S. Hoyer, M. H. van Kerkwijk, M. Brett, A. Haldane, J. F. del Río, M. Wiebe, P. Peterson, P. Gérard-Marchant, K. Sheppard, T. Reddy, W. Weckesser, H. Abbasi, C. Gohlke, and T. E. Oliphant. Array programming with NumPy. *Nature*, 585(7825):357–362, Sept. 2020. doi: [10.1038/s41586-020-2649-2](https://doi.org/10.1038/s41586-020-2649-2). URL <https://doi.org/10.1038/s41586-020-2649-2>.
- W. E. Harris. A Catalog of Parameters for Globular Clusters in the Milky Way. *AJ*, 112: 1487, Oct. 1996. doi: [10.1086/118116](https://doi.org/10.1086/118116).
- W. E. Harris. A New Catalog of Globular Clusters in the Milky Way. *arXiv e-prints*, art. arXiv:1012.3224, Dec. 2010. doi: [10.48550/arXiv.1012.3224](https://doi.org/10.48550/arXiv.1012.3224).
- M. Haywood, P. Di Matteo, M. D. Lehnert, D. Katz, and A. Gómez. The age structure of stellar populations in the solar vicinity. Clues of a two-phase formation history of the Milky Way disk. *A&A*, 560:A109, Dec. 2013. doi: [10.1051/0004-6361/201321397](https://doi.org/10.1051/0004-6361/201321397).
- A. Helmi. Streams, Substructures, and the Early History of the Milky Way. *ARA&A*, 58:205–256, Aug. 2020. doi: [10.1146/annurev-astro-032620-021917](https://doi.org/10.1146/annurev-astro-032620-021917).
- A. Helmi and S. D. M. White. Simple dynamical models of the Sagittarius dwarf galaxy. *MNRAS*, 323(3):529–536, May 2001. doi: [10.1046/j.1365-8711.2001.04238.x](https://doi.org/10.1046/j.1365-8711.2001.04238.x).
- A. Helmi, C. Babusiaux, H. H. Koppelman, D. Massari, J. Veljanoski, and A. G. A. Brown. The merger that led to the formation of the Milky Way’s inner stellar halo and thick disk. *Nature*, 563(7729):85–88, Oct. 2018. doi: [10.1038/s41586-018-0625-x](https://doi.org/10.1038/s41586-018-0625-x).
- M. Hilker, A. Kayser, T. Richtler, and P. Willemse. The extended star formation history of ω Centauri. *A&A*, 422:L9–L12, July 2004. doi: [10.1051/0004-6361:20040188](https://doi.org/10.1051/0004-6361:20040188).
- D. W. Hogg, A.-C. Eilers, and H.-W. Rix. Spectrophotometric Parallaxes with Linear Models: Accurate Distances for Luminous Red-giant Stars. *AJ*, 158(4):147, Oct. 2019. doi: [10.3847/1538-3881/ab398c](https://doi.org/10.3847/1538-3881/ab398c).
- N. Hoyer, N. Neumayer, I. Y. Georgiev, A. C. Seth, and J. E. Greene. The nucleation fraction of local volume galaxies. *MNRAS*, 507(3):3246–3266, Nov. 2021. doi: [10.1093/mnras/stab2277](https://doi.org/10.1093/mnras/stab2277).

- J. D. Hunter. Matplotlib: A 2d graphics environment. *Computing in Science & Engineering*, 9(3):90–95, 2007. doi: [10.1109/MCSE.2007.55](https://doi.org/10.1109/MCSE.2007.55).
- T. O. Husser, S. Wende-von Berg, S. Dreizler, D. Homeier, A. Reiners, T. Barman, and P. H. Hauschildt. A new extensive library of PHOENIX stellar atmospheres and synthetic spectra. *A&A*, 553:A6, May 2013. doi: [10.1051/0004-6361/201219058](https://doi.org/10.1051/0004-6361/201219058).
- T.-O. Husser, S. Kamann, S. Dreizler, M. Wendt, N. Wulff, R. Bacon, L. Wisotzki, J. Brinchmann, P. M. Weilbacher, M. M. Roth, and A. Monreal-Ibero. MUSE crowded field 3D spectroscopy of over 12 000 stars in the globular cluster NGC 6397. I. The first comprehensive HRD of a globular cluster. *A&A*, 588:A148, Apr. 2016. doi: [10.1051/0004-6361/201526949](https://doi.org/10.1051/0004-6361/201526949).
- T.-O. Husser, M. Latour, J. Brinchmann, S. Dreizler, B. Giesers, F. Göttgens, S. Kamann, M. M. Roth, P. M. Weilbacher, and M. Wendt. A stellar census in globular clusters with MUSE. Extending the CaT-metallicity relation below the horizontal branch and applying it to multiple populations. *A&A*, 635:A114, Mar. 2020. doi: [10.1051/0004-6361/201936508](https://doi.org/10.1051/0004-6361/201936508).
- R. Ibata, K. Malhan, W. Tenachi, A. Ardern-Arentsen, M. Bellazzini, P. Bianchini, P. Bonifacio, E. Caffau, F. Diakogiannis, R. Errani, B. Famaey, S. Ferrone, N. Martin, P. di Matteo, G. Monari, F. Renaud, E. Starkenburg, G. Thomas, A. Viswanathan, and Z. Yuan. Charting the Galactic acceleration field II. A global mass model of the Milky Way from the STREAMFINDER Atlas of Stellar Streams detected in Gaia DR3. *arXiv e-prints*, art. arXiv:2311.17202, Nov. 2023. doi: [10.48550/arXiv.2311.17202](https://doi.org/10.48550/arXiv.2311.17202).
- R. A. Ibata, R. F. G. Wyse, G. Gilmore, M. J. Irwin, and N. B. Suntzeff. The Kinematics, Orbit, and Survival of the Sagittarius Dwarf Spheroidal Galaxy. *AJ*, 113:634–655, Feb. 1997. doi: [10.1086/118283](https://doi.org/10.1086/118283).
- R. A. Ibata, M. Bellazzini, K. Malhan, N. Martin, and P. Bianchini. Identification of the long stellar stream of the prototypical massive globular cluster ω Centauri. *Nature Astronomy*, 3:667–672, Apr. 2019. doi: [10.1038/s41550-019-0751-x](https://doi.org/10.1038/s41550-019-0751-x).
- K. Inayoshi, E. Visbal, and Z. Haiman. The Assembly of the First Massive Black Holes. *ARA&A*, 58:27–97, Aug. 2020. doi: [10.1146/annurev-astro-120419-014455](https://doi.org/10.1146/annurev-astro-120419-014455).
- J. Janz, M. A. Norris, D. A. Forbes, A. Huxor, A. J. Romanowsky, M. J. Frank, C. G. Escudero, F. R. Faifer, J. C. Forte, S. J. Kannappan, C. Maraston, J. P. Brodie, J. Strader, and B. R. Thompson. The AIMSS Project - III. The stellar populations of compact stellar systems. *MNRAS*, 456(1):617–632, Feb. 2016. doi: [10.1093/mnras/stv2636](https://doi.org/10.1093/mnras/stv2636).
- J. H. Jeans. On the theory of star-streaming and the structure of the universe. *MNRAS*, 76:70–84, Dec. 1915. doi: [10.1093/mnras/76.2.70](https://doi.org/10.1093/mnras/76.2.70).
- J. H. Jeans. The Motions of Stars in a Kapteyn Universe. *MNRAS*, 82:122–132, Jan. 1922. doi: [10.1093/mnras/82.3.122](https://doi.org/10.1093/mnras/82.3.122).
- Y. Jin, L. Zhu, R. J. Long, S. Mao, D. Xu, H. Li, and G. van de Ven. Evaluating the ability of triaxial Schwarzschild modelling to estimate properties of galaxies from the Illustris simulation. *MNRAS*, 486(4):4753–4772, Jul 2019. doi: [10.1093/mnras/stz1170](https://doi.org/10.1093/mnras/stz1170).

- C. I. Johnson and C. A. Pilachowski. Chemical Abundances for 855 Giants in the Globular Cluster Omega Centauri (NGC 5139). *ApJ*, 722(2):1373–1410, Oct. 2010. doi: [10.1088/0004-637X/722/2/1373](https://doi.org/10.1088/0004-637X/722/2/1373).
- C. I. Johnson, A. K. Dupree, M. Mateo, I. Bailey, John I., E. W. Olszewski, and M. G. Walker. The Most Metal-poor Stars in Omega Centauri (NGC 5139). *AJ*, 159(6):254, June 2020. doi: [10.3847/1538-3881/ab8819](https://doi.org/10.3847/1538-3881/ab8819).
- S.-J. Joo and Y.-W. Lee. Star Formation Histories of Globular Clusters with Multiple Populations. I. ω CEN, M22, and NGC 1851. *ApJ*, 762(1):36, Jan. 2013. doi: [10.1088/0004-637X/762/1/36](https://doi.org/10.1088/0004-637X/762/1/36).
- Y. C. Joshi. Displacement of the Sun from the Galactic plane. *MNRAS*, 378:768–776, June 2007. doi: [10.1111/j.1365-2966.2007.11831.x](https://doi.org/10.1111/j.1365-2966.2007.11831.x).
- M. Jurić, Ž. Ivezić, A. Brooks, R. H. Lupton, D. Schlegel, D. Finkbeiner, N. Padmanabhan, N. Bond, B. Sesar, C. M. Rockosi, G. R. Knapp, J. E. Gunn, T. Sumi, D. P. Schneider, J. C. Barentine, H. J. Brewington, J. Brinkmann, M. Fukugita, M. Harvanek, S. J. Kleinman, J. Krzesinski, D. Long, E. H. Neilsen, Jr., A. Nitta, S. A. Snedden, and D. G. York. The Milky Way Tomography with SDSS. I. Stellar Number Density Distribution. *ApJ*, 673:864–914, Feb. 2008. doi: [10.1086/523619](https://doi.org/10.1086/523619).
- N. Kacharov, N. Neumayer, A. C. Seth, M. Cappellari, R. McDermid, C. J. Walcher, and T. Böker. Stellar populations and star formation histories of the nuclear star clusters in six nearby galaxies. *MNRAS*, 480(2):1973–1998, Oct. 2018. doi: [10.1093/mnras/sty1985](https://doi.org/10.1093/mnras/sty1985).
- N. Kacharov, M. Alfaro-Cuello, N. Neumayer, N. Lützgendorf, L. L. Watkins, A. Mastrobuono-Battisti, S. Kamann, G. van de Ven, A. C. Seth, K. T. Voggel, I. Y. Georgiev, R. Leaman, P. Bianchini, T. Böker, and S. Mieske. A Deep View into the Nucleus of the Sagittarius Dwarf Spheroidal Galaxy with MUSE. III. Discrete Multi-component Population-dynamical Models Based on the Jeans Equations. *ApJ*, 939(2):118, Nov. 2022. doi: [10.3847/1538-4357/ac9280](https://doi.org/10.3847/1538-4357/ac9280).
- S. Kamann, L. Wisotzki, and M. M. Roth. Resolving stellar populations with crowded field 3D spectroscopy. *A&A*, 549:A71, Jan. 2013. doi: [10.1051/0004-6361/201220476](https://doi.org/10.1051/0004-6361/201220476).
- S. Kamann, T. O. Husser, J. Brinchmann, E. Emsellem, P. M. Weilbacher, L. Wisotzki, M. Wendt, D. Krajnović, M. M. Roth, R. Bacon, and S. Dreizler. MUSE crowded field 3D spectroscopy of over 12 000 stars in the globular cluster NGC 6397. II. Probing the internal dynamics and the presence of a central black hole. *A&A*, 588:A149, Apr. 2016. doi: [10.1051/0004-6361/201527065](https://doi.org/10.1051/0004-6361/201527065).
- S. Kamann, T. O. Husser, S. Dreizler, E. Emsellem, P. M. Weilbacher, S. Martens, R. Bacon, M. den Brok, B. Giesers, D. Krajnović, M. M. Roth, M. Wendt, and L. Wisotzki. A stellar census in globular clusters with MUSE: The contribution of rotation to cluster dynamics studied with 200 000 stars. *MNRAS*, 473(4):5591–5616, Feb. 2018. doi: [10.1093/mnras/stx2719](https://doi.org/10.1093/mnras/stx2719).
- F. J. Kerr. A Magellanic effect on the galaxy. *AJ*, 62:93–93, May 1957. doi: [10.1086/107466](https://doi.org/10.1086/107466).

- N. V. Kharchenko, A. E. Piskunov, E. Schilbach, S. Röser, and R. D. Scholz. Global survey of star clusters in the Milky Way. II. The catalogue of basic parameters. *A&A*, 558:A53, Oct. 2013. doi: [10.1051/0004-6361/201322302](https://doi.org/10.1051/0004-6361/201322302).
- S. Khoperskov, P. Di Matteo, O. Gerhard, D. Katz, M. Haywood, F. Combes, P. Berczik, and A. Gomez. The echo of the bar buckling: Phase-space spirals in Gaia Data Release 2. *A&A*, 622:L6, Feb. 2019. doi: [10.1051/0004-6361/201834707](https://doi.org/10.1051/0004-6361/201834707).
- M. Kilic, J. A. Munn, H. C. Harris, T. von Hippel, J. W. Liebert, K. A. Williams, E. Jeffery, and S. DeGennaro. The Ages of the Thin Disk, Thick Disk, and the Halo from Nearby White Dwarfs. *ApJ*, 837(2):162, Mar. 2017. doi: [10.3847/1538-4357/aa62a5](https://doi.org/10.3847/1538-4357/aa62a5).
- B. Kimmig, A. Seth, I. I. Ivans, J. Strader, N. Caldwell, T. Anderton, and D. Gregersen. Measuring Consistent Masses for 25 Milky Way Globular Clusters. *AJ*, 149(2):53, Feb. 2015. doi: [10.1088/0004-6256/149/2/53](https://doi.org/10.1088/0004-6256/149/2/53).
- J. R. King, A. Stephens, A. M. Boesgaard, and C. Deliyannis. Keck HIRES Spectroscopy of M92 Subgiants: Surprising Abundances near the Turnoff. *AJ*, 115(2):666–684, Feb. 1998. doi: [10.1086/300209](https://doi.org/10.1086/300209).
- H. H. Koppelman, A. Helmi, D. Massari, A. M. Price-Whelan, and T. K. Starkenburg. Multiple retrograde substructures in the Galactic halo: A shattered view of Galactic history. *A&A*, 631:L9, Nov. 2019a. doi: [10.1051/0004-6361/201936738](https://doi.org/10.1051/0004-6361/201936738).
- H. H. Koppelman, A. Helmi, D. Massari, A. M. Price-Whelan, and T. K. Starkenburg. Multiple retrograde substructures in the Galactic halo: A shattered view of Galactic history. *A&A*, 631:L9, Nov. 2019b. doi: [10.1051/0004-6361/201936738](https://doi.org/10.1051/0004-6361/201936738).
- H. H. Koppelman, A. Helmi, D. Massari, S. Roelenga, and U. Bastian. Characterization and history of the Helmi streams with Gaia DR2. *A&A*, 625:A5, May 2019c. doi: [10.1051/0004-6361/201834769](https://doi.org/10.1051/0004-6361/201834769).
- J. Kormendy and L. C. Ho. Coevolution (Or Not) of Supermassive Black Holes and Host Galaxies. *ARA&A*, 51(1):511–653, Aug. 2013. doi: [10.1146/annurev-astro-082708-101811](https://doi.org/10.1146/annurev-astro-082708-101811).
- J. Kormendy and J. Kennicutt, Robert C. Secular Evolution and the Formation of Pseudobulges in Disk Galaxies. *ARA&A*, 42(1):603–683, Sept. 2004. doi: [10.1146/annurev.astro.42.053102.134024](https://doi.org/10.1146/annurev.astro.42.053102.134024).
- A. J. Korn, F. Grundahl, O. Richard, L. Mashonkina, P. S. Barklem, R. Collet, B. Gustafsson, and N. Piskunov. Atomic Diffusion and Mixing in Old Stars. I. Very Large Telescope FLAMES-UVES Observations of Stars in NGC 6397. *ApJ*, 671(1):402–419, Dec. 2007. doi: [10.1086/523098](https://doi.org/10.1086/523098).
- D. Krajnović, M. Cappellari, P. T. de Zeeuw, and Y. Copin. Kinemetry: a generalization of photometry to the higher moments of the line-of-sight velocity distribution. *MNRAS*, 366(3):787–802, Mar. 2006. doi: [10.1111/j.1365-2966.2005.09902.x](https://doi.org/10.1111/j.1365-2966.2005.09902.x).
- J. M. D. Kruijssen, J. L. Pfeffer, M. Reina-Campos, R. A. Crain, and N. Bastian. The formation and assembly history of the Milky Way revealed by its globular cluster population. *MNRAS*, 486(3):3180–3202, July 2019. doi: [10.1093/mnras/sty1609](https://doi.org/10.1093/mnras/sty1609).

- P.-Y. Lablanche, M. Cappellari, E. Emsellem, F. Bournaud, L. Michel-Dansac, K. Alatalo, L. Blitz, M. Bois, M. Bureau, R. L. Davies, T. A. Davis, P. T. de Zeeuw, P.-A. Duc, S. Khochfar, D. Krajnović, H. Kuntschner, R. Morganti, R. M. McDermid, T. Naab, T. Oosterloo, M. Sarzi, N. Scott, P. Serra, A.-M. Weijmans, and L. M. Young. The ATLAS 3D project - XII. Recovery of the mass-to-light ratio of simulated early-type barred galaxies with axisymmetric dynamical models. *MNRAS*, 424:1495–1521, Aug. 2012. doi: [10.1111/j.1365-2966.2012.21343.x](https://doi.org/10.1111/j.1365-2966.2012.21343.x).
- C. F. P. Laporte, K. V. Johnston, F. A. Gómez, N. Garavito-Camargo, and G. Besla. The influence of Sagittarius and the Large Magellanic Cloud on the stellar disc of the Milky Way Galaxy. *MNRAS*, 481(1):286–306, Nov. 2018. doi: [10.1093/mnras/sty1574](https://doi.org/10.1093/mnras/sty1574).
- M. Latour, A. Calamida, T. O. Husser, S. Kamann, S. Dreizler, and J. Brinchmann. A stellar census in globular clusters with MUSE. A new perspective on the multiple main sequences of ω Centauri. *A&A*, 653:L8, Sept. 2021. doi: [10.1051/0004-6361/202141791](https://doi.org/10.1051/0004-6361/202141791).
- M. Latour, S. Hämerich, M. Dorsch, U. Heber, T. O. Husser, S. Kamman, S. Dreizler, and J. Brinchmann. SHOTGLAS. II. MUSE spectroscopy of blue horizontal branch stars in the core of ω Centauri and NGC6752. *A&A*, 677:A86, Sept. 2023. doi: [10.1051/0004-6361/202346597](https://doi.org/10.1051/0004-6361/202346597).
- R. Leaman, D. A. Vandenberg, and J. T. Mendel. The bifurcated age-metallicity relation of Milky Way globular clusters and its implications for the accretion history of the galaxy. *MNRAS*, 436(1):122–135, Nov. 2013. doi: [10.1093/mnras/stt1540](https://doi.org/10.1093/mnras/stt1540).
- M. G. Lee, J. H. Bae, and I. S. Jang. Detection of Intracluster Globular Clusters in the First JWST Images of the Gravitational Lens Cluster SMACS J0723.3-7327 at $z = 0.39$. *ApJ*, 940(1):L19, Nov. 2022. doi: [10.3847/2041-8213/ac990b](https://doi.org/10.3847/2041-8213/ac990b).
- Y. W. Lee, J. M. Joo, Y. J. Sohn, S. C. Rey, H. C. Lee, and A. R. Walker. Multiple stellar populations in the globular cluster ω Centauri as tracers of a merger event. *Nature*, 402(6757):55–57, Nov. 1999. doi: [10.1038/46985](https://doi.org/10.1038/46985).
- G. Y. C. Leung, R. Leaman, G. van de Ven, M. Lyubenova, L. Zhu, A. D. Bolatto, J. Falcón-Barroso, L. Blitz, H. Dannerbauer, D. B. Fisher, R. C. Levy, S. F. Sanchez, D. Utomo, S. Vogel, T. Wong, and B. Ziegler. The EDGE-CALIFA survey: validating stellar dynamical mass models with CO kinematics. *MNRAS*, 477:254–292, June 2018. doi: [10.1093/mnras/sty288](https://doi.org/10.1093/mnras/sty288).
- C. Li, G. Zhao, Y. Jia, S. Liao, C. Yang, and Q. Wang. Flare and Warp of Galactic Disk with OB Stars from Gaia DR2. *ApJ*, 871(2):208, Feb. 2019. doi: [10.3847/1538-4357/aafa17](https://doi.org/10.3847/1538-4357/aafa17).
- H. Li, R. Li, S. Mao, D. Xu, R. J. Long, and E. Emsellem. Assessing the Jeans Anisotropic Multi-Gaussian Expansion method with the Illustris simulation. *MNRAS*, 455:3680–3692, Feb. 2016. doi: [10.1093/mnras/stv2565](https://doi.org/10.1093/mnras/stv2565).
- X. Y. Li, Y. Huang, B. Q. Chen, H. F. Wang, W. X. Sun, H. L. Guo, Q. Z. Li, and X. W. Liu. Mapping the Galactic Disk with the LAMOST and Gaia Red Clump Sample. IV. The Kinematic Signature of the Galactic Warp. *ApJ*, 901(1):56, Sept. 2020. doi: [10.3847/1538-4357/aba61e](https://doi.org/10.3847/1538-4357/aba61e).

M. Libralato, A. Bellini, R. P. van der Marel, J. Anderson, L. L. Watkins, G. Piotto, F. R. Ferraro, D. Nardiello, and E. Vesperini. Hubble Space Telescope Proper Motion (HSTPROMO) Catalogs of Galactic Globular Cluster. VI. Improved Data Reduction and Internal-kinematic Analysis of NGC 362. *ApJ*, 861(2):99, July 2018. doi: [10.3847/1538-4357/aac6c0](https://doi.org/10.3847/1538-4357/aac6c0).

M. Libralato, A. Bellini, E. Vesperini, G. Piotto, A. P. Milone, R. P. van der Marel, J. Anderson, A. Aparicio, B. Barbuy, L. R. Bedin, L. Borsato, S. Cassisi, E. Dalessandro, F. R. Ferraro, I. R. King, B. Lanzoni, D. Nardiello, S. Ortolani, A. Sarajedini, and S. T. Sohn. The Hubble Space Telescope UV Legacy Survey of Galactic Globular Clusters. XXIII. Proper-motion Catalogs and Internal Kinematics. *ApJ*, 934(2):150, Aug. 2022. doi: [10.3847/1538-4357/ac7727](https://doi.org/10.3847/1538-4357/ac7727).

G. Limberg, S. O. Souza, A. Pérez-Villegas, S. Rossi, H. D. Perottoni, and R. M. Santucci. Reconstructing the Disrupted Dwarf Galaxy Gaia-Sausage/Enceladus Using Its Stars and Globular Clusters. *ApJ*, 935(2):109, Aug. 2022. doi: [10.3847/1538-4357/ac8159](https://doi.org/10.3847/1538-4357/ac8159).

L. Lindegren, J. Hernández, A. Bombrun, S. Klioner, U. Bastian, M. Ramos-Lerate, A. de Torres, H. Steidelmüller, C. Stephenson, D. Hobbs, U. Lammers, M. Biermann, R. Geyer, T. Hilger, D. Michalik, U. Stampa, P. J. McMillan, J. Castañeda, M. Clotet, G. Comoretto, M. Davidson, C. Fabricius, G. Gracia, N. C. Hambly, A. Hutton, A. Mora, J. Portell, F. van Leeuwen, U. Abbas, A. Abreu, M. Altmann, A. Andrei, E. Anglada, L. Balaguer-Núñez, C. Barache, U. Becciani, S. Bertone, L. Bianchi, S. Bouquillon, G. Bourda, T. Brüsemeister, B. Bucciarelli, D. Busonero, R. Buzzi, R. Cancelliere, T. Carlucci, P. Charlot, N. Cheek, M. Crosta, C. Crowley, J. de Bruijne, F. de Felice, R. Drimmel, P. Esquej, A. Fienga, E. Fraile, M. Gai, N. Garralda, J. J. González-Vidal, R. Guerra, M. Hauser, W. Hofmann, B. Holl, S. Jordan, M. G. Lattanzi, H. Lenhardt, S. Liao, E. Licata, T. Lister, W. Löffler, J. Marchant, J. M. Martin-Fleitas, R. Messineo, F. Mignard, R. Morbidelli, E. Poggio, A. Riva, N. Rowell, E. Salguero, M. Sarasso, E. Sciacca, H. Siddiqui, R. L. Smart, A. Spagna, I. Steele, F. Taris, J. Torra, A. van Elteren, W. van Reeven, and A. Vecchiato. Gaia Data Release 2. The astrometric solution. *A&A*, 616:A2, Aug. 2018. doi: [10.1051/0004-6361/201832727](https://doi.org/10.1051/0004-6361/201832727).

L. Lindegren, U. Bastian, M. Biermann, A. Bombrun, A. de Torres, E. Gerlach, R. Geyer, J. Hernández, T. Hilger, D. Hobbs, S. A. Klioner, U. Lammers, P. J. McMillan, M. Ramos-Lerate, H. Steidelmüller, C. A. Stephenson, and F. van Leeuwen. Gaia Early Data Release 3. Parallax bias versus magnitude, colour, and position. *A&A*, 649: A4, May 2021a. doi: [10.1051/0004-6361/202039653](https://doi.org/10.1051/0004-6361/202039653).

L. Lindegren, S. A. Klioner, J. Hernández, A. Bombrun, M. Ramos-Lerate, H. Steidelmüller, U. Bastian, M. Biermann, A. de Torres, E. Gerlach, R. Geyer, T. Hilger, D. Hobbs, U. Lammers, P. J. McMillan, C. A. Stephenson, J. Castañeda, M. Davidson, C. Fabricius, G. Gracia-Abril, J. Portell, N. Rowell, D. Teyssier, F. Torra, S. Bartolomé, M. Clotet, N. Garralda, J. J. González-Vidal, J. Torra, U. Abbas, M. Altmann, E. Anglada Varela, L. Balaguer-Núñez, Z. Balog, C. Barache, U. Becciani, M. Berne, S. Bertone, L. Bianchi, S. Bouquillon, A. G. A. Brown, B. Bucciarelli, D. Busonero, A. G. Butkevich, R. Buzzi, R. Cancelliere, T. Carlucci, P. Charlot, M. R. L. Cioni, M. Crosta, C. Crowley, E. F. del Peloso, E. del Pozo, R. Drimmel, P. Esquej, A. Fienga, E. Fraile, M. Gai, M. Garcia-Reinaldos, R. Guerra, N. C. Hambly,

- M. Hauser, K. Janßen, S. Jordan, Z. Kostrzewska-Rutkowska, M. G. Lattanzi, S. Liao, E. Licata, T. A. Lister, W. Löfller, J. M. Marchant, A. Masip, F. Mignard, A. Mints, D. Molina, A. Mora, R. Morbidelli, C. P. Murphy, C. Pagani, P. Panuzzo, X. Peñalosa Esteller, E. Poggio, P. Re Fiorentin, A. Riva, A. Sagristà Sellés, V. Sanchez Gimenez, M. Sarasso, E. Sciacca, H. I. Siddiqui, R. L. Smart, D. Souami, A. Spagna, I. A. Steele, F. Taris, E. Utrilla, W. van Reeven, and A. Vecchiato. Gaia Early Data Release 3. The astrometric solution. *A&A*, 649:A2, May 2021b. doi: [10.1051/0004-6361/202039709](https://doi.org/10.1051/0004-6361/202039709).
- C. Liu, Y. Xu, J.-C. Wan, H.-F. Wang, J. L. Carlin, L.-C. Deng, H. J. Newberg, Z.-H. Cao, Y.-H. Hou, Y.-F. Wang, and Y. Zhang. Mapping the Milky Way with LAMOST I: method and overview. *Research in Astronomy and Astrophysics*, 17(9):096, Sept. 2017. doi: [10.1088/1674-4527/17/9/96](https://doi.org/10.1088/1674-4527/17/9/96).
- G. Lodato and P. Natarajan. Supermassive black hole formation during the assembly of pre-galactic discs. *MNRAS*, 371(4):1813–1823, Oct. 2006. doi: [10.1111/j.1365-2966.2006.10801.x](https://doi.org/10.1111/j.1365-2966.2006.10801.x).
- A. Loeb and F. A. Rasio. Collapse of Primordial Gas Clouds and the Formation of Quasar Black Holes. *ApJ*, 432:52, Sept. 1994. doi: [10.1086/174548](https://doi.org/10.1086/174548).
- M. López-Corredoira and J. Molgó. Flare in the Galactic stellar outer disc detected in SDSS-SEGUE data. *A&A*, 567:A106, July 2014. doi: [10.1051/0004-6361/201423706](https://doi.org/10.1051/0004-6361/201423706).
- M. López-Corredoira, A. Cabrera-Lavers, F. Garzón, and P. L. Hammersley. Old stellar Galactic disc in near-plane regions according to 2MASS: Scales, cut-off, flare and warp. *A&A*, 394:883–899, Nov. 2002. doi: [10.1051/0004-6361:20021175](https://doi.org/10.1051/0004-6361:20021175).
- J. T. Mackereth and J. Bovy. Weighing the stellar constituents of the galactic halo with APOGEE red giant stars. *MNRAS*, 492(3):3631–3646, Mar. 2020. doi: [10.1093/mnras/staa047](https://doi.org/10.1093/mnras/staa047).
- J. T. Mackereth, R. P. Schiavon, J. Pfeffer, C. R. Hayes, J. Bovy, B. Anguiano, C. Allende Prieto, S. Hasselquist, J. Holtzman, J. A. Johnson, S. R. Majewski, R. O’Connell, M. Shetrone, P. B. Tissera, and J. G. Fernández-Trincado. The origin of accreted stellar halo populations in the Milky Way using APOGEE, Gaia, and the EAGLE simulations. *MNRAS*, 482(3):3426–3442, Jan. 2019. doi: [10.1093/mnras/sty2955](https://doi.org/10.1093/mnras/sty2955).
- S. R. Majewski, D. L. Nidever, V. V. Smith, G. J. Damke, W. E. Kunkel, R. J. Patterson, D. Bizyaev, and A. E. García Pérez. Exploring Halo Substructure with Giant Stars: Substructure in the Local Halo as Seen in the Grid Giant Star Survey Including Extended Tidal Debris from ω Centauri. *ApJ*, 747(2):L37, Mar. 2012. doi: [10.1088/2041-8205/747/2/L37](https://doi.org/10.1088/2041-8205/747/2/L37).
- S. R. Majewski, R. P. Schiavon, P. M. Frinchaboy, C. Allende Prieto, R. Barkhouser, D. Bizyaev, B. Blank, S. Brunner, A. Burton, R. Carrera, S. D. Chojnowski, K. Cunha, C. Epstein, G. Fitzgerald, A. E. García Pérez, F. R. Hearty, C. Henderson, J. A. Holtzman, J. A. Johnson, C. R. Lam, J. E. Lawler, P. Maseman, S. Mészáros, M. Nelson, D. C. Nguyen, D. L. Nidever, M. Pinsonneault, M. Shetrone, S. Smee, V. V. Smith, T. Stolberg, M. F. Skrutskie, E. Walker, J. C. Wilson, G. Zasowski, F. Anders, S. Basu, S. Beland, M. R. Blanton, J. Bovy, J. R. Brownstein, J. Carlberg, W. Chaplin, C. Chiappini, D. J. Eisenstein, Y. Elsworth, D. Feuillet, S. W. Fleming, J. Galbraith-Frew,

- R. A. García, D. A. García-Hernández, B. A. Gillespie, L. Girardi, J. E. Gunn, S. Has selquist, M. R. Hayden, S. Hekker, I. Ivans, K. Kinemuchi, M. Klaene, S. Mahadevan, S. Mathur, B. Mosser, D. Muna, J. A. Munn, R. C. Nichol, R. W. O’Connell, J. K. Pare jko, A. C. Robin, H. Rocha-Pinto, M. Schultheis, A. M. Serenelli, N. Shane, V. Silva Aguirre, J. S. Sobeck, B. Thompson, N. W. Troup, D. H. Weinberg, and O. Zamora. The Apache Point Observatory Galactic Evolution Experiment (APOGEE). *AJ*, 154 (3):94, Sep 2017. doi: [10.3847/1538-3881/aa784d](https://doi.org/10.3847/1538-3881/aa784d).
- K. Malhan, R. A. Ibata, and N. F. Martin. Ghostly tributaries to the Milky Way: charting the halo’s stellar streams with the Gaia DR2 catalogue. *MNRAS*, 481(3):3442–3455, Dec. 2018. doi: [10.1093/mnras/sty2474](https://doi.org/10.1093/mnras/sty2474).
- P. Marigo, L. Girardi, A. Bressan, P. Rosenfield, B. Aringer, Y. Chen, M. Dussin, A. Nanni, G. Pastorelli, T. S. Rodrigues, M. Trabucchi, S. Bladh, J. Dalcanton, M. A. T. Groenewegen, J. Montalbán, and P. R. Wood. A New Generation of PARSEC-COLIBRI Stellar Isochrones Including the TP-AGB Phase. *ApJ*, 835(1):77, Jan. 2017. doi: [10.3847/1538-4357/835/1/77](https://doi.org/10.3847/1538-4357/835/1/77).
- A. Marín-Franch, A. Aparicio, G. Piotto, A. Rosenberg, B. Chaboyer, A. Sarajedini, M. Siegel, J. Anderson, L. R. Bedin, A. Dotter, M. Hempel, I. King, S. Majewski, A. P. Milone, N. Paust, and I. N. Reid. The ACS Survey of Galactic Globular Clusters. VII. Relative Ages. *ApJ*, 694(2):1498–1516, Apr. 2009. doi: [10.1088/0004-637X/694/2/1498](https://doi.org/10.1088/0004-637X/694/2/1498).
- A. F. Marino, A. P. Milone, A. Renzini, F. D’Antona, J. Anderson, L. R. Bedin, A. Bellini, G. Cordini, E. P. Lagioia, G. Piotto, and M. Tailo. The Hubble Space Telescope UV Legacy Survey of Galactic Globular Clusters - XIX. A chemical tagging of the multiple stellar populations over the chromosome maps. *MNRAS*, 487(3):3815–3844, Aug. 2019. doi: [10.1093/mnras/stz1415](https://doi.org/10.1093/mnras/stz1415).
- D. Massari, H. H. Koppelman, and A. Helmi. Origin of the system of globular clusters in the Milky Way. *A&A*, 630:L4, Oct. 2019. doi: [10.1051/0004-6361/201936135](https://doi.org/10.1051/0004-6361/201936135).
- J. May, L. Bronfman, H. Alvarez, D. C. Murphy, and P. Thaddeus. A deep CO survey of the third galactic quadrant. *A&AS*, 99:105–165, May 1993. URL <https://ui.adsabs.harvard.edu/abs/1993A&AS...99..105M>.
- J. May, H. Alvarez, and L. Bronfman. Physical properties of molecular clouds in the southern outer Galaxy. *A&A*, 327:325–332, Nov. 1997. URL <https://ui.adsabs.harvard.edu/abs/1997A&A...327..325M>.
- L. Mayer, B. Moore, T. Quinn, F. Governato, and J. Stadel. Tidal debris of dwarf spheroidals as a probe of structure formation models. *MNRAS*, 336(1):119–130, Oct. 2002. doi: [10.1046/j.1365-8711.2002.05721.x](https://doi.org/10.1046/j.1365-8711.2002.05721.x).
- M. Mayor, A. Duquennoy, S. Udry, J. Andersen, and B. Nordstrom. Primordial Binaries in the Globular Cluster ω Centauri. In E. F. Milone and J. C. Mermilliod, editors, *The Origins, Evolution, and Destinies of Binary Stars in Clusters*, volume 90 of *Astronomical Society of the Pacific Conference Series*, page 190, Jan. 1996. URL <https://ui.adsabs.harvard.edu/abs/1996ASPC...90..190M>.
- C. F. McKee, A. Parravano, and D. J. Hollenbach. Stars, Gas, and Dark Matter in the Solar Neighborhood. *ApJ*, 814:13, Nov. 2015. doi: [10.1088/0004-637X/814/1/13](https://doi.org/10.1088/0004-637X/814/1/13).

- P. J. McMillan. Mass models of the Milky Way. *MNRAS*, 414(3):2446–2457, July 2011. doi: [10.1111/j.1365-2966.2011.18564.x](https://doi.org/10.1111/j.1365-2966.2011.18564.x).
- P. J. McMillan. The mass distribution and gravitational potential of the Milky Way. *MNRAS*, 465:76–94, Feb. 2017. doi: [10.1093/mnras/stw2759](https://doi.org/10.1093/mnras/stw2759).
- A. McWilliam and M. Zoccali. Two Red Clumps and the X-shaped Milky Way Bulge. *ApJ*, 724(2):1491–1502, Dec. 2010. doi: [10.1088/0004-637X/724/2/1491](https://doi.org/10.1088/0004-637X/724/2/1491).
- S. Mészáros, T. Masseron, J. G. Fernández-Trincado, D. A. García-Hernández, L. Szigeti, K. Cunha, M. Shetrone, V. V. Smith, R. L. Beaton, T. C. Beers, J. R. Brownstein, D. Geisler, C. R. Hayes, H. Jönsson, R. R. Lane, S. R. Majewski, D. Minniti, R. R. Munoz, C. Nitschelm, A. Roman-Lopes, and O. Zamora. Homogeneous analysis of globular clusters from the APOGEE survey with the BACCHUS code - III. ω Cen. *MNRAS*, 505(2):1645–1660, Aug. 2021. doi: [10.1093/mnras/stab1208](https://doi.org/10.1093/mnras/stab1208).
- S. Mieske, M. J. Frank, H. Baumgardt, N. Lützgendorf, N. Neumayer, and M. Hilker. On central black holes in ultra-compact dwarf galaxies. *A&A*, 558:A14, Oct. 2013. doi: [10.1051/0004-6361/201322167](https://doi.org/10.1051/0004-6361/201322167).
- A. P. Milone, A. F. Marino, G. Piotto, L. R. Bedin, J. Anderson, A. Renzini, I. R. King, A. Bellini, T. M. Brown, S. Cassisi, F. D’Antona, H. Jerjen, D. Nardiello, M. Salaris, R. P. v. d. Marel, E. Vesperini, D. Yong, A. Aparicio, A. Sarajedini, and M. Zoccali. The Hubble Space Telescope UV Legacy Survey of galactic globular clusters - II. The seven stellar populations of NGC 7089 (M2)*. *MNRAS*, 447(1):927–938, Feb. 2015a. doi: [10.1093/mnras/stu2446](https://doi.org/10.1093/mnras/stu2446).
- A. P. Milone, A. F. Marino, G. Piotto, A. Renzini, L. R. Bedin, J. Anderson, S. Cassisi, F. D’Antona, A. Bellini, H. Jerjen, A. Pietrinferni, and P. Ventura. The Hubble Space Telescope UV Legacy Survey of Galactic Globular Clusters. III. A Quintuple Stellar Population in NGC 2808. *ApJ*, 808(1):51, July 2015b. doi: [10.1088/0004-637X/808/1/51](https://doi.org/10.1088/0004-637X/808/1/51).
- A. P. Milone, A. F. Marino, L. R. Bedin, J. Anderson, D. Apai, A. Bellini, P. Bergeron, A. J. Burgasser, A. Dotter, and J. M. Rees. The HST large programme on ω Centauri - I. Multiple stellar populations at the bottom of the main sequence probed in NIR-Optical. *MNRAS*, 469(1):800–812, July 2017a. doi: [10.1093/mnras/stx836](https://doi.org/10.1093/mnras/stx836).
- A. P. Milone, G. Piotto, A. Renzini, A. F. Marino, L. R. Bedin, E. Vesperini, F. D’Antona, D. Nardiello, J. Anderson, I. R. King, D. Yong, A. Bellini, A. Aparicio, B. Barbuy, T. M. Brown, S. Cassisi, S. Ortolani, M. Salaris, A. Sarajedini, and R. P. van der Marel. The Hubble Space Telescope UV Legacy Survey of Galactic globular clusters - IX. The Atlas of multiple stellar populations. *MNRAS*, 464(3):3636–3656, Jan. 2017b. doi: [10.1093/mnras/stw2531](https://doi.org/10.1093/mnras/stw2531).
- A. P. Milone, A. F. Marino, A. Renzini, F. D’Antona, J. Anderson, B. Barbuy, L. R. Bedin, A. Bellini, T. M. Brown, S. Cassisi, G. Cordoni, E. P. Lagioia, D. Nardiello, S. Ortolani, G. Piotto, A. Sarajedini, M. Tailo, R. P. van der Marel, and E. Vesperini. The Hubble Space Telescope UV legacy survey of galactic globular clusters – XVI. The helium abundance of multiple populations. *Monthly Notices of the Royal Astronomical Society*, 481(4):5098–5122, 09 2018. ISSN 0035-8711. doi: [10.1093/mnras/sty2573](https://doi.org/10.1093/mnras/sty2573). URL <https://doi.org/10.1093/mnras/sty2573>.

- M. Milosavljević. On the Origin of Nuclear Star Clusters in Late-Type Spiral Galaxies. *ApJ*, 605(1):L13–L16, Apr. 2004. doi: [10.1086/420696](https://doi.org/10.1086/420696).
- I. Misgeld and M. Hilker. Families of dynamically hot stellar systems over 10 orders of magnitude in mass. *MNRAS*, 414(4):3699–3710, July 2011. doi: [10.1111/j.1365-2966.2011.18669.x](https://doi.org/10.1111/j.1365-2966.2011.18669.x).
- M. Miyamoto and R. Nagai. Three-dimensional models for the distribution of mass in galaxies. *PASJ*, 27:533–543, Jan. 1975. URL <https://ui.adsabs.harvard.edu/abs/1975PASJ...27..533M>.
- A. F. J. Moffat. A Theoretical Investigation of Focal Stellar Images in the Photographic Emulsion and Application to Photographic Photometry. *A&A*, 3:455, Dec. 1969. URL <https://ui.adsabs.harvard.edu/abs/1969A&A.....3..455M>.
- Y. Momany, S. Zaggia, G. Gilmore, G. Piotto, G. Carraro, L. R. Bedin, and F. de Angeli. Outer structure of the Galactic warp and flare: explaining the Canis Major over-density. *A&A*, 451(2):515–538, May 2006. doi: [10.1051/0004-6361:20054081](https://doi.org/10.1051/0004-6361:20054081).
- G. Monari, B. Famaey, A. Siebert, R. J. J. Grand, D. Kawata, and C. Boily. The effects of bar-spiral coupling on stellar kinematics in the Galaxy. *MNRAS*, 461(4):3835–3846, Oct. 2016. doi: [10.1093/mnras/stw1564](https://doi.org/10.1093/mnras/stw1564).
- L. Mowla, K. G. Iyer, G. Desprez, V. Estrada-Carpenter, N. S. Martis, G. Noiro, G. T. Sarrouh, V. Strait, Y. Asada, R. G. Abraham, G. Brammer, M. Sawicki, C. J. Willott, M. Bradac, R. Doyon, A. Muzzin, C. Pacifici, S. Ravindranath, and J. Zabl. The Sparkler: Evolved High-redshift Globular Cluster Candidates Captured by JWST. *ApJ*, 937(2):L35, Oct. 2022. doi: [10.3847/2041-8213/ac90ca](https://doi.org/10.3847/2041-8213/ac90ca).
- L. Mowla, K. Iyer, Y. Asada, G. Desprez, V. Y. Y. Tan, N. Martis, G. Sarrouh, V. Strait, R. Abraham, M. Bradač, G. Brammer, A. Muzzin, C. Pacifici, S. Ravindranath, M. Sawicki, C. Willott, V. Estrada-Carpenter, N. Jahan, G. Noiro, J. Matharu, G. Rihtarsič, and J. Zabl. The Firefly Sparkle: The Earliest Stages of the Assembly of A Milky Way-type Galaxy in a 600 Myr Old Universe. *arXiv e-prints*, art. arXiv:2402.08696, Feb. 2024. doi: [10.48550/arXiv.2402.08696](https://doi.org/10.48550/arXiv.2402.08696).
- G. C. Myeong, E. Vasiliev, G. Iorio, N. W. Evans, and V. Belokurov. Evidence for two early accretion events that built the Milky Way stellar halo. *MNRAS*, 488(1):1235–1247, Sept. 2019. doi: [10.1093/mnras/stz1770](https://doi.org/10.1093/mnras/stz1770).
- D. M. Nataf, A. Udalski, A. Gould, P. Fouqué, and K. Z. Stanek. The Split Red Clump of the Galactic Bulge from OGLE-III. *ApJ*, 721(1):L28–L32, Sept. 2010. doi: [10.1088/2041-8205/721/1/L28](https://doi.org/10.1088/2041-8205/721/1/L28).
- J. F. Navarro, C. S. Frenk, and S. D. M. White. The Structure of Cold Dark Matter Halos. *ApJ*, 462:563, May 1996. doi: [10.1086/177173](https://doi.org/10.1086/177173).
- S. Nayakshin, M. I. Wilkinson, and A. King. Competitive feedback in galaxy formation. *MNRAS*, 398(1):L54–L57, Sept. 2009. doi: [10.1111/j.1745-3933.2009.00709.x](https://doi.org/10.1111/j.1745-3933.2009.00709.x).
- M. Ness, K. Freeman, E. Athanassoula, E. Wylie-De-Boer, J. Bland-Hawthorn, G. F. Lewis, D. Yong, M. Asplund, R. R. Lane, L. L. Kiss, and R. Ibata. The Origin of the

Split Red Clump in the Galactic Bulge of the Milky Way. *ApJ*, 756(1):22, Sept. 2012. doi: [10.1088/0004-637X/756/1/22](https://doi.org/10.1088/0004-637X/756/1/22).

N. Neumayer and C. J. Walcher. Are Nuclear Star Clusters the Precursors of Massive Black Holes? *Advances in Astronomy*, 2012:709038, Jan. 2012. doi: [10.1155/2012/709038](https://doi.org/10.1155/2012/709038).

N. Neumayer, A. Seth, and T. Böker. Nuclear star clusters. *A&A Rev.*, 28(1):4, July 2020. doi: [10.1007/s00159-020-00125-0](https://doi.org/10.1007/s00159-020-00125-0).

D. D. Nguyen, A. C. Seth, N. Neumayer, S. Iguchi, M. Cappellari, J. Strader, L. Chomiuk, E. Tremou, F. Pacucci, K. Nakanishi, A. Bahramian, P. M. Nguyen, M. den Brok, C. C. Ahn, K. T. Voggel, N. Kacharov, T. Tsukui, C. K. Ly, A. Dumont, and R. Pechetti. Improved Dynamical Constraints on the Masses of the Central Black Holes in Nearby Low-mass Early-type Galactic Nuclei and the First Black Hole Determination for NGC 205. *ApJ*, 872(1):104, Feb. 2019. doi: [10.3847/1538-4357/aafe7a](https://doi.org/10.3847/1538-4357/aafe7a).

M. S. Nitschai, M. Cappellari, and N. Neumayer. First Gaia dynamical model of the Milky Way disc with six phase space coordinates: a test for galaxy dynamics. *MNRAS*, 494(4):6001–6011, Apr. 2020a. doi: [10.1093/mnras/staa1128](https://doi.org/10.1093/mnras/staa1128).

M. S. Nitschai, N. Neumayer, and A. Feldmeier-Krause. Three-dimensional Analysis of the Minispiral at the Galactic Center: Orbital Parameters, Periods, and the Mass of the Black Hole. *ApJ*, 896(1):68, June 2020b. doi: [10.3847/1538-4357/ab8ea8](https://doi.org/10.3847/1538-4357/ab8ea8).

M. S. Nitschai, A.-C. Eilers, N. Neumayer, M. Cappellari, and H.-W. Rix. Dynamical Model of the Milky Way Using APOGEE and Gaia Data. *ApJ*, 916(2):112, Aug. 2021. doi: [10.3847/1538-4357/ac04b5](https://doi.org/10.3847/1538-4357/ac04b5).

M. S. Nitschai, N. Neumayer, C. Clontz, M. Häberle, A. C. Seth, T. O. Husser, S. Kamann, M. Alfaro-Cuello, N. Kacharov, A. Bellini, A. Dotter, S. Dreizler, A. Feldmeier-Krause, M. Latour, M. Libralato, A. P. Milone, R. Pechetti, G. van de Ven, K. Voggel, and D. R. Weisz. oMEGACat. I. MUSE Spectroscopy of 300,000 Stars within the Half-light Radius of ω Centauri. *ApJ*, 958(1):8, Nov. 2023. doi: [10.3847/1538-4357/acf5db](https://doi.org/10.3847/1538-4357/acf5db).

M. S. Nitschai, N. Neumayer, M. Häberle, C. Clontz, A. C. Seth, A. P. Milone, M. Alfaro-Cuello, A. Bellini, S. Dreizler, T. O. Feldmeier-Krause, Husser, N. Kacharov, S. Kamann, A., M. Latour, M. Libralato, G. van de Ven, K. Voggel, and Z. Wang. oMEGACat III. Multi-band photometry and metallicities reveal spatially well-mixed populations within ω Centauri’s half-light radius. *submitted to ApJ*, 2024.

T. Nordlander, A. J. Korn, O. Richard, and K. Lind. Atomic Diffusion and Mixing in Old Stars. III. Analysis of NGC 6397 Stars under New Constraints. *ApJ*, 753(1):48, July 2012. doi: [10.1088/0004-637X/753/1/48](https://doi.org/10.1088/0004-637X/753/1/48).

J. E. Norris. The Helium Abundances of ω Centauri. *ApJ*, 612(1):L25–L28, Sept. 2004. doi: [10.1086/423986](https://doi.org/10.1086/423986).

M. A. Norris and S. J. Kannappan. The ubiquity and dual nature of ultra-compact dwarfs. *MNRAS*, 414(1):739–758, June 2011. doi: [10.1111/j.1365-2966.2011.18440.x](https://doi.org/10.1111/j.1365-2966.2011.18440.x).

- E. Noyola, K. Gebhardt, and M. Bergmann. Gemini and Hubble Space Telescope Evidence for an Intermediate-Mass Black Hole in ω Centauri. *ApJ*, 676(2):1008–1015, Apr. 2008. doi: [10.1086/529002](https://doi.org/10.1086/529002).
- E. Noyola, K. Gebhardt, M. Kissler-Patig, N. Lützgendorf, B. Jalali, P. T. de Zeeuw, and H. Baumgardt. Very Large Telescope Kinematics for Omega Centauri: Further Support for a Central Black Hole. *ApJ*, 719(1):L60–L64, Aug. 2010. doi: [10.1088/2041-8205/719/1/L60](https://doi.org/10.1088/2041-8205/719/1/L60).
- J. H. Oort, F. J. Kerr, and G. Westerhout. The galactic system as a spiral nebula (Council Note). *MNRAS*, 118:379, Jan. 1958. doi: [10.1093/mnras/118.4.379](https://doi.org/10.1093/mnras/118.4.379).
- S. Ortolani, A. Renzini, R. Gilmozzi, G. Marconi, B. Barbuy, E. Bica, and R. M. Rich. Near-coeval formation of the Galactic bulge and halo inferred from globular cluster ages. *Nature*, 377(6551):701–704, Oct. 1995. doi: [10.1038/377701a0](https://doi.org/10.1038/377701a0).
- E. Pancino, F. R. Ferraro, M. Bellazzini, G. Piotto, and M. Zoccali. New Evidence for the Complex Structure of the Red Giant Branch in ω Centauri. *ApJ*, 534(1):L83–L87, May 2000. doi: [10.1086/312658](https://doi.org/10.1086/312658).
- E. Pancino, A. Seleznev, F. R. Ferraro, M. Bellazzini, and G. Piotto. The multiple stellar population in ω Centauri: spatial distribution and structural properties. *MNRAS*, 345(2):683–690, Oct. 2003. doi: [10.1046/j.1365-8711.2003.06981.x](https://doi.org/10.1046/j.1365-8711.2003.06981.x).
- R. Pechetti, S. Kamann, D. Krajnović, A. Seth, G. van de Ven, N. Neumayer, S. Dreizler, P. M. Weilbacher, S. Martens, and F. Wragg. ω Centauri: A MUSE discovery of a counter-rotating core. *MNRAS*, Jan. 2024. doi: [10.1093/mnras/stae294](https://doi.org/10.1093/mnras/stae294).
- F. Pedregosa, G. Varoquaux, A. Gramfort, V. Michel, B. Thirion, O. Grisel, M. Blondel, P. Prettenhofer, R. Weiss, V. Dubourg, J. Vanderplas, A. Passos, D. Cournapeau, M. Brucher, M. Perrot, and E. Duchesnay. Scikit-learn: Machine learning in Python. *Journal of Machine Learning Research*, 12:2825–2830, 2011.
- J. Pfeffer and H. Baumgardt. Ultra-compact dwarf galaxy formation by tidal stripping of nucleated dwarf galaxies. *MNRAS*, 433(3):1997–2005, Aug. 2013. doi: [10.1093/mnras/stt867](https://doi.org/10.1093/mnras/stt867).
- J. Pfeffer, B. F. Griffen, H. Baumgardt, and M. Hilker. Contribution of stripped nuclear clusters to globular cluster and ultracompact dwarf galaxy populations. *MNRAS*, 444(4):3670–3683, Nov. 2014. doi: [10.1093/mnras/stu1705](https://doi.org/10.1093/mnras/stu1705).
- J. Pfeffer, C. Lardo, N. Bastian, S. Saracino, and S. Kamann. The accreted nuclear clusters of the Milky Way. *MNRAS*, 500(2):2514–2524, Jan. 2021. doi: [10.1093/mnras/staa3407](https://doi.org/10.1093/mnras/staa3407).
- T. Piffl, J. Binney, P. J. McMillan, M. Steinmetz, A. Helmi, R. F. G. Wyse, O. Bienaymé, J. Bland-Hawthorn, K. Freeman, B. Gibson, G. Gilmore, E. K. Grebel, G. Kordopatis, J. F. Navarro, Q. Parker, W. A. Reid, G. Seabroke, A. Siebert, F. Watson, and T. Zwitter. Constraining the Galaxy’s dark halo with RAVE stars. *MNRAS*, 445(3):3133–3151, Dec. 2014. doi: [10.1093/mnras/stu1948](https://doi.org/10.1093/mnras/stu1948).

- G. Piotto, S. Villanova, L. R. Bedin, R. Gratton, S. Cassisi, Y. Momany, A. Recio-Blanco, S. Lucatello, J. Anderson, I. R. King, A. Pietrinferni, and G. Carraro. Metallicities on the Double Main Sequence of ω Centauri Imply Large Helium Enhancement. *ApJ*, 621(2):777–784, Mar. 2005. doi: [10.1086/427796](https://doi.org/10.1086/427796).
- G. Piotto, A. P. Milone, L. R. Bedin, J. Anderson, I. R. King, A. F. Marino, D. Nardiello, A. Aparicio, B. Barbuy, A. Bellini, T. M. Brown, S. Cassisi, A. M. Cool, A. Cunial, E. Dalessandro, F. D’Antona, F. R. Ferraro, S. Hidalgo, B. Lanzoni, M. Monelli, S. Ortolani, A. Renzini, M. Salaris, A. Sarajedini, R. P. van der Marel, E. Vesperini, and M. Zoccali. The Hubble Space Telescope UV Legacy Survey of Galactic Globular Clusters. I. Overview of the Project and Detection of Multiple Stellar Populations. *AJ*, 149(3):91, Mar. 2015. doi: [10.1088/0004-6256/149/3/91](https://doi.org/10.1088/0004-6256/149/3/91).
- H. C. Plummer. On the problem of distribution in globular star clusters. *MNRAS*, 71: 460–470, Mar. 1911. doi: [10.1093/mnras/71.5.460](https://doi.org/10.1093/mnras/71.5.460).
- M. Portail, O. Gerhard, C. Wegg, and M. Ness. Dynamical modelling of the galactic bulge and bar: the Milky Way’s pattern speed, stellar and dark matter mass distribution. *MNRAS*, 465:1621–1644, Feb. 2017. doi: [10.1093/mnras/stw2819](https://doi.org/10.1093/mnras/stw2819).
- S. F. Portegies Zwart and S. L. W. McMillan. The Runaway Growth of Intermediate-Mass Black Holes in Dense Star Clusters. *ApJ*, 576(2):899–907, Sept. 2002. doi: [10.1086/341798](https://doi.org/10.1086/341798).
- L. Posti and A. Helmi. Mass and shape of the Milky Way’s dark matter halo with globular clusters from Gaia and Hubble. *A&A*, 621:A56, Jan. 2019. doi: [10.1051/0004-6361/201833355](https://doi.org/10.1051/0004-6361/201833355).
- E. Pouliasis, P. Di Matteo, and M. Haywood. A Milky Way with a massive, centrally concentrated thick disc: new Galactic mass models for orbit computations. *A&A*, 598: A66, Feb. 2017. doi: [10.1051/0004-6361/201527346](https://doi.org/10.1051/0004-6361/201527346).
- C. Pryor and G. Meylan. Velocity Dispersions for Galactic Globular Clusters. In S. G. Djorgovski and G. Meylan, editors, *Structure and Dynamics of Globular Clusters*, volume 50 of *Astronomical Society of the Pacific Conference Series*, page 357, Jan. 1993. URL <https://ui.adsabs.harvard.edu/abs/1993ASPC...50..357P>.
- M. J. Reid and A. Brunthaler. The Proper Motion of Sagittarius A*. II. The Mass of Sagittarius A*. *ApJ*, 616:872–884, Dec. 2004. doi: [10.1086/424960](https://doi.org/10.1086/424960).
- M. J. Reid, K. M. Menten, X. W. Zheng, A. Brunthaler, L. Moscadelli, Y. Xu, B. Zhang, M. Sato, M. Honma, T. Hirota, K. Hachisuka, Y. K. Choi, G. A. Moellenbrock, and A. Bartkiewicz. Trigonometric Parallaxes of Massive Star-Forming Regions. VI. Galactic Structure, Fundamental Parameters, and Noncircular Motions. *ApJ*, 700:137–148, July 2009. doi: [10.1088/0004-637X/700/1/137](https://doi.org/10.1088/0004-637X/700/1/137).
- M. J. Reid, K. M. Menten, A. Brunthaler, X. W. Zheng, T. M. Dame, Y. Xu, J. Li, N. Sakai, Y. Wu, K. Immer, B. Zhang, A. Sanna, L. Moscadelli, K. L. J. Rygl, A. Bartkiewicz, B. Hu, L. H. Quiroga-Nuñez, and H. J. van Langevelde. Trigonometric Parallaxes of High-mass Star-forming Regions: Our View of the Milky Way. *ApJ*, 885(2):131, Nov. 2019. doi: [10.3847/1538-4357/ab4a11](https://doi.org/10.3847/1538-4357/ab4a11).

- C. Reylé, D. J. Marshall, A. C. Robin, and M. Schultheis. The Milky Way's external disc constrained by 2MASS star counts. *A&A*, 495(3):819–826, Mar. 2009. doi: [10.1051/0004-6361/200811341](https://doi.org/10.1051/0004-6361/200811341).
- S. Rezaei Kh., C. A. L. Bailer-Jones, D. W. Hogg, and M. Schultheis. Detection of the Milky Way spiral arms in dust from 3D mapping. *A&A*, 618:A168, Oct. 2018. doi: [10.1051/0004-6361/201833284](https://doi.org/10.1051/0004-6361/201833284).
- H.-W. Rix and J. Bovy. The Milky Way's stellar disk. Mapping and modeling the Galactic disk. *A&A Rev.*, 21:61, May 2013. doi: [10.1007/s00159-013-0061-8](https://doi.org/10.1007/s00159-013-0061-8).
- H.-W. Rix, P. T. de Zeeuw, N. Cretton, R. P. van der Marel, and C. M. Carollo. Dynamical Modeling of Velocity Profiles: The Dark Halo around the Elliptical Galaxy NGC 2434. *ApJ*, 488:702–719, Oct. 1997. doi: [10.1086/304733](https://doi.org/10.1086/304733).
- B. E. Robertson, S. Tacchella, B. D. Johnson, K. Hainline, L. Whitler, D. J. Eisenstein, R. Endsley, M. Rieke, D. P. Stark, S. Alberts, A. Dressler, E. Egami, R. Hausen, G. Rieke, I. Shavaei, C. C. Williams, C. N. A. Willmer, S. Arribas, N. Bonaventura, A. Bunker, A. J. Cameron, S. Carniani, S. Charlot, J. Chevallard, M. Curti, E. Curtis-Lake, F. D'Eugenio, P. Jakobsen, T. J. Looser, N. Lützgendorf, R. Maiolino, M. V. Maseda, T. Rawle, H. W. Rix, R. Smit, H. Übler, C. Willott, J. Witstok, S. Baum, R. Bhatawdekar, K. Boyett, Z. Chen, A. de Graaff, M. Florian, J. M. Helton, R. E. Hviding, Z. Ji, N. Kumari, J. Lyu, E. Nelson, L. Sandles, A. Saxena, K. A. Suess, F. Sun, M. Topping, and I. E. B. Wallace. Identification and properties of intense star-forming galaxies at redshifts $z > 10$. *Nature Astronomy*, 7:611–621, May 2023. doi: [10.1038/s41550-023-01921-1](https://doi.org/10.1038/s41550-023-01921-1).
- A. C. Robin, C. Reylé, S. Derrière, and S. Picaud. A synthetic view on structure and evolution of the Milky Way. *A&A*, 409:523–540, Oct. 2003. doi: [10.1051/0004-6361:20031117](https://doi.org/10.1051/0004-6361:20031117).
- J. Rybizki, H.-W. Rix, M. Demleitner, C. A. L. Bailer-Jones, and W. J. Cooper. Characterizing the Gaia radial velocity sample selection function in its native photometry. *MNRAS*, 500(1):397–409, Jan. 2021. doi: [10.1093/mnras/staa3089](https://doi.org/10.1093/mnras/staa3089).
- M. Salaris, A. Chieffi, and O. Straniero. The alpha -enhanced Isochrones and Their Impact on the FITS to the Galactic Globular Cluster System. *ApJ*, 414:580, Sept. 1993. doi: [10.1086/173105](https://doi.org/10.1086/173105).
- R. Sánchez-Janssen, P. Côté, L. Ferrarese, E. W. Peng, J. Roediger, J. P. Blakeslee, E. Emsellem, T. H. Puzia, C. Spengler, J. Taylor, K. A. Álamo-Martínez, A. Boselli, M. Cantiello, J.-C. Cuillandre, P.-A. Duc, P. Durrell, S. Gwyn, L. A. MacArthur, A. Lançon, S. Lim, C. Liu, S. Mei, B. Miller, R. Muñoz, J. C. Mihos, S. Paudel, M. Powalka, and E. Toloba. The Next Generation Virgo Cluster Survey. XXIII. Fundamentals of Nuclear Star Clusters over Seven Decades in Galaxy Mass. *ApJ*, 878(1):18, June 2019. doi: [10.3847/1538-4357/aaf4fd](https://doi.org/10.3847/1538-4357/aaf4fd).
- A. Sarajedini, L. R. Bedin, B. Chaboyer, A. Dotter, M. Siegel, J. Anderson, A. Aparicio, I. King, S. Majewski, A. Marín-Franch, G. Piotto, I. N. Reid, and A. Rosenberg. The ACS Survey of Galactic Globular Clusters. I. Overview and Clusters without Previous Hubble Space Telescope Photometry. *AJ*, 133(4):1658–1672, Apr. 2007. doi: [10.1086/511979](https://doi.org/10.1086/511979).

- E. F. Schlafly and D. P. Finkbeiner. Measuring Reddening with Sloan Digital Sky Survey Stellar Spectra and Recalibrating SFD. *ApJ*, 737(2):103, Aug. 2011. doi: [10.1088/0004-637X/737/2/103](https://doi.org/10.1088/0004-637X/737/2/103).
- R. Schönrich, J. Binney, and W. Dehnen. Local kinematics and the local standard of rest. *MNRAS*, 403:1829–1833, Apr. 2010. doi: [10.1111/j.1365-2966.2010.16253.x](https://doi.org/10.1111/j.1365-2966.2010.16253.x).
- R. Schönrich, P. McMillan, and L. Eyer. Distances and parallax bias in Gaia DR2. *MNRAS*, May 2019. doi: [10.1093/mnras/stz1451](https://doi.org/10.1093/mnras/stz1451).
- M. Schwarzschild. A numerical model for a triaxial stellar system in dynamical equilibrium. *ApJ*, 232:236–247, Aug. 1979. doi: [10.1086/157282](https://doi.org/10.1086/157282).
- A. Seth, M. Agüeros, D. Lee, and A. Basu-Zych. The Coincidence of Nuclear Star Clusters and Active Galactic Nuclei. *ApJ*, 678(1):116–130, May 2008. doi: [10.1086/528955](https://doi.org/10.1086/528955).
- A. C. Seth, R. van den Bosch, S. Mieske, H. Baumgardt, M. D. Brok, J. Strader, N. Neumayer, I. Chilingarian, M. Hilker, R. McDermid, L. Spitler, J. Brodie, M. J. Frank, and J. L. Walsh. A supermassive black hole in an ultra-compact dwarf galaxy. *Nature*, 513(7518):398–400, Sept. 2014. doi: [10.1038/nature13762](https://doi.org/10.1038/nature13762).
- J. Shen, R. M. Rich, J. Kormendy, C. D. Howard, R. De Propris, and A. Kunder. Our Milky Way as a Pure-disk Galaxy—A Challenge for Galaxy Formation. *ApJ*, 720(1):L72–L76, Sept. 2010. doi: [10.1088/2041-8205/720/1/L72](https://doi.org/10.1088/2041-8205/720/1/L72).
- M. H. Siegel, A. Dotter, S. R. Majewski, A. Sarajedini, B. Chaboyer, D. L. Nidever, J. Anderson, A. Marín-Franch, A. Rosenberg, L. R. Bedin, A. Aparicio, I. King, G. Piotto, and I. N. Reid. The ACS Survey of Galactic Globular Clusters: M54 and Young Populations in the Sagittarius Dwarf Spheroidal Galaxy. *ApJ*, 667(1):L57–L60, Sept. 2007. doi: [10.1086/522003](https://doi.org/10.1086/522003).
- D. M. Skowron, J. Skowron, P. Mróz, A. Udalski, P. Pietrukowicz, I. Soszyński, M. K. Szymański, R. Poleski, S. Kozłowski, K. Ulaczyk, K. Rybicki, P. Iwanek, M. . Wrona, and M. Gromadzki. Mapping the Northern Galactic Disk Warp with Classical Cepheids. *Acta Astron.*, 69(4):305–320, Dec. 2019. doi: [10.32023/0001-5237/69.4.1](https://doi.org/10.32023/0001-5237/69.4.1).
- M. F. Skrutskie, R. M. Cutri, R. Stiening, M. D. Weinberg, S. Schneider, J. M. Carpenter, C. Beichman, R. Capps, T. Chester, J. Elias, J. Huchra, J. Liebert, C. Lonsdale, D. G. Monet, S. Price, P. Seitzer, T. Jarrett, J. D. Kirkpatrick, J. E. Gizis, E. Howard, T. Evans, J. Fowler, L. Fullmer, R. Hurt, R. Light, E. L. Kopan, K. A. Marsh, H. L. McCallon, R. Tam, S. Van Dyk, and S. Wheelock. The Two Micron All Sky Survey (2MASS). *AJ*, 131(2):1163–1183, Feb. 2006. doi: [10.1086/498708](https://doi.org/10.1086/498708).
- A. Sollima, F. R. Ferraro, E. Pancino, and M. Bellazzini. On the discrete nature of the red giant branch of ω Centauri. *MNRAS*, 357(1):265–274, Feb. 2005. doi: [10.1111/j.1365-2966.2005.08646.x](https://doi.org/10.1111/j.1365-2966.2005.08646.x).
- A. Sollima, F. R. Ferraro, M. Bellazzini, L. Origlia, O. Straniero, and E. Pancino. Deep FORS1 Observations of the Double Main Sequence of ω Centauri. *ApJ*, 654(2):915–922, Jan. 2007. doi: [10.1086/509711](https://doi.org/10.1086/509711).

- K. R. Stewart, J. S. Bullock, R. H. Wechsler, A. H. Maller, and A. R. Zentner. Merger Histories of Galaxy Halos and Implications for Disk Survival. *ApJ*, 683(2):597–610, Aug. 2008. doi: [10.1086/588579](https://doi.org/10.1086/588579).
- O. Streicher. Python-CPL: Python interface for the ESO Common Pipeline Library, Dec. 2016. URL <https://ascl.net/1612.001>.
- S. Ströbele, P. La Penna, R. Arsenault, R. D. Conzelmann, B. Delabre, M. Duchateau, R. Dorn, E. Fedrigo, N. Hubin, J. Quentin, P. Jolley, M. Kiekebusch, J. P. Kirchbauer, B. Klein, J. Kolb, H. Kuntschner, M. Le Louarn, J. L. Lizon, P. Y. Madec, L. Pettaffi, C. Soenke, S. Tordo, J. Vernet, and R. Muradore. GALACSI system design and analysis. In *Adaptive Optics Systems III*, volume 8447 of *Society of Photo-Optical Instrumentation Engineers (SPIE) Conference Series*, page 844737, July 2012. doi: [10.1117/12.926110](https://doi.org/10.1117/12.926110).
- D. Syer and S. Tremaine. Made-to-measure N-body systems. *MNRAS*, 282(1):223–233, Sept. 1996. doi: [10.1093/mnras/282.1.223](https://doi.org/10.1093/mnras/282.1.223).
- M. Tailo, M. Di Criscienzo, F. D’Antona, V. Caloi, and P. Ventura. The mosaic multiple stellar populations in ω Centauri: the horizontal branch and the main sequence. *MNRAS*, 457(4):4525–4535, Apr. 2016. doi: [10.1093/mnras/stw319](https://doi.org/10.1093/mnras/stw319).
- The pandas development team. pandas-dev/pandas: Pandas, v1.5.3, 2023. URL <https://doi.org/10.5281/zenodo.7549438>.
- Y.-S. Ting, H.-W. Rix, C. Conroy, A. Y. Q. Ho, and J. Lin. Measuring 14 Elemental Abundances with $R = 1800$ LAMOST Spectra. *ApJ*, 849(1):L9, Nov. 2017a. doi: [10.3847/2041-8213/aa921c](https://doi.org/10.3847/2041-8213/aa921c).
- Y.-S. Ting, H.-W. Rix, C. Conroy, A. Y. Q. Ho, and J. Lin. Measuring 14 Elemental Abundances with $R = 1800$ LAMOST Spectra. *ApJ*, 849(1):L9, Nov. 2017b. doi: [10.3847/2041-8213/aa921c](https://doi.org/10.3847/2041-8213/aa921c).
- J. Tonry and M. Davis. A survey of galaxy redshifts. I. Data reduction techniques. *AJ*, 84:1511–1525, Oct. 1979. doi: [10.1086/112569](https://doi.org/10.1086/112569).
- F. Torra, J. Castañeda, C. Fabricius, L. Lindegren, M. Clotet, J. J. González-Vidal, S. Bartolomé, U. Bastian, M. Bernet, M. Biermann, N. Garralda, A. Gúrpide, U. Lammers, J. Portell, and J. Torra. Gaia Early Data Release 3. Building the Gaia DR3 source list - Cross-match of Gaia observations. *A&A*, 649:A10, May 2021. doi: [10.1051/0004-6361/202039637](https://doi.org/10.1051/0004-6361/202039637).
- G. van de Ven, R. C. E. van den Bosch, E. K. Verolme, and P. T. de Zeeuw. The dynamical distance and intrinsic structure of the globular cluster ω Centauri. *A&A*, 445(2):513–543, Jan. 2006a. doi: [10.1051/0004-6361:20053061](https://doi.org/10.1051/0004-6361:20053061).
- G. van de Ven, R. C. E. van den Bosch, E. K. Verolme, and P. T. de Zeeuw. The dynamical distance and intrinsic structure of the globular cluster ω Centauri. *A&A*, 445:513–543, Jan. 2006b. doi: [10.1051/0004-6361:20053061](https://doi.org/10.1051/0004-6361:20053061).
- R. C. E. van den Bosch, G. van de Ven, E. K. Verolme, M. Cappellari, and P. T. de Zeeuw. Triaxial orbit based galaxy models with an application to the (apparent) decoupled

- core galaxy NGC 4365. *MNRAS*, 385(2):647–666, Apr. 2008. doi: [10.1111/j.1365-2966.2008.12874.x](https://doi.org/10.1111/j.1365-2966.2008.12874.x).
- R. P. van der Marel and J. Anderson. New Limits on an Intermediate-Mass Black Hole in Omega Centauri. II. Dynamical Models. *ApJ*, 710(2):1063–1088, Feb. 2010. doi: [10.1088/0004-637X/710/2/1063](https://doi.org/10.1088/0004-637X/710/2/1063).
- R. P. van der Marel, N. Cretton, P. T. de Zeeuw, and H.-W. Rix. Improved Evidence for a Black Hole in M32 from HST/FOS Spectra. II. Axisymmetric Dynamical Models. *ApJ*, 493(2):613–631, Jan 1998. doi: [10.1086/305147](https://doi.org/10.1086/305147).
- D. A. Vandenberg, O. Richard, G. Michaud, and J. Richer. Models of Metal-poor Stars with Gravitational Settling and Radiative Accelerations. II. The Age of the Oldest Stars. *ApJ*, 571(1):487–500, May 2002. doi: [10.1086/339895](https://doi.org/10.1086/339895).
- E. Vasiliev and H. Baumgardt. Gaia EDR3 view on galactic globular clusters. *MNRAS*, 505(4):5978–6002, Aug. 2021. doi: [10.1093/mnras/stab1475](https://doi.org/10.1093/mnras/stab1475).
- R. A. Vázquez, J. May, G. Carraro, L. Bronfman, A. Moitinho, and G. Baume. Spiral Structure in the Outer Galactic Disk. I. The Third Galactic Quadrant. *ApJ*, 672(2):930–939, Jan. 2008. doi: [10.1086/524003](https://doi.org/10.1086/524003).
- S. Villanova, G. Piotto, I. R. King, J. Anderson, L. R. Bedin, R. G. Gratton, S. Cassisi, Y. Momany, A. Bellini, A. M. Cool, A. Recio-Blanco, and A. Renzini. The Multiplicity of the Subgiant Branch of ω Centauri: Evidence for Prolonged Star Formation. *ApJ*, 663(1):296–314, July 2007. doi: [10.1086/517905](https://doi.org/10.1086/517905).
- S. Villanova, D. Geisler, R. G. Gratton, and S. Cassisi. The Metallicity Spread and the Age-Metallicity Relation of ω Centauri. *ApJ*, 791(2):107, Aug. 2014. doi: [10.1088/0004-637X/791/2/107](https://doi.org/10.1088/0004-637X/791/2/107).
- P. Virtanen, R. Gommers, T. E. Oliphant, M. Haberland, T. Reddy, D. Cournapeau, E. Burovski, P. Peterson, W. Weckesser, J. Bright, S. J. van der Walt, M. Brett, J. Wilson, K. J. Millman, N. Mayorov, A. R. J. Nelson, E. Jones, R. Kern, E. Larson, C. J. Carey, İ. Polat, Y. Feng, E. W. Moore, J. VanderPlas, D. Laxalde, J. Perktold, R. Cimrman, I. Henriksen, E. A. Quintero, C. R. Harris, A. M. Archibald, A. H. Ribeiro, F. Pedregosa, P. van Mulbregt, and SciPy 1.0 Contributors. SciPy 1.0: Fundamental Algorithms for Scientific Computing in Python. *Nature Methods*, 17:261–272, 2020. doi: [10.1038/s41592-019-0686-2](https://doi.org/10.1038/s41592-019-0686-2).
- M. Vogelsberger, S. Genel, V. Springel, P. Torrey, D. Sijacki, D. Xu, G. Snyder, S. Bird, D. Nelson, and L. Hernquist. Properties of galaxies reproduced by a hydrodynamic simulation. *Nature*, 509:177–182, May 2014. doi: [10.1038/nature13316](https://doi.org/10.1038/nature13316).
- M. G. Walker, M. Mateo, E. W. Olszewski, B. Sen, and M. Woodroffe. Clean Kinematic Samples in Dwarf Spheroidals: An Algorithm for Evaluating Membership and Estimating Distribution Parameters When Contamination is Present. *AJ*, 137(2):3109–3138, Feb. 2009. doi: [10.1088/0004-6256/137/2/3109](https://doi.org/10.1088/0004-6256/137/2/3109).
- Z. Wang, M. R. Hayden, S. Sharma, M. Xiang, Y.-S. Ting, J. Bland-Hawthorn, and B. Chen. Reliable stellar abundances of individual stars with the MUSE integral-field spectrograph. *MNRAS*, 514(1):1034–1053, July 2022. doi: [10.1093/mnras/stac1425](https://doi.org/10.1093/mnras/stac1425).

- L. L. Watkins, R. P. van der Marel, A. Bellini, and J. Anderson. Hubble Space Telescope Proper Motion (HSTPROMO) Catalogs of Galactic Globular Clusters. III. Dynamical Distances and Mass-to-Light Ratios. *ApJ*, 812:149, Oct. 2015a. doi: [10.1088/0004-637X/812/2/149](https://doi.org/10.1088/0004-637X/812/2/149).
- L. L. Watkins, R. P. van der Marel, A. Bellini, and J. Anderson. Hubble Space Telescope Proper Motion (HSTPROMO) Catalogs of Galactic Globular Cluster. II. Kinematic Profiles and Maps. *ApJ*, 803(1):29, Apr. 2015b. doi: [10.1088/0004-637X/803/1/29](https://doi.org/10.1088/0004-637X/803/1/29).
- L. L. Watkins, R. P. van der Marel, S. T. Sohn, and N. W. Evans. Evidence for an Intermediate-mass Milky Way from Gaia DR2 Halo Globular Cluster Motions. *ApJ*, 873(2):118, Mar. 2019. doi: [10.3847/1538-4357/ab089f](https://doi.org/10.3847/1538-4357/ab089f).
- C. Wegg, O. Gerhard, and M. Portail. The structure of the Milky Way’s bar outside the bulge. *MNRAS*, 450:4050–4069, July 2015a. doi: [10.1093/mnras/stv745](https://doi.org/10.1093/mnras/stv745).
- C. Wegg, O. Gerhard, and M. Portail. The structure of the Milky Way’s bar outside the bulge. *MNRAS*, 450(4):4050–4069, July 2015b. doi: [10.1093/mnras/stv745](https://doi.org/10.1093/mnras/stv745).
- C. Wegg, O. Gerhard, and M. Bieth. The Gravitational Force Field of the Galaxy Measured From the Kinematics of RR Lyrae in Gaia. *MNRAS*, Feb. 2019. doi: [10.1093/mnras/stz572](https://doi.org/10.1093/mnras/stz572).
- J. L. Weiland, R. G. Arendt, G. B. Berriman, E. Dwek, H. T. Freudenreich, M. G. Hauser, T. Kelsall, C. M. Lisse, M. Mitra, S. H. Moseley, N. P. Odegard, R. F. Silverberg, T. J. Sodroski, W. J. Spiesman, and S. W. Stemwedel. COBE Diffuse Background Experiment Observations of the Galactic Bulge. *ApJ*, 425:L81, Apr. 1994. doi: [10.1086/187315](https://doi.org/10.1086/187315).
- P. M. Weilbacher, O. Streicher, and R. Palsa. MUSE-DRP: MUSE Data Reduction Pipeline, Oct. 2016. URL <https://ascl.net/1610.004>.
- P. M. Weilbacher, R. Palsa, O. Streicher, R. Bacon, T. Urrutia, L. Wisotzki, S. Conseil, B. Husemann, A. Jarno, A. Kelz, A. Pécontal-Rousset, J. Richard, M. M. Roth, F. Selman, and J. Vernet. The data processing pipeline for the MUSE instrument. *A&A*, 641:A28, Sept. 2020. doi: [10.1051/0004-6361/202037855](https://doi.org/10.1051/0004-6361/202037855).
- B. Welch, D. Coe, J. M. Diego, A. Zitrin, E. Zackrisson, P. Dimauro, Y. Jiménez-Teja, P. Kelly, G. Mahler, M. Oguri, F. X. Timmes, R. Windhorst, M. Florian, S. E. de Mink, R. J. Avila, J. Anderson, L. Bradley, K. Sharon, A. Vikaeus, S. McCandliss, M. Bradač, J. Rigby, B. Frye, S. Toft, V. Strait, M. Trenti, S. Sharma, F. Andrade-Santos, and T. Broadhurst. A highly magnified star at redshift 6.2. *Nature*, 603(7903):815–818, Mar. 2022. doi: [10.1038/s41586-022-04449-y](https://doi.org/10.1038/s41586-022-04449-y).
- Wes McKinney. Data Structures for Statistical Computing in Python. In Stéfan van der Walt and Jarrod Millman, editors, *Proceedings of the 9th Python in Science Conference*, pages 56 – 61, 2010. doi: [10.25080/Majora-92bf1922-00a](https://doi.org/10.25080/Majora-92bf1922-00a).
- L. M. Widrow, S. Gardner, B. Yanny, S. Dodelson, and H.-Y. Chen. Galactoseismology: Discovery of Vertical Waves in the Galactic Disk. *ApJ*, 750:L41, May 2012. doi: [10.1088/2041-8205/750/2/L41](https://doi.org/10.1088/2041-8205/750/2/L41).

- B. Willman and J. Strader. “Galaxy,” Defined. AJ, 144(3):76, Sept. 2012. doi: [10.1088/0004-6256/144/3/76](https://doi.org/10.1088/0004-6256/144/3/76).
- E. L. Wright, P. R. M. Eisenhardt, A. K. Mainzer, M. E. Ressler, R. M. Cutri, T. Jarrett, J. D. Kirkpatrick, D. Padgett, R. S. McMillan, M. Skrutskie, S. A. Stanford, M. Cohen, R. G. Walker, J. C. Mather, D. Leisawitz, I. Gautier, Thomas N., I. McLean, D. Benford, C. J. Lonsdale, A. Blain, B. Mendez, W. R. Irace, V. Duval, F. Liu, D. Royer, I. Heinrichsen, J. Howard, M. Shannon, M. Kendall, A. L. Walsh, M. Larsen, J. G. Cardon, S. Schick, M. Schwalm, M. Abid, B. Fabinsky, L. Naes, and C.-W. Tsai. The Wide-field Infrared Survey Explorer (WISE): Mission Description and Initial On-orbit Performance. AJ, 140(6):1868–1881, Dec. 2010. doi: [10.1088/0004-6256/140/6/1868](https://doi.org/10.1088/0004-6256/140/6/1868).
- J. S. B. Wyithe, E. L. Turner, and D. N. Spergel. Gravitational Lens Statistics for Generalized NFW Profiles: Parameter Degeneracy and Implications for Self-Interacting Cold Dark Matter. ApJ, 555(1):504–523, Jul 2001. doi: [10.1086/321437](https://doi.org/10.1086/321437).
- M. Xiang, Y.-S. Ting, H.-W. Rix, N. Sandford, S. Buder, K. Lind, X.-W. Liu, J.-R. Shi, and H.-W. Zhang. Abundance Estimates for 16 Elements in 6 Million Stars from LAMOST DR5 Low-Resolution Spectra. ApJS, 245(2):34, Dec. 2019. doi: [10.3847/1538-4365/ab5364](https://doi.org/10.3847/1538-4365/ab5364).
- D. G. York, J. Adelman, J. Anderson, John E., S. F. Anderson, J. Annis, N. A. Bahcall, J. A. Bakken, R. Barkhouser, S. Bastian, E. Berman, W. N. Boroski, S. Bracker, C. Briegel, J. W. Briggs, J. Brinkmann, R. Brunner, S. Burles, L. Carey, M. A. Carr, F. J. Castander, B. Chen, P. L. Colestock, A. J. Connolly, J. H. Crocker, I. Csabai, P. C. Czarapata, J. E. Davis, M. Doi, T. Dombeck, D. Eisenstein, N. Ellman, B. R. Elms, M. L. Evans, X. Fan, G. R. Federwitz, L. Fiscelli, S. Friedman, J. A. Frieman, M. Fukugita, B. Gillespie, J. E. Gunn, V. K. Gurbani, E. de Haas, M. Haldeman, F. H. Harris, J. Hayes, T. M. Heckman, G. S. Hennessy, R. B. Hindsley, S. Holm, D. J. Holmgren, C.-h. Huang, C. Hull, D. Husby, S.-I. Ichikawa, T. Ichikawa, Ž. Ivezić, S. Kent, R. S. J. Kim, E. Kinney, M. Klaene, A. N. Kleinman, S. Kleinman, G. R. Knapp, J. Korienek, R. G. Kron, P. Z. Kunszt, D. Q. Lamb, B. Lee, R. F. Leger, S. Limmongkol, C. Lindenmeyer, D. C. Long, C. Loomis, J. Loveday, R. Lucinio, R. H. Lupton, B. MacKinnon, E. J. Mannery, P. M. Mantsch, B. Margon, P. McGehee, T. A. McKay, A. Meiksin, A. Merelli, D. G. Monet, J. A. Munn, V. K. Narayanan, T. Nash, E. Neilsen, R. Neswold, H. J. Newberg, R. C. Nichol, T. Nicinski, M. Nonino, N. Okada, S. Okamura, J. P. Ostriker, R. Owen, A. G. Pauls, J. Peoples, R. L. Peterson, D. Petravick, J. R. Pier, A. Pope, R. Pordes, A. Prosapio, R. Rechenmacher, T. R. Quinn, G. T. Richards, M. W. Richmond, C. H. Rivetta, C. M. Rockosi, K. Ruthmansdorfer, D. Sandford, D. J. Schlegel, D. P. Schneider, M. Sekiguchi, G. Sergey, K. Shimasaku, W. A. Siegmund, S. Smee, J. A. Smith, S. Snedden, R. Stone, C. Stoughton, M. A. Strauss, C. Stubbs, M. SubbaRao, A. S. Szalay, I. Szapudi, G. P. Szokoly, A. R. Thakar, C. Tremonti, D. L. Tucker, A. Uomoto, D. Vanden Berk, M. S. Vogeley, P. Waddell, S.-i. Wang, M. Watanabe, D. H. Weinberg, B. Yanny, N. Yasuda, and SDSS Collaboration. The Sloan Digital Sky Survey: Technical Summary. AJ, 120(3):1579–1587, Sept. 2000. doi: [10.1086/301513](https://doi.org/10.1086/301513).
- I. Yusifov. Pulsars and the Warp of the Galaxy. In B. Uyaniker, W. Reich, and R. Wielebinski, editors, *The Magnetized Interstellar Medium*, pages 165–169, Feb. 2004. URL <https://ui.adsabs.harvard.edu/abs/2004mim..proc..165Y>.

- L. Zhang, H.-W. Rix, G. van de Ven, J. Bovy, C. Liu, and G. Zhao. The Gravitational Potential near the Sun from SEGUE K-dwarf Kinematics. *ApJ*, 772(2):108, Aug. 2013. doi: [10.1088/0004-637X/772/2/108](https://doi.org/10.1088/0004-637X/772/2/108).
- J. C. Zinn, M. H. Pinsonneault, D. Huber, and D. Stello. Confirmation of the Gaia DR2 Parallax Zero-point Offset Using Asteroseismology and Spectroscopy in the Kepler Field. *ApJ*, 878(2):136, June 2019. doi: [10.3847/1538-4357/ab1f66](https://doi.org/10.3847/1538-4357/ab1f66).
- A. Zocchi, M. Gieles, and V. Hénault-Brunet. The effect of stellar-mass black holes on the central kinematics of ω Cen: a cautionary tale for IMBH interpretations. *MNRAS*, 482(4):4713–4725, Feb. 2019. doi: [10.1093/mnras/sty1508](https://doi.org/10.1093/mnras/sty1508).